

POLITECNICO DI TORINO

DOCTORATE SCHOOL

Ph. D. In Informatics and Systems – XXV cycle

Doctor of Philosophy Thesis

Glove Exoskeleton for Extra-Vehicular Activities Analysis of Requirements and Prototype Design (Part Two)



Favetto Alain

Advisor:

Prof. Giuseppe Carlo Calafiore

Coordinator:

Prof. Pietro Laface

This page is intentionally left blank

Dedicato a mio Padre...

Al tuo modo ruvido di trasmettere le emozioni.

Al tuo senso del dovere ed al tuo altruismo.

Ai tuoi modi di fare che da piccolo non capivo e oggi sono parte del mio essere.

A tutti i pensieri e le parole che vorrei averti detto e che sono rimasti solo nella mia testa.

A te che mi hai sempre trattato come un adulto.

A te che te ne sei andato prima che adulto lo potessi diventare davvero.

This page is intentionally left blank

INDEX

Index	5
Extra Vehicular Activities.....	8
Brief EVAs History	9
The EVA Spacesuit.....	10
<i>Brief U.S. Spacesuit History.....</i>	12
<i>Brief Soviet Union/Russian Spacesuit History.....</i>	13
<i>New Concepts of Spacesuit</i>	14
The EVA Glove.....	14
The Future of EVAs.....	16
<i>Tomorrow's EVA needs</i>	16
<i>Tomorrow's EVA Glove needs</i>	18
The Smart EVA Glove Project.....	19
State of The Art.....	20
Exoskeletons	21
<i>Rehabilitation Exoskeleton.....</i>	22
<i>Haptic Exoskeleton.....</i>	29
<i>Assistive Exoskeleton.....</i>	34
Robotic Hands	37
Sensors.....	40
Actuators.....	42
The Human Hand	45
Human Hand Anatomy.....	45
<i>Anthropometric Dimensions</i>	47
<i>Finger Constraints</i>	49
Static constraints.....	49
Dynamic Intra-Finger constraints.....	49
Dynamic Inter-Finger constraints.....	51
Hand Grasp Taxonomy.....	53
<i>Hand Tasks and the Number of Fingers</i>	54

Index

Hand Capabilities	55
<i>Finger Joint's Force and Torque</i>	55
<i>Finger Joint's Velocity</i>	60
<i>Finger Joint's Power</i>	60
Human Hand Model.....	60
<i>Human Hand Kinematics</i>	61
Direct Kinematics	63
Inverse Kinematics	65
<i>Human Hand Dynamics</i>	69
Test on EVA Glove.....	76
Test EVA Glove	77
Glove Box	78
Test on Human Hand Performances.....	81
<i>Test Subjects</i>	81
<i>Experimental Measurement Setup</i>	81
<i>Test Protocol</i>	82
<i>Test Results</i>	84
<i>Discussion of the results</i>	87
Measuring of Glove Stiffness	89
<i>First Test: Experimental Measurement Setup</i>	89
<i>First Test: The Protocol</i>	92
<i>First Test: Results</i>	93
<i>Second Test: Experimental Measurement Setup</i>	97
<i>Second Test: The Protocol</i>	100
<i>Second Test: Results</i>	101
The Exoskeleton.....	109
Main idea and overview of the possibilities	111
The Wire Actuated Solution.....	113
<i>The First Wire Actuated Solution</i>	115
Static Analysis.....	118
Optimization	124

Index

Algorithm	127
Results.....	130
Observations.....	138
<i>The second Wire Actuated Solution</i>	139
Static Analysis.....	141
Optimization	144
Algorithm	145
Results.....	147
Observations.....	171
The Double Parallelogram Solution	172
Conclusions	177
Elements of Roto-translation Matrix Q	181
Four Fingers Matrix Qi	181
Thumb Matrix $Q0$	182
Euler-Lagrange Equation Coefficients.....	183
List of Tables.....	184
List of Figures.....	185
Bibliography	190

CHAPTER 4:

“If an astronaut cannot use his or her hands adequately in a pressurized suit there is simply no reason to send humans into space...”

Durant, 1995

TEST ON EVA GLOVE

Human hand capabilities, such as dexterity and perception, are one of the main reasons in man's superiority to robotic devices, in presence of unpredictable and adaptive tasks and where procedures and strategies cannot be defined in advance, becoming too diverse and complex. In EVA environment the hand is not only a multi-purpose tool, but it is also the main mean of locomotion and material handling. However, existing pressure gloves significantly reduce the hand performances and, in addition, they are uncomfortable, sometimes leading to pain or minor injuries. The gloves have been causing of great chagrin since the very first space mission, they have been changed and improved since the Apollo Program and are under investigation also today.

Glove evaluation has been highly subjective in the past; generally, astronauts with extensive experience in EVA provided their opinions and feedback regarding the virtues and vices of gloves, but no quantitative analysis was performed. A new concept of less subjective and more scientific studies has been developed in the last decade. Several works have been conducted to determine the influence of EVA glove on manual capabilities. Perhaps the most comprehensive study performed on the assessment of performance decrements wearing EVA gloves has been done by O'Hara [33]. In this article, two levels of hand conditions (barehanded and gloved), two levels of pressure and three hand sizes have been changed in order to obtain the data collection. Other important studies have been done utilizing different methods and approaches [40, 125, 126]. Six basic hand characteristics have been identified: range of motion, strength, tactility, dexterity, fatigue and comfort; each of them presents a list of parameters considered important indicators of the category or especially relevant in EVA (Table 23). It has to be underlined that the hand is a complex and integrated system in which each category influences and is influenced by other categories, generating a combined effect. The six categories can be divided into two groups. The first group comprises the capabilities directly connected to the hand physiology and anatomy: range of motion, strength and tactility. The remaining categories have been

Test on EVA Glove

Group	Capability	Main Parameters
1	Range of motion	Thumb Movement Finger Movement Wrist Movement
	Strength	Pinch and Grip force Pinch and Grip torque
	Tactile perception	Continuous Sensitivity Object Characterization Tactile Feedback
2	Dexterity	Precise Positioning Multiple object manipulation <u>Flexible object manipulation</u>
	Fatigue	Physiological Decay Manipulation Decay Performance Decay
	Comfort	Glove Characteristics Hand/Glove Interaction Local Hand Environment

Table 23: Hand Capabilities and related Performances

included in the second group. These categories are more complex than the previous ones, they represent a strict integration between the categories of group one and a series of physiological and psychological aspects. Wearing the glove reduces basic hand grip strength and the introduction of a differential pressure further reduces it; however, the effects on grips and pinches strength are sharply reduced. The tactile perception degradation is mainly influenced by the structure of the gloves and it remains unchanged with pressure change. Dexterity is reduced both by glove and pressure; this is caused by the limitation in the range of motion and sensitivity and increases up to six times the duration of every hand work.

In this section, two different tests on EVA gloves are reported. The first test aims at studying the influence of a specific model of EVA glove on the human hand capabilities and, in particular, on strength and fatigue. The second test is performed in order to empirically model the stiffness of the EVA glove, through the development of two different measurement setups.

Test EVA Glove

All the tests have been performed employing one single EVA glove model. The EVA Glove utilized for the tests is a left-handed Russian Orlan-DM glove [25]. Testing only one model of EVA glove can seem a limitation in terms of generalization of the results. However, it is important to underline that the methodology and the protocols developed can be applied to any, present or future, EVA glove model. The glove used in our tests is basically composed by three elements (Figure 46). Starting from the inner element it can be find the bladder, the restraint and the ITMG. The bladder is the first element of the glove and is designed to maintain the internal pressurized environment. The bladder is made of nylon, drawn to fiber as fine as silk and then dipped into rubber (urethane) six times to create an impermeable barrier between the human being and the vacuum of the space environment. A layer of Dacron is added to restrain the pressure bladder. Nylon is used because it is a good thermal and electrical insulator, it



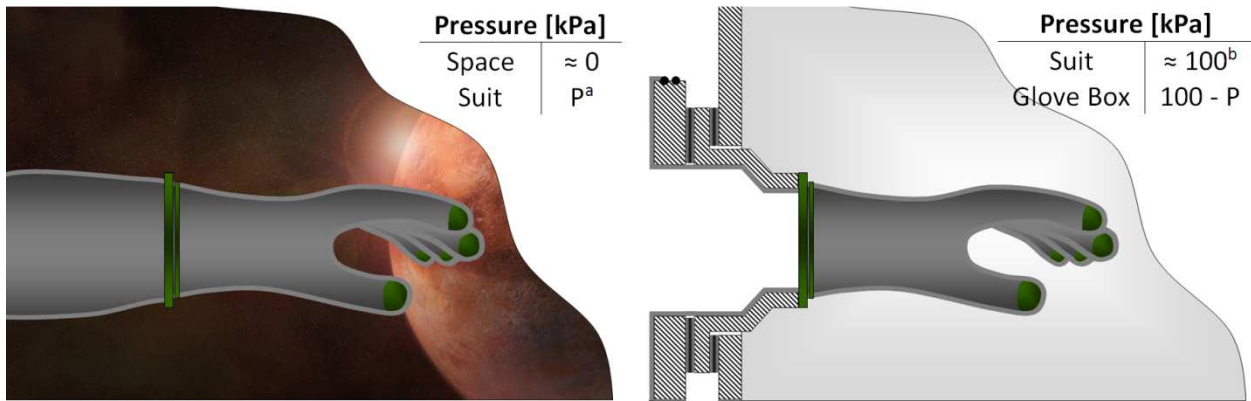
Figure 46: Three elements of Orlan-DM EVA glove; from left to right: bladder, restraint, ITMG

exhibits excellent resilience and melts instead of burning, a very important feature in a pure oxygen environment [127, 128]. Dacron is a polyester fiber used for its long flex life, high resilience and resistance to heat, chemicals and organic agents [129]. The restraint is the middle element and is responsible for carrying all pressure and loads both from the suit and from the astronaut. The ITMG is the external element of the glove and the main protection against thermal swings and the impact of hyper velocity micrometeoroid particles. The ITMG is a multilayer system with a very complex structure involving many materials. The main materials of ITMG are Nylon Ripstop, a very though material with high resistance to tearing and ripping, aluminized Mylar, mixed with layer of thermal insulator for heat protection [130], Teflon/Gore-Tex, Kevlar and Nomex for the mechanical protection from micrometeoroids particles [127]. The Fingertip is made of Room Temperature Vulcanized (RTV) silicon and Nomex. Silicon is essential to enhance tactility and protection at the same time. At the bottom of each phalanx and palm some jagged silicon rubber plates are placed in order to improve the friction grip. The operating pressure and the multilayer structure have a noticeable effect on the hand because the wearer is fighting against the internal pressure and the friction between the layers.

Glove Box

As previously explained, the negatives effects of the EVA gloves, and more generally of the EVA suit, are due to two factors: the multilayer structure of the vest and its own internal pressure. It is therefore necessary to reproduce both these two effects in order to fully understand the characteristics and to model the effects acting on the human being.

Test on EVA Glove



^a the internal pressure changes on the basis of the glove model

^b the internal pressure is equal to the atmosphere pressure

Figure 47: The glove into the space (left) and the glove inside the glove box (right)

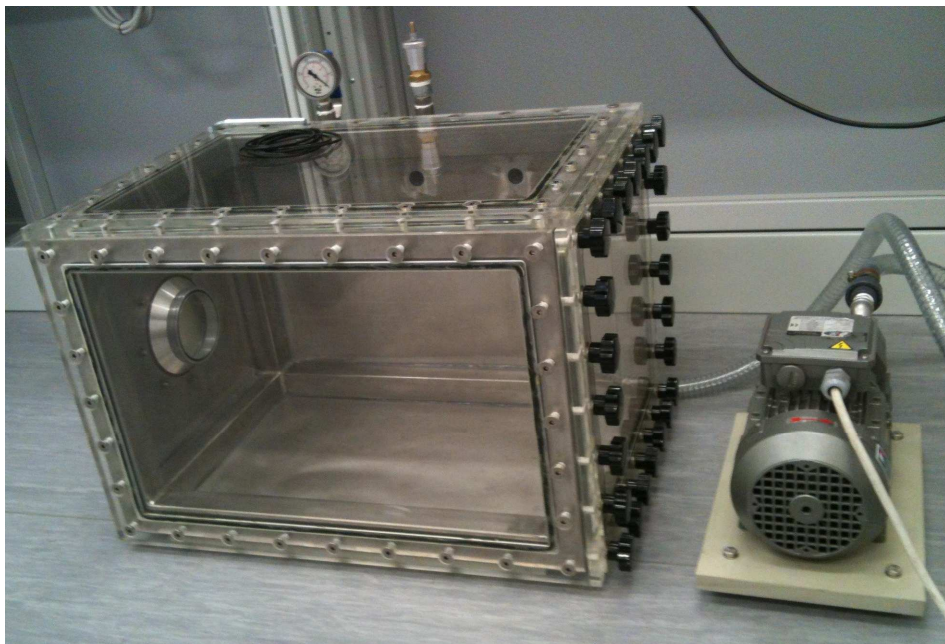


Figure 48: The custom-made glove box and all its elements

Reproducing the internal pressure of the glove by inflating air is very complicated in the course of tests. During EVA missions the astronaut's body is fully wrapped by the impermeable bladder and contained by the restraint granting no leakage; vice-versa during the glove tests the subject only wears a portion of spacesuit and, in this case, it is hard to ensure a fully impermeability. It has been decided to reduce the pressure of the external environment instead of increasing the internal pressure of the glove, using a custom made Glove Box in order to overcome this problem (Figure 47). A Glove Box is a sealed container of various forms and dimensions that is designed to allow the operator to manipulate objects in a controlled and desired atmosphere. Built into one side of the glove box, there are usually one or two gloves arranged in such a way to allow the user to insert their hands and to perform tasks inside the box without breaking the containment. The glove box (Figure 48) was designed and realized in order to reproduce the internal pressurization of the glove. The structure consists of a 430x440x630 mm aluminum parallelepiped, with three walls made of aluminum and the other three of transparent

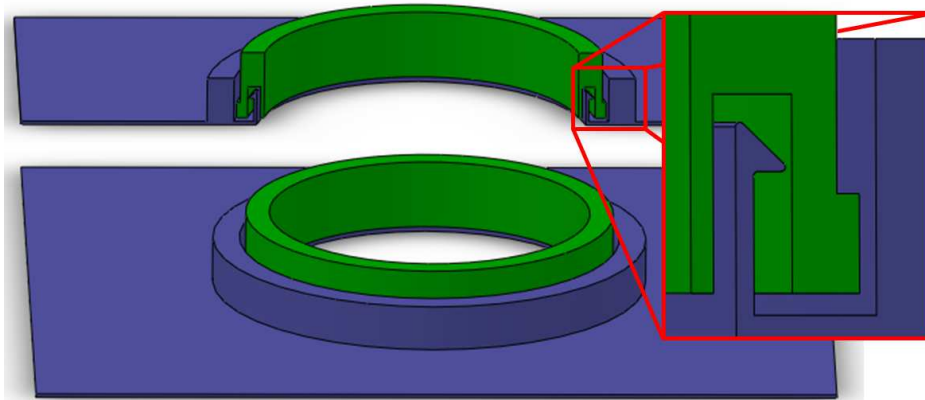


Figure 49: Detail of the airtight locking joint between the custom-made flange (blue) and the forearm Orlan-DM seal (green)



Figure 50: The Orlan-DM EVA glove inside the custom-made glove box with ITMG (left) and without ITMG (right)

Plexiglas 20mm thick. One of the aluminum sides shows an opening to permit the insertion of the forearm in an airtight flange. The flange ends with a joint made in such way to be exactly coupled with the forearm of the EVA glove (Figure 49).

Thus, different models of EVA gloves can be tested by substituting the flange with another one, custom made for the particular glove under test. One Plexiglas side is removable and kept close by a series of screws; it can be opened to insert or remove instruments when the vacuum pump is switched down. Air tightness is guaranteed by a gasket placed along the perimeter. The aluminum rear side shows the pneumatic connections. The pneumatic circuit consists of a vacuum pump, a manually adjustable safety valve and a vacuum manometer. The relative internal pressure level can be adjusted acting on the safety valve and seeing the manometer. The EVA Glove is fixed to the custom made flange by means of the restraint locking coupling (Figure 50); the internal bladder grants the separation between external environment pressure and internal pressure, thus obtaining the same differential pressure as in actual EVA missions.

Test on Human Hand Performances

Fully understanding the behavior of the EVA gloves and its interaction with the human hand are a fundamental requirement to be able to define constraints and to propose improvements for the next generation of EVA gloves. The following study is mainly focused on EVA glove performances in terms of hand and finger strength reduction and hand fatigue augmentation. Among all the six previously explained hand capabilities, it has been decided to primarily concentrate on these two performances because they result to be the most related to the device planned to be realized, influencing its constraints and concept. This study presents two main peculiarities with respect to other works that can be found in literature: the choice of the main focus on the left hand instead of the right hand and the measuring system. The left hand results to be the “weaker hand” for a great percentage of the human beings, but covers a fundamental role in any kind of job and activity. Usually, in order to perform tasks that implicate both hands, a human being uses its main hand to execute precision works (e.g. pull the trigger of a drill, turn a screwdriver), whereas utilizes his weak hand to perform power tasks (e.g. hold in position objects). Testing the left hand results to be a very interesting and useful activity. Finally, regarding the measuring system, it has been decided to utilize a home-made pneumatic hand dynamometer as following explained.

Test Subjects

A total of thirteen test subjects took part in this study. Test subjects were chosen following an initial pre selection based on the hand size. The main requirement, mandatory for each subject, was that their left hand had to fit inside the Orlan-DM glove. In particular, the subject's finger had to reach the glove fingertip and, at the same time, the finger crotch had to correspond to the bases of the glove fingers without uncomfortable sensations. To ascertain this, to each subject was asked to perform a series of movements wearing the EVA glove that involved all the articulations of the hand; at the end each of them gave a qualitative feedback of their sensations. This pre-selection can appear a trivial work but is indeed a key factor. EVA gloves are usually custom-made and adapted on the hand of astronauts; each astronaut possesses his own glove that fits exactly on his hand. If the subject pool is not carefully selected all the tests results can be useless and sidetracking. The subject pool included five females and eight males, ranging in age 25-36 years. Among the thirteen test subjects, two were left handed and eleven were right handed. All subjects were volunteers and consisted of IIT@Polito employees; none of them had ever worn an EVA glove before.

Experimental Measurement Setup

There are several technological possibilities to measure the force applied during hand grips and pinches using different technologies and sensors. A simple home-made pneumatic setup has been realized in order to measure the hand strength. The sensor is composed by three elements (a bulb syringe, a constant volume and a manometer) connected to each other by means of a pipe (Figure 51). When a force is applied to the syringe, it causes the variation of the internal pressure of the pneumatic circuit; this variation is then measured by the manometer (Figure 52). Other typologies of sensors usually have a favorite measurement direction which implies that not all the forces exchanged between the hand and the device can be correctly measured. Moreover, more common hand dynamometers, available on the market, are not multipurpose sensors but, on the contrary, are custom made on a specific kind of grip and pinch. The pneumatic hand dynamometer allows every force that the hand applies to the sensitive part to be measured independently from its direction and application point.

Test Protocol

Literature identifies and classifies several types of hand grips mainly divided into power and precision grips, according to the force exerted [131]. This distinction not only aims at classifying the grips on the basis of the magnitude of the applied force, but also implies a more complex difference. Power grips largely involve the use of the muscles placed into the forearm and are typically performed by the whole hand. On the contrary, precision grips make an extensive use of the muscles placed inside the palm of the hand and are usually performed by two or three fingers and called pinches. Not all the types of grips and pinches can be significant in this kind of experiment. It has to be considered that the activities that the astronauts have to perform into space are limited by the EVA glove; therefore only a subset of every possible hand grip can be effectively performed in that particular environment. In this test, four different tasks, shown in Figure 53, have been chosen to be representative of the common astronaut tasks during EVA. The choice of the tasks to be performed also stems from a particular study by Mishkin and Jau [106], in which the authors claim that, varying the number of finger involved in a specific task, the number of performable tasks change as following: two fingers can perform 40% of the possible hand tasks, three fingers can accomplish up to 90% and four fingers can complete the 99%. It is therefore interesting to examine the influence of the glove on the different fingers and while varying the number of fingers involved in each task. The grip nomenclature is not universally defined, thus the four chosen grips have been named as follows:

- *Power Grip*: spherical power grasp performed using all the five fingers, with the thumb opposing the four fingers
- *Two Finger Pinch*: precision pinch performed using only the thumb and the index finger

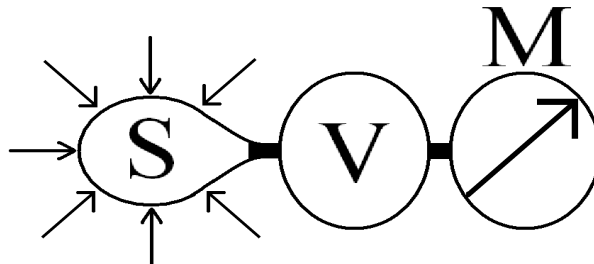


Figure 51: Pneumatic Dynamometer Circuit Scheme composed by Bulb Syringe (S), Constant Volume (V) and Manometer (M)



Figure 52: Home Made Measurement Setup outside (Left) and inside (Right) the Glove Box

Test on EVA Glove

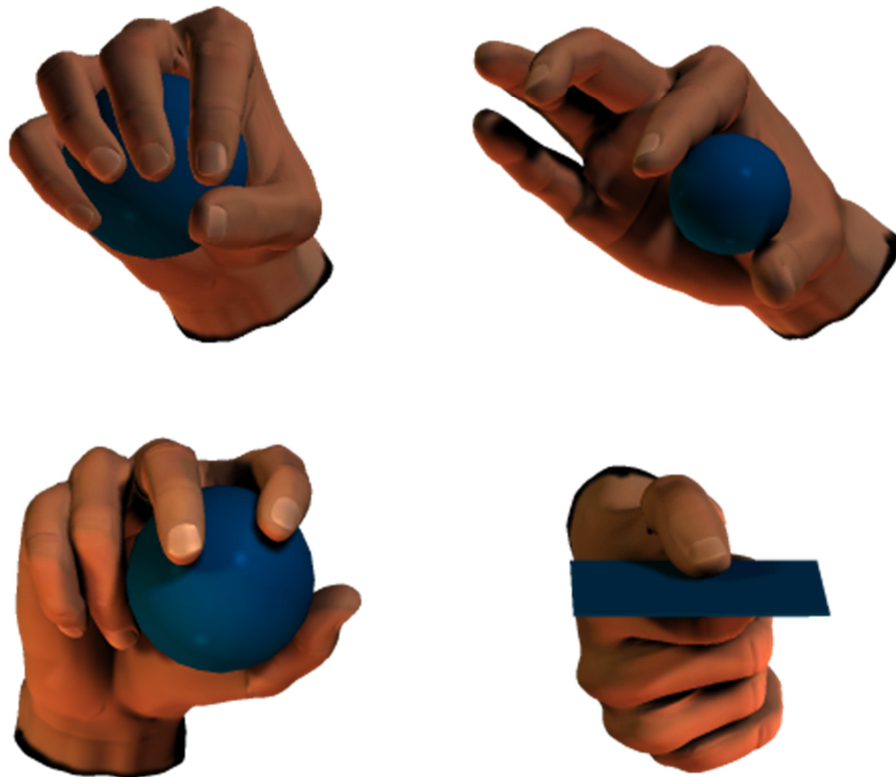


Figure 53: The four typologies of Hand Tasks: Power Grip (Top Left), Two Finger Pinch (Top Right), Three Finger Pinch (Bottom Left) and Lateral Pinch (Bottom Right)

- *Three Finger Pinch*: precision pinch performed with the thumb in opposition to the index and the middle finger
- *Lateral Pinch*: intermediate pinch performed with the thumb opposing the side of the fist

Once decided the typology of the task to be performed, it is necessary to define a series of standardized instructions to be followed by the subject during the tests, in order to guarantee the highest possible uniformity of the results. Before each test task, the corresponding grip position was shown to the involved subject. Furthermore the following instructions were provided:

1. Hold the bulb syringe with the left hand as shown in the relative task picture
2. Apply the highest possible force
3. Maintain this force for about one second
4. Return to the relax position

5. Repeat from point two to point four until it feels too tired to continue or it becomes too painful
Each subject had to perform the four grips in three different conditions: barehanded, wearing the unpressurized Orlan-DM glove and wearing the pressurized glove, with a total value of twelve tests. It was necessary to impose a time lapse between two subsequent tests in order to guarantee the reliability of the results. If the subject performed one test session in the morning, he was prevented from performing another one, at least until the late afternoon; the main reason to take this precaution was to assure that each task started with no initial fatigue. A test session is a complete series of repetitions of the instructions related to a single grip, performed barehanded or wearing the EVA glove. Since the previous explained instructions did not impose a fixed number of cycles of hand grips, the subject would

Test on EVA Glove

stop after a variable number of repetitions. Many factors could influence the amount of performed cycles; some of them were physiological, like fatigue and pain, but, on the basis of some post-execution declaration, also some strictly psychological elements, like motivation and stubbornness, could have a strong effect on the number of executions. It is important to underline that also the fatigue is a very subjective characteristic that combines physical and mental effects, which can be influenced by factors such as motivations, commitment and wellness at the time of the tests [33]. For each grip repetition, the maximum value measured by the manometer was acquired. The maximum value of force applied by the hand on bulb syringe is directly related to the maximum value of pressure registered by the manometer, whereas the fatigue can be associated both with the decrease of the maximum pressure value during a test session and with the total number of cycles performed.

Test Results

After collecting all the repetitions for each test session, the resulting data were analyzed. In this session the result is discussed in order to provide the main conclusions and observations achievable. The results of the test show a main trend common to each subject. The effects of the EVA glove on hand capabilities are specific of the executed task, whereas the effect of pressurization drastically worsens performances independently from the typology of the performed grip.

The hand strength, during power grip and lateral pinch, results significantly reduced wearing the unpressurized EVA glove in almost all test subjects and, at the same time, the effects of fatigue are considerably augmented, both in terms of total number of executed cycles and in performance decay in time. A different behaviour has been noticed during the execution of the other two hand grips. Wearing the unpressurized glove, two and three fingers pinches were performed with hardly any difference, as if the glove had almost no effect on these specific tasks. On the contrary, when the EVA glove is pressurized, the performances were dramatically reduced independently from the executed task. The results presented no relevant differences between male and female. If, on the one hand, the results collected during man's test present on average a higher maximum strength with respect to the woman ones, on the other hand, processing data for each subject as a percentage of their maximum value allowed to cancel the effects directly related to each subject's physical presence. In physiology the higher value of applied force is called Maximum Voluntary Contraction (MVC). Figure 54 shows an

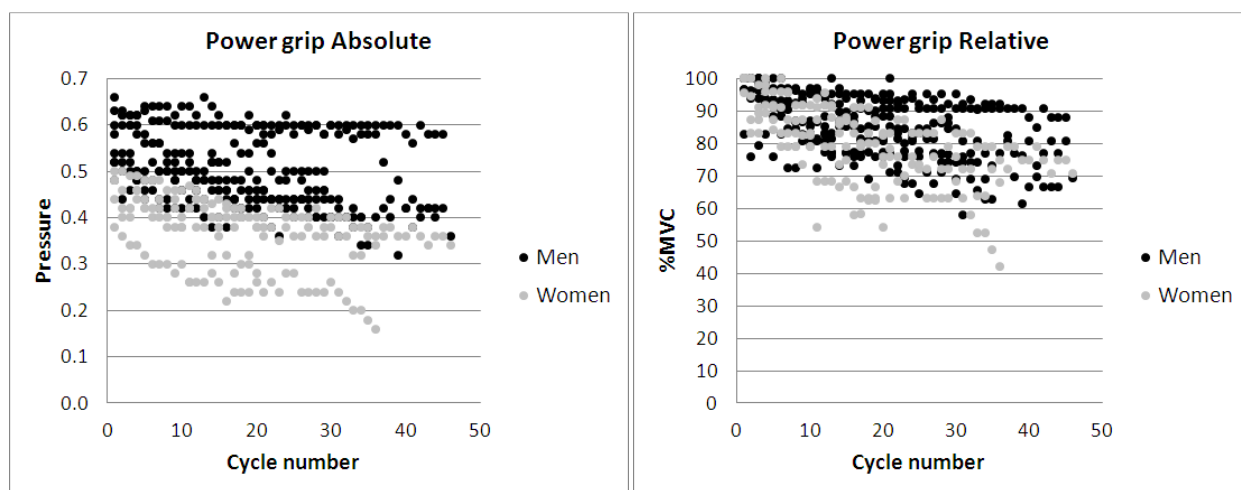


Figure 54: Difference between Man and Women barehanded Power Grip; results represented in absolute values (left) and represented as MVC percentage (right)

Test on EVA Glove

example of the difference between the data series represented using absolute values and MVC percentage; as it is clearly noticeable the latter allow comparing data collections coming from people with different physical presence.

From Figure 55 to Figure 58 the acquired data for the four different tasks are shown. Each of these figures shows all the executed cycles related to a single hand grip in three different configurations: barehanded, wearing the unpressurized EVA glove and wearing the pressurized one. All values are expressed as a percentage of the highest value of force that each subject obtained for the specific task; in this way all the data for all subjects can be significant also if represented together on the same graph. In each graph the “black X” points are related to the barehanded performed test, “grey squares” are related to the test performed wearing the unpressurized EVA glove and, finally, the “black dots” are related to the test performed wearing the pressurized EVA glove.

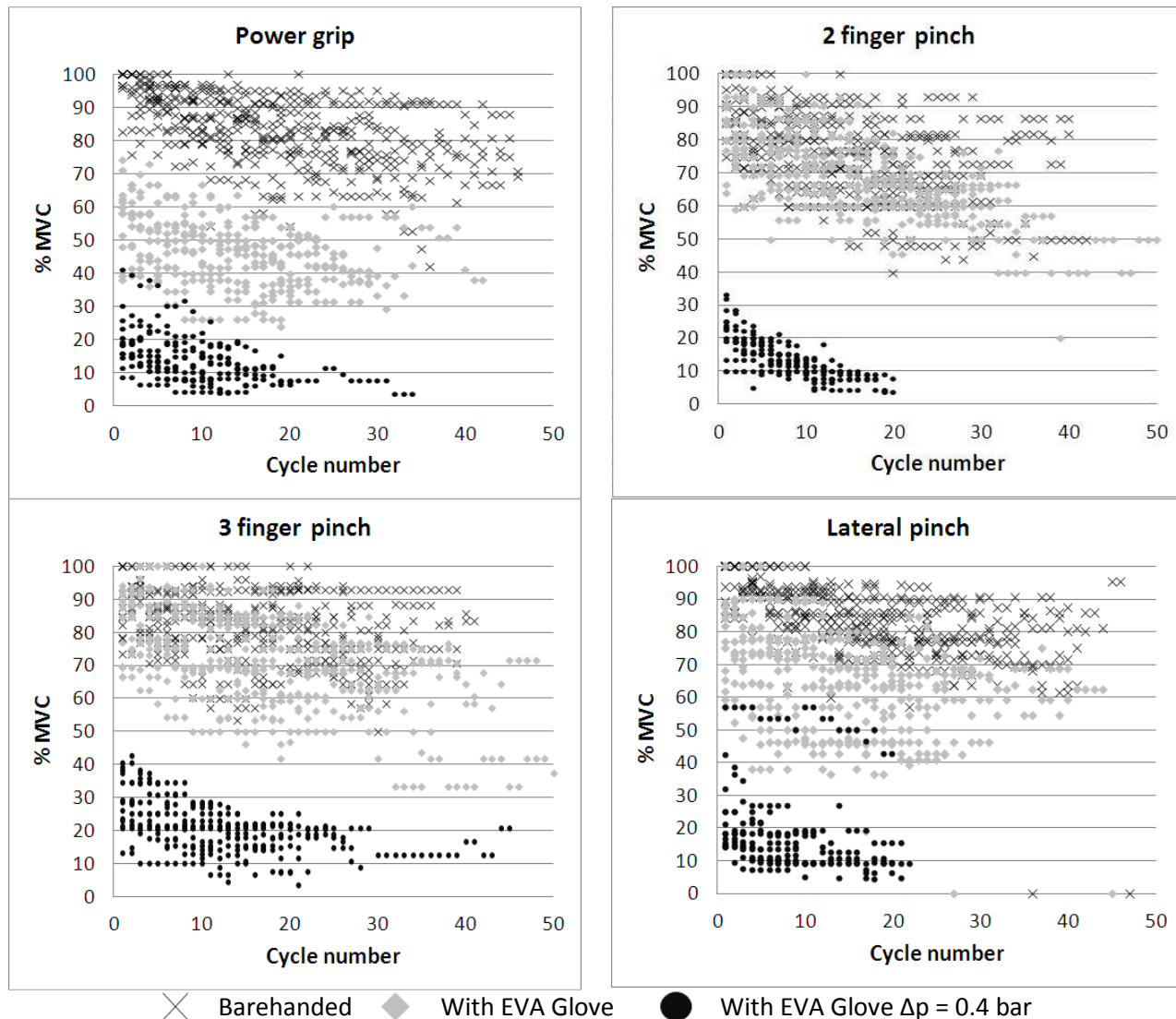


Figure 55: Effects of wearing the EVA glove in different conditions on power grip performances (top left)

Figure 56: Effects of wearing the EVA glove in different conditions on two-finger pinch performances (top right)

Figure 57: Effects of wearing the EVA glove in different conditions on three-finger pinch performances (bottom left)

Figure 58: Effects of wearing the EVA glove in different conditions on lateral pinch performances (bottom right)

Test on EVA Glove

It is evident how the pressurized EVA glove deeply hinders hand performances independently from the performed task; however, this is not always true for the unpressurized glove, whose effects result to be strictly related to the typology of hand grips. Figure 55 shows the data collection related to the power grip. In this graph three distinct data clouds are clearly visible: for all the subjects, performances wearing the unpressurized EVA glove were significantly inferior to the barehanded ones and the capabilities measured wearing the pressurized EVA glove were even worse. Figure 58 shows the variation of the MVC percentage related to the lateral pinch during the three tests conditions: in this graph the effects are slightly different. The data related to the barehanded and unpressurized conditions present different mean values, but are partially overlapped, whereas the cloud related to the pressurized condition is almost entirely distinct with respect to the others and clearly lower. Few test subjects actually performed similar results related to lateral pinches when barehanded and wearing the unpressurized EVA glove, whereas all other subjects' performances are clearly subjected to a decline. As concerns the results obtained wearing a pressurized EVA glove, the lateral pinch shows a significantly decrement of all subjects' performances both in terms of number of cycles and degradation in time. Finally Figure 56 and Figure 57 show the data collection related to the two and three fingers pinches; wearing the unpressurized EVA glove seems to produce in these two cases little or no effect at all on hand performances compared to the barehanded repetitions. In both this graphs the relative data clouds results to be mixed together and almost indistinguishable; there isn't any prevalence of one data series over the others in certain areas. Moreover, also the total number of performed cycles, in barehanded and unpressurized conditions, is almost the same. On the contrary, the effects of glove pressurization are evident in both cases; the correspondent data clouds in Figure 56 and Figure 57 are clearly separate from the other clouds. As regards the three fingers pinch task, the maximum strength performances wearing the pressurized EVA glove drop between the 30% and 10% with respect to the barehanded conditions and the number of executed cycles is also reduced. Regarding the two fingers pinch task, the results are even worse: the maximum strength with the pressurized EVA glove drops down to 10% and 20% and the number of repetitions is drastically diminished.

Figure 59 provides a clearer and more statistical approach on the effect of the EVA glove on the number of executed cycles for each task. In this graph the average number of executed cycles, with the

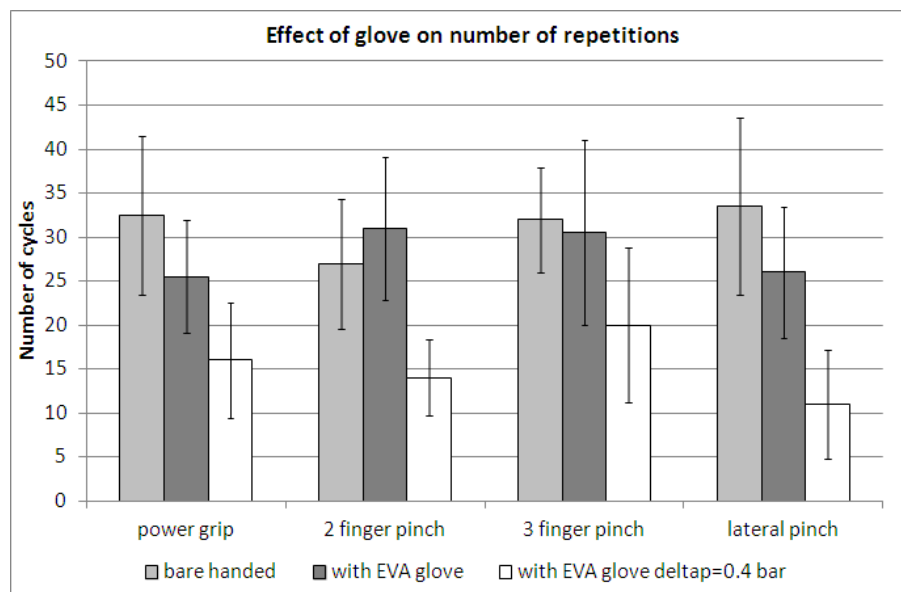


Figure 59: Effects of wearing the EVA glove in different conditions on the total number of repetitions for different tasks

Test on EVA Glove

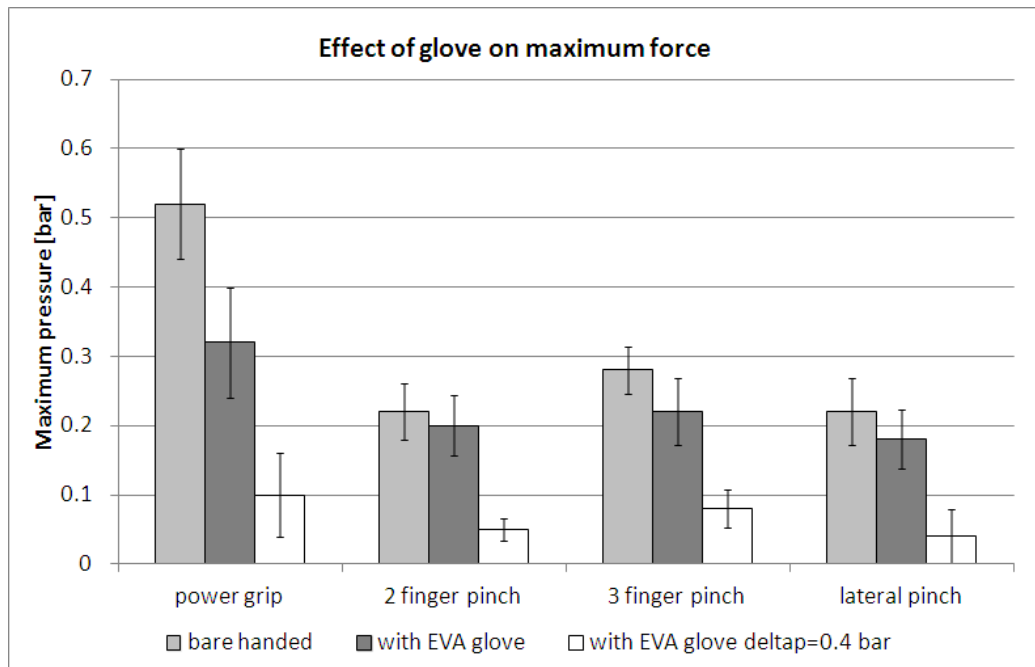


Figure 60: Effects of wearing the EVA glove in different conditions on the maximum force exerted for different tasks

associated standard deviation, is shown in the three different conditions: barehanded (light gray), wearing the unpressurized glove (dark grey) and wearing the pressurized glove (white). It can be noticed that, while the number of cycles with the pressurized glove is significantly reduced for all tasks, a slight difference of the four behaviours is shown in case of unpressurized glove condition. In this case only the tests related to the power grip and lateral pinch reveal a noticeable difference with respect to the barehanded condition as far as the number of executed cycles is concerned. Observing the three fingers pinch, the effects of the unpressurized EVA glove are not very significant. Finally, the results related to the two fingers pinch result to be completely unpredicted: wearing the unpressurized glove the results obtained are better than the barehanded ones, which is absolutely unexpected. On the basis of some post-test declaration, this behaviour can be due to the fact that the unpressurized glove does not particularly hamper this specific task and, at the same time, wearing an authentic EVA glove can provide a boost of motivations for some people, improving the related performances.

Figure 60 shows the effects of the EVA glove on the maximum pressure value measured by grasping or pinching the bulb syringe, which is directly correlated to the exerted force. For each different task condition, the highest pressure measured for each test subject has been selected. In this graph the average value of these measures, with the associated standard deviation, has been reported. It can be noticed that wearing the pressurized EVA glove the maximum strength is reduced by about 80% (only 70% in the best case: the three fingers pinch); whereas with the unpressurized EVA glove only the power grip shows a remarkable reduction, by about 40%, while the three pinching strengths are about 10% - 20% lower than the barehanded conditions.

Discussion of the results

The results obtained for the pressurized and unpressurized EVA glove will be discussed separately, since they are strongly different.

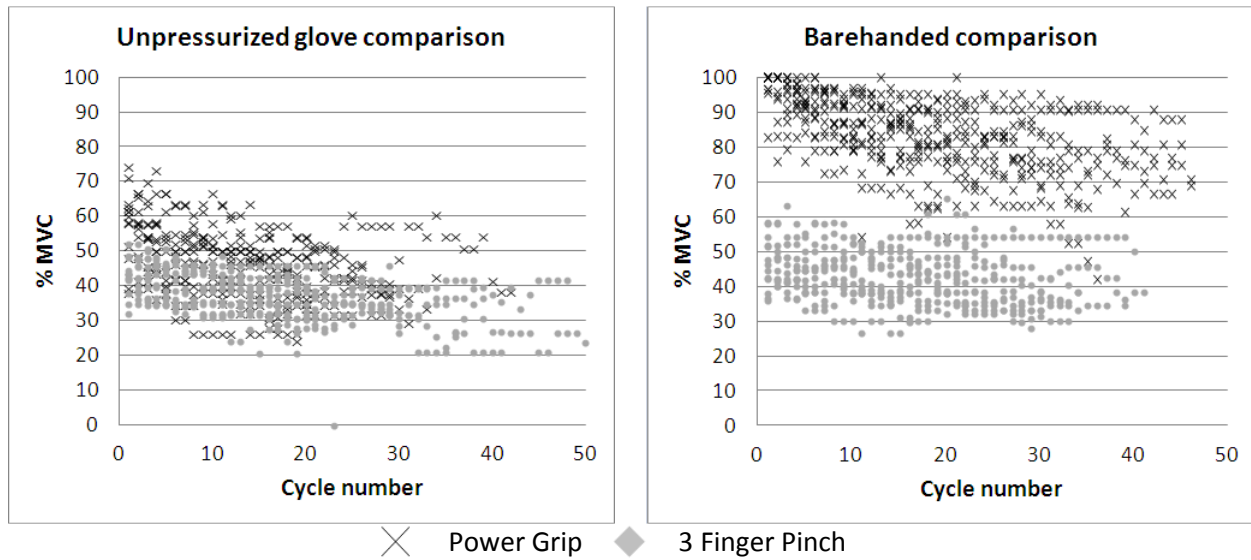


Figure 61: Comparison between the performances obtained by executing the power grip and the three-finger pinch tasks in barehanded conditions (left) and wearing the unpressurized glove (right)

Unpressurized Glove

Although the results of the various tasks performed wearing the unpressurized glove may seem a little bit puzzling, in particular regarding the pinches, they are in line with the previously done research. Literature states that the grip strength is reduced by the 50% for men and by 30% for women in case of unpressurized conditions, whereas the pinch strength is not modified [40]. Other studies also assess an average strength reduction of 40% as regards grip force and a negligible effect on pinch force wearing an unpressurized glove [33]. All these considerations lead to the hypothesis that the real problem when wearing an unpressurized EVA glove may be its bulk, especially between the fingers, more than its stiffness. Supporting this claim, the results of our tests show that, wearing the EVA glove in the unpressurized condition, the performances related to the power grip, that involve the whole hand, are almost the same associated to the three fingers pinch occurring when only three fingers are involved (Figure 61). It can be supposed that the ring finger and the little finger were too far away, too weak or too hampered to contribute in a significant way to the exerted force. Figure 61 shows the difference between power grip and three fingers pinch, in barehanded conditions and with the unpressurized glove, with regard to the maximum overall performance of the test subject as a percentage of MVC. It is interesting to notice that the results coming from the barehanded condition present two distinct data cloud, related to the three fingers and power grip: passing to the unpressurized condition, these two clouds are completely overlapped. This may be due in part to the particular kind of grip and to the shape and dimension of the bulb syringe used for the tests.

Pressurized Glove

Wearing the pressurized EVA glove, the effects on the hand are immediately perceived by the human being as a very stiff, rigid and uncomfortable garment. The collected results show that the performances drastically decline for all tasks performed in these conditions. The results are slightly different from those found in literature. Several articles reporting tests executed on different models of EVA gloves still state that performances decline when wearing an EVA glove, but not as dramatically. Some authors report grip strength reduction by 70% in barehanded conditions for men and 50% for women and pinch strength reduction by 25% for men and 20% for women [40]. Other authors report grip strength

reduction by 55% with respect to the barehanded, while lateral pinch strength reduction by 14% and two fingers pinch strength increasing by 15% when wearing a pressurized glove [37]. Finally, in another study [33], grip strength is reduced by 47%, lateral pinch by 10% and two fingers pinch maintain the same value of force measured in barehanded conditions. From the data collected during these tests, it appears that pressurization restrains hand performances by about 80% to 90% of barehanded performance for all tasks, which is a higher drop. There are many reasons for these differences, from the different model of the glove to the fact that the left hand has been tested, which means that most of the subjects used their weaker hand. Another point of interest is the shape of the grasped object; in some cases, especially for pinch tasks, some subjects found it hard to hold the bulb syringe in the correct position during the repetitions, due to its dimensions. Finally, in some cases, subjects would suspend the task execution not due to fatigue, but because it was getting too painful to continue; they were aching, either at the fingertip, in particular near the nails, or at the finger crotches because of the local stiffness of the glove.

Measuring of Glove Stiffness

The goal of this series of tests was to measure the torque applied by the glove on each articulation of the human hand. The knowledge of the magnitudes of the torques is very important in an exoskeleton design because it became an important constraint on the elements that compound the device. On the one hand, the actuation system needs to be able to overcome the stiffness of the EVA glove generating a torque on the joints of the exoskeleton higher enough to compensate, in part at least, the opposing force due to the various elements of the garment. On the other hand, the structure of the exoskeleton has to be able to carry the internal stresses caused by the exchange of forces and torques between the hand, the exoskeleton and the actuation system without deforming and/or breaking. The knowledge of, at least, the order of magnitude of the exchanged torques is then a fundamental step to be able to realize something useful and not dangerous for the user.

Several technological solutions could be utilized in order to measure the torque applied by the glove on each articulation of the human hand. One of the main problems related to the choice of the measurement setup is to be able to measure the desired quantities without interfere with the normal functioning of the glove. During the hand activities the glove is bent in a continuous way along the finger length; the glove is indeed composed only by flexible layers, as already explained, and the particular shapes on which the joints are made cannot reproduce a discrete bending movement. When inflated, the glove behaves like a pressurized balloon, which time by time distributes evenly the force applied by the pressure on its surface. Constraining the movements of the finger into a discrete bending, only in correspondence of the articulations, results therefore a strong restriction. It is also necessary to consider that, if the measurement setup has to be inserted into the glove, it must not modify the dimensions and the shape of the human hand. These are only some examples regarding the limitations that have to be taken into account for the choice of the measurement setup. Two different series of tests, with two different measurements setups, have been performed. In the first one a thin distributed pressure sensor has been placed on the whole hand, while in the second one a robotic finger probe, equipped with accelerometers, has been utilized to achieve the goal.

First Test: Experimental Measurement Setup

In this first test the torques applied by the glove on each articulation of the human hand have been measured by means of a commercial sensor system: the Grip™ System [132] by Tekscan Inc. The Grip™ System measures static and dynamic pressure coming from grasping objects.

Test on EVA Glove

The sensor is composed by a special ink, which works like a piezo-resistive material, placed between two thin polyester sheets. On each sheet a series of conductive electrodes have been deposited in such way that, once combined together, the two sheets create a grid-like pattern. The conductive electrodes of one sheet cross the electrodes of the other one and, in correspondence of the junctions, the sensing points have been realized. Each hand sensor has eighteen sensing zones grouped into five sensing

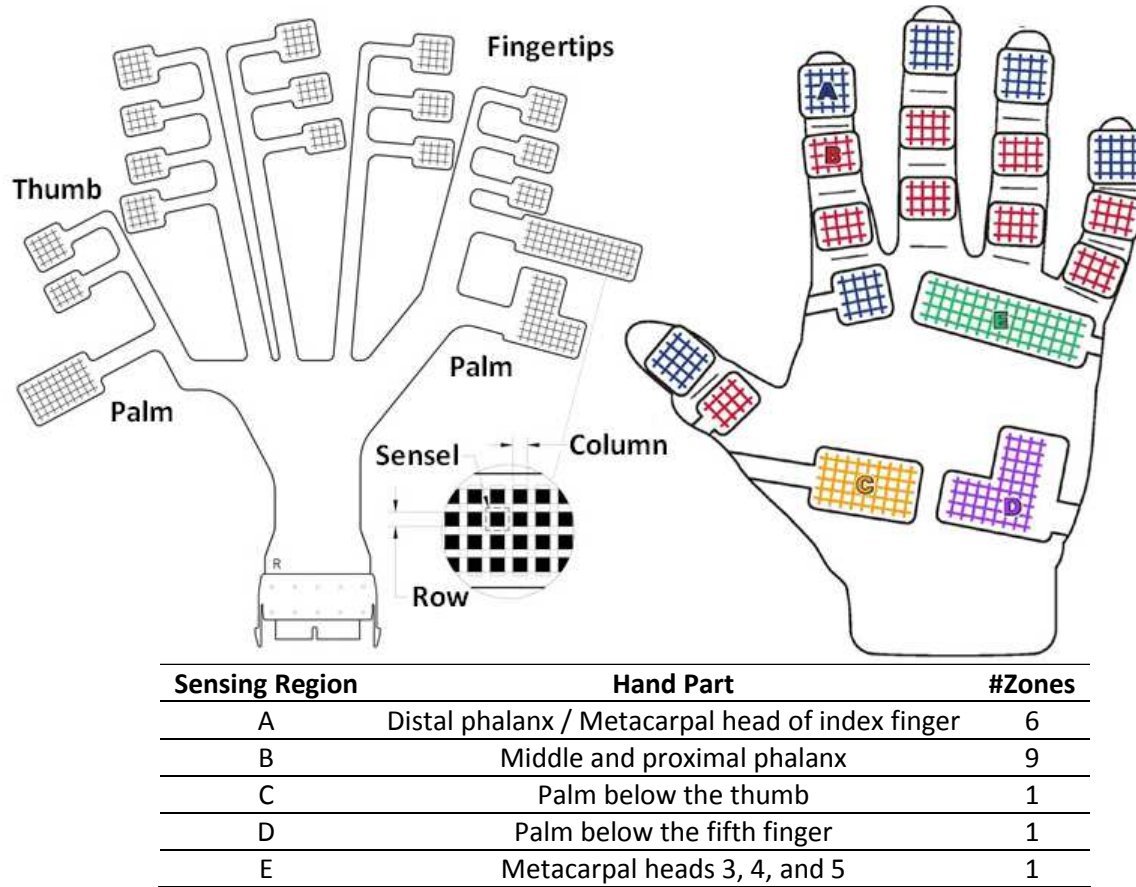


Figure 62: Distributed pressure sensor Grip™ (left) and the suggested sensor placement on hand or glove (right)

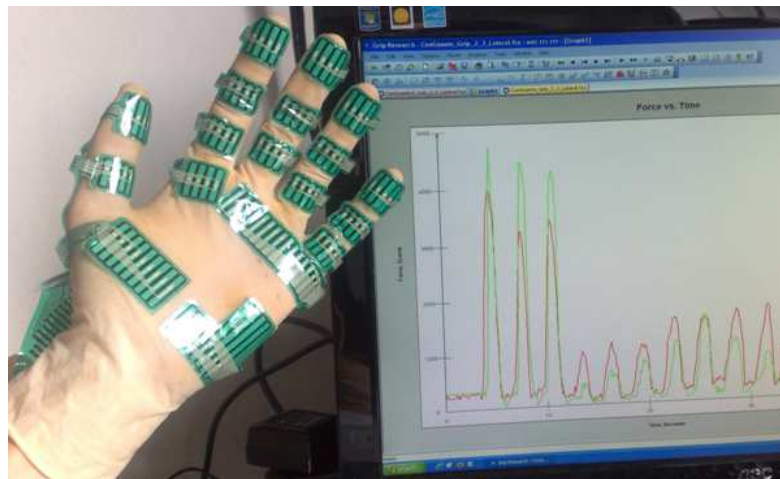


Figure 63: Distributed pressure sensor fixed on the latex glove

Test on EVA Glove

regions Figure 62. Each region had to be separately calibrated and compensated. The sensor could be directly used on a hand or attached on a glove. The system also comprises software that allows calibration, real time visualization and post processing. It has been decided to fix the sensor on a glove in order to keep it in place, granting a better repeatability of the tests. A latex glove has been chosen due to its thinness, which does not add significant resistance, and to its close fitting, that guarantees a

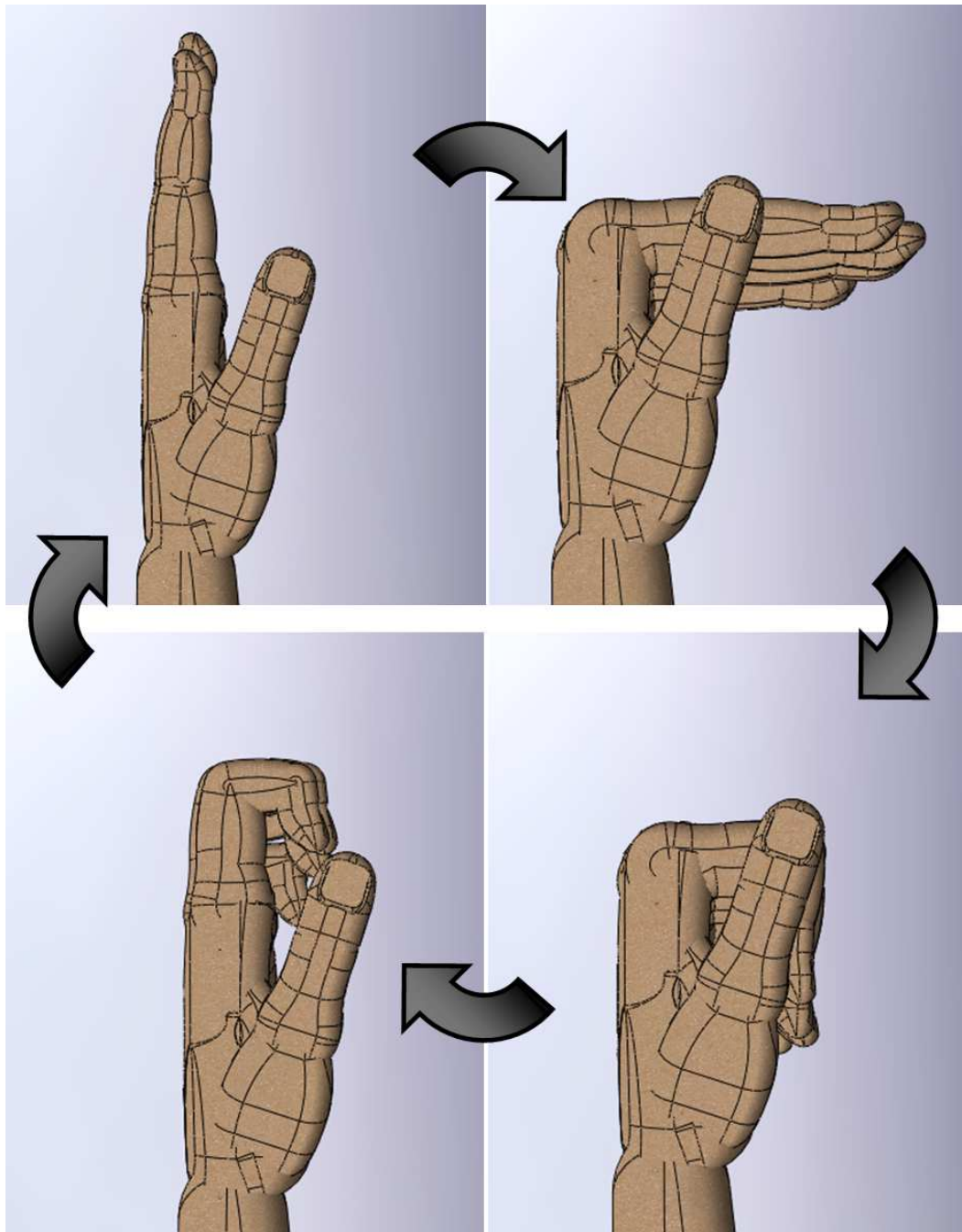


Figure 64: The Test Protocol composed by the sequence of Four Hand positions: finger straight (top left), only first phalanx bended (top right), first and second phalanges bended (bottom right) and second and third phalanx bended (bottom left)

Test on EVA Glove

good positioning of the sensors also with hands of different dimensions Figure 63. Once fixed the distributed sensor on the glove, each sensing region has been calibrated by means of a series of calibrated weights. Moreover, placing the sensing zones on curved shapes, like the fingers and the palm, causes an initial bending of the sensor. This bending is measured by the sensor and interpreted like a force acting on the sensor; it is necessary once worn the glove to bring all residual stresses to zero, in order to minimize the measurements errors.

First Test: The Protocol

In order to measure the torque that the EVA glove applies to the human hand utilizing only a distributed pressure sensor, it is necessary to define a series of standardized and temporized movements to know, time by time, the attitude of each phalanx of the hand. The resistive forces and torques applied by the glove on the hand are caused by a complex combined effect of the operating pressure and the multilayer system. With every movement, the wearer fights against the internal pressure and the friction between the layers; moving a single phalanx generates a global counter acting force that is not only applied on that phalanx but partly act on the whole finger. Test procedure consisted in repeating a series of predetermined movements of the hand; these movements were chosen in order to try to partially decouple the complex effect of the glove on the phalanges of the fingers Figure 64.

The repetitions of the standardized movements were performed in free space, without grasping anything in order to measure only the mechanical stiffness of the glove and no undesired external forces. The operator had to perform the test procedure in two different conditions: wearing only the latex sensorized glove and wearing the unpressurized EVA glove on top of it. In this case no test wearing the pressurized EVA glove has been performed. Due to the fact that the goal of the test is to measure the stiffness of the EVA glove, the execution done wearing only the latex glove can seem useless; the

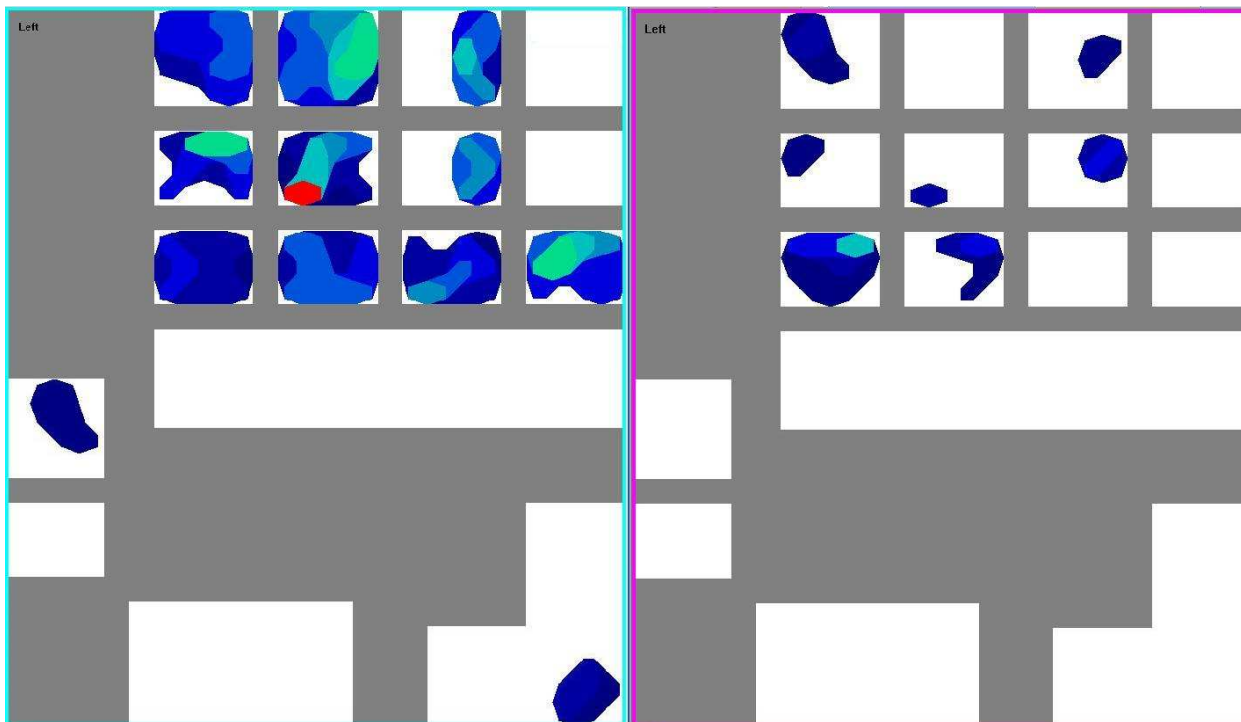


Figure 65: Two examples of the instantaneous pressure distribution plotted on the Hand-Like graph obtained from the acquisition system of the GripTM sensor

Test on EVA Glove

main reason to perform the test in this condition is that, as previously mentioned, the sensor perceives and measures a force also as a consequence of the bending of the various zones that compound it; reproducing the test without the EVA glove allows to know, and then subtract, this effect to the other test. A metronome provided the timing for the execution of the movements, in order to easier evaluate the corresponding position of the data during the post processing. The sensor provided time by time the value of pressure on each sensing point of each zone and represented it on a hand-like graph Figure 65. With the sensor's software it was possible to select a specific region of the hand and to calculate the force acting on this area, as integral of the pressure, and the position of the correspondent center of force during time. Knowing the position of the instantaneous center of force and the behaviour of force in time, the torque can be easily obtained.

First Test: Results

After collecting all the repetitions for both test conditions, the results have been analyzed and processed in order to achieve the final goal: obtaining the estimation of the torque applied by the glove on the human hand articulations. At the end of the data acquisition, two files related to the two different hand conditions and containing the behaviors of the pressures were obtained. Each file showed the behaviour

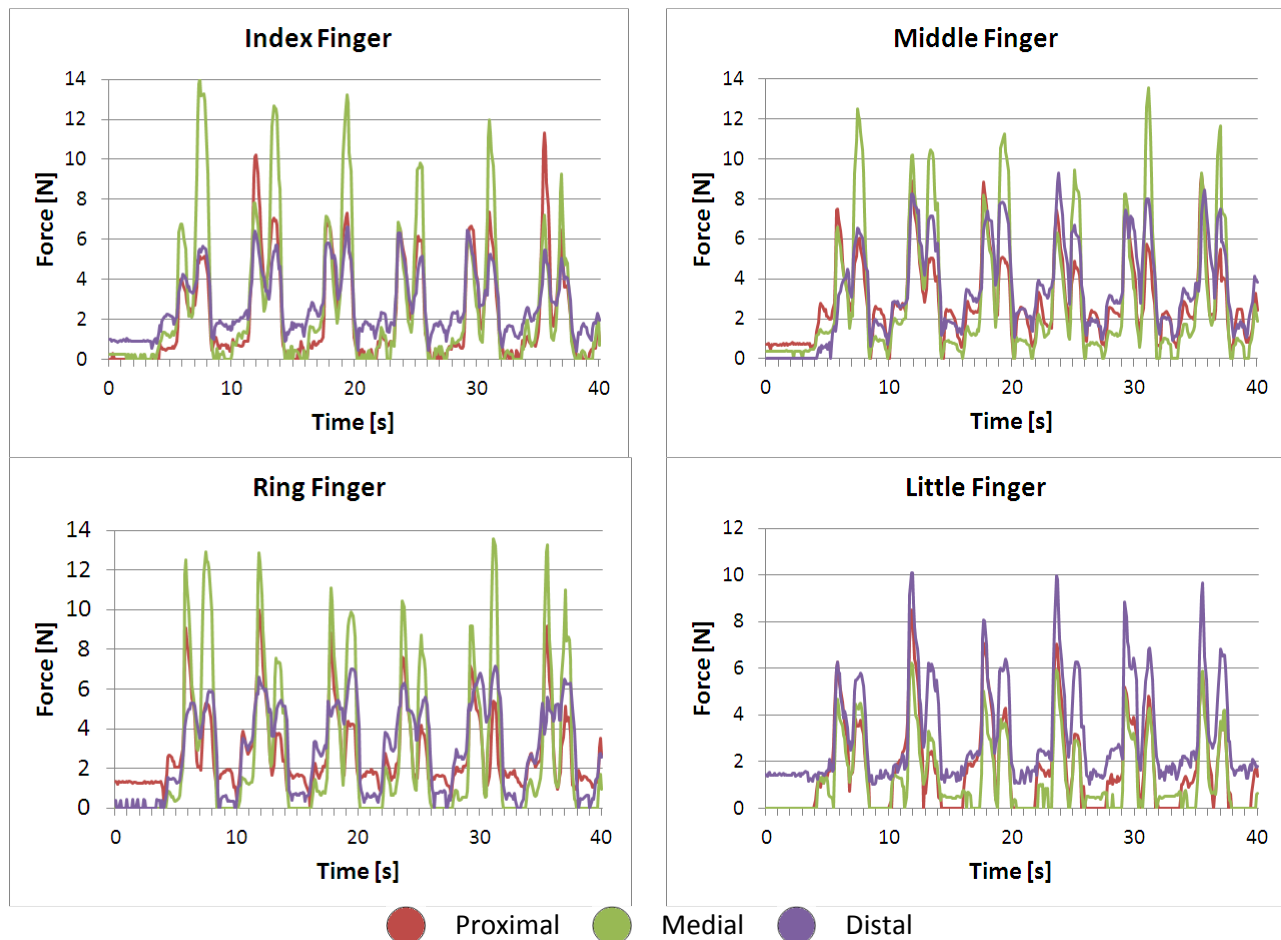


Figure 66: First 40 second of data acquired related to the force applied by the EVA glove on the Index Finger (top left)

Figure 67: First 40 second of data acquired related to the force applied by the EVA glove on the Middle Finger (top right)

Figure 68: First 40 second of data acquired related to the force applied by the EVA glove on the Ring Finger (bottom left)

Figure 69: First 40 second of data acquired related to the force applied by the EVA glove on the Little Finger (bottom right)

Test on EVA Glove

of the values of pressures for each of the 360 contact points, which compound the eighteen sensing zone of the distributed sensor. For each phalanx of the fingers the data files were elaborated and, knowing the dimension of the sensing area, the behavior of the forces have been calculated. At this point the values of forces related to the two different conditions during time are known for each phalanx.

The effective force applied by the glove on the hand, purged of the parasite effect due to the bending of the sensing zones, could be easily obtained making the difference between the instantaneous values of

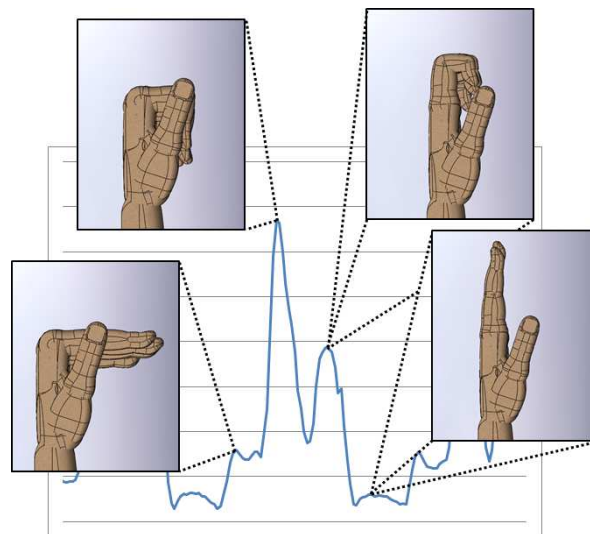


Figure 70: The Four Hand Position with respect to the behavior of a general data collection

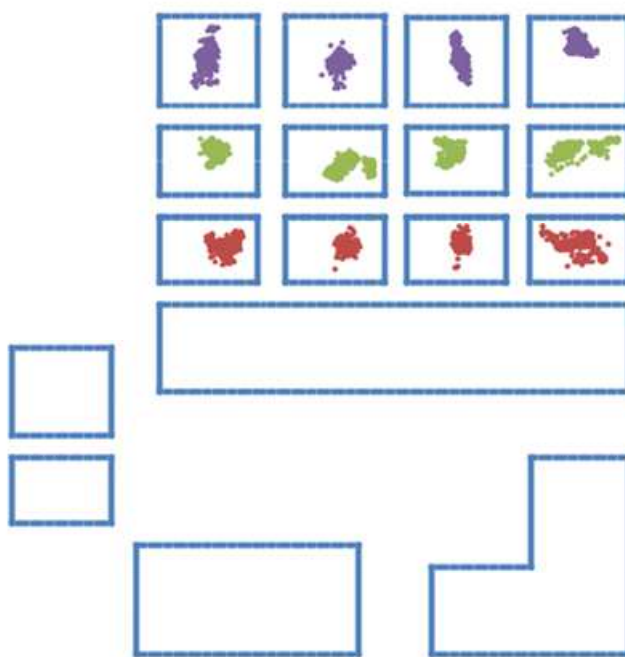


Figure 71: Behaviour of the position of instantaneous Centre of Force on each phalanx of the hand

Test on EVA Glove

the two forces. From Figure 66 to Figure 69 the behaviours of the first forty seconds of each measured force are shown. Each of those figures reports the three trends of forces related to the phalanges of a single finger.

In each graph the red line is related to the forces applied on the proximal phalanx, while the green line is the force related to the medium phalanx and, finally, the blue line is related to the distal phalanx. It can be noticed that the trends of forces are quite periodic, due to the repetition of the standardized movements; furthermore, values related to the four different positions of the hand can be clearly distinguished Figure 70. From the data files, which contain the pressure values, the instantaneous centers of forces, for each phalanx of each finger of the hand, could be obtained. Figure 71 shows the position of the centers of forces on each phalanx, plotted inside a hand like graph, in order to be easily understandable. This graph shows the same color setup related to the phalanges, already used in the previous. Knowing the behaviour of force and distance, time by time, between the articulation's joint and the center of force, the instantaneous value of the torque can be calculated. From Figure 72 to Figure 75 the behaviours of the torque of each phalanx are shown; each of these figures shows the

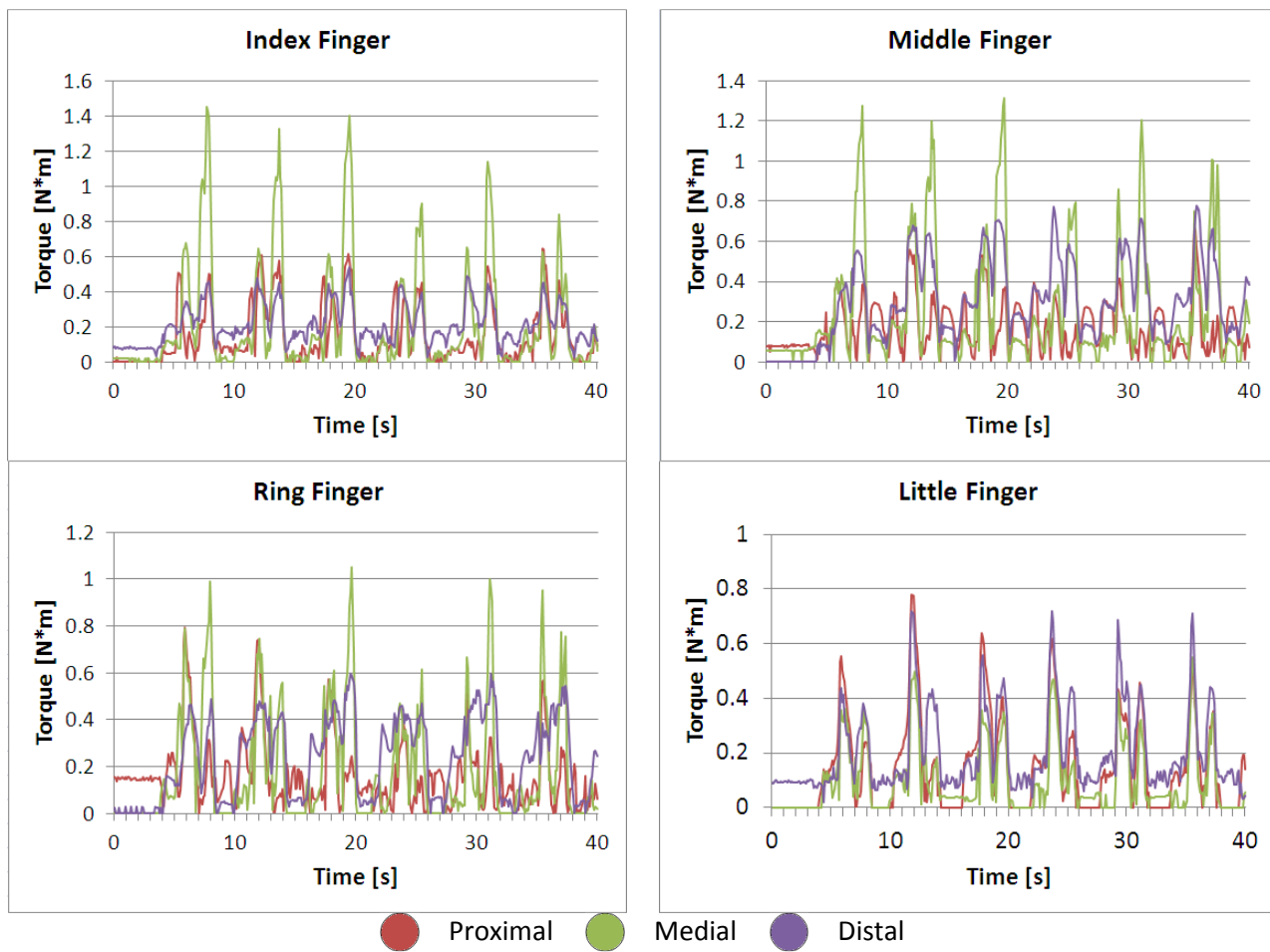


Figure 72: Behaviour of the first 40 second of torques applied by the EVA glove on the Index Finger (top left)

Figure 73: Behaviour of the first 40 second of torques applied by the EVA glove on the Middle Finger (top right)

Figure 74: Behaviour of the first 40 second of torques applied by the EVA glove on the Ring Finger (bottom left)

Figure 75: Behaviour of the first 40 second of torques applied by the EVA glove on the Little Finger (bottom right)

Test on EVA Glove

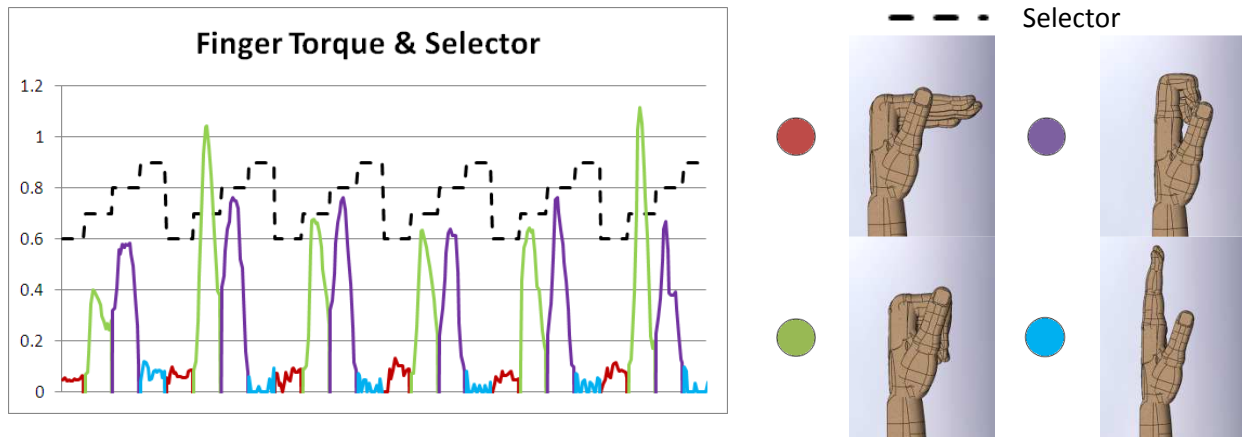


Figure 76: Torque selector and the behaviour of the torques related to the four different hand positions

torques related to the three phalanges of a single finger. For each trend of torque, corresponding to a specific phalanx, the torque values related to the four different hand positions have been distinguished through a selector signal specifically made on the basis of the instant of time (Figure 76).

At this point, for each torque signal four different trends corresponding to the four different hand positions, have been obtained. From each trend of torques previously obtained, all local maximum values have been taken. From Figure 77 to Figure 80 the average values, with the associated standard deviation of all set of maximum values are shown. Each figure is related to a single finger and shows three series of bars, one for each phalanx. Each bar represents the mean value of the peaks of forces and the associated standard deviation in the four different finger positions: finger straight (dark grey), only first phalanx bended (light grey), first and second phalanges bended (white) and second and third phalanx bended (variable gray).

Some considerations related to these results must be done. As it can be easily seen, each phalanx of each finger was differently influenced by the EVA glove and, at the same time, the corresponding phalanges of different fingers (e.g. all the proximal) show different effects against the four hand position, without a completely predictable trend. Some common traits can be observed between the four graphs. First of all, it can be noticed that the mean values of the first and the fourth hand positions are, in general, smaller than the other two. This result is easily understandable because the first position involves only the bending of the first phalanx and the fourth is the finger strait position, while both the others involve the bending of two phalanges. The only exception of this trend is the value of the medial phalanx of the middle finger that reaches an unpredictable high value. It can be noticed a non-null torque, applied by the glove on the hand, also in the straight position. This effect let to understand that the multilayer garment applies contact forces on the hand, independently from the position, as a consequence of its structure. It can be supposed, that this effect acts like an offset on the others resultant torques. Another effect can be noticed: starting from the index finger, the mean values of torques decrease going to the side of the hand, reaching the lowest values in correspondence of the little finger. The medial phalanx is the most stressed for the index, middle and ring finger; vice versa for the little finger the most stressed phalanx is the distal. The highest obtained torque is related to the index medial phalanx during the position with first and second phalanges bended with a value of around 0.9 Nm. The obtained values of torques result to be incredibly high considering that they only come from an unpressurized glove.

It has to be considered that the human finger is not exactly like a rigid robotic structure; its soft and partially elastic skin and flesh change the bulkiness of the various phalanges of the fingers during movements. In the measurement setup each sensing element is placed on the bottom part of each

Test on EVA Glove

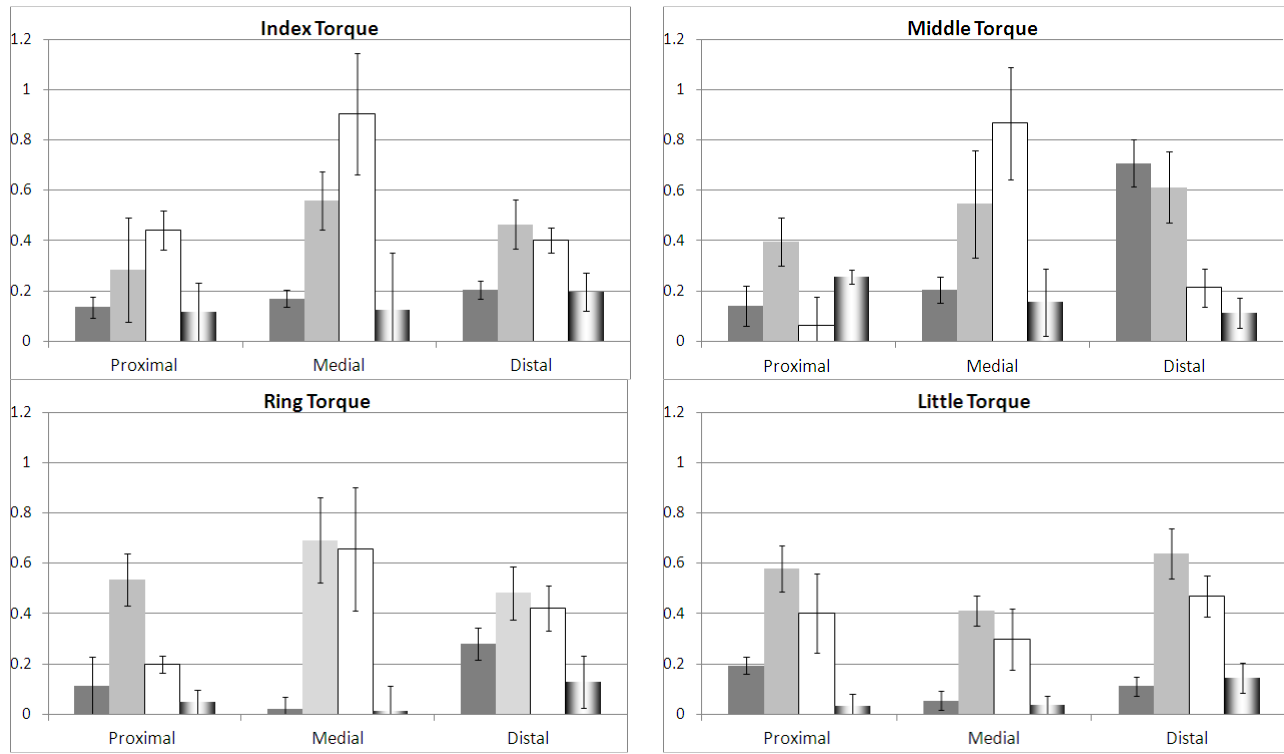


Figure 77: Average values and associated standard deviation of the maximum torques applied on the Index finger phalanges during the four position of the hand protocol.

Figure 78: Average values and associated standard deviation of the maximum torques applied on the Middle finger phalanges during the four position of the hand protocol.

Figure 79: Average values and associated standard deviation of the maximum torques applied on the Ring finger phalanges during the four position of the hand protocol.

Figure 80: Average values and associated standard deviation of the maximum torques applied on the Little finger phalanges during the four position of the hand protocol.

phalanx; during the movements two adjoining sensing zones could touch together, measuring a virtual effect due to the contact between the two phalanges. This effect has been partially compensated by the measures performed wearing only the latex glove and subtracting its trend from the values obtained wearing the EVA glove. However, the EVA glove has its own bulk that, during the interaction with the human hand, could cause a similar effect to the previously explained. This effect could increase the torque measured and cannot be easily distinguished from the true value, caused by the real stiffness of the glove. On the basis of that, obtained values are probably overestimated. For this reason this typology of tests were not reproduced wearing a pressurized EVA glove. It has been decided to develop a new experimental setup in order to overcome this problem.

Second Test: Experimental Measurement Setup

In this second test the torque applied by the glove on each articulation of the human hand has been measured by means of a home-made tendon actuated finger probe, equipped with sensors and able to measure the relative position of each joint. The finger probe, shown in Figure 81, is a robotic structure composed by 3 DoFs and four links that aim to emulate the kinematic structure of the human finger. The device allows only the flexion and extension movements, whereas the DoF related to the abduction has been completely neglected. The finger probe will substitute the human finger during the tests inside the

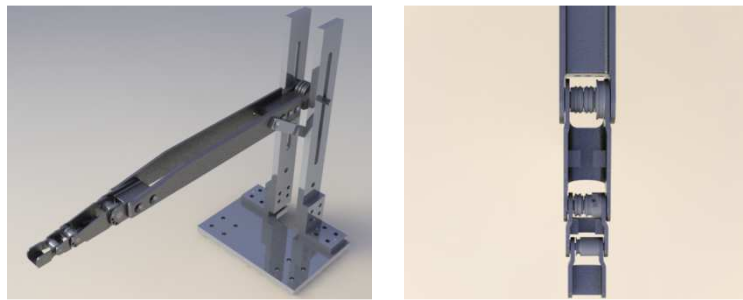


Figure 81: The finger probe

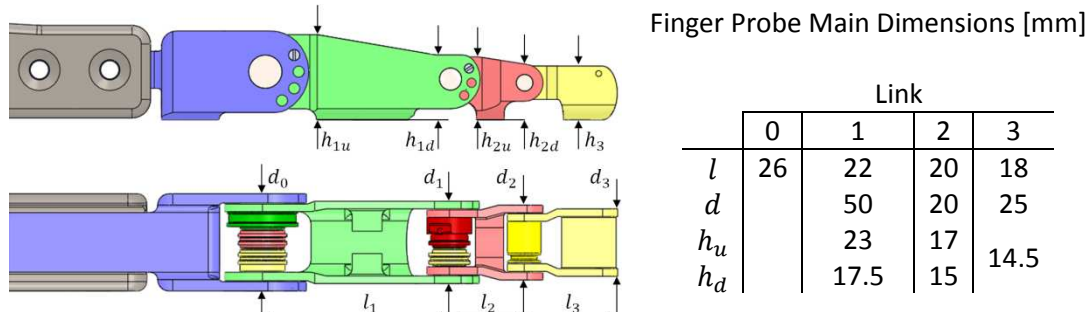


Figure 82: Main dimensions of the finger probe

EVA glove, allowing the operator to measure the position assumed by each phalanx as a consequence of a well-known actuation input. Since the main idea is to place the device inside the EVA glove and to emulate the human index finger, the dimension of the finger probe have to be as similar as possible of a human index finger. The study on the biometric parameters of the human hand could provide the information needed; however it is important to remember that the EVA gloves are actually custom-made, and then it has been decided to design the finger probe able to perfectly fit inside the Orlan-DM in our possession. This approach is applicable to any other EVA glove, by using elements which enable size variations of the device. Figure 82 show the main dimensions of the realized finger probe. For each phalanx, there are two quantities that have to be known in order to be able to measure the stiffness of the EVA glove: the torque applied by the actuation system, and the equilibrium angle reached by the phalanges during the interaction with the EVA glove. The obtained bending angle is the position in which the glove compensates exactly the torque provided by the actuation system. In order to obtain the torque applied by the glove on each "phalanx" of the device, each DoF has to be actuated independently. The actuation has been done by applying a well-known force on the tendons; knowing the dimensions of the device, the torques applied on each joint could be easily obtained from the tendon tensions. Along the entire structure, a series of holes and pulleys have been designed in order to house and keep in position the three wires needed to transmit the forces and to actuate the three DoF of the index finger in the sagittal plane. Three small slots, one on each phalanx of the finger probe, have been designed in order fix the end of each wire. Figure 83 show the system of pulleys placed into the three joints. On the MCP joint three coaxial pulleys have been designed; one of them is fixed and integral with the proximal phalanx, while the others two can rotate independently, guiding the other wires towards the other phalanges. A similar situation is shown on the PIP joint where there are two pulleys, one of them is fixed with the middle phalanx and the other is free to move. Finally, in the last joint, the DIP, there is only a pulley fixed and integral with distal phalanx. Moreover, small threaded holes have been designed on the lateral side of the phalanges in correspondence of a specific joint angle. The holes are designed to fix each phalanx into a specific position. This solution permit to study

Test on EVA Glove

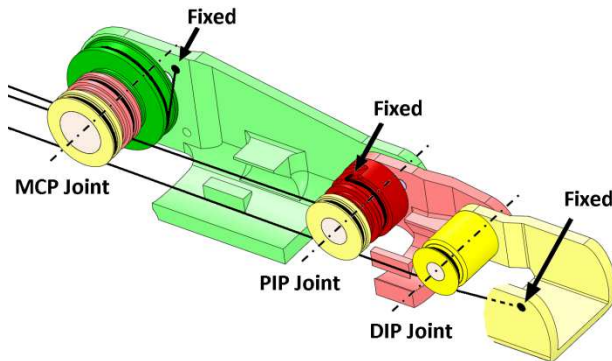


Figure 83: The pulley mechanism of the finger probe



Figure 84: Finger probe in front and inside the glove box

the behavior of the torques required flexing each phalanx when the others are kept into a specific position. The proximal phalange can be fixed at the angles of 0° , 30° , 60° and 90° and the middle phalange can be fixed at the angles of 0° , 40° and 80° . Finally the finger probe is mounted on a base with which it could be fixed on a breadboard. The two legs of the frame allow the height and orientation to be adjusted on the base of the needs. Figure 84 show the realized finger probe in front of and inside the glove box. The finger probe is equipped with a series of sensors that have to measure the instantaneous position of each phalanx of the robotic structure. To accomplish this task three accelerometers have been used as gravitometers. The angle of each phalanx is measured by sensing its orientation with respect to the gravitational acceleration g . In order to measure the relative direction of the gravitational acceleration, a commercial accelerometer has been employed: the ADXL237. This is a very small and low power, complete 3-axis accelerometers manufactured by Analog Devices Inc. This sensor is a MEMS device that senses accelerations within a range included between $\pm 2g$ and generates a proportional analog voltage output. Given the reduced range of acceleration and the high accuracy ($420mV/g$) of the device, the ADXL327 is suitable for static gravitational acceleration measurements in tilt sensing applications. Another important aspect of this sensor is the small and low profile ($4 \times 4 \times 1.45$ mm) package that can be easily installed in the small empty space of each finger probe phalanx.

To host the complete MEMS system a mini-PCB prototype has been designed and fabricated. The PCB comprises three additional external capacitors (C_x , C_y and C_z) which are required by the device to impose the read-out bandwidth for each of the three output channels. Finally a fourth filtering capacitor C_{DC} has been placed to reject the power supply noise and ripple. In this specific case, due to the fact

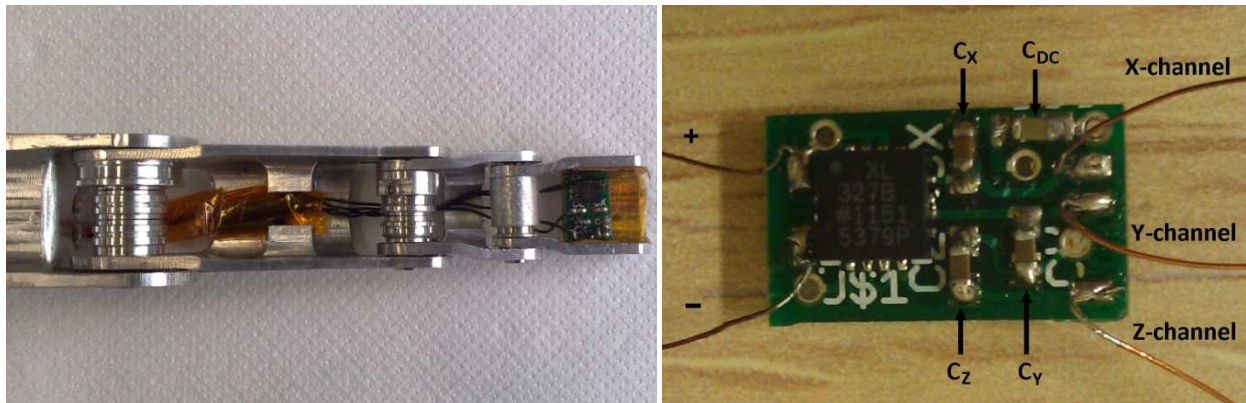


Figure 85: The mini-PCB installed on the distal phalange of the finger probe on a thin film of Kapton®

that a dynamic measurement is not required, the output channel bandwidth could be reduced up to 10Hz and filter out the noise contribution with three SMD capacitors, with a capacity value equal to $0.47\mu F$. As suggested by the manufacturer data sheet, a $0.1\mu F$ capacitor is chosen for C_{DC} . The mechanical design of the finger probe imposes the dimensional constraints of the PCB area limiting it to an overall 16×9 mm size. The mini-PCB has been designed as double layer; the top layer maps all the components footprints and routes all the interconnections, while the bottom layer is the uniform ground plane. By means of a thin film of Kapton, the bottom of the mini-PCB has been isolated from the metallic part of the phalanx of the finger probe in order to avoid short circuits and electrostatic discharges, hence decrease the fail probability of the sensitive accelerometer. The three output channels are then connected to a National Instrument Acquisition Data, allowing to acquire and to process the trend of the bending angles. Figure 85 show the complete mini-PCB prototype mounted on the distal phalange of the finger probe, and un-mounted.

Second Test: The Protocol

The test protocol in this case results to be very simple; applying a series of well-known tendon tensions the phalanx bent and the relative angles of each joint of the finger probe were then measured using the accelerometers and the acquisition system. Once the trend of the applied torques and the angles are known, the behavior of the glove stiffness could be obtained. In order to be able to understand and evaluate the effect of the differential pressure on the stiffness of the EVA glove, all the tests were performed in three different pressure conditions (Δp): non pressurized ($\Delta p = 0bar$), partially

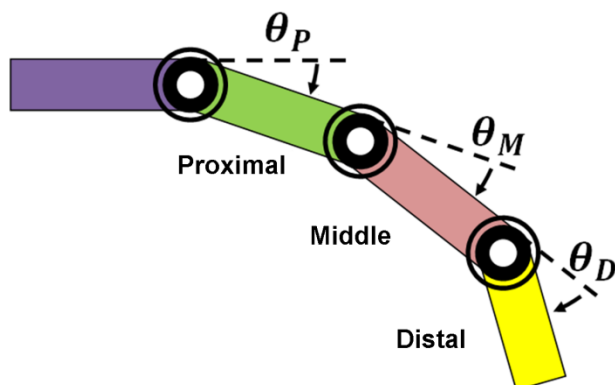


Figure 86: The sign convention of θ_P , θ_M and θ_D

Test on EVA Glove

pressurized ($\Delta p = 0.2\text{bar}$) and fully pressurized ($\Delta p = 0.4\text{bar}$). Each performed test was repeated at least three times in order to increase the precision. To test the MCP joint stiffness, different tendon tensions were applied on the proximal wire which is directly connected to the proximal phalange, while other phalanges are kept free to rotate. The test starts from null tension and increases with a predefined interval. For each tension applied, the angle of the MCP joint has been measured and recorded by means of the previously exposed sensor. For the PIP joint, the tendon tensions were applied on the middle wire that is fixed with the middle phalanx. While the distal phalange is left free to rotate, the angle between the proximal and middle phalange is fixed at different values (0° , 30° and 60°) and tests have been performed for each pressure condition. Finally, for the DIP joint, the distal wire is actuated and the tests are performed for each combination of MCP joint angle (0° , 30° and 60°) and PIP joint angle (0° , 40° and 80°). In total, 9 tests have been performed for different combinations of the joints angles with regard the DIP joint.

Second Test: Results

All the data collected were analyzed and processed in order to obtain the relationship between the bending angle of each joint and the torque applied on each articulation. The actuation system generates a traction force through the tendons of the transmission, thus, knowing all the geometrical parameters of the device, it was possible to calculate the arm of the forces for each phalange in each conditions and then the value of torque applied on each joint. All the following results and graph show the behaviour of the angles of each phalange as a function of the applied torques for each angle composition. The three angles shown in the following graphs and called θ_P , θ_M and θ_D are respectively the bending values of the proximal, middle and distal phalanges with respect the previous one; Figure 86 shows this convention. In the following part the tests and their results related to pressurized and non-pressurized condition will be presented separately. Finally the effect of pressurization, comparing the fully pressurized with the partially pressurized will then be described.

Non Pressurized conditions

The first series of data acquired and shown here is related to the MCP joint. The study of the MCP joint involves only one configuration due to the fact that the two following articulation are both kept free to move without a fixed position. Four set of data were acquired during this test and are shown in Figure 87. For each repetition the best-fit curve was obtained using a specific MATLAB code. The graph correlates the values of torques applied on the MCP joint with the bending value of the proximal

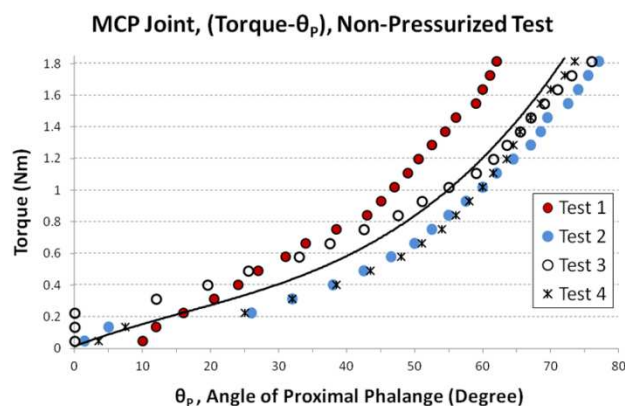


Figure 87: Torque vs. angle of the proximal phalange θ_P in non-pressurized conditions

Test on EVA Glove

phalange: θ_p . The obtained results show that, due to the effects of the multilayer system of the EVA glove, the stiffness in non-pressurized conditions result to be strongly nonlinear.

The second series of data acquired and shown here is related to the PIP joint. The study of PIP joint involves three different configuration based on different fixed position of the MCP joint. As previously reported the proximal phalange can be fixed at the angles of 0° , 30° , 60° and 90° but the fourth position, with $\theta_p = 90^\circ$, resulted impossible to be inserted inside the glove; for that reason only the other three configurations were taken into account. Figure 88 shows the data collected in the three different angle configurations. Also in this case multiple repetitions were performed. It was decided to do not show all the point of each test but only a mean repetition, in which the graph show the mean value of the measurements for each torque value. It can be noticed that without applying any torque to the middle phalange, when the MCP is equal from 0° to 30° and 60° , the PIP result to be equal to 22° to 12° and 0° . This means that the angle measured in the zero torque condition decrease when the MCP increases. This is probably due to the counteraction of the finger glove during flexion, which tends to be straight, extending the middle phalanx. The easily visible shifting of the results obtained also in correspondence

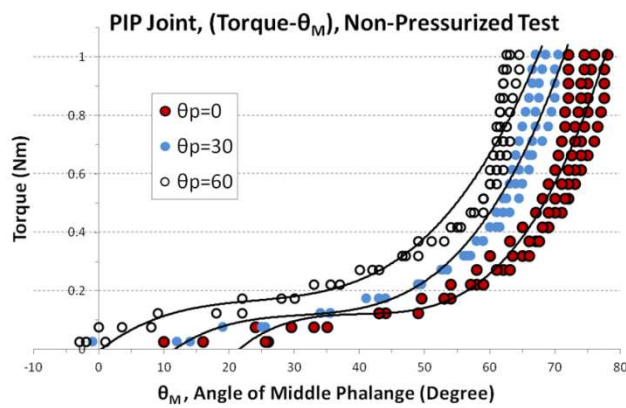


Figure 88: Torque vs. angle of the middle phalange θ_M for three values of θ_p in non-pressurized conditions

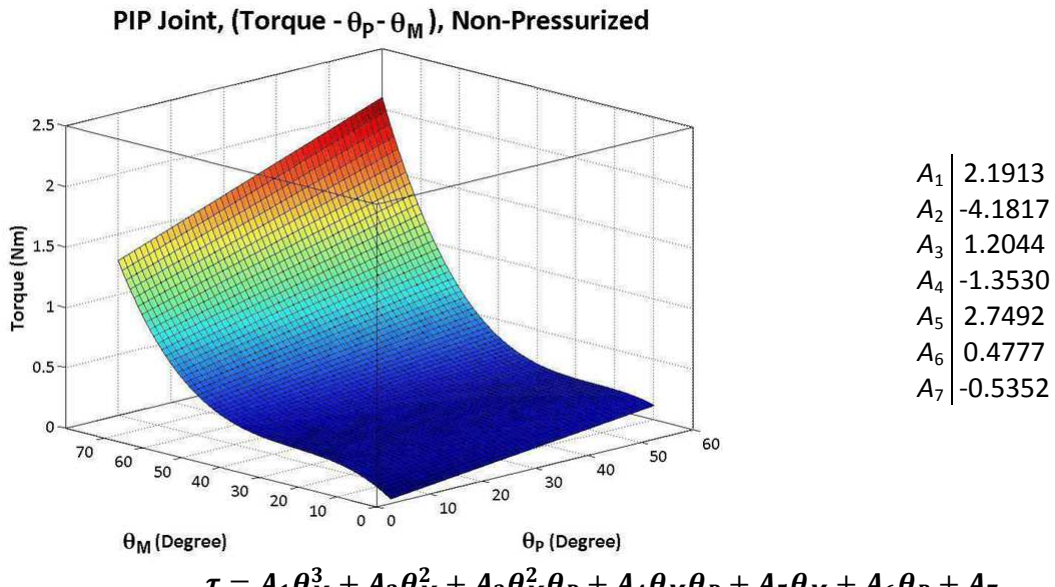


Figure 89: Interpolation surface describing the torque of the PIP joint in non-pressurized conditions

Test on EVA Glove

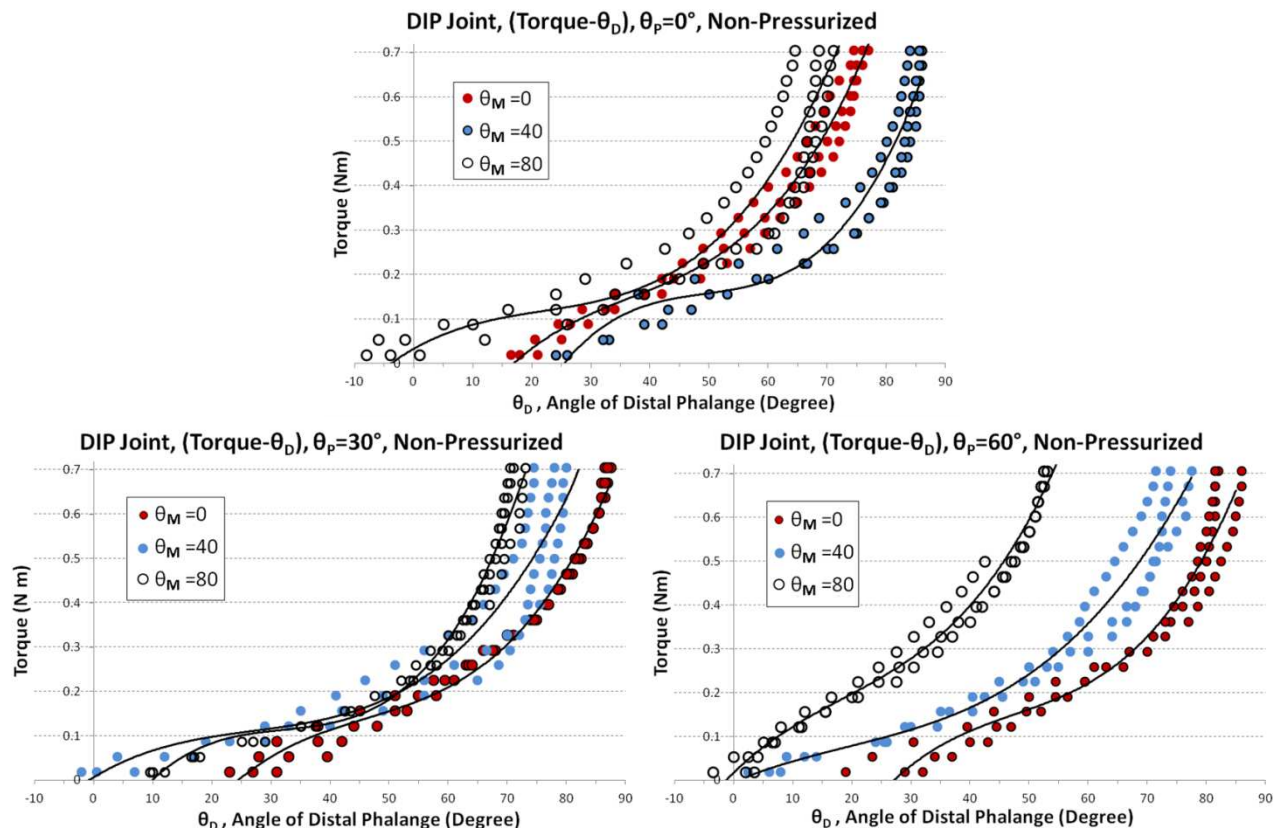
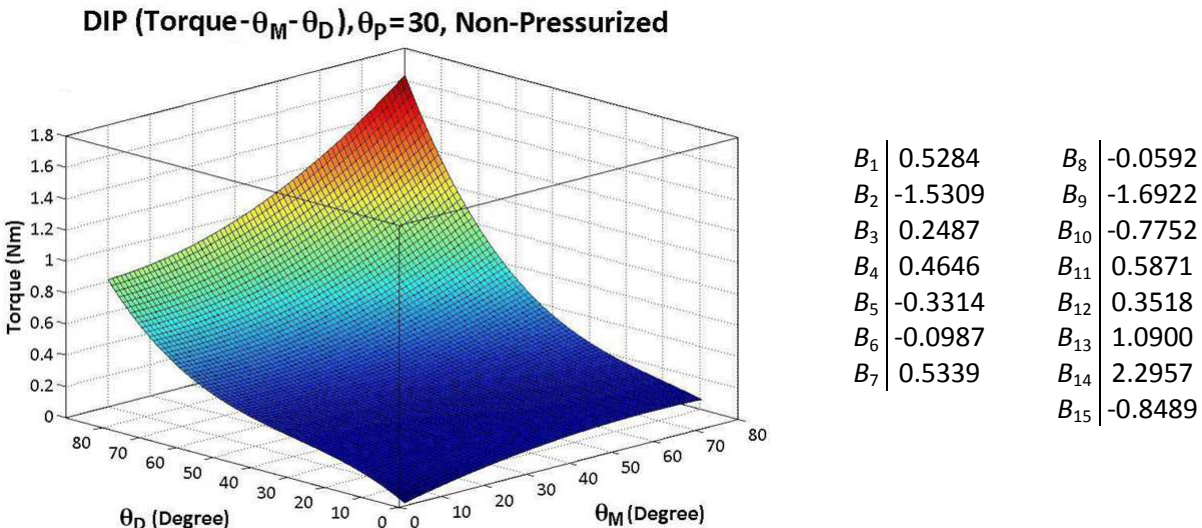


Figure 90: Torque vs. angle of the distal phalange θ_D non-pressurized conditions

of higher values of torques probably occurs for the same reason. It has been decided to perform a data interpolation in order to generate a surface able to describe the behaviour of the torque as a function of the two bending angles θ_P and θ_M . Figure 89 shows the obtained result both graphically and analytically.

The third and last series of data acquired is related to the DIP joint. The study of DIP joint involves nine different configurations based on different fixed position of the MCP and PIP joints. Both MCP and PIP can be fixed at three specific values; these angles are 0° , 30° and 60° for MCP and 0° , 40° and 80° for PIP. Figure 90 shows the data collected for the nine different configurations; each of the subfigure reports the three series of data related to a specific value of the MCP joint. The subfigure placed on top shows the behaviour of the torque with $\theta_P = 0^\circ$. It can be noticed that, with the same value of torque applied on the DIP joint, the rotation angles result to be higher when $\theta_M = 40^\circ$ compared to $\theta_M = 0^\circ$ and $\theta_M = 80^\circ$. There is no clear positive correlation between the torque applied on the DIP joint and its bending angle in this specific configuration. However, in the other two subfigure ($\theta_P = 30^\circ$ and $\theta_P = 60^\circ$), this positive relation can be noticed and, in particular for $\theta_P = 60^\circ$, result to be very clear and defined. In order to explain the behaviour just described, the following hypothesis can be formulated involving the interaction between the layers of the multilayer structure. The glove layers are not perfectly fitted in each finger position; on the contrary they are folded or stretched at different points and in different ways depending on the angular combination of the three articulations. When MCP and PIP joints are fixed at zero degree the stiffness curve of the DIP joint results to be shifted toward the left; this effect is caused by the strong interaction between the layers of the glove. Although this translation causes the rotations angles to be lower and the derivative of the curve, which is the stiffness, does not change significantly. Vice versa, when the MCP and PIP are fixed to their maximum



$$\begin{aligned} \tau = & B_1 \theta_D^3 + B_2 \theta_D^2 + B_3 \theta_D^2 \theta_P + B_4 \theta_D^2 \theta_M + B_5 \theta_M^2 + B_6 \theta_M^2 \theta_P + B_7 \theta_M^2 \theta_D + B_8 \theta_P \theta_M + B_9 \theta_M \theta_D \\ & + B_{10} \theta_P \theta_D + B_{11} \theta_P \theta_M \theta_D + B_{12} \theta_P + B_{13} \theta_M + B_{14} \theta_D + B_{15} \end{aligned}$$

Figure 91: Interpolation surface describing the torque of the DIP joint non-pressurized conditions

values, the stiffness value increase sharply since low values of torque. In fact, when the previous phalanges are bent, the external surfaces of the glove come partially into contact with itself, increasing the perceived stiffness. Also in this case, given the values of θ_P , θ_M and θ_D , a data interpolation has been performed to describe the behaviour of the torque required to flex the distal phalange as a function of the bending angles. Since τ is a function of the three bending angles, in order to show a graphical representation of this equation is mandatory fix one of them. Figure 91 show the equation of the surface and the graphically representation fixing $\theta_P = 30^\circ$.

Pressurized conditions

All the tests performed within unpressurized conditions were then repeated pressurizing the EVA glove, with a differential pressure of 0.4 bar. Also in those conditions the first series of data acquired is related to the MCP joint. Figure 92 shows four set of data and correlates values of torques applied on the MCP joint with the bending value of the proximal phalange. Comparing the results of tests related to MCP

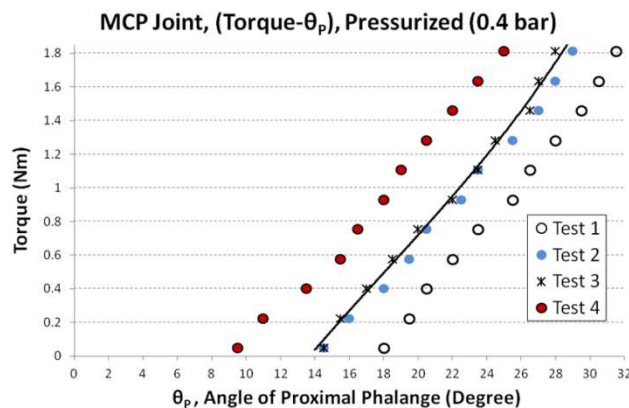


Figure 92: Torque vs. angle of the proximal phalange θ_P in pressurized conditions

Test on EVA Glove

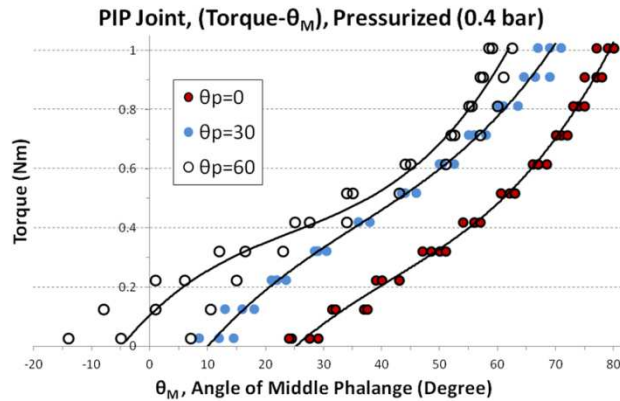
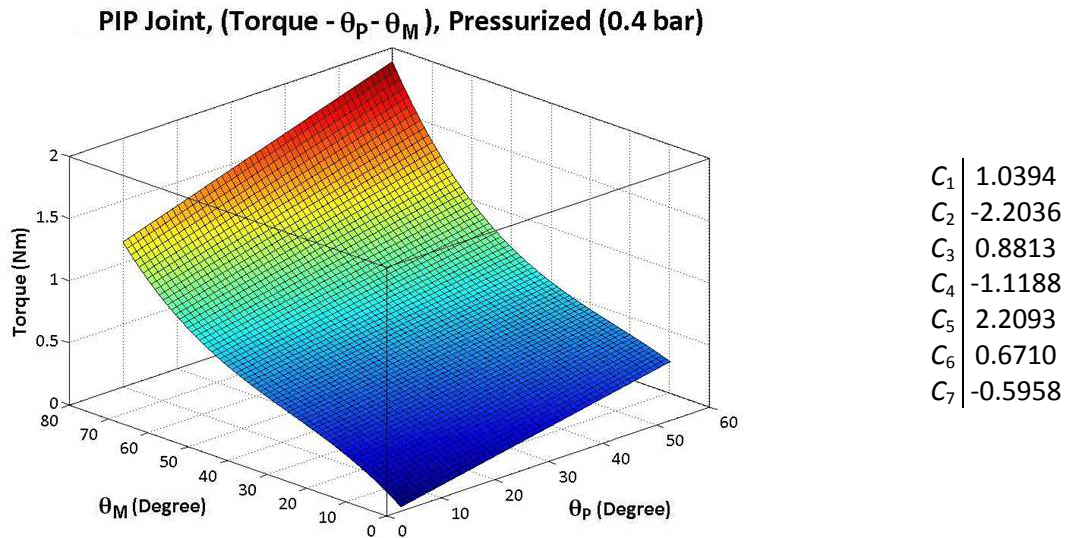


Figure 93: Torque vs. angle of the middle phalange θ_M for three values of θ_P in pressurized conditions



$$\tau = C_1 \theta_M^3 + C_2 \theta_M^2 + C_3 \theta_M^2 \theta_P + C_4 \theta_M \theta_P + C_5 \theta_M + C_6 \theta_P + C_7$$

Figure 94: Interpolation surface describing the torque of the PIP joint in pressurized conditions

joint in unpressurized conditions (Figure 87) and the pressurized conditions, it can be noticed that the stiffness in the second case shows a much more linear behavior with respect the first one. This change in the behaviour is due to the effect of the pressurization on the layers of the glove. Under the effect of pressure the three layers (bladder restraint and TMG) tend to remain extended and in contact one with each other and their folds, which are the main cause of the non-linearity, are eliminated. For what concern the angular displacement in view of the torque excitement; it can be noticed that the bending angle related to the pressurized conditions results to be far less than the ones relate do the unpressurized conditions. In particular, it is noteworthy that applying a torque of 1.8Nm generates a rotation of about 15° in pressurized tests, against of about 70° of the non-pressurized ones. The application of a delta differential pressure increase strongly the stiffness of the glove related to the proximal phalange.

Also in this pressure condition the second series of data acquired is related to the PIP joint. Figure 93 show the data collected in the three different configuration of MCP.

Test on EVA Glove

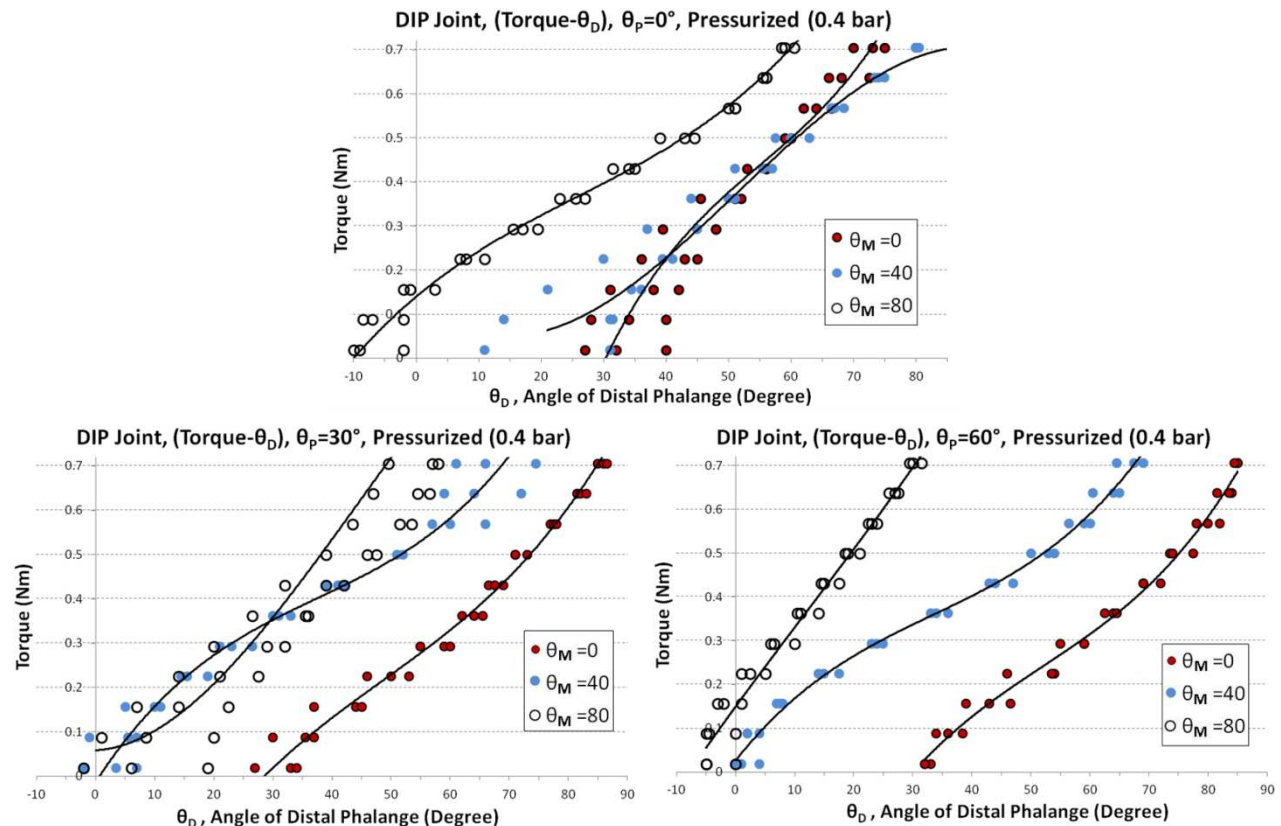
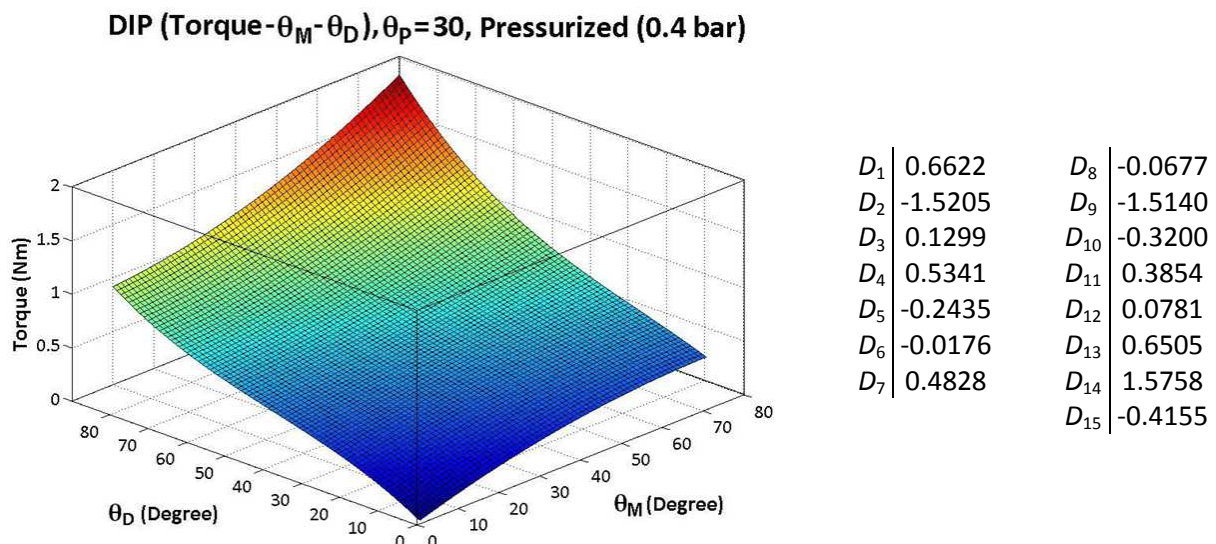


Figure 95: Torque vs. angle of the distal phalange θ_D pressurized conditions



$$\begin{aligned} \tau = & D_1 \theta_D^3 + D_2 \theta_D^2 + D_3 \theta_D^2 \theta_P + D_4 \theta_D^2 \theta_M + D_5 \theta_M^2 + D_6 \theta_M^2 \theta_P + D_7 \theta_M^2 \theta_D + D_8 \theta_P \theta_M + D_9 \theta_M \theta_D \\ & + D_{10} \theta_P \theta_D + D_{11} \theta_P \theta_M \theta_D + D_{12} \theta_P + D_{13} \theta_M + D_{14} \theta_D + D_{15} \end{aligned}$$

Figure 96: Interpolation surface describing the torque of the DIP joint pressurized conditions

Test on EVA Glove

Due to the counteraction of the glove, which tend to remain straight, when the proximal phalange is bent the middle phalanx is extent; this effect cause the shifting of the curves diminishing the values of the angles θ_M when θ_p increases. Also in this case it has been decided to perform a data interpolation to obtain a surface able to describe the torque required to flex the middle phalange for each combination of θ_p and θ_M . Figure 94 shows the obtained result both graphically and analytically.

The third and last series of data acquired is related to the DIP joint. Figure 95 show the data collected for the nine configurations. Also in this case each of the subfigure reports the three configuration of PIP joint related to a specific value of the MCP joint. The test results related to $\theta_p = 60^\circ$ show three curves that are distinctly separated. On the contrary, in the other two subfigure concerning $\theta_p = 0^\circ$ and $\theta_p = 30^\circ$, the cloud of data are partially overlapped. The reason for the strong non linearity shown in this test has to be researched in the complex structure of the glove and in the interaction between the pressurized layers. Finally the Figure 95 shows that the trends related to $\theta_M = 80^\circ$ are sharper than the others. It means that in those specific configurations the folded layers in the preceding phalanges generate a great stiffness on the distal phalange. Given the values of θ_p , θ_M and θ_D it is possible to obtain the surface able to describe the behaviour of the torque acting on the distal phalange. Also in this case, since τ is a function of three angles, it has been decided to fix one of them in order to show a graphical representation. Figure 96 show the equation of the surface and the graphically representation fixing $\theta_p = 30^\circ$.

Effect of Pressure

In this last part the effects of pressurization on the glove stiffness have been analysed. Two different pressure values have been compared; it has been decided to paragon the fully pressurized configuration, differential pressure equal to 0.4 bar, with the partially pressurized configuration, differential pressure equal to 0.2 bar. In order to observe the effect of pressure on the glove stiffness, all the graph show comparison between the joint angles obtained, applying the desired torque, in the two different pressure conditions. As could be seen from Figure 97 to Figure 99, differential pressure has enormous effect on the compliance of the EVA glove.

Figure 97 show the effect of pressure on the MCP joint. It can be appreciated that the difference between the two curves is very noticeable; θ_p decrease to at least half to up one third when the differential pressure is doubled. Figure 98 and Figure 99 show the effect on the PIP and the DIP joint respectively. In this case the effect between them is very similar, but it result to be strongly reduced with respect the MCP one. In order to analyse the effect of the pressurization on the PIP and DIP joint, it has been decided to acquire only one configuration among all the possibilities granted by the finger

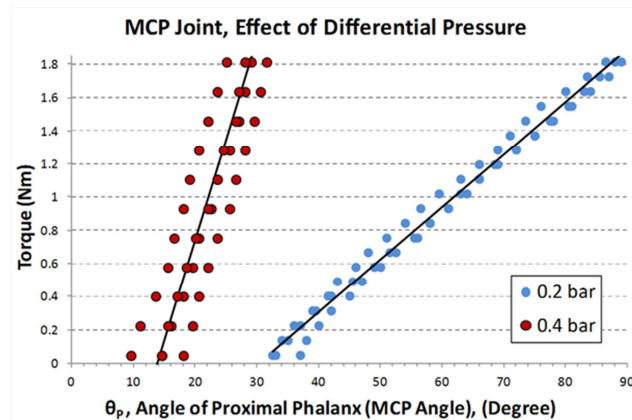


Figure 97: Torque vs. angle of the proximal phalange θ_p in the two pressure conditions

Test on EVA Glove

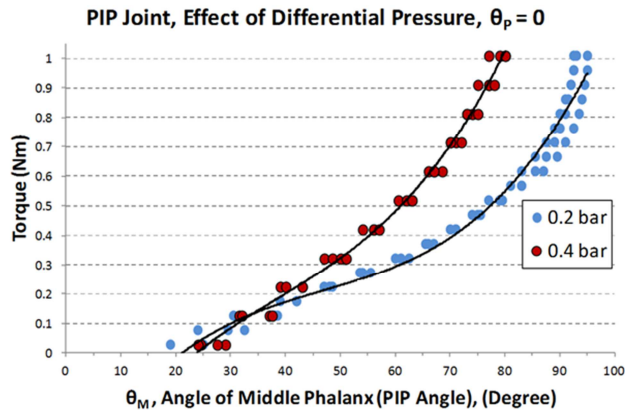


Figure 98: Torque vs. angle of the middle phalange θ_M in the two pressure conditions

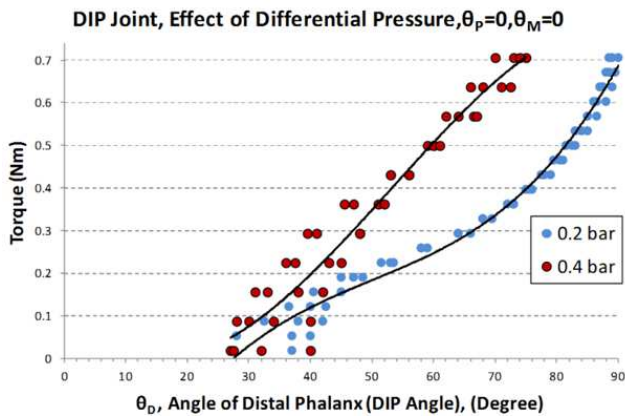


Figure 99: Torque vs. angle of the distal phalange θ_D in the two pressure conditions

probe, fixing the other articulations at 0° .

The MCP joint shows quite linear stiffness behaviour in both the curves. On the other hand, both PIP and DIP show an initial overlapping, due probably to the effects of interaction between the elements of multilayer system that constraint the movement preventing the flexion. Increasing the torque the effects due to the internal interaction became less incisive and the pressurization acquires the main role, influencing the stiffness in a stronger way.

CHAPTER 5:

“A human being will always suppose that, the more human a robot is, the more advanced, complicated, and intelligent he will be.”

Isaac Asimov, 1983

THE EXOSKELETON

As already introduced, the present study aims to develop a prototype of a hand exoskeleton designed to help astronauts during EVA missions, able to overcome the stiffness of the pressurized spacesuit, enhancing the strength of the human hand and reducing the overall fatigue required during tasks. The realization of a hand exoskeleton able to grant a high level of dexterity, and small enough to be really utilizable, results to be a very complex objective which presents several problems, sometimes completely unexpected. During the design and the implementation of a hand exoskeleton made for EVA missions it may run up against plenty of difficulties, mainly due to the extremely complex structure of the human hand and to the extreme environment in which the device is intended to work. Different typologies of devices could be realized in order to reach the goal aimed; different kinds of technologies, components and strategies can be utilized and assembled in order to cooperate towards the final goal, each of them with different strength and weakness.

The possible alternatives of installing the exoskeleton outside the EVA glove instead of inside it, or of realizing a sort of remote robotic hand instead of a true exoskeleton, would change completely the constraints and the issues that have to be taken into account during the preliminary study and during the development of the device. As explanatory example, the choice to realize an exoskeleton which has to be embedded inside the EVA glove, changes the application environment of the project from the space to the glove. This means that some problems and constraints related to the space environment become less incisive or can be completely neglected, because they are already screened by the protective multilayer system of the TMG; on the contrary, other issues, like dimensions and working space, arise, becoming much more important.

The present section briefly analyses the main constraints and the consequents preliminary design choices related to the application scenario of the project.

Dimensions, Weight and Working space

The Exoskeleton

The exoskeleton dimensions and weight are two of the main constraints in this project. Limited mass and inertia are important requirements for the device because they strongly influence the ability of the human being of performing manipulation tasks. Moreover, size and mass result not only involved into the shape and aspect of the structure, but they are also a major constraint on the choice of each component that compounds the device, in particular those related to actuation system and structural materials. As already shown in the state of art, nowadays exoskeleton found in literature or commercially available result to be generally bulky and heavy, because they are built for tasks, such as rehabilitation or virtual reality, that do not require strong size limitations. In this project, on the contrary, designing a device as small as possible is fundamental, in particular if it is planned to be embedded it into the glove, which became the size limiter.

Another critical point in the development of a hand exoskeleton is related to the extremely wide possibilities of movement and typologies of grips that the human hand can perform. It results to be unthinkable to realize a robotic device that does not impede the hand movements at all, but, at the same time, it is mandatory that the device does not impose excessive restrictions to the hand dexterity, limiting the overall working space. Enhance the performances granted by the EVA glove would be a good result for the hand exoskeleton. Some examples of constraints, related to the dexterity problem, could be provided, taking into account only the shape of the structure of the exoskeleton. First of all, the palm should be as free as possible in order to avoid limitation of the ability to grasp and handle object, so it is strongly preferable to place all the bulky components on the back of the hand. Furthermore the lateral thickness of each finger must be reduced in order to allow all movements related to the finger abduction – adduction. These represent only some examples of limiting factors on the structure and on the technologies that can be used.

It is necessary to consider that today's EVA gloves are not designed to be filled of robotics components in addition to the human hand, but they are usually realized to fit as best as possible the specific astronaut's hand. Considering this, in the future it would be required to redesign completely the glove itself, granting more space to place components and realizing a garment able to coexists with a robotic device. Some dimensions could be increased and some elements could be completely removed: for example, inserting a robotic device into the exoskeleton no more restraint layer will be needed. This would probably be an essential further step in case the hand exoskeleton becomes a standard component of the astronaut's equipment.

Degree of Freedom and Joints

As already exposed, the hand is a very complex limb with 23 Degrees of Freedom placed in a significantly reduced space. It is difficult to faithfully reproduce every possible movement by means of a robotic structure, especially under the constraints related to weight and size analysed above. Another big challenge arises considering the first joint of the thumb that causes the displacement of a great portion of the palm. Therefore two requirements are in conflict one with each other: the desire to ensure high dexterity to the operator, realizing a structure with an elevated number of DoF and able to reproduce faithfully the motion of the hand, and the need to create a device with limited size and weight. Since it will be hardly possible to actuate and sense 23 DoFs in an appropriate way, and conversely it would be useless to create a basic device with few DoFs unable to really help the operator, a compromise should be found. Analysing the various movements which the hand has to perform during typical tasks and studying the intra and extra constraints of the human hand, the number of active DoFs of the exoskeleton can be reduced using appropriate kinematic dependencies and passive joints.

Furthermore the articulation itself results to be another critical point related to the human hand. The finger phalanges rotate around an axis located inside the finger. Logically, in order to replicate the movement of the operator's finger avoiding mechanical interference between the human being and the

The Exoskeleton

robotic device, the positions of the two centres of rotation have to be the same. If the actuation system could be placed on the side of the finger, applying directly the motion on the articulation, the latter exposed problem would be trivially solved without particular tricks. However, if the actuation system is placed on the back of the hand in order to reduce the lateral thickness of each phalanx, the actuating structure becomes more complex because it has to lengthen and shorten during finger movements, in order to guarantee the correct instantaneous centre of rotation.

Space Environment

Space is a highly dynamic environment that presents many threats related to several different aspects [133]. All the various factors must be taken into account designing a robotic device and, in particular in the choice of the different components and materials that compound the exoskeleton. The glove, and the suit in general, guarantee a certain level of protection from a wide range of effects through the TMG multilayer system. Despite the protective layers, some problems related to the space environment, such as cosmic dust, electromagnetic interferences, high temperature variations, micro-meteoroids still persist.

Cosmic dust is a variety of dust composed by very small particles which are molecules up to $0.1\text{ }\mu\text{m}$ in size. These dust particles are able to penetrate through the seals of the space suit, thanks to the extremely reduced dimensions, causing many problems to the astronaut's health or the mechanical components; cosmic dust is a well-known problem that affects every EVA mission made on the planet surface since the first moon landing [31, 32]. Electromagnetic interferences are due to many causes in the space: solar activities, high energy particles, electromagnetic radiations and space plasma can degrade or damage all the electronic devices and also generate a high background noise possibly leading to permanent damage and component failure. Sensors in particular are very sensitive to these effects because the high level of background noise can cause wrong data acquisition and make useless the information obtained. Micro-meteoroids are small particles, made of various types of materials, which travel with high relative velocity through space. Despite the mass of these particles are usually very small, the high velocity generates an elevate kinetic energy that can result dangerous upon direct impact. Another important indirect effect of the space scenario is represented by the strict requirements in terms of energy consumption needed to work in this specific environment; it is very important to reduce as much as possible the energy consumption of all the components in order to increase autonomy and allow the use of smaller batteries. Finally, in order to guarantee a high safety level to astronauts during their activities, the space companies imposed a series of constraints, limiting the technological possibilities for components to be used into space environment and in the spacesuit in general. For example, devices based on high pressure fluids, like pneumatic or hydraulic actuators, were forbidden and cannot be used inside a spacesuit.

Main idea and overview of the possibilities

In order to simplify the approach towards a hand exoskeleton it has been decided to start from the realization of a single finger exoskeleton, which represents the first approach towards the final device. The modular structure of the human hand allows a single finger device to be realized and then replicated on each human finger, with the appropriate wisdom. The design of the finger exoskeleton already includes all the requirements for the whole hand exoskeleton: it has to support the finger movements, ensure the correct kinematics and it must not interfere with the palm or with the other fingers of the hand.

As already explained, the human finger is composed of three articulations, distal-interphalangeal (DIP), proximal-interphalangeal (PIP), metacarpophalangeal (MCP), and of four phalanges, distal, middle,



Figure 100: Three possible solutions to overcome the problem of the finger crotch: sliding concentric surfaces (left), four bars mechanism (middle) and asymmetric design (right)

proximal and metacarpal phalanx. Each finger can be modeled with a kinematic chain composed of four links and four DoFs. Three of them are related to the flexion-extension movement and one is related to the adduction-abduction movement. At this stage it was decided to neglect the DoF related to the adduction-abduction movement and kept passive. Thus it was realized a concept model composed of only the three DoFs which have parallel axes. The MCP articulation presents another problem, which result to be probably the biggest difficulty related to the mechanical design of the finger structure: the crotch. The webbings between fingers impose strong restrictions on the location and shape of the elements of the device and require the designer to look for non-trivial solutions. Figure 100 shows three possible solutions to overcome the crotch problem; as it is easily understandable, the complexity of the device, in correspondence of the first finger joint, increases sharply. It is mandatory that the center of rotation of the mechanism related to the MCP joint must be coaxial to the corresponding human joint. It should be noted that the main concepts are applicable to any finger of the hand (and to any similar serial structure). Only the final design will require distinctions between fingers, because the relative position of each finger inside the hand needs different solutions. For example the third solution showed in Figure 100 (right) could be only applied to the index finger and to the little finger because it requires a completely free side of the finger on which being mounted. As already mentioned, in this project a key factor is to carefully plan the bulk of each element of the design in order to avoid self-interference and to guarantee the desired high level of dexterity and grasping. All mentioned concepts can be generalized and applied to different solutions that maintain the general idea of a finger exoskeleton.

The human knuckles are not pure rotational joints. They have a behaviour which is more similar to a sliding convex-concave couple of profiles with different and varying radii, as shown in Figure 101 [134]. The faithful reproduction of this type of joint is an unnecessary complication in the design and would be excessively demanding in terms of size and weight. A pure rotational joint is an acceptable compromise between simplicity and faithfulness, which guarantees a kinematical behaviour very similar to the real one, since the human finger has enough flexibility to compensate such small differences without problems or risks. Three different solutions to design pure rotational joints were analysed: traditional joints, virtual joints and no joints. Traditional joints, i.e. a classic coupling of two or more rigid elements, such as a hinge, have the advantage of ensuring the right kinematics and allowing the distribution of a large part of the resultant forces directly on the structure; this solution is demanding in terms of dimension and weight. The “no joints” solution is the best one in terms of dimension and weight, but it has some disadvantages: first, the entire resultant forces act on the finger and stress the articulation, while only the human finger guarantees the correctness of kinematics. Finally virtual joints are elements

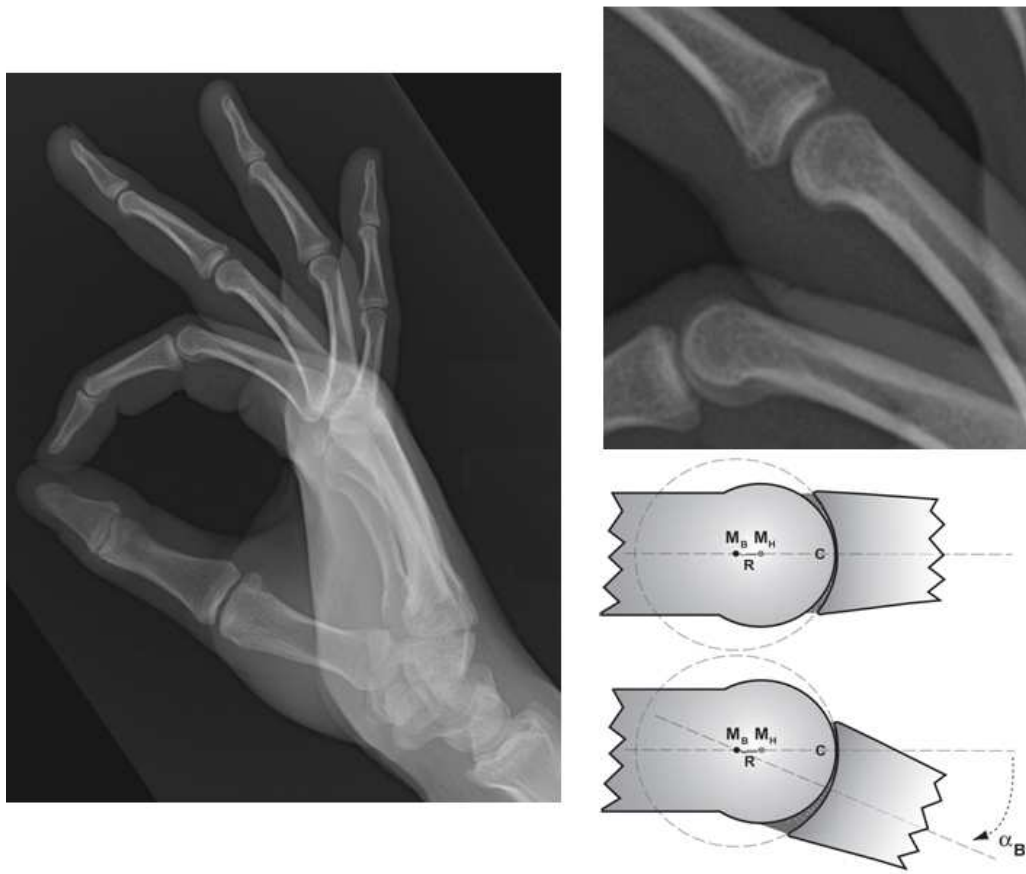


Figure 101: Human knuckles Behaviour

that ensure kinematics without being true joints, such as elastic components, e.g. flexures; they are a compromise between traditional joints and the “no joints” solutions.

The Wire Actuated Solution

Robotic devices like exoskeletons can differ one from each other for their initial requirements and constraints, for their general architecture and finally for the elements composing them. Once the architecture is set, actuation and transmission constitute two of the fundamental elements that characterize every robotic structure. For the first concept of the device a specific typology of actuation and transmission system has been considered: the single effect wire actuation. This is an asymmetric transmission system made up by a series of wires that act the structure only in one direction. This kind of actuation system was chosen in order to minimize the dimensions and weight of the final device because, as already explained, the bulk of the device is a fundamental requirement for this specific project. Cable (or wire, or tendon) actuation is widely used in robotics, in particular for parallel manipulators or robotic hands. Several examples of parallel manipulators can be found in literature: the WiRo [135, 136], WARP [137], NIST Robocrane [138], Falcon-7 [139]. Extensive theoretical work was performed by J.P. Merlet [140, 141, 142]. Regarding robotic hands, the Shadow Hand [143] and the DLR-Hand II [144] are two very important examples of the state of the art. The main advantage of using wire actuation is represented by the possibility of lightening the most critical points, by placing the actuators

The Exoskeleton

in a less problematic position. An explanatory example of this possibility is the Shadow Hand where all the actuators, i.e. pneumatic muscles, are placed in the forearm thus realizing a human sized robotic hand. The obvious inconvenience of the use of a wire actuated device is that the cables can only work by traction: therefore, special solutions are required to obtain the complete control of each Degree of Freedom (DoF).

In order to overcome the problem of traction and still maintain the reduced complexity of the device, it was decided to study a single effect actuation. Therefore, each DoF of the robotic structure is actuated actively only in one direction, while the recall movement is effected through passive elements, e.g. elastic components. As mentioned before, wire actuation allows dimensions and weight to be reduced by keeping the actual device unhampered. Moreover, the placement of the actuation system in a non-critical position means that it can be neglected completely during the first steps of the design and its actual definition postponed. Furthermore, the intrinsic stiffness of the EVA glove, caused by its multiple layers and its internal pressurization, allows the realization of the single effect strategy. The glove itself can act as the passive elastic element to perform the return stroke. This choice simplifies the structure and the actuating system greatly and contributes in part achieving the goal of lightness and reduced dimensions. This analysis can be applied to any joint solution (true, virtual or no joint), provided that there is an element which ensures extension movements, e.g. an elastic element, otherwise, the whole concept of “single effect” cannot be applied. The transmission proposed here is achieved by mono-directional tendons (wires), which pull each phalanx (or link) only in its flexion movements. The extension movement is guaranteed by passive elements coaxial with the joints. A possible example of passive elements could be achieved by a series of elastic elements placed at the joints. These elements can represent a real elastic component, e.g. a torsion spring, or any element that can be modelled like an elastic component, e.g. the intrinsic stiffness of the EVA glove.

Tendon transmission allows using as little space as possible in correspondence with joints and links, by placing the actuation system in a non-critical position, for example the forearm. For this reason, the actuation itself is not treated in this study, since we are considering having any means of applying a controllable motion and tension to the wires to create transmission. This solution considers that, in this project, the actuation and transmission system cannot be directly linked to the joints. The wires pass through the links and are fixed to their “final” link without guaranteeing a fixed arm with respect to the joints. This assumption means that the concept could also be generalized both for virtual joints and “no joints” solutions, where it is not possible to impose the passage of the cables through a point that is fixed with respect to the joint. This choice has two main consequences: the minimum distances between the cables and the joints will not remain fixed during movements, and the passage of the cables through the center of rotation of the joints cannot be imposed. Figure 102 shows the differences between the classical wire actuation with access to the joint (left) and the solution proposed in this paper with no



Figure 102: Wire actuation with (left) and without (right) access to the joint

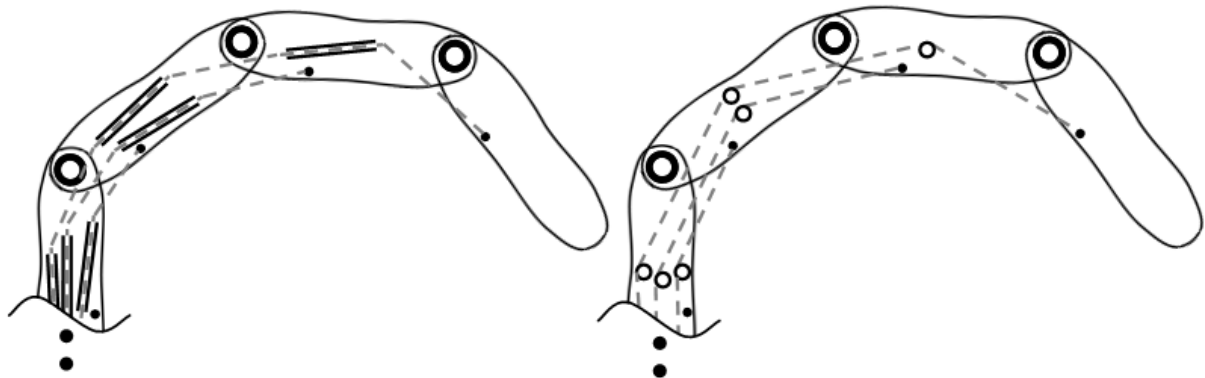


Figure 103: Concept structure with micro-machined holes (left) and with micro-pulleys (right)

access to the joint (right). These assumptions also imply that the movements of the joints cannot be decoupled from one another, thus transmission of the joint i also acts on the previous $i-1$ joints.

The above discussion provides a series of motivations for each choice and a functional idea of each element of the future physical device. This means that a family of devices could be unified under the same previously treated “*guidelines*”, independently from the specific technological solutions. The choices to place real springs or not, to allow the passage of the cables with micro-machined holes rather than micro-pulleys are examples of different technological solutions for the same concept, each of them with different advantages and disadvantages. Figure 103 represents the conceptual scheme under study. Each link of the robotic device is represented by a generic rounded block that has to be designed in order to fit with the human hand. Two adjoining blocks are linked together with a pure rotational joint that can be real, virtual or fictitious (in the case of “no joint” solution). An elastic component is placed inside each joint in order to guarantee the extension movement (not represented in the pictures). A certain number of tendons pass through each block. They are used to transmit motion, depending on the position of the block in the kinematic chain. The passage of the wires through the links can be achieved in different ways. Figure 103 shows two examples, i.e. micro-machined holes (left) and pulleys (right). Other solutions are also possible.

Once defined the main guidelines under which the device has to be subordinated it was necessary to create the mechanical design of the prototype. The mechanical design required a lot of time to be finalized and it is the result of a series of continuous and successive modifications ongoing even today. Figure 104 show the main steps of the evolution of the mechanical design: the two biggest pictures represent the two versions of wire actuated analyzed in the following part.

The First Wire Actuated Solution

The first wire actuated solution is proposed here and shown in Figure 105; it is based on the main guidelines previously reported in the introduction: a 3DoF structure without the abduction-adduction joint and actuated by wires. A modular test bench, on which the device will have to be mounted, was designed contemporaneously with the exoskeleton. The goal of the test bench consists in granting better stability of the device and helping the operator to perform all the future tests related on it. The test bench allows also the motors to be easily mounted and kept in position independently from their dimensions and weight. The exoskeleton proposed here presents an asymmetric design, with three elements placed in correspondence of the finger phalanges alternated with three torsions springs.

The Exoskeleton

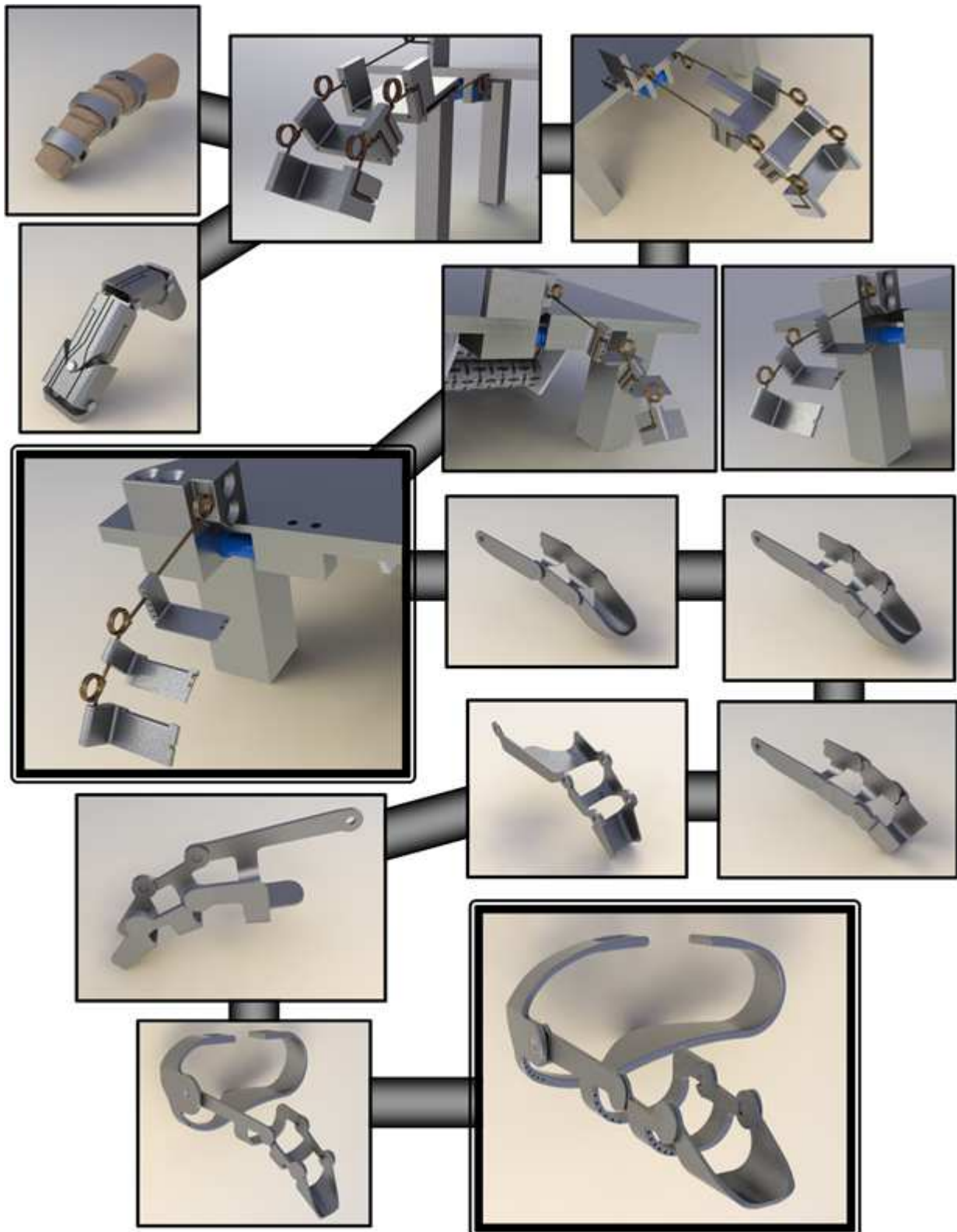


Figure 104: Main steps of the evolution of the wire actuated exoskeleton

The Exoskeleton

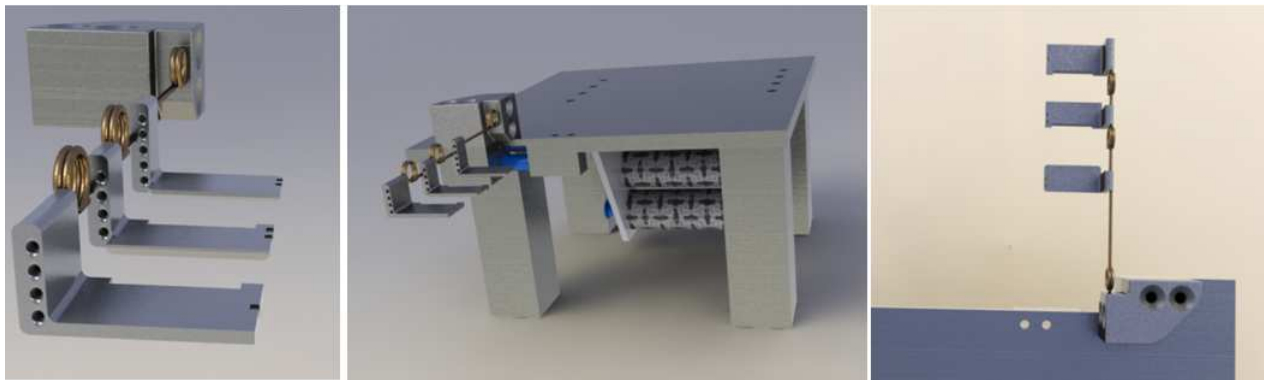


Figure 105: First wire actuated design: detail of the phalanges (left), the whole test bench (middle) and the top view of the test bench (right)

The three torsion springs act like virtual joints, granting the bending movement and were placed in correspondence with the finger articulations. There were two main reasons to choose an asymmetric design. The first reason was to reduce the dimensions of each element of the exoskeleton; removing completely one lateral wall permit to decrease the lateral thickness of each finger. Moreover this solution allows the designer to overcome the problem caused by the finger crotch. It results trivial to underline that different fingers require different solutions in order to fix the exoskeleton through the spring placed in correspondence of the MCP articulation. Figure 106 shows a mechanical design feasible only for the index finger of the left hand because, in this case, the support of the MCP spring is realized with a wall placed on the right side of the hand. The little finger will need a mirror solution whereas the middle and ring finger will require a completely different typology of support, probably placed on the back of the hand. Each of the three elements of the exoskeleton, which from now will be called phalanges for simplicity, is different from the others, with custom dimension chosen on the basis of the biometric parameters. Figure 106 shows in details one phalanx of the exoskeleton. Each phalanx presents a pair of caves made to jam the springs; each cave starts from one side of the phalanx, runs along the bottom side and gets up on the other side. Through each phalanx passes a series of holes, made to allow the wires to pass along the exoskeleton. In this design holes are parallel between them and to the surface on which the finger lays; moreover, all the holes of the phalanx were placed vertically in order to reduce further the lateral thickness.

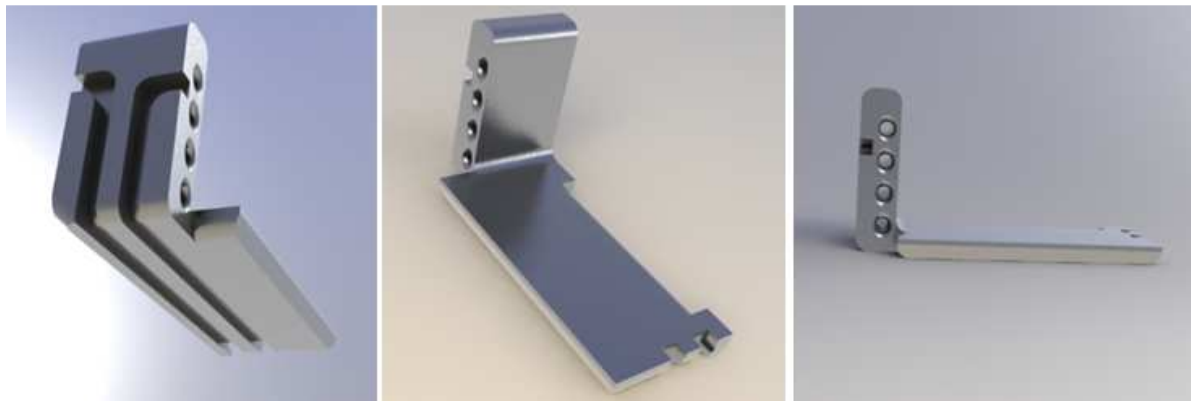


Figure 106: Three view of the exoskeleton phalanx

Static Analysis

The static analysis of the device allows understanding the equilibrium of the exoskeleton in its interaction with the human finger. It is mandatory to know the forces and the torques, in terms of direction and magnitude, exchanged by the device with the external world and between the various elements that compound it, in order to be able to mould the dimensions and geometries of the device. For that reason, the behaviours of the tendon tensions and the constraining reactions were obtained as a function of the geometrical parameters, the bending angles and the design choices; this allows to check and model the mechanical structure in order to obtain the desired range of variation of developed forces.

Figure 107 represents the scheme of the generic i -th link of the robotic structure. The generic i -th link is placed between two axis of rotation: the i -th axis and the $(i+1)$ -th axis. The i -th axis connects the i -th link with the $(i-1)$ -th (the previous one), it is placed upstream and shown on the left part of the figure; on the contrary the $(i+1)$ -th axis connect the i -th link with the $(i+1)$ -th (the following one), it is placed downstream and visible on the right of the figure. Each link is associated to a local coordinate reference system \mathcal{R}_i , which uniquely defines its position and orientation. The origin of the i -th reference system was chosen coincident with the i -th axis of rotation. The axis of \mathcal{R}_i , x_i and y_i , were chosen to be respectively parallel and perpendicular to an hypothetical support surface of the finger. Two adjoining rotational joints are apart from each other of a length equal to L_i along the x_i axis and e_i along the y_i axis. The angle of rotation between two adjoining links has been defined θ_i and it is equal to the corresponding bending angle of the finger. Each link is driven by a corresponding wire, represented by the dotted lines in Figure 107. The architecture consists of a serial chain of three links, each of them hosting the holes for the wire that drives the following elements. It is easy to demonstrate that 4- i wires pass through the general i -th link; in particular three tendons pass into the first link and only one passes into the third. The tension of the j -th tendon has been called T_j . The holes of each tendon j are designed to be parallel to the x_i axis and described by a parameter that represents the position along the y_i axis, which is called h_{ji} . The wire $j=i$ acts specifically on the i -th link and ends there. The generic wire j ($j > i$) enters the i -th link, coming from the previous one, and continues to the following one. Passing from the

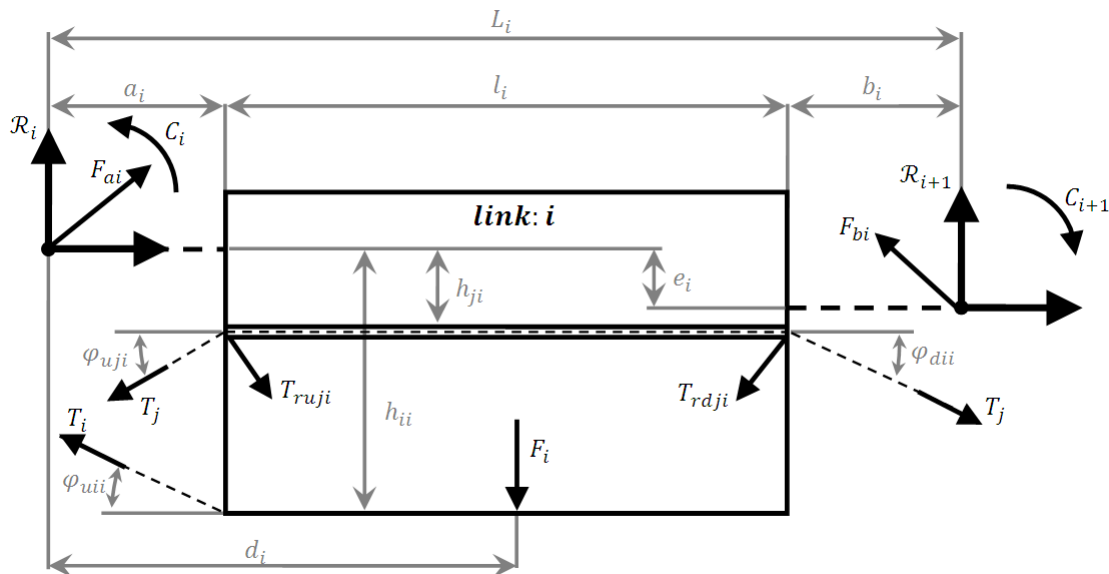


Figure 107: Generic i -th link of the exoskeleton

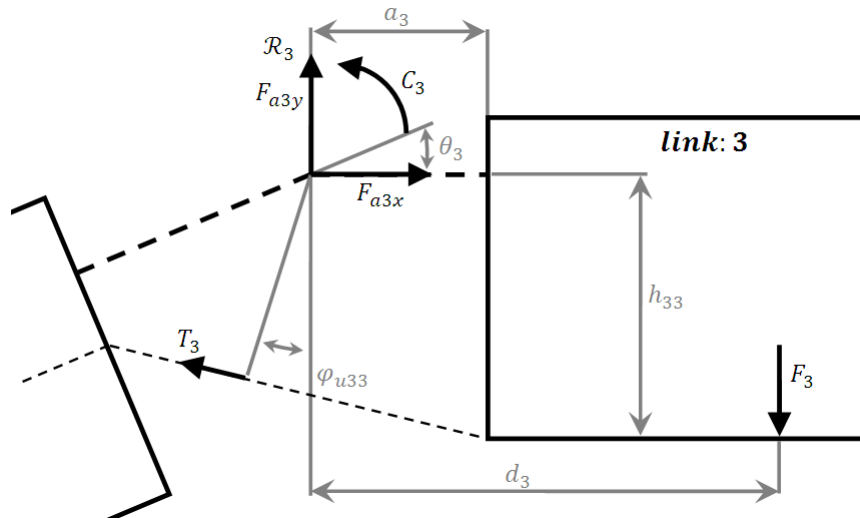


Figure 108: Third link of the exoskeleton

i-th link to the following one, each tendon *j* is bent by an angle equal to φ_{dji} (*d* for downstream). The same effect happen with respect the previous link, but in this case, the angle is defined φ_{uji} (*u* for upstream). The tendon tensions T_i , and the previously explained angles, generate two reaction forces on the extremes of the tendon holes, called T_{rdji} and T_{ruji} . Each phalanx of the human finger applies a contact force on the correspondent link, which has been defined F_i ; for simplicity it was decided to consider F_i normal to the resting surface and applied at one distance equal to d_i . The forces and the torques acting on each link generate some constraining reactions that the generic *i*-th link applies on the two adjoining bodies. Each body exerts on the previous one a reaction force called F_{ai} and receives from the following a force called F_{bi} . In Figure 107 the two forces F_{ai} and F_{bi} are decomposed into the components along the x_i and y_i axes. Similarly to what happens with reactive forces, the bodies exchange between them reactive torques that take into account the effect of the elastic element placed at the joints. Each body exerts on the previous one a reaction torque called C_i and receives from the following a reactive torque called C_{i+1} . The remaining geometric parameters are clearly visible in the Figure 107. All the holes of the wires of the *i*-th link are parallel to the x_i axis and coplanar, moreover they start and end at the same x coordinate. No effect of friction of the wires inside the holes was taken into account and then the tension T_i results being constant along the wire length. Finally, all the masses were considered negligible in this approach.

The best way to obtain the equations of the system is to start to the last link (the farther from the hand) and then walk back up through the kinematic chain obtaining, time by time, the reaction applied on the previous. Figure 108 shows the free body diagram of the third body and all the forces and torques applied on it. The translational equilibrium of the third link could be easily obtained as a follow:

$$\left\{ \begin{array}{l} F_{a3x} = T_3 \cdot \cos(\varphi_{u33}) \\ F_{a3y} = F_3 - T_3 \cdot \sin(\varphi_{u33}) \end{array} \right. \quad 40$$

And the rotational equilibrium results to be equal to:

$$F_3 \cdot d_3 + T_3 \cdot [h_{33} - a_3 \cdot \tan(\varphi_{u33})] \cdot \cos(\varphi_{u33}) - C_3 = 0 \quad 41$$

The Exoskeleton

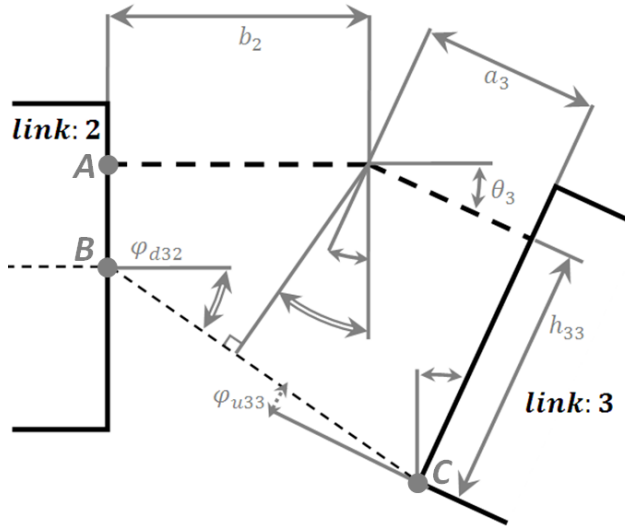


Figure 109: Third joint of the exoskeleton

Where, the arm of the torque generated by the tension T_3 has been obtained by means of simply trigonometric passages. Re-writing the tangent as the ratio between sine and cosine and then simplifying, the equation 41 can be written as follow:

$$F_3 \cdot d_3 + T_3 \cdot [h_{33} \cdot \cos(\varphi_{u33}) - a_3 \cdot \sin(\varphi_{u33})] - C_3 = 0 \quad 42$$

C_3 is a torque that takes into account the effect of the elastic element acting on the joint three. Regarding the equation 42, all the variables are known except the bending angle of the tendon, φ_{u33} . Figure 109 shows in detail the third joint and all the dimensions related to it. If the third link is bent with respect the second one by an angle equal to θ_3 , it can be easily demonstrated that the bending angle of the wire 3 performed going out from the second link, φ_{d23} it is equal to:

$$\varphi_{d23} = \varphi_{u33} + \theta_3 \quad 43$$

Three points shown in Figure 109 (A, B and C) are now defined. The next step is to calculate the distances between the points A and B, A and C along the axis x_i and y_i . The distances \overline{AB} and \overline{AC} result to be equal to:

$$\left\{ \begin{array}{l} \overline{AB}_x = 0 \\ \overline{AB}_y = h_{32} - e_2 \end{array} \right. \quad 44$$

And

$$\left\{ \begin{array}{l} \overline{AC}_x = a_3 \cdot \cos \theta_3 - h_{33} \cdot \sin \theta_3 + b_2 \\ \overline{AC}_y = a_3 \cdot \sin \theta_3 + h_{33} \cdot \cos \theta_3 \end{array} \right. \quad 45$$

At this point, using trigonometric relations, the angle φ_{d23} can be easily obtained:

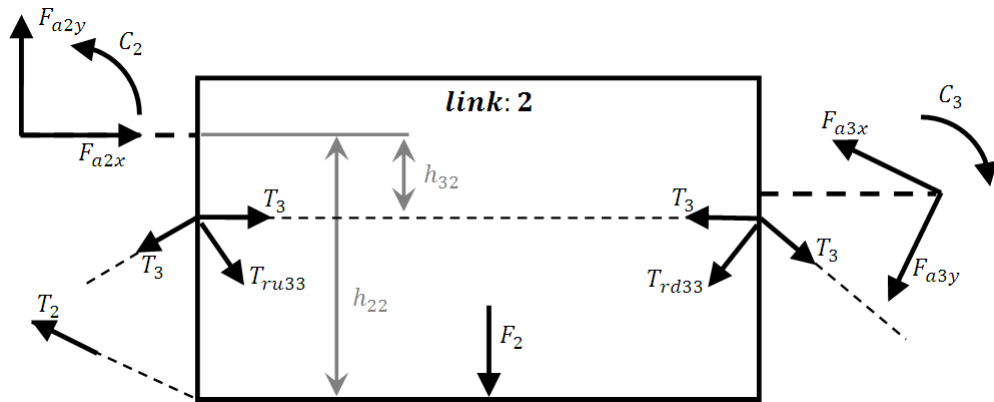


Figure 110: Second link of the exoskeleton

$$\varphi_{d23} = \tan^{-1} \frac{\overline{AC_y} - \overline{AB_y}}{\overline{AC_x} - \overline{AB_x}} \quad 46$$

Substituting equations 43, 44 and 45 into the equation 46 the final equation of φ_{u33} can be obtained:

$$\varphi_{u33} = \tan^{-1} \frac{(a_3 \cdot \sin \theta_3 + h_{33} \cdot \cos \theta_3) - (h_{32} - e_2)}{(a_3 \cdot \cos \theta_3 - h_{33} \cdot \sin \theta_3 + b_2)} - \theta_3 \quad 47$$

At this point the tension of the third wire and the reaction torque and forces acting on the joint two, are obtained. Figure 110 shows in detail the second joint and all the dimensions related to it. The first step at this point was to calculate the effect of the constraint force F_{a3} and of the tendon tension T_3 on the link two into the reference system \mathcal{R}_2 shown in Figure 111. F_{b2} is the vector of the constraining reaction F_{a3} mapped into the reference system \mathcal{R}_2 and result to be equal to:

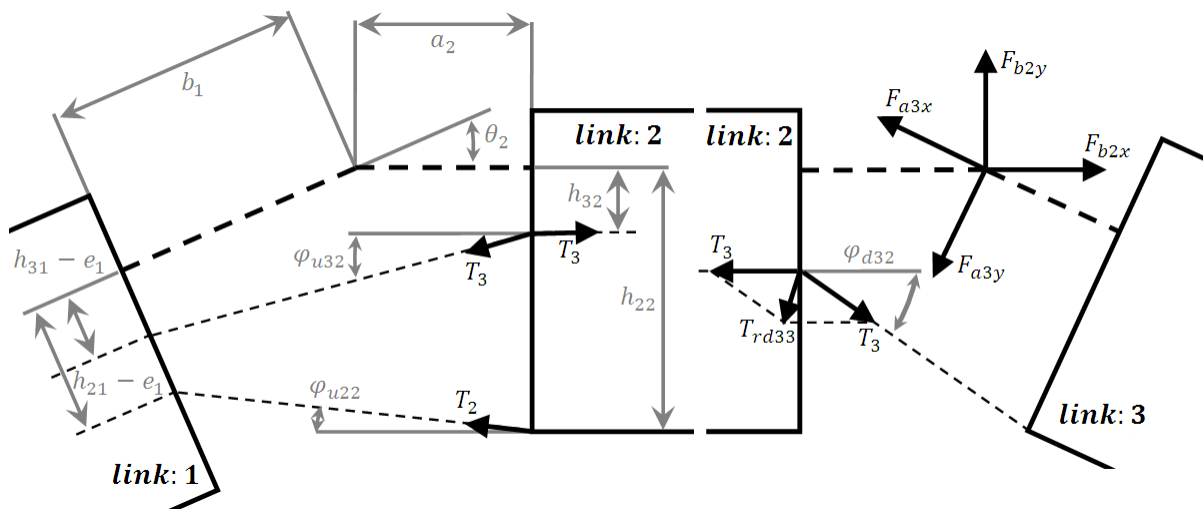


Figure 111: Second and third joint of the exoskeleton

The Exoskeleton

$$\begin{cases} F_{b2x} = -F_{a3x} \cdot \cos\theta_3 - F_{a3y} \cdot \sin\theta_3 \\ F_{b2y} = F_{a3x} \cdot \sin\theta_3 - F_{a3y} \cdot \cos\theta_3 \end{cases} \quad 48$$

The tension of the wire three T_3 generates two forces on the edges of the corresponding hole of link two. These two forces are called T_{rd32} , located on the downstream side, and T_{ru32} , located on the upstream side. Observing Figure 111, T_{rd32} can be calculated as follow:

$$\begin{cases} T_{rd32x} = T_3 - T_3 \cdot \cos(\varphi_{d32}) \\ T_{rd32y} = T_3 \cdot \sin(\varphi_{d32}) \end{cases} \quad 49$$

Similarly to the previous one the force T_{ru32} results to be equal to:

$$\begin{cases} T_{ru32x} = T_3 - T_3 \cdot \cos(\varphi_{u32}) \\ T_{ru32y} = T_3 \cdot \sin(\varphi_{u32}) \end{cases} \quad 50$$

Where φ_{u32} can be obtained by means of an analogous reasoning utilized for φ_{u33} and results to be equal to:

$$\varphi_{u32} = \tan^{-1} \frac{(a_2 \cdot \sin \theta_2 + h_{32} \cdot \cos \theta_2) - (h_{31} - e_1)}{a_2 \cdot \cos \theta_2 - h_{32} \cdot \sin \theta_2 + b_1} - \theta_2 \quad 51$$

The translational equilibrium of the third link can be easily obtained as follows:

$$\begin{cases} F_{a2x} = T_2 \cdot \cos(\varphi_{u22}) - F_{b2x} - T_{ru32x} + T_{rd32x} \\ F_{a2y} = F_2 - T_2 \cdot \sin(\varphi_{u22}) - F_{b2y} + T_{ru32y} + T_{rd32y} \end{cases} \quad 52$$

And the rotational equilibrium results to be equal to:

$$\begin{aligned} & F_2 \cdot d_2 + T_2 \cdot [h_{22} \cdot \cos(\varphi_{u22}) - a_2 \cdot \sin(\varphi_{u22})] + C_3 - C_2 + \dots \\ & \dots + T_{rd32y} \cdot (a_2 + l_2) + T_{rd32x} \cdot h_{32} + T_{ru32y} \cdot a_2 - T_{ru32x} \cdot h_{32} + \dots \\ & \dots - F_{b2y} \cdot (a_2 + b_2 + l_2) - F_{b2x} \cdot e_2 = 0 \end{aligned} \quad 53$$

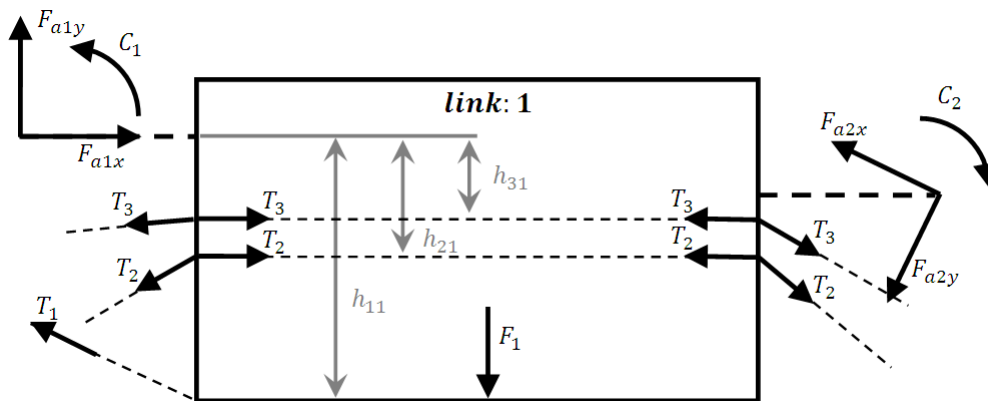


Figure 112: First link of the exoskeleton

The Exoskeleton

Where φ_{u22} can be obtained similarly to equation 47:

$$\varphi_{u22} = \tan^{-1} \frac{(a_2 \cdot \sin \theta_2 + h_{22} \cdot \cos \theta_2) - (h_{21} - e_1)}{a_2 \cdot \cos \theta_2 - h_{22} \cdot \sin \theta_2 + b_1} - \theta_2 \quad 54$$

The procedure to obtain the equation of the link one is the same utilized for the body two. Starting from the reaction force of the second link, the force F_{a2} can be re-written mapped into the reference system \mathcal{R}_1 obtaining the vector F_{b1} as follows:

$$\begin{cases} F_{b1x} = -F_{a2x} \cdot \cos \theta_2 - F_{a2y} \cdot \sin \theta_2 \\ F_{1yb} = F_{a2x} \cdot \sin \theta_2 - F_{a2y} \cdot \cos \theta_2 \end{cases} \quad 55$$

Into the body one two wires pass and their tensions T_2 and T_3 generate two forces each. The two forces located downstream and the two located upstream can be calculated with an equation similar to the 49 and result to be equal to:

$$\begin{cases} T_{rd31x} = T_3 - T_3 \cdot \cos(\varphi_{d31}) \\ T_{rd31y} = T_3 \cdot \sin(\varphi_{d31}) \end{cases} \quad 56$$

$$\begin{cases} T_{rd21x} = T_2 - T_2 \cdot \cos(\varphi_{d21}) \\ T_{rd21y} = T_2 \cdot \sin(\varphi_{d21}) \end{cases} \quad 57$$

$$\begin{cases} T_{ru31x} = T_2 - T_2 \cdot \cos(\varphi_{u31}) \\ T_{ru31y} = T_2 \cdot \sin(\varphi_{u31}) \end{cases} \quad 58$$

$$\begin{cases} T_{ru21x} = T_2 - T_2 \cdot \cos(\varphi_{u21}) \\ T_{ru21y} = T_2 \cdot \sin(\varphi_{u21}) \end{cases} \quad 59$$

The angles φ_{d31} and φ_{d21} shown into the equations 56 and 57 result to be similar to equation 43 and equal to:

$$\varphi_{d31} = \varphi_{u32} + \theta_2 \quad 60$$

$$\varphi_{d21} = \varphi_{u22} + \theta_2 \quad 61$$

The angles φ_{u31} and φ_{u21} are calculated in the same way shown into equation 47:

$$\varphi_{u31} = \tan^{-1} \frac{a_1 \cdot \sin \theta_1 + h_{31} \cdot \cos \theta_1 - (h_{30})}{a_1 \cdot \cos \theta_1 - h_{31} \cdot \sin \theta_1 + b_0} - \theta_1 \quad 62$$

$$\varphi_{u21} = \tan^{-1} \frac{a_1 \cdot \sin \theta_1 + h_{21} \cdot \cos \theta_1 - (h_{20})}{a_1 \cdot \cos \theta_1 - h_{21} \cdot \sin \theta_1 + b_0} - \theta_1 \quad 63$$

The translational equilibrium of the third link can be easily obtained as follows:

$$\left\{ \begin{array}{l} F_{a1x} = T_1 \cdot \cos(\varphi_{u11}) - F_{b1x} - T_{ru31x} - T_{ru21x} + T_{rd31x} + T_{rd21x} \\ F_{a1y} = F_1 - T_1 \cdot \sin(\varphi_{u11}) - F_{b1y} + T_{ru31y} + T_{rd31y} + T_{ru21y} + T_{rd21y} \end{array} \right. \quad 64$$

And the rotational equilibrium results to be equal to:

$$\begin{aligned} & F_1 \cdot d_1 + T_1 \cdot [h_{11} \cdot \cos(\varphi_{u11}) - a_1 \cdot \sin(\varphi_{u11})] + C_2 - C_1 + \dots \\ & \dots + T_{rd31y} \cdot (a_1 + l_1) + T_{rd31x} \cdot h_{31} + T_{ru31y} \cdot a_1 - T_{ru31x} \cdot h_{31} + \dots \\ & \dots + T_{rd21y} \cdot (a_1 + l_1) + T_{rd21x} \cdot h_{21} + T_{ru21y} \cdot a_1 - T_{rd21x} \cdot h_{21} + \dots \\ & \dots - F_{b1y} \cdot (a_1 + b_1 + l_1) - F_{b1x} \cdot e_1 = 0 \end{aligned} \quad 65$$

Where φ_{u22} can be obtained similarly to equation 47:

$$\varphi_{u11} = \tan^{-1} \frac{a_1 \cdot \sin \theta_1 + h_{11} \cdot \cos \theta_1 - (h_{10})}{a_1 \cdot \cos \theta_1 - h_{11} \cdot \sin \theta_1 + b_0} - \theta_1 \quad 66$$

Equations 42, 53 and 65 describe the behaviour of the three tendons tension as a function of the various geometrical and designing parameter of the device.

Optimization

The previously explained study of the statics describes the relationship between the various elements of the robotic structure. Each set of parameters contributes to provide a specific and determined behaviour of the target variables. The optimization process aims to find the best set of parameters in order to minimize internal stresses and to limit the range of tendon tensions. The generic tension T_i must be limited between two extreme values:

$$T_{min} < T_i < T_{max} \quad 67$$

- T_{min} represents the minimum acceptable wire tension value. Since tendons are not rigid components and can work only by traction, only positive values of internal tension are acceptable, otherwise the system cannot be actuated, becoming uncontrollable. In order to increase the controllability margin a value of T_{min} greater than zero has to be introduced to compensate undesired effects, not modeled dynamics and non idealities.
- T_{max} represents the maximum acceptable wire tension value. This value is given by the maximum stress that the wires can sustain, without deforming and/or breaking, and by the maximum value of T that the actuators can (directly or indirectly) provide.

The next step is to obtain the best possible parameter combination in order to achieve the previously mentioned goals. There are two typologies of parameters:

- Fixed parameters: they are intrinsic and unchangeable parameters specific to each design (e.g. geometrical parameters, position of the joints, DoFs, length of each elements and so on).
- Tuneable parameters: they are parameters that can vary within a determined range of values on the basis of the design choices. These parameters can be adjusted in order to tune and optimize the performance (e.g. the possible positions of the passing points of the wires inside the structure).

It is necessary to underline that different projects, though based on the same concept, can have different sets of fixed and tuneable parameters according to the characteristics of the device itself or on the reasons for which the device is designed. The distance between two joints is an example of a fixed

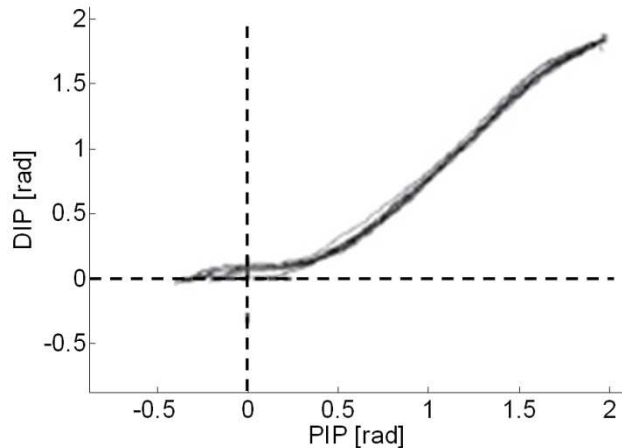


Figure 113: Relationship between DIP and PIP joint

parameter in an exoskeleton design because the device has to be worn, while it could be tuneable for another application. Another example of a parameter that could be both fixed and tuneable, depending on the specific design goal, is the external force applied to the links of the structure. This force could be unchangeable, fixed and equal to a certain value if the interaction between the device and the external world is well known and univocally defined, e.g. manipulator devices. In the case of a manipulator, where contact happens only through the end effector, a fixed value of the external force equal to zero for all the $N-1$ previous links is a justified choice. Vice versa the external force could be a tuneable parameter if the system is designed to apply a certain force which can be arbitral chosen by the designer. In the specific case of the exoskeleton design, the goal is to keep the finger in contact with the exoskeleton with a known small target force, measured by specific sensors. If every link is planned to be actuated independently from the others, then every contact force could be considered a tuneable parameter; otherwise, in case of fixed kinematic relations, the number of tuneable forces has to be reduced.

The finger soft constraint

During the study of the characteristics of the human hand, intra and inter finger constraints were analyzed. These relationships are caused by the structure of the hand and the tendon/ligament properties; they couple various degrees of freedom of the human hand linking together the displacement of many hand parts. In particular it has been noticed that there is a relationship constraint between DIP and PIP articulations [145]. This is not a strict kinematic ratio between the two articulations, in fact the human beings can force partially independent motion on the two phalanges, but it can be defined as a “soft constraint” applied during normal movements. Figure 113 shows the relationship between these two articulations; the constraint can be approximated with a fixed ratio between the two bending angles.

$$\theta_{DIP} = \frac{2}{3} \theta_{PIP} \quad 68$$

In order to simplify the calculation of the exoskeleton equation and reducing the computation time, it has been decided to introduce the previously explained constraint between the bending angles θ_3 and θ_2 . In this way the tendon tensions T_2 and T_3 are function of the only bending angle θ_2 , instead of both θ_2 and θ_3 , and T_1 depends only by θ_1 and θ_2 , instead all of three.

The Exoskeleton

The elastic element

Another simplification has been introduced. During the static analysis, it has been discussed about the effect of an elastic element with a generic torque C_i . The equation and the behaviour of C_i depend on the element used to guarantee the extension movement. Non-linear springs, discrete elastic elements or even more exotic components are equally possible solutions that can be treated in a similar way using their respective transfer functions:

$$C_i = f(\theta_i) \quad 69$$

As mentioned above, the elastic elements act in opposition to the tendons. This means that there is an additional design possibility because more rigid elements can be compensated by a larger tendon tension. A good shaping of the transfer function of the elastic elements means that the behaviour of the tensions could be modeled by imposing the passage through fixed points, which then modify peaks and slopes. In this case it has been decided to model the elastic element as a linear torsion spring, with a certain free angle and constrained to yield a given torque at a certain bending angles values. The free angle Figure 114 guarantees a value of torque, different from zero in $\theta_i = 0$; while the fixed torque value, comes from the tests on EVA glove, assuring the correctness of the force applied in a certain bending angle and allowing the glove to be correctly emulated. The equation of the generic elastic element is:

$$C_i = k_i \cdot (\theta_i - \theta_i^*) + C_i^* \quad 70$$

Where θ_i^* and C_i^* come from preliminary studies and tests performed on EVA glove:

- θ_i^* is the maximum bending angle of the i -th articulation wearing the EVA glove;
- C_i^* is the torque applied by the glove to the i -th phalange when is bent by the angle θ_i^* .

The maximum absolute value of the free angle has been guaranteed through the limitation of the minimum value of stiffness during \hat{k}_i the simulations:

$$\hat{k}_i = \frac{C_i^*}{\theta_i^* + \hat{\theta}_i} \quad 71$$

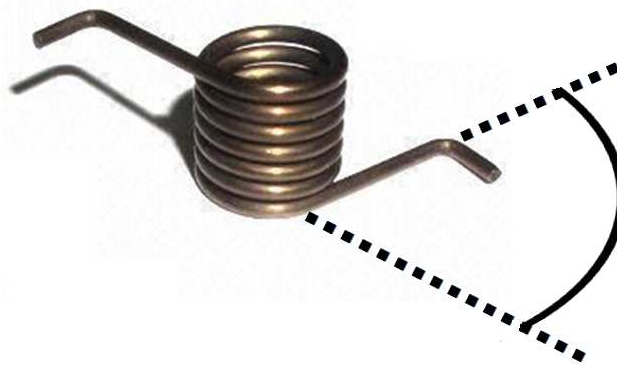


Figure 114: The free angle is the bending value obtained when no external torque is applied to the torsion spring.

Algorithm

The optimization has been performed with an algorithm shown in Figure 115 that calculates the best possible configuration of the tunable parameters. The “best” configuration is not univocal; since it depends on the specific necessity of the device, different projects may have different requirements for their internal variables. In some cases the peak of a specific internal variable must be reduced as much as possible; in other cases a variable has to be kept as constant as possible to reduce its oscillations. Using the kinematic relationships between parameters, see equations 42, 53 and 65, the set of values of parameters that optimizes a certain target can be called the “best” configuration of the tunable parameters.

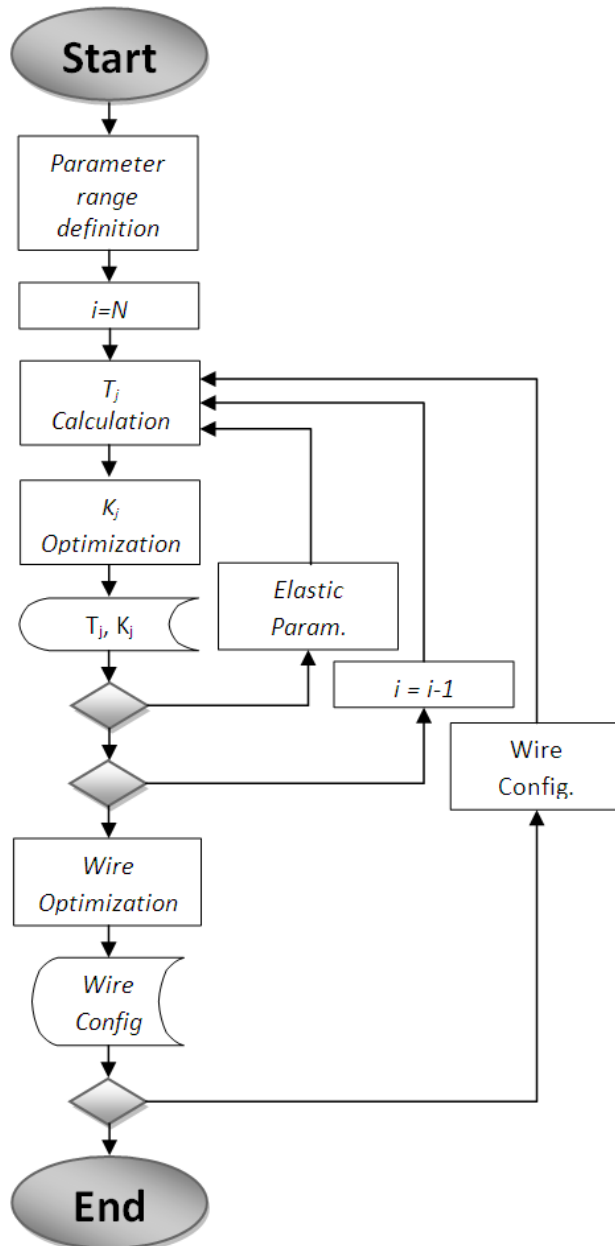


Figure 115: Concept flow chart of the algorithm

The Exoskeleton

The first step is to define the tuneable parameters and the range through which they can vary. Many choices are possible depending on the knowledge of each component of the future device and on the computing power available. The parameters of elastic components and the minimum value of tendon tension depend on the extension strategy and on the actuators respectively. The granularity of the parameter range depends on the computing power and on the complexity of the optimization algorithm. The main tuneable parameters for the robotic structures according to the previously presented concept are:

- the position of wire hole;
- the parameters of the elastic components (different typologies of elastic elements show different parameters)
- the minimum tendon tension range T_{min}
- the range of the external force F

For each value of F and T_{min} and for each specific wire hole position, an analysis of every possible wire configuration has been carried out. At the end of this analysis the following values are calculated for each configuration:

- the elastic parameters that best satisfy the design requirements;
- the mean and the peak values of the third tendon tensions.

Given these values for each wire position combination, it is possible to optimize and find the best configuration. During each iteration (corresponding to a specific wire configuration), the goal is to calculate the three tendon tensions and to optimize the stiffness values of the elastic components. Due to the superposition effect, the generic i -th link also applies an effect on the previous $i-1$. The algorithm begins by calculating and optimizing the parameters of the last link (the third) and then proceeds backwards along the kinematic chain. The first step of the iteration is to calculate the tension T_3 of the tendon acting on the link three. At this point all parameters except the stiffness of the elastic element are known. For each combination of the elastic parameters, within the desired range, the trend of T_3 is calculated as a function of the bending angle θ_3 . A 2 - D matrix containing the values of the tension T_3 versus the angle θ_3 and the elastic parameters of the third elastic component is obtained. This matrix has to be analysed and optimized. Studying the matrix the following values are obtained:

- the best elastic parameters of the third elastic component;
- the mean value and the peak value of T_3 .

The above procedure, which calculates the variables related to the third link, has to be repeated for all the remaining links. The procedure is always the same with only one difference due to the superposition effect: the generic tension T_i depends on the previously calculated values of tensions. Moreover, it is a function of all the bending angles of the following links. Thus at the end of each iteration the obtained matrix has an additional dimension with respect to the previous one. The generic output matrix obtained from the study of the i -th link is a $(N-i+2)$ -dimensional matrix where, in case of a 3DoF exoskeleton, N is equal to three. The introduction of the previously explained *soft constraint* between the DIP and PIP articulations, allows to diminish the dimensions of every matrix and therefore the computation time. This resulted in a 2-D matrix instead of a 3-D matrix for the tension T_2 and to a 3-D matrix instead a 4-D matrix for the tension T_1 . At the end of each iteration the following values are obtained:

- the best elastic parameters of the i -th elastic component;
- the mean and peak value of T_i .

Optimization of K

The calculation of the wire tensions gives a matrix describing the behaviour of T_i as a function of a certain number of bending angles, defined for the values of the elastic parameters of the i -th elastic

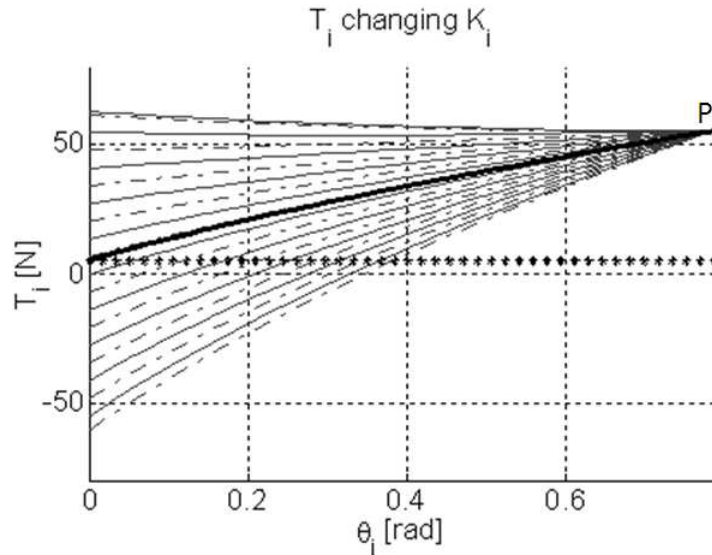


Figure 116: Wire tension with different values of elastic parameters

element. The number and typology of the elastic parameters depend on the typology of the elastic components and on its model, e.g. linear torsion springs can be defined using their stiffness and free angle. First of all, it is necessary to define in which way the elastic parameters must be optimized, in other words, what "*best solution*" means in that specific case. Many different possibilities are available for the choice of the best parameters, depending on various constraints and design choices. Some examples are the minimization of the p-norm related to specific Lebesgue spaces L_p:

- minimization of the L_{∞} norm = minimization of the peak value of the signal;
- minimization of the L_2 norm = minimization of the energy of the signal;
- minimization of the L_1 norm = minimization of the total resources of the signal.

Figure 116 represents an example of the result of the optimization of the generic T_i . In the specific case the elastic component was modeled in a similar way to a linear stiffness torsion spring. This spring applies a torque proportional to the angle, but with a fixed target torque for a particular angle (corresponding to point P), that comes from the study of the EVA glove. Due to the specific model of the elastic component the parameters are its stiffness value k_i and its free angle $\hat{\theta}_i$. In this simulation the minimization of the L_2 norm of the signal T_i was imposed, i.e. the underlying the area of the signal. Figure 116 shows a family of curves; each of them represents the trend of T_i for a certain value of k_i and the corresponding free angle. All the lines pass through the fixed point P, as explained before. The horizontal star-dot line shows the minimum threshold of the tendon tension T_{min} . The thick line corresponds to the curve with the optimized value of k_i . As already said, this is only one possible example of the model of the elastic component that can be used in the kinematic chain; non-linear springs, discrete elastic elements or even more exotic components are equally possible solutions that can be treated in a similar way. A good shaping of the transfer function of the elastic elements allow the behaviour of the tensions to be modelled by imposing the passage through fixed points, which then modify the peaks and slopes.

Optimization of the tendon configurations

At the end of each iteration, the value of the parameters for a specific set of tendon configurations is obtained. The change of the tendon configuration allows to study the effects of different combinations on internal forces and torques and in particular the tendon tensions. In this way it is possible to find the

The Exoskeleton

most suitable combination according to specific design criteria. At the end of all iterations, the peak and mean values of the three tendon tensions are obtained for all the analysed configurations. At this point the goal is to find the *best solution* between the previously analysed. Minimizing the demand of the actuators, or reducing the stresses of the structure are only few examples of the possible criteria suitable for the choice of the best wire configuration. Depending on the requirements of the specific project, it could be chosen to minimize different values:

- $\min[\max_i(T_i)] \quad i = 1 \dots 3$
- $\min[\text{mean}_i(T_i)] \quad i = 1 \dots 3$

Results

Many simulations were performed changing the values of the various tunable parameters; each different combination or set of parameters provides a completely different base on which the device has to work. Some parameters configurations could generate small variations hardly appreciable of the variables of interest, while others sets of parameters may cause drastic modifications of the behaviour of the tensions, the shapes of the graphs and the maximum values. These big variations could be brought back to many factors; probably the most influential is a direct consequence of the actuation transmission system chosen in this device: the wire actuation. As already partially explained, the wire actuation designed in this device does not have direct access to the actuated joint; this means that the tension of the wires generates torques by means of a variable arm. It is possible that the combination of some geometrical dimensions with a specific configuration of wire holes causes the variable arm of the tendon tension to decrease, becoming zero in a specific finger asset as shown in Figure 117. The cancelling out of the arm generates singularities that have to be avoided and kept as far as possible in order to try to reduce the internal stress and the work of the actuators. On the contrary parameters like the free angle and the minimum value of contact influence the values of tensions for small values of bending angles determining the difference between uncontrollable configurations (with negative tendon tensions) and useful ones. The input parameters preliminarily defined for each simulation are the following:

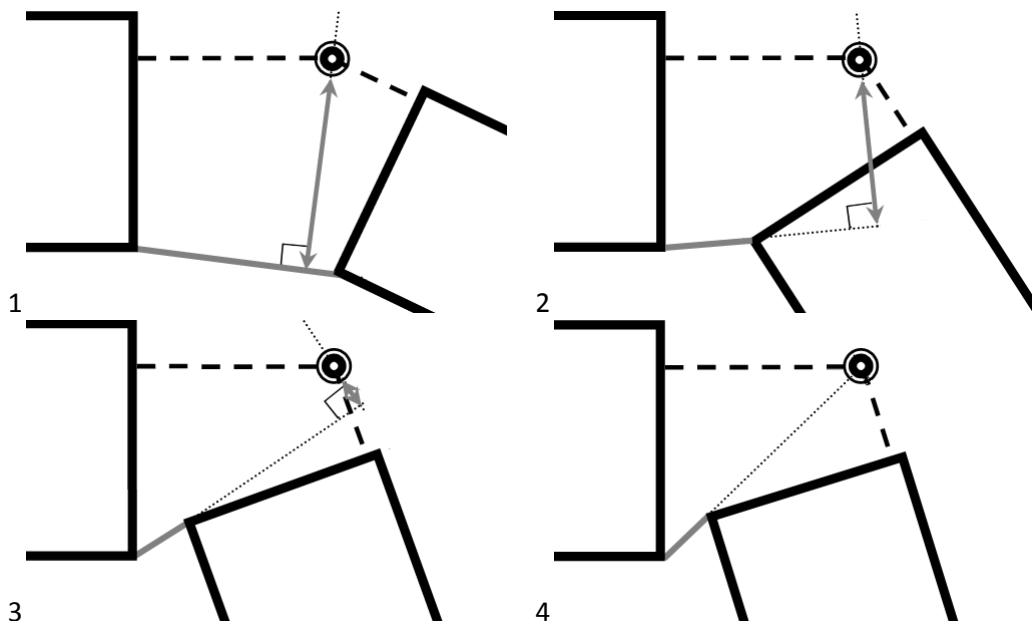


Figure 117: Approaching towards a singularity configuration. From 1 to 3 the arm of the tension of wire decreases until it reaches the value zero in the fourth image.

The Exoskeleton

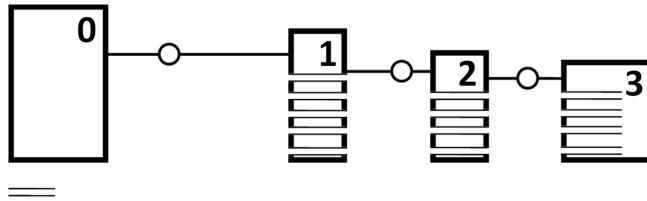


Figure 118: Possible passing points of the wires through the phalanges

- The minimum tendon tensions T_{min}
- The contact force between the human finger and the exoskeleton (which becomes the threshold value of the contact force)
- The free angle of the springs: the materials used to build the springs were not ideal and have a finite range of internal stress they can bear. Fixing the value of the free angle (as a function of the material) means that only usable values of the spring parameters can be obtained.
- The acceptable passing points of the holes through the structure and the minimum distance between two adjacent holes.
- The structure of the hole in terms of length, radius and shape; reducing the length of the holes, for instance, allows the design to be changed simulating the behaviour of micro pulleys instead of micro-machined holes.

In the following part the results related to two different performed simulations with two different parameter configurations will be presented. For these simulations the parameters were fixed at the following values:

- Minimum tendon tension $T_{min} = 0.1 \text{ N}$
- Minimum external force $F_{min} = 0.2 \text{ N}$
- Maximum free angle $\hat{\theta}_i = 0.3 \text{ rad}$
- Discrete tendon passing point; Figure 118 show the possibilities, which are the following:
 - five possible passing points through the phalanx one
 - four possible passing points through the phalanx two
 - four possible passing points through the phalanx three
 - one possible passing point through the phalanx zero (the palm)

The results of the two simulations will be analyzed and, for each one, three examples of solution will be presented, two non-optimal and one optimal. In all the reported results of simulations the three bending angles θ_i were considered positive with the bending movements, for simplicity, convenience and clarity of interpretation. For each proposed solution a series of information were provided:

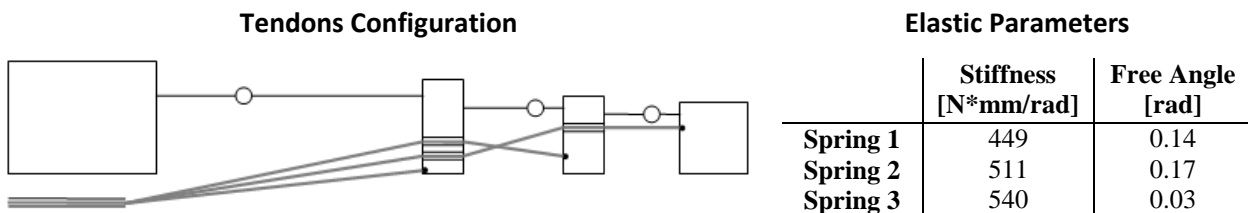
- Tendon configurations. It is the schematic graphical representation of the passage of the wires through the different links of the robotic structure.
- Elastic parameter values. The values of stiffness and free angle were obtained by minimizing the L_2 norm of the tendon tensions.
- Behaviour of the three tendon tensions as a function of the respective bending angles. As stated before, the soft constraint between DIP and PIP articulations was introduced. The tensions T_2 and T_3 are functions of only one bending angle, so their behaviours are shown as a 2-D graph. On the contrary the tension T_1 is a function of two bending angles, thus it is represented through a 3-D graph.
- Maximum and mean values of the three tendon tensions.

The Exoskeleton

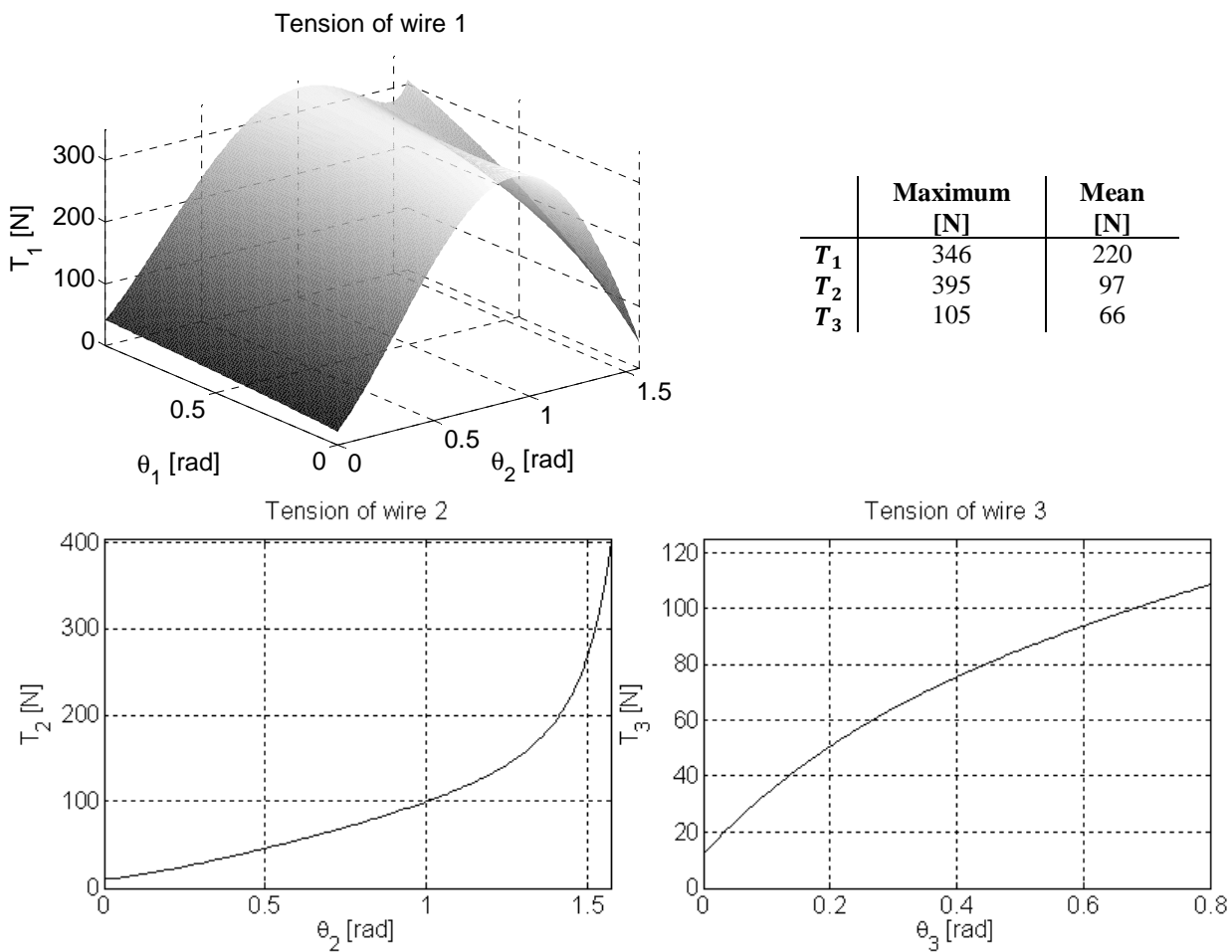
Micro-machined Holes

In this first proposed simulation it has been decided to emulate the behaviour of the device in case of micro-machined holes, so an opening that passes through the entire length of the phalanx. Two non-optimal solutions (Solution 1 and Solution 2) and an optimal one, found with the algorithm, will be presented. For each set of parameters chosen a priori there are 2880 different wire configurations, which determine a specific design. There are some configurations similar to the optimized one and others that result to be completely different both in terms of magnitude and trend. Among all the possible solutions, it was decided to pick up as paragon two configurations that do not differ significantly from the optimized one.

MICRO-MACHINED HOLES NON OPTIMAL SOLUTION 1:

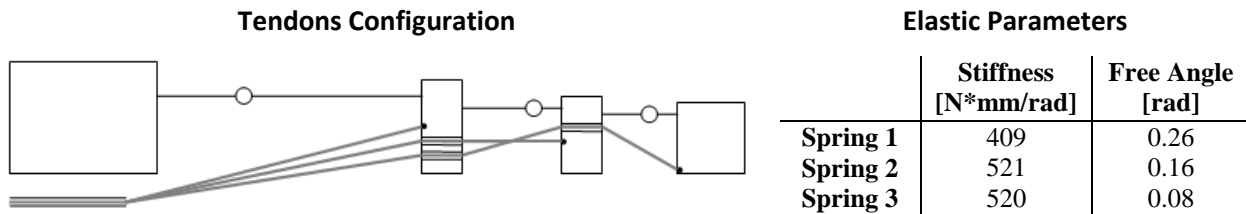


Behaviour, maximum and mean values of the tendon tensions

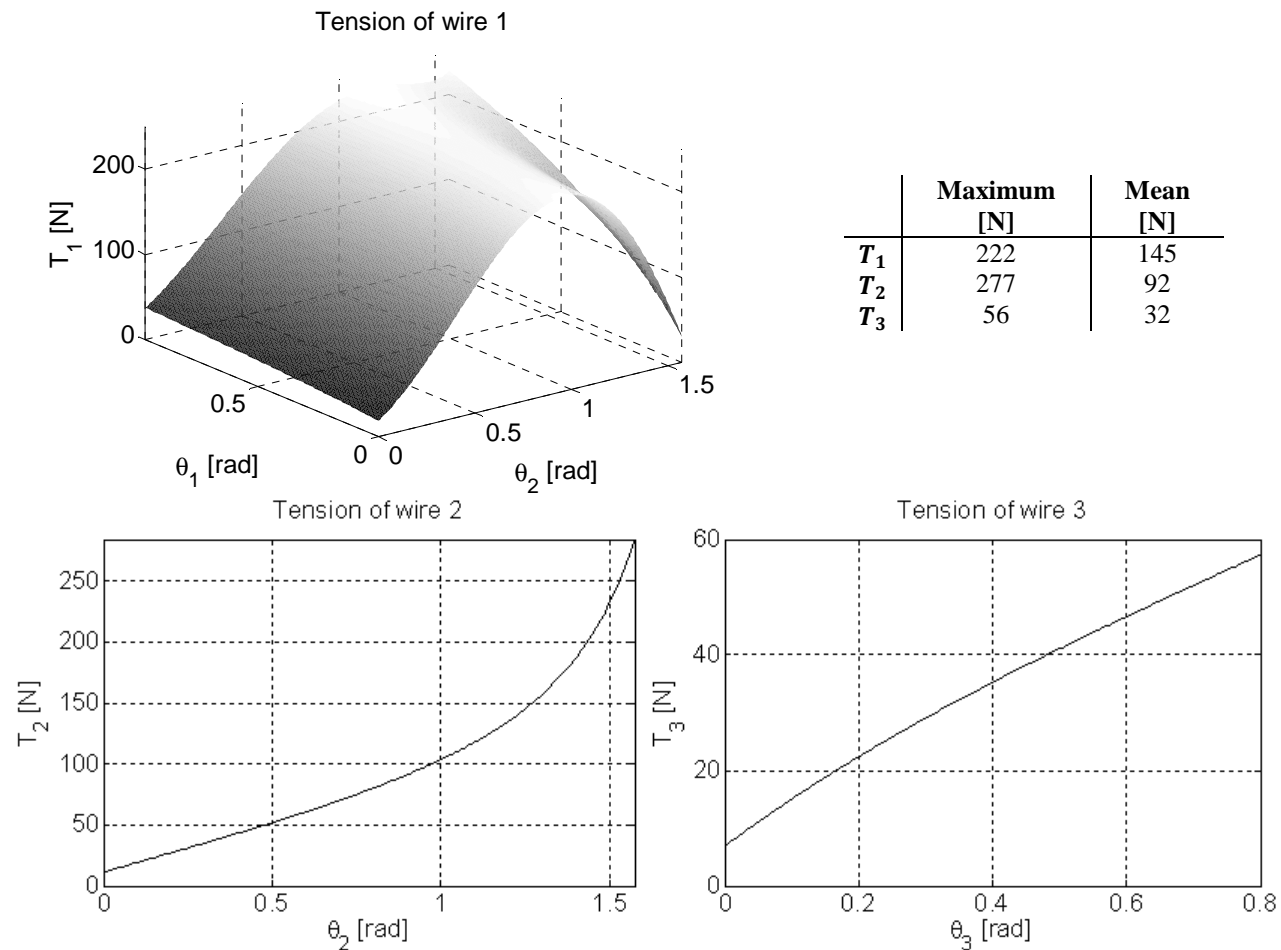


The Exoskeleton

MICRO-MACHINED HOLES NON OPTIMAL SOLUTION 2:

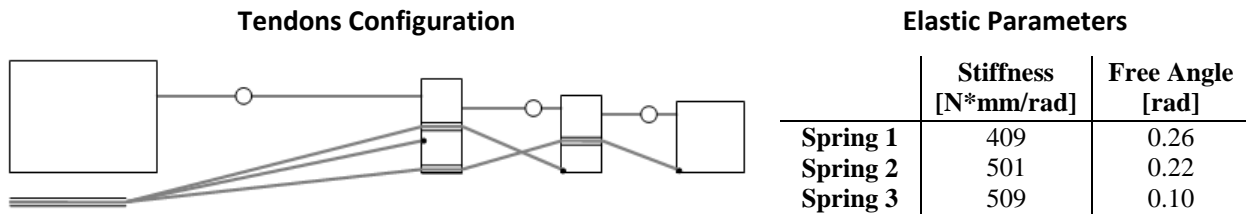


Behaviour, maximum and mean values of the tendon tensions

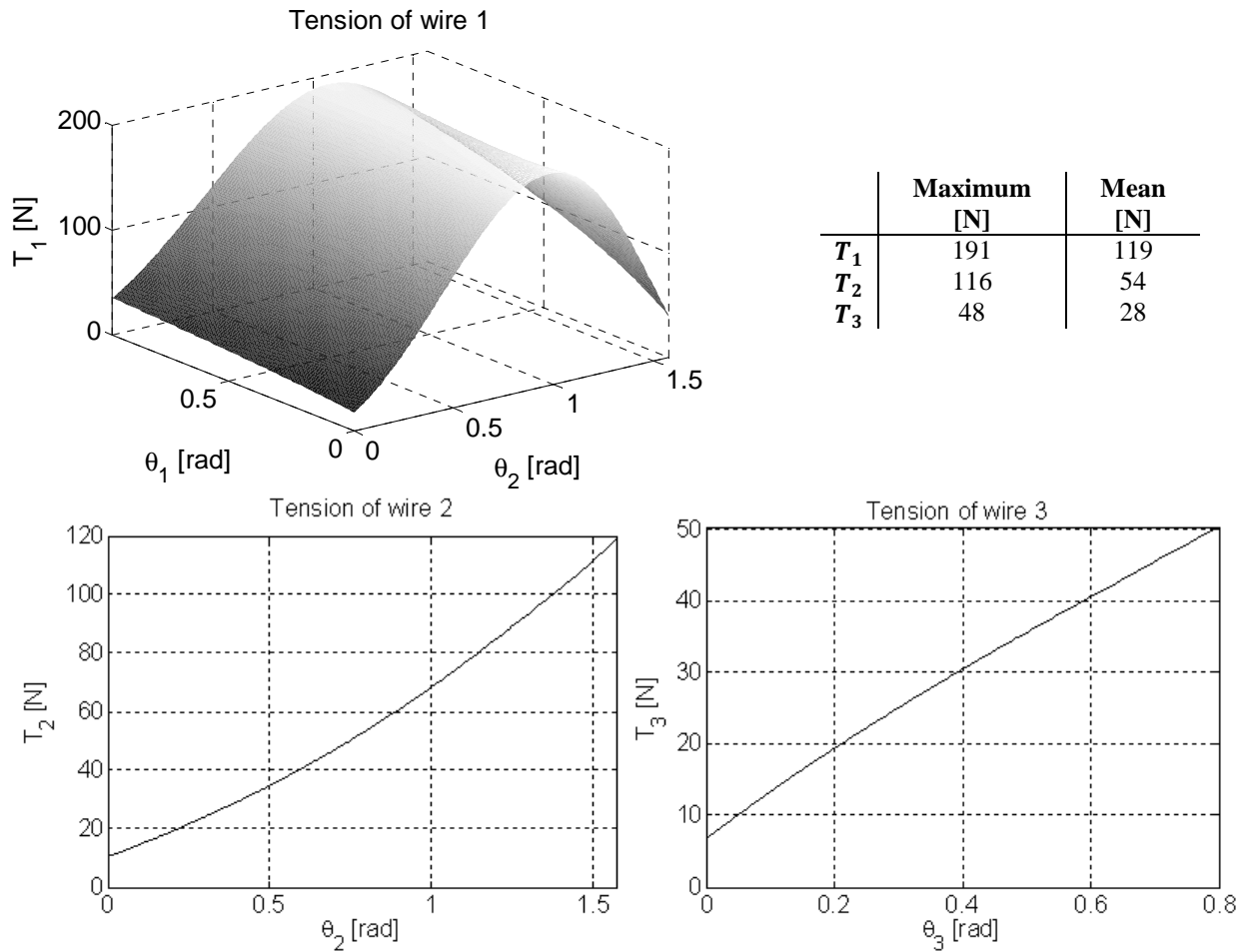


The Exoskeleton

MICRO-MACHINED HOLES OPTIMAL SOLUTION:



Behaviour, maximum and mean values of the tendon tensions



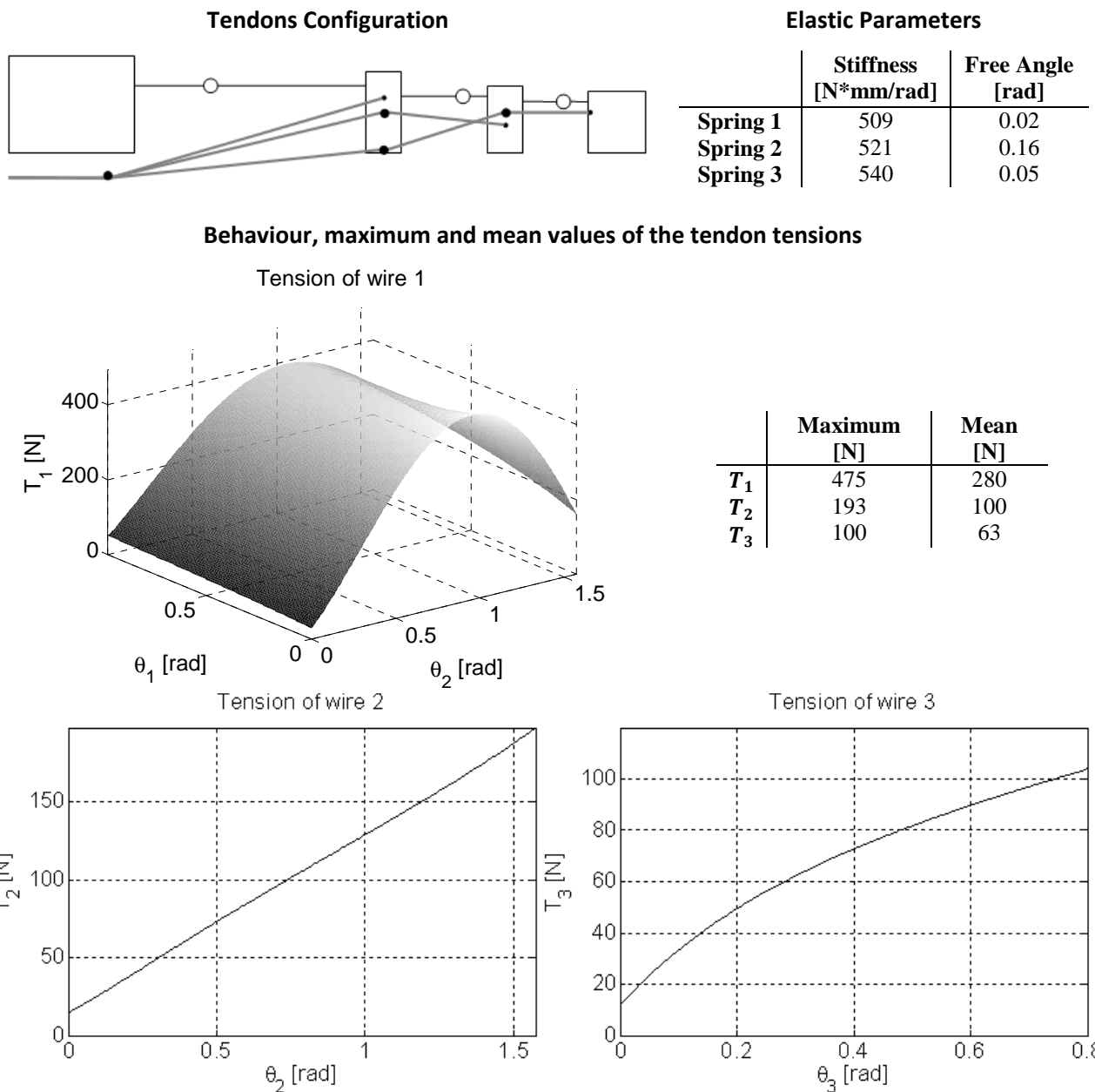
It can be noticed that the values of tendon tensions obtained with the optimal solution are sensibly lower than the others two. The different values of tensions are mainly due to the wire positioning scheme because, as shown in the respective tables, the value of k and $\hat{\theta}$ are very similar. As mentioned above, each link has an effect on the previous ones. This effect is complex and generally it favours the extension movement of one of the previous phalanges; this can be seen in the increase of the mean value of the tendon tension moving backwards along the kinematic chain.

The Exoskeleton

Micro-Pulleys

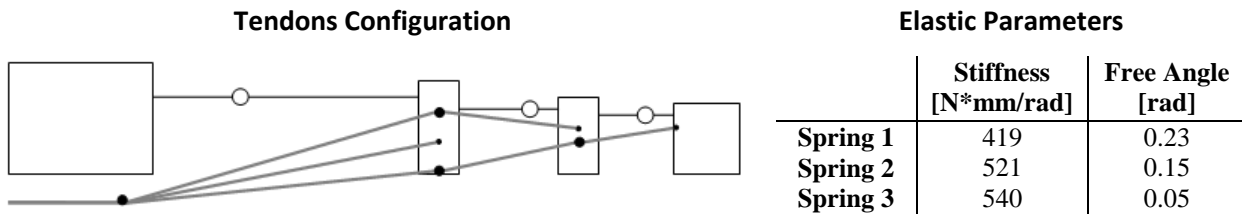
In this second proposed simulation it was decided to emulate the behaviour of the device in case of micro-pulleys, so the wires result to lay on a very short surface (the pulley itself) placed in the middle of the phalanx. Placing the pulley on one side of the phalanges instead of putting it in the middle could completely change the achieved solution, resulting in another parameter choice. In this case again two non-optimal solutions (Solution 1 and Solution 2) and an optimal one, found with the algorithm, will be presented. Again it has been decided to analyze two configurations that do not differ significantly from the optimized one.

MICRO-PULLEYS NON OPTIMAL SOLUTION 1:

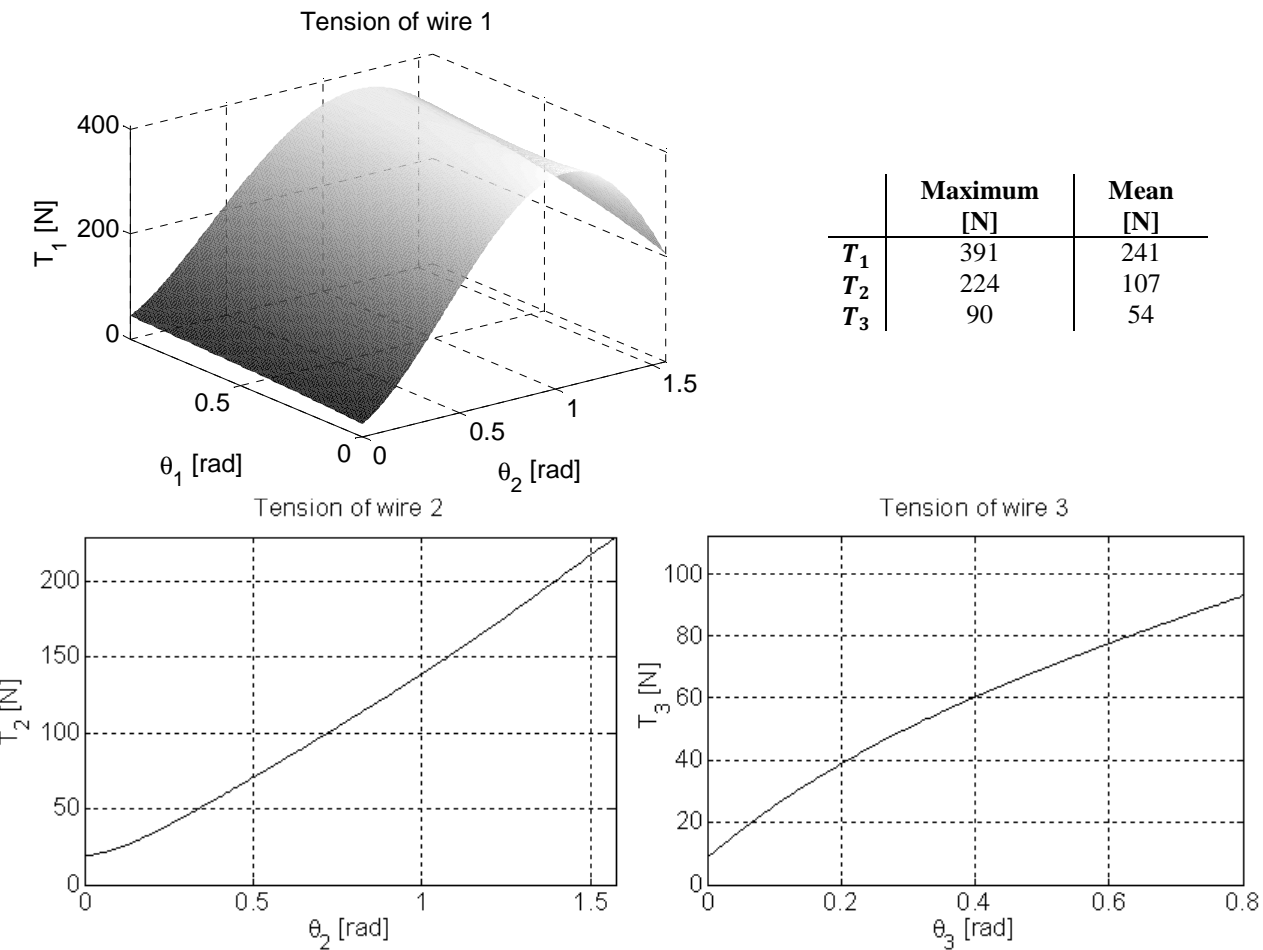


The Exoskeleton

MICRO- PULLEYS NON OPTIMAL SOLUTION 2:

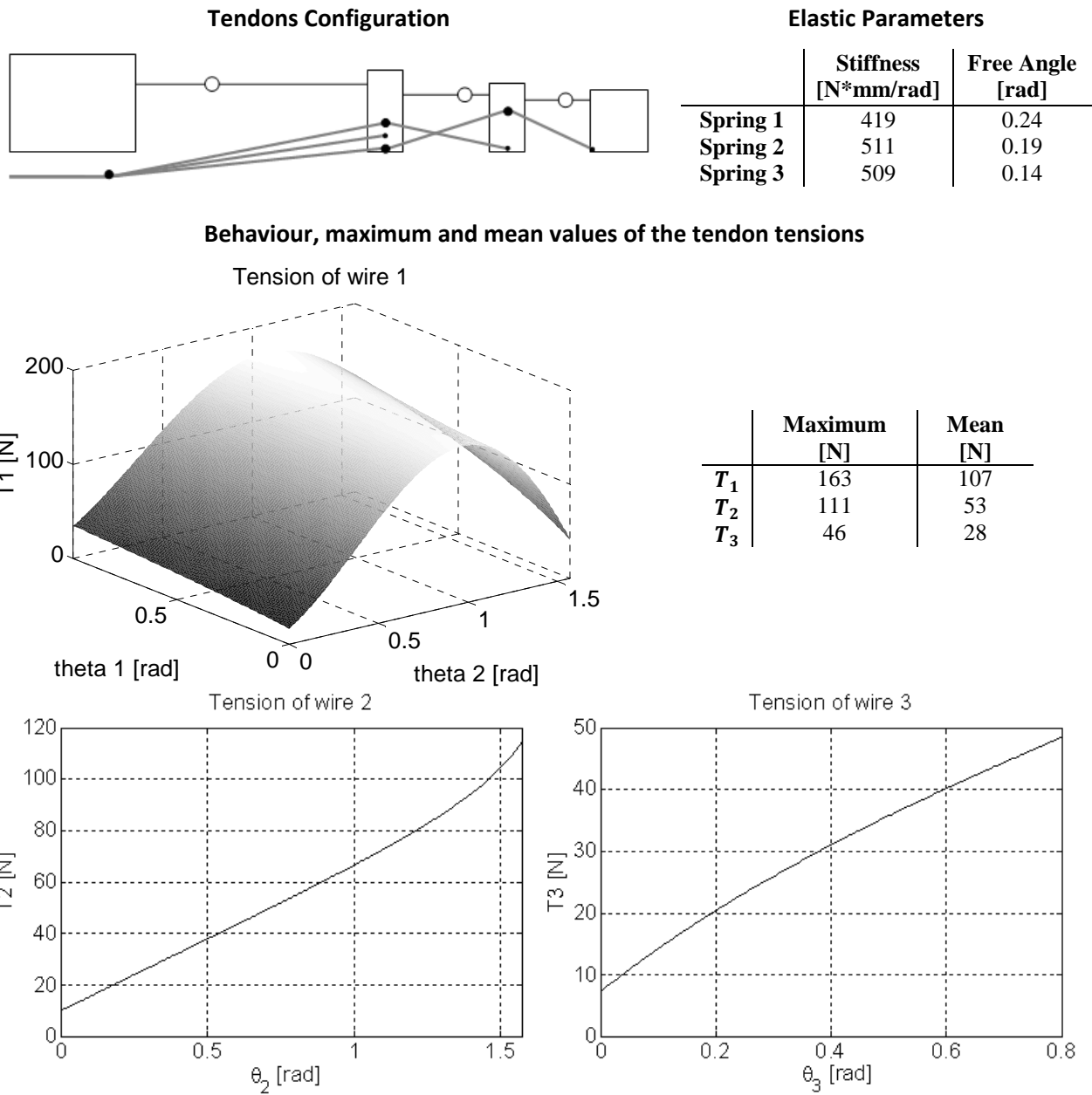


Behaviour, maximum and mean values of the tendon tensions



The Exoskeleton

MICRO- PULLEYS OPTIMAL SOLUTION:



In this second set of simulations the same observation, already performed for the first one, could be confirmed. The tensions obtained with the optimal solution result to be lower than the others. Furthermore the tendon tensions achieved in the simulation related to the micro-pulley are lower than the ones obtained with micro-machined holes. This trend could be motivated by the fact that, in the micro-pulley simulation, the arms of the torques generated by the tendon tensions are longer and so, a lower value of tendon tensions is necessary in order to obtain the same result.

The Exoskeleton

Observations

At this point, with the results obtained from the study and optimization of the first wire actuated solution, it was possible to create a prototype of wire actuated exoskeleton mounted on the test bench, as previously explained.

The mechanical structure of test bench and exoskeleton were created by means of a standard tooling machine, while the springs were ordered to a specialized company. The correctness of the values of springs, in terms of stiffness and free angle, results to be fundamental in this design; these values come from the optimization, which allows the exact range of tendon tension to be achieved. It is so essential to realize the springs in the best possible way. As far as the tendons are concerned, it is very important to find a wire that guarantees a good performance in terms of stretching resistance and maximum tension supported. Twisted wire made of synthetic fibers called Dyneema, widely utilized in climbing and fishing, were found. Dyneema is a gel spun from oriented strand microfibers of UHMWPE (Ultra-high-molecular-weight polyethylene), which have yield strength of 2.4 GPa (350000 psi); high strength steels have a comparable value. It is a very tough material with very high impact strength, is highly resistive to corrosive chemicals and physical abrasion; it has extremely low moisture absorption; it is self-lubricating and has a very low coefficient of friction, which is comparable with the Teflon one. Finally, as regards the actuator, a long research about all possibilities was performed. Many technological solutions for actuators exist today, but very few of them are suitable for this typology of design. Size and weight constraints, the need to produce high torques and relative low velocities and the

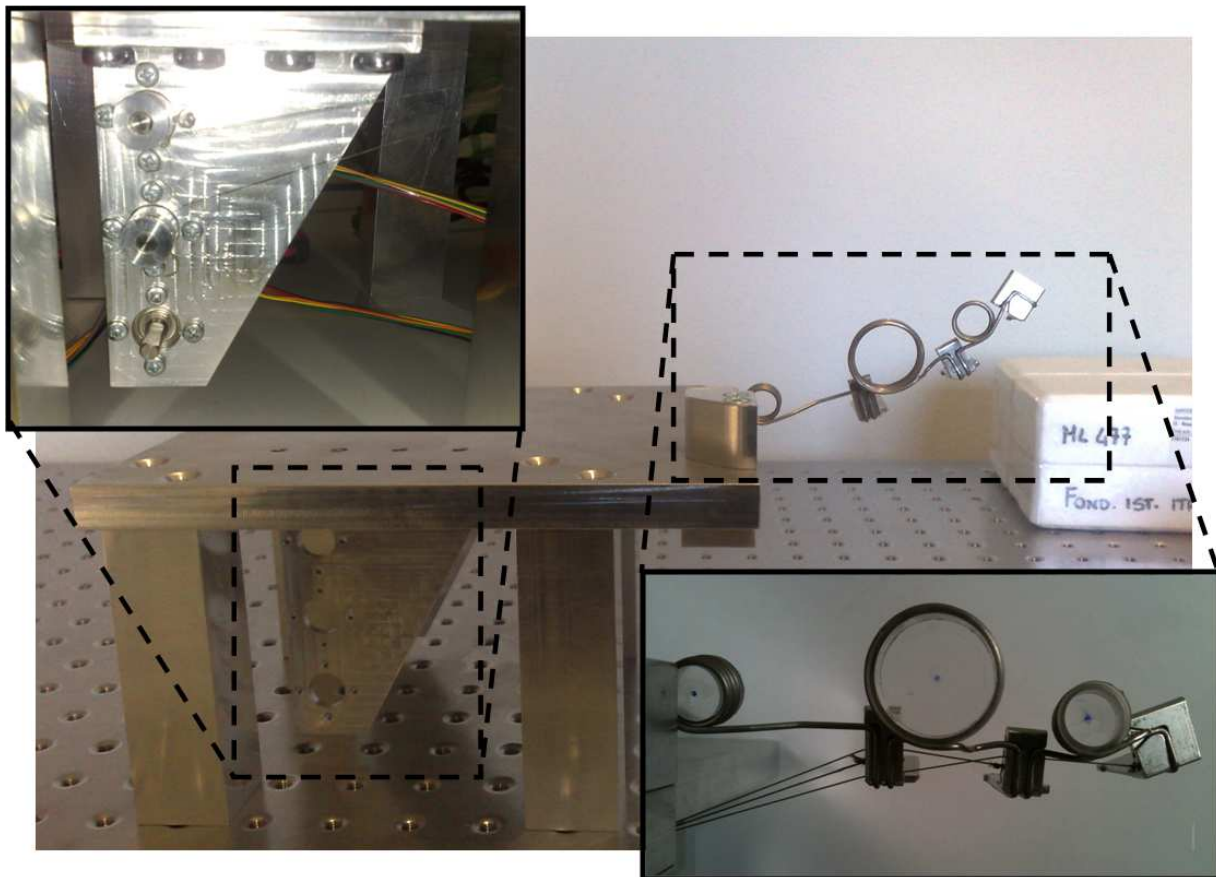


Figure 119: The first prototype of exoskeleton with its test bench

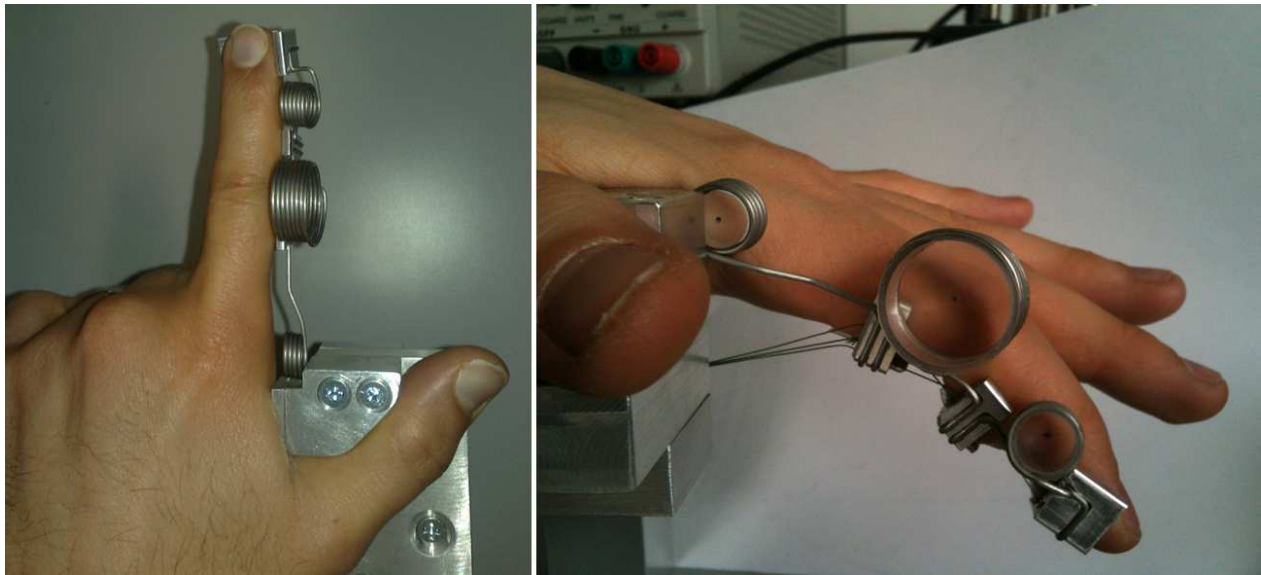


Figure 120: Operator hand and exoskeleton; top view (left) and side view (right)

limitations related to the environment reduce the options. It was decided to utilize, as first solution, classical brushless motors equipped with gearboxes.

Unfortunately a series of problems related to the device arose, mainly related to the springs. Due to the non-idealities of the material of which the springs were made, the correct values of stiffness, free angle and maximal excursion result hardly achievable. The values of the elastic parameters theoretically obtained have to be translated into torsion springs characteristics: number of coils, diameters of coils, diameter of the metal wire and material. In certain design schemes, in order to achieve a specific value of stiffness, the number of the spring loops and/or the diameter of the coil increases over an acceptable value resulting in an unserviceable object. Furthermore, the wire of the springs cannot exceed a specific diameter due to the limitations on the thickness of the elements of the test bench. Wrong values of elastic parameters cause completely different trends of tendon tensions. Finally the elevate magnitude of the internal forces (it could be seen in the various simulation results previously reported) generate high reactive forces on the joints. The virtual joint, excited by these forces, cannot support the movement without deforming or bending. In order to partially solve this problem, three plastic cylinders were placed inside the spring coil, in order to limit the tangential deformation of the springs. Figure 119 show the wholes test bench: in the two small details the actuation and transmission system can be seen. The top left window shows the three brushless motors mounted on their flange; two of them with their pulley and tendons. The bottom right window shows the detail of the finger exoskeleton with the three tendons that follow the micro-machined holes optimal configuration. In this picture the problem related to the springs can easily be seen; in particular the second spring result to be bulky. Figure 120 shows the operator hand acting on the test bench. On the basis of the previously reported motivation the concept was modified and a new solution proposed.

The second Wire Actuated Solution

The second wire actuated solution proposed here is shown in Figure 121. This design is based on the main guidelines reported in the introduction and already utilized for the previous one: a 3DoF structure without the abduction-adduction joint and actuated by wires.

The Exoskeleton

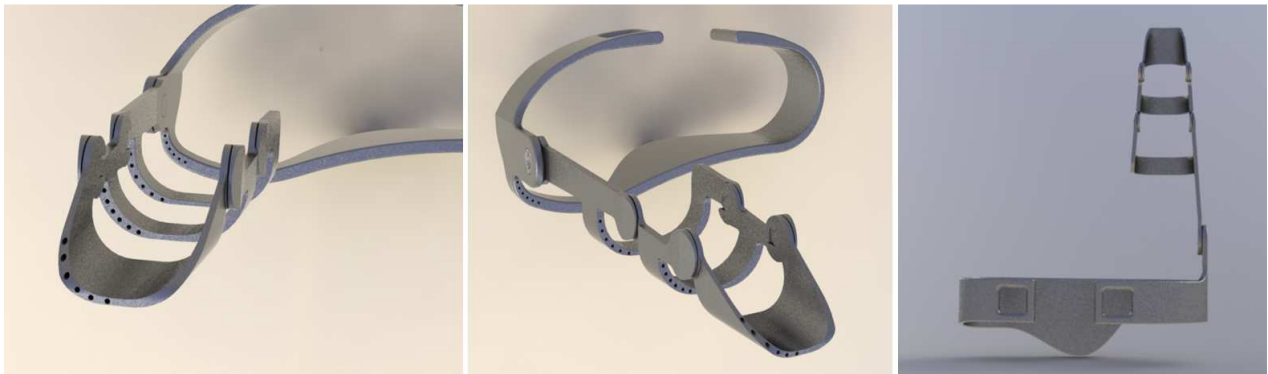


Figure 121: Second wire actuated design: front view (left), the whole design (center) and the top view (right)

This second solution didn't preview the realization of a test bench on which the exoskeleton will have to be mounted. In case of necessity, the previously created test bench could be easily readjusted in order to act as support for the new device. An ergonomic palmar support that imitates the shape of the hand and allows the exoskeleton to be worn and kept in position was designed and realized, granting the correctness of the position of all the centers of rotation. Similarly to the first proposed solution, the problem of the finger crotch was overcome by means of an asymmetric design of the shape of the proximal phalanx. All the exoskeleton elements support the human finger by means of a "U-shape" structure that hugs the finger phalanges on both sides. Both the palmar support and the phalanges were designed in order to be inserted into the EVA glove, so each thickness was carefully planned to fit with its internal space. The "U-shape" of the exoskeleton phalanges allows the bulky to be reduced with respect the "L-shape" used in the previous design; in this case the holes of the wires cannot belong to the same plane; on the contrary they have to be placed following the curved shape of the phalanges. This fact generates an important consequence: the loss of co-planarity of the entire transmission system generates torques and forces that cannot be constrained into a plane. It is therefore necessary to study the trends of the variables of the device into a 3-D space; furthermore reactive torques and forces will generate both compression and shear stresses along all directions. The main difference compared to the previous one is represented by the typology of the joints. In this second solution traditional joints substitute the virtual ones utilized in the first design. Traditional joints contribute to solve problems related to the deformation of the structure found earlier; moreover, it is not necessary anymore to dimension, and then realize, the elastic elements. In this second design the whole extension movement results to be ensured by only the EVA glove. Figure 122 shows two different solutions for the design of the joints. On the left it can be seen the two-pieces joint: in this typology of solution, the first link can be



Figure 122: Two different joint solutions: two-piece joint (left) and one-piece joint (right)

coupled with the second one inserting the pin into the holes with a determined relative angle between the two phalanges, thanks to a slot specially realized on the pin. The particular shape of the joint grants that, once coupled the pin with the hole, the two elements cannot be detached unless the bending angle between the two phalanges results equal to the “insertion angle”. This design was studied to be realized with standard tooling machines. On the right the one-piece joint, where the two adjoining elements of the structure have to be realized into one shot, can be seen. The relative movement is guaranteed by a play between the two phalanges. This design was studied to be realized with DLMS (direct metal laser sintering).

Static Analysis

It is mandatory to study again the analysis of statics of the new concept of exoskeleton. As already said, the statics results very useful to understand the behaviour of the tendon tensions as a function of geometrical parameters, bending angles, external forces and design choices. This also allows the range of variation of the tendon tensions to be checked, by verifying that they always stay within acceptable values. In the following analysis the conceptual design of the robotic structure was generalized as much as possible and partially decoupled from the specific project. It was decided to study a generic single effect, wire actuated n-R robotic structure. This means that the analysis could be applied to different designs and structures provided that they adhere to the main guidelines previously reported.

Figure 123 represents the scheme of the generic i -th link of the robotic structure. Each link is associated with a coordinate reference system \mathcal{R}_i which uniquely defines its position and orientation. In this study the apex i on the generic vector $^i\mathbf{x}$ states that that vector is expressed in the i -th reference frame \mathcal{R}_i . The i -th reference system is placed on the i -th rotational joint, which connects the i -th link to the previous one. \mathcal{R}_i can be obtained from \mathcal{R}_{i-1} through a translation represented by the position vector $^i\mathbf{l}_{i-1}$ and a subsequent rotation around it of an angle θ_i . Each link is driven by a corresponding wire. The architecture consists of a serial chain of N links, each of them hosting the holes for the wires that drive the following elements. Hence, as shown in Figure 123, $N+1-i$ wires enter the i -th link from the previous one, while $N-i$ of them go to the following link. The wire $j=i$ acts specifically on the link i and ends there. The generic wire j ($j > i$) enters the link i coming from the previous one and continues to the following one. If the wire doesn't pass exactly through the origin of \mathcal{R}_i , it has a non null torque effect on the i -th link, which must be controlled and optimized. The position vector that identifies the entrance of the hole for the generic j -th wire in the i -th link is called $^i\mathbf{u}_{ij}$ (u for upstream). The position vector of the end of the same hole is referred to as $^i\mathbf{d}_{ij}$ (d for downstream). $^i\mathbf{t}_{ij}$ is the unit vector that identifies the direction of the generic j -th wire on the i -th link and it is defined as follows:

$$^i\mathbf{t}_{ij} = \frac{^i\mathbf{u}_{ij} + ^i\mathbf{A}_{i-1}(^{i-1}\mathbf{l}_{i-1} - ^{i-1}\mathbf{d}_{(i-1)j})}{\| ^i\mathbf{u}_{ij} + ^i\mathbf{A}_{i-1}(^{i-1}\mathbf{l}_{i-1} - ^{i-1}\mathbf{d}_{(i-1)j}) \|} \quad 72$$

Where $^i\mathbf{A}_{i-1}$ is the linear operator which maps vectors and points from the reference \mathcal{R}_{i-1} to the reference \mathcal{R}_i .

$$^i\mathbf{A}_{i-1} = \begin{bmatrix} \cos(\theta_i) & \sin(\theta_i) \\ -\sin(\theta_i) & \cos(\theta_i) \end{bmatrix} \quad 73$$

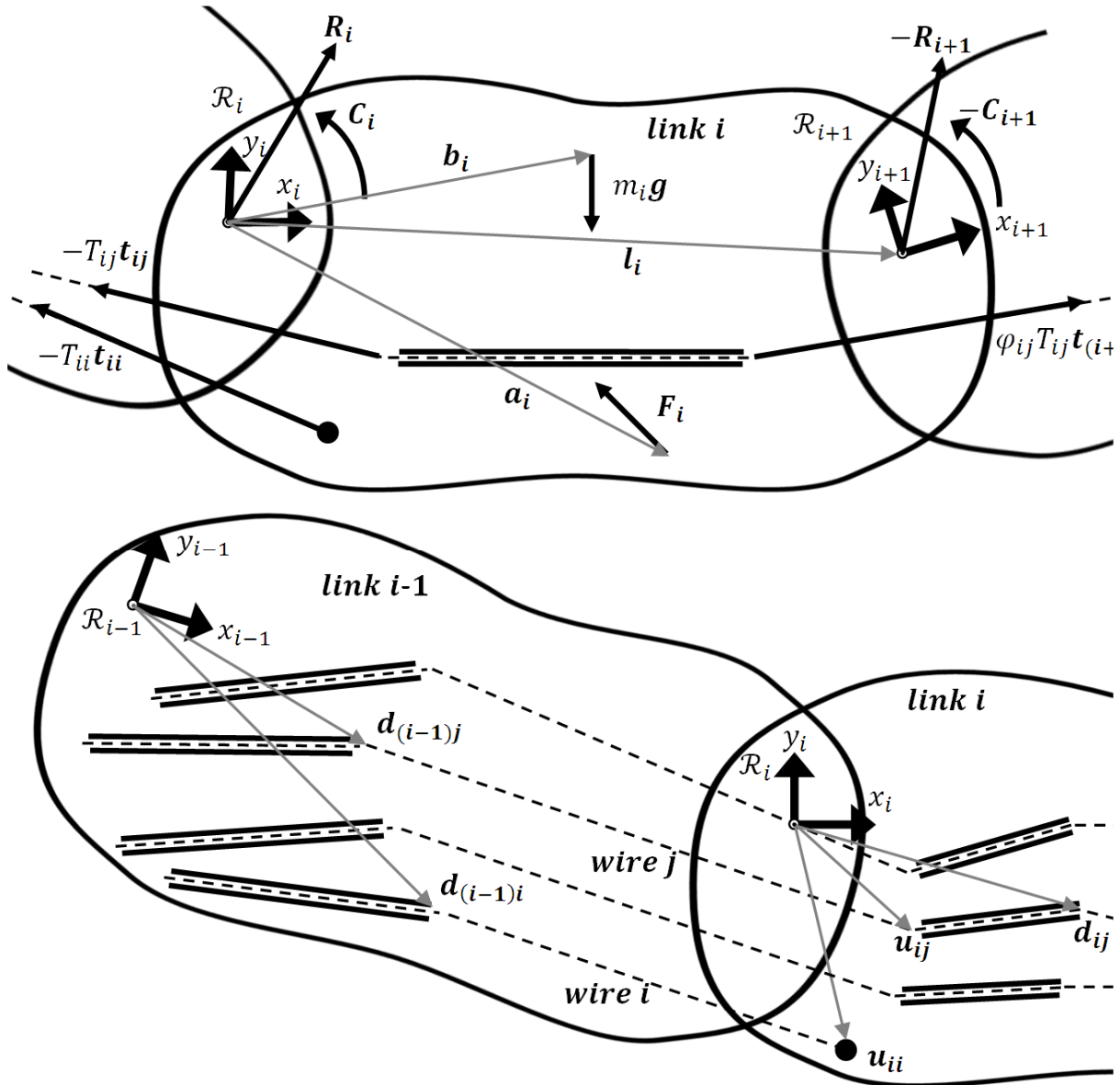


Figure 123: Generic i -th link of the robotic structure

And θ_i is the counterclockwise angle between \mathcal{R}_{i-1} and \mathcal{R}_i .

As it can be seen in Figure 123, the generic i -th link is subject to a number of forces and torques:

- ${}^i\mathbf{R}_i$ and ${}^i\mathbf{C}_i$, exerted by the previous link at the i -th joint;
- $-{}^i\mathbf{R}_{i+1}$ and $-{}^i\mathbf{C}_{i+1}$, exerted by the following link at the $(i+1)$ -th joint;
- ${}^i\mathbf{F}_i$, external force applied on the i -th link (e.g. exerted by the user), whose point of application is identified by vector ${}^i\mathbf{a}_i$;
- $m_i \mathbf{g}$, link weight applied in its center of mass, identified by vector ${}^i\mathbf{b}_i$. Vector \mathbf{g} is gravity, typically expressed in the fixed, or 0-th, reference system: ${}^0\mathbf{g}$;

The Exoskeleton

- $-T_{ij}^i \mathbf{t}_{ij}$, tension exerted by the j -th wire, whose point of application is given by the vector \mathbf{u}_{ij} . Given that the force is a traction one, its direction is opposite to the unit vector \mathbf{t}_{ij} , while its magnitude is T_{ij} . The index j varies from i to N ;
- $\varphi_{ij} T_{ij}^i \mathbf{t}_{(i+1)j}$, tension exerted by the j -th wire, whose point of application is given by the vector \mathbf{d}_{ij} . Its direction coincides with the unit vector $\mathbf{t}_{(i+1)j}$, while its magnitude is $\varphi_{ij} T_{ij}$. The coefficient φ_{ij} is a variable factor that considers the reduction of force along the j -th wire due to the friction associated with the sliding of the wire into the hole. The index j varies from $(i+1)$ to N .

A study of the dissipative coefficient φ_{ij} follows. When the wires pass inside their holes, they are bent into a certain angle. This bending reduces the tension of the wires because of friction between the wire and the internal surface of the holes. If the ends of the holes are supposed to be well rounded, this can be studied in a way similar to the theory of belts. Figure 124 depicts this friction effect. The constant f is the Coulomb friction coefficient between a wire and the walls of its hole. This effect appears twice for each wire in each hole, at the entrance and at the exit.

The total effect of friction in the hole is equal to [146]:

$$\frac{\| -T_{ij}^i \mathbf{t}_{ij} \|}{\| \varphi_{ij} T_{ij}^i \mathbf{t}_{(i+1)j} \|} = e^{f(|\alpha_{ij}| + |\beta_{ij}|)} \quad 74$$

which leads to:

$$\varphi = e^{-f(|\alpha_{ij}| + |\beta_{ij}|)} \quad 75$$

where the two bending angles α_{ij} and β_{ij} can be calculated as follows:

$$\alpha_{ij} = \arccos \left[\frac{\mathbf{t}_{ij} \cdot (\mathbf{d}_{ij} - \mathbf{u}_{ij})}{\| \mathbf{d}_{ij} - \mathbf{u}_{ij} \|} \right] \quad 76$$

$$\beta_{ij} = \arccos \left[\frac{\mathbf{t}_{(i+1)j} \cdot (\mathbf{d}_{ij} - \mathbf{u}_{ij})}{\| \mathbf{d}_{ij} - \mathbf{u}_{ij} \|} \right] \quad 77$$

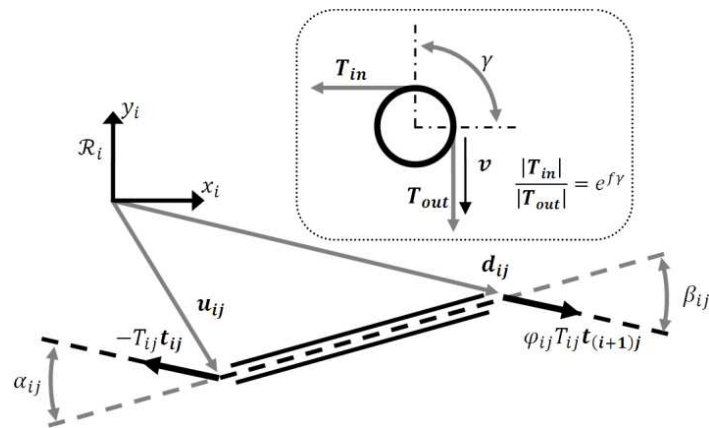


Figure 124: Friction effect due to the sliding of the wires inside the holes

Thus, the equations of the translational (7) and rotational (8) equilibrium of the generic i -th link can be written as:

$${}^i\mathbf{R}_i - {}^i\mathbf{R}_{i+1} + m_i {}^i\mathbf{A}_0 \mathbf{0} \mathbf{g} + {}^i\mathbf{F}_i - \sum_{j=i}^N T_{ij} {}^i\mathbf{t}_{ij} + \sum_{j=i+1}^N \varphi_{ij} T_{ij} {}^i\mathbf{A}_{i+1} {}^{i+1}\mathbf{t}_{(i+1)j} = 0 \quad 78$$

and

$$\begin{aligned} & {}^i\mathbf{C}_i - {}^i\mathbf{C}_{i+1} - {}^i\mathbf{l}_i \wedge {}^i\mathbf{R}_{i+1} + m_i {}^i\mathbf{b}_i \wedge {}^i\mathbf{A}_0 \mathbf{0} \mathbf{g} + {}^i\mathbf{a}_i \wedge {}^i\mathbf{F}_i + \\ & + \sum_{j=i+1}^N {}^i\mathbf{d}_{ij} \wedge \varphi_{ij} T_{ij} {}^i\mathbf{A}_{i+1} {}^{i+1}\mathbf{t}_{(i+1)j} - \sum_{j=i}^N {}^i\mathbf{u}_{ij} \wedge T_{ij} {}^i\mathbf{t}_{ij} = 0 \end{aligned} \quad 79$$

The equations of the i -th link require the solutions of the following $N-1$ links to be solved.

Optimization

As previously said the study of the statics describes the relationship between all the elements of the robotic structure. Each combination of parameters contributes to provide a specific and determined trend of all system variables. The optimization process aims to find the best configuration of parameters in order to keep limited, within defined boundaries, the variables of interest. Similarly to the previous optimization process, also in this version of device the generic tension T_i must be limited between two extreme values:

$$T_{min} < T_i < T_{max} \quad 80$$

- T_{min} represents the minimum acceptable wire tension value. Since tendons are not rigid components and can work only by traction, only positive values of internal tension are acceptable, otherwise the system cannot be actuated becoming uncontrollable. In order to increase the controllability margin a value of T_{min} greater than zero has to be introduced to compensate undesired effects, not modeled dynamics and non idealities.
- T_{max} represents the maximum acceptable wire tension value. This value is given by the maximum stress that the wires can sustain, without deforming and/or breaking, and by the maximum value of T that the actuators can (directly or indirectly) provide.

Due to the structure of the joints of this second version of the device, there are no more elastic elements to be optimized. In this case the elastic element is represented by the only EVA glove, which possesses a determined and unchangeable trend of torque on varying of the bending angles. The contribute of the glove enters like a generic torque that act on each joint and depends on the values of all the bending angles, on the basis of the results obtained from the analysis of the stiffness of the EVA glove.

$$C_{EVAi} = f(\theta_1 \dots \theta_i \dots \theta_N) \quad 81$$

In addition to these elements, due to the structure of the joints, there are other elements that have to be controlled: the reactive torques and forces acting on each joint C_i

$$\|C_i\| < C_{max}$$

82

- C_{max} represents the maximum acceptable constraint reaction torque value. This value is related to the maximum stress that the joints can sustain without plasticizing and/or breaking.

It is necessary to define again which parameters could be tuned and which are strictly fixed by the design. The final step will be to obtain the best possible parameter combination to achieve the overall goals.

Algorithm

The optimization was performed with a series of algorithms which calculates the best possible configuration of tunable parameters under specific conditions. The “best” configuration is not univocal: since it depends on the specific necessities of the device, different projects may have different requirements for their internal variables. In some cases the peak of a specific internal variable must be reduced as much as possible; in others a variable has to be kept as constant as possible to reduce its oscillations. Using the kinematic relationships between parameters (see the equation 79) the set of values of parameters that optimizes a certain target can be called the “best” configuration of the tunable parameters. The main tunable parameters for robotic structures according to the previously presented concept are:

- the position of wire hole;
- the range of the external force F ; the external force takes into account also the elastic torque provided by the glove.

For each value of external force and wire holes position, an analysis of every possible wire configuration was carried out. It is important to underline that, due to the fact that the holes are defined through a unit vector, they can assume whatever direction the designer plans. During each iteration (corresponding to a specific wire configuration), the goal is to calculate the behaviour of the three tendons tensions and the reactive forces and torques acting on each joint. Due to the superposition effect, the generic i -th link also applies an effect on the previous $i-1$. Moreover, the effect of friction reduces the tendon tensions at each passage inside a link of the structure; the value of tension upstream, perceived by the actuators, could be only obtained once all the links have been studied. On the basis of the equation obtained, the algorithm has to begin by calculating the trend of the variables of the last link (the N -th), and then proceeds backwards the kinematic chain. At each passage the trend of the variables related to the generic i -th link were calculated. Once all the N links were studied, for each of them the following variables were obtained:

- the i -th tendon tension T_i ;
- the reactive torque applied on the i -th joint C_i ;
- the reactive force applied on the i -th joint R_i ;

Each of these variables depends on all the bending angles θ_i ; they depend on the downstream because of the superposition effect and on the upstream because of friction. At the end of each iteration all the variables referred to a specific wire configuration were obtained and saved in a file. The introduction of constraints between the joints, e.g. the *soft constraint* between DIP and PIP articulation, allows to diminish the dimensions of the obtained matrix and reduce the required memory. Once all the information related to all wire positions were obtained, the research of the most suitable configuration can start.

Optimization of the tendon configurations

The following steps, performed to obtain the best possible configuration, are completely different from the ones presented for the first design choice. The key point of this optimization version is represented by what could be defined as the “*operating area*”. The *operating area* is a quality factor invented to describe in a simple and easy to understand way the part of the whole working space in which the device grant determined performances. The *area* is represented by a convex surface, function of the bending angles, in which the tendon tension T_i results to be positive and lesser than a previously chosen limit value of tension T_{lim} ; moreover the origin of the space of the joints ($\theta_i = 0, \forall i$) has to be an interior point of the surface. The *operating area* allows the designer to know the range of motion in which the device assures a limited value of tendon tension, previously chosen and suitable for the design. Once the limit value of the tensions is decided, the optimization process has to calculate N operating areas, each of them related to one T_i . At this point is necessary to merge all the areas in order to obtain a comprehensive operating area that takes into account all the limits on all the tensions. Figure 125 shows an example of operating area related to a tension that depends only on two bending angles. In each cell the value of tendon tension is reported; the grey space is the operating area itself; as it could be seen there are cells in which the tension is lesser than the T_{lim} that are not included into the operating area due to the requirement of convexity. Figure 126 shows an example of how the overall operating area (on the right) is made, starting from a couple of operating areas (on the left). The obtained overall operating area represents the range of motion in which the device guarantees the required performances and has to operate; the remaining part of the whole working space could be neglected. It is then necessary to study the behaviour of all the others variables of interest into the operating area, calculating their trend and maximum values. The maximum values of torques and forces acting on each joint, limited to the operating area, and the operating area itself are all the quality factors needed to determine the best possible configuration. Starting from these factors, it is then necessary to determine a value to describe the overall goodness of a specific wire configuration; in order to accomplish this goal the optimization function was introduced:

$$Q = f(K_i \cdot q_i)$$

83

where:

<i>Operating area of T_i</i>									
$T > T_{lim}$	$T > T_{lim}$	$T > T_{lim}$	$T > T_{lim}$	$T > T_{lim}$	$T > T_{lim}$	$T < T_{lim}$	$T < T_{lim}$	$T < T_{lim}$	$T < T_{lim}$
$T > T_{lim}$	$T > T_{lim}$	$T > T_{lim}$	$T > T_{lim}$	$T > T_{lim}$	$T > T_{lim}$	$T > T_{lim}$	$T < T_{lim}$	$T < T_{lim}$	$T < T_{lim}$
$T < T_{lim}$	$T > T_{lim}$	$T > T_{lim}$	$T > T_{lim}$	$T > T_{lim}$	$T > T_{lim}$	$T > T_{lim}$	$T < T_{lim}$	$T < T_{lim}$	$T < T_{lim}$
$T < T_{lim}$	$T < T_{lim}$	$T < T_{lim}$	$T < T_{lim}$	$T > T_{lim}$	$T > T_{lim}$	$T > T_{lim}$	$T < T_{lim}$	$T < T_{lim}$	$T < T_{lim}$
$T < T_{lim}$	$T < T_{lim}$	$T < T_{lim}$	$T < T_{lim}$	$T > T_{lim}$	$T > T_{lim}$	$T > T_{lim}$	$T < T_{lim}$	$T < T_{lim}$	$T < T_{lim}$
$T < T_{lim}$	$T < T_{lim}$	$T < T_{lim}$	$T < T_{lim}$	$T < T_{lim}$	$T > T_{lim}$	$T > T_{lim}$	$T > T_{lim}$	$T < T_{lim}$	$T < T_{lim}$
$T < T_{lim}$	$T < T_{lim}$	$T < T_{lim}$	$T < T_{lim}$	$T < T_{lim}$	$T > T_{lim}$	$T > T_{lim}$	$T > T_{lim}$	$T < T_{lim}$	$T < T_{lim}$
$T < T_{lim}$	$T < T_{lim}$	$T < T_{lim}$	$T < T_{lim}$	$T < T_{lim}$	$T < T_{lim}$	$T > T_{lim}$	$T > T_{lim}$	$T < T_{lim}$	$T < T_{lim}$
$T < T_{lim}$	$T < T_{lim}$	$T < T_{lim}$	$T < T_{lim}$	$T < T_{lim}$	$T < T_{lim}$	$T < T_{lim}$	$T > T_{lim}$	$T < T_{lim}$	$T < T_{lim}$
$T < T_{lim}$	$T < T_{lim}$	$T < T_{lim}$	$T < T_{lim}$	$T < T_{lim}$	$T < T_{lim}$	$T < T_{lim}$	$T < T_{lim}$	$T < T_{lim}$	$T > T_{lim}$
$T < T_{lim}$	$T < T_{lim}$	$T < T_{lim}$	$T < T_{lim}$	$T < T_{lim}$	$T < T_{lim}$	$T < T_{lim}$	$T < T_{lim}$	$T < T_{lim}$	$T > T_{lim}$

Figure 125: Example of operating area. The green written cells respect the limit of tension.

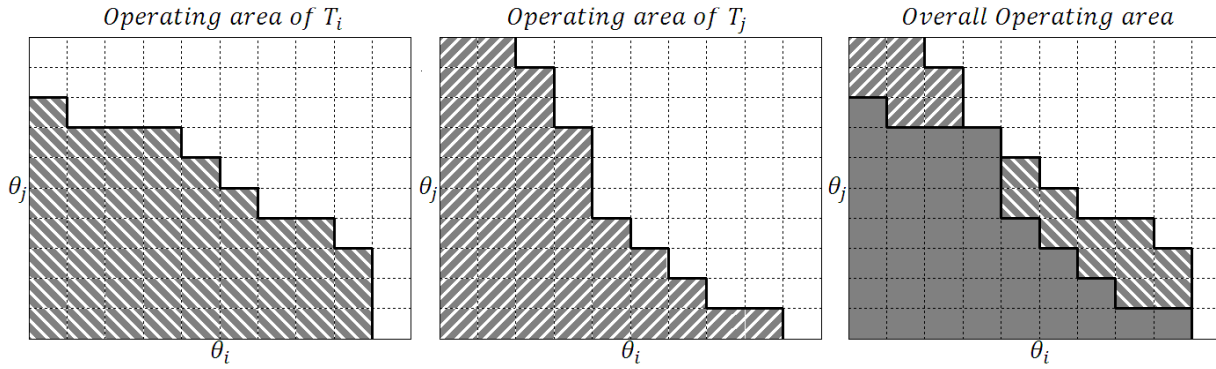


Figure 126: Overall operating area (on the right), starting from a couple of operating areas (on the left).

- Q is the value that describes the overall goodness of the specific configuration
- q_i is the i -th quality factor. It has to be underlined that, in case of the operating area, the true quality factor is not the area itself but its complementary with respect the whole working space.
- K_i is the coefficient related to the i -th quality factor. These coefficients could be changed by the operator in order to modify the importance of the specific quality factor. A bigger value of K_i means that the unitary variation of q_i is more important than those of others factors (with lesser coefficients).
- f is a generic function that can be chosen on the basis of the needs. The function could be the sum, the norm or a more complex equation, each of them with its specific behaviour. Just to provide an explanatory example, in case of sum the variation of a quality factor value contributes to the goodness independently from the specific value of the factor itself; this consideration is no longer true in case of norm function.

Once the goodness values for each wire position were obtained, it is necessary to obtain the best possible configuration, that corresponds to that which minimizes the value of Q .

Results

Many simulations were performed changing the values of the various tunable parameters; each different combination of parameters provides a completely different base on which the device has to work. Each parameter influence the trend of the interested variables in a very specific way; some of them generate hardly appreciable variations, while others may cause drastic modifications on the behaviour of the device. The input parameters preliminary defined for each simulation are the following:

- The acceptable passing points of the holes through the structure;
- The structure of the hole in terms of length, radius and shape;
- The behaviour of the external forces applied on the structure by the glove and the human being;
- The limit value of tendon tension, T_{lim} ;
- The quality factors coefficients, $K_i \forall i$;
- The optimization function, f ;

In the following part the results related to different performed simulations with different parameter configurations will be presented. For all these simulations the fixed parameters are the following:

- Behaviour of the external force modeled on the basis of the results coming from the test on EVA glove.
- Discrete tendon passing points. Each phalanx has a limited number of possible downstream and upstream passages of the tendons (described by ${}^i\mathbf{d}_{ij}$ and ${}^i\mathbf{u}_{ij}$ respectively). In order to limit the

	Quality Factor				T_{lim}
	Op. Area	C_1	C_2	C_3	
Set \hat{K}_{10}	1	10	10	10	100 N
Set \hat{K}_{20}	1	20	20	20	200 N
Set \hat{K}_{100}	1	100	100	100	300 N
Set \hat{K}_{200}	1	200	200	200	∞

Table 24: Values of quality factors coefficient used during the following simulations

possible combinations, in the following simulations each ${}^i\mathbf{d}_{ij}$ is directly connected by one, and only one ${}^i\mathbf{u}_{ij}$. Moreover the holes cannot cross each other and, except for the palmar, only one tendon can pass inside each hole. There are six possible passing points through each of three phalanges and other six into the palmar support.

In the following simulations the limit value of tendon tensions and the quality factor coefficient will change. In the first series of simulations the limit tendon value has been chosen and kept constant while the quality factors coefficients changed. Vice-versa in the second series the quality factor has been kept constant while T_{lim} changed. In this way the dependence of the results on the variations of the two parameters could be easily understood. Finally, in the last simulation it was decided to emulate a device composed by only two DoF: the third phalanx was removed, keeping it passive in order to see the difference between a structure with three or two degrees of freedom. All the following simulations were performed utilizing as optimization function f the sum of all the elements (quality factor multiplied by the relative coefficient). The sum is not the only optimization function utilized during the simulations (e.g. all the configuration were also performed using the norm) however the results related to this variation generate hardly appreciable variations and so it was decided not to show them here.

Table 24 shows four different set of values of quality factor coefficients and four values of tension limit. For each obtained solution a series of information were provided:

- The overall operating area obtained.
- The behaviour of the reactive torque applied on the first joint in terms of trend and maximum value. This information was shown into two graphs. On the left the values of torque, obtained into a certain configuration, are inserted in each cell of the operating area graph; a gradient coloration allows to more easily understanding the trend. On the right a 3D graph shows the trend of the torque on the whole working space.
- The behaviour of the three tendon tensions. The same two graphs, previously described, were provided for each tendon tension.
- Tendon configurations. It is the schematic graphical representation of the passage of the wires through the different links of the robotic structure.

It was decided to apply the soft constraint between PIP and DIP in order to simplify the calculation and obtain tensions that depend only by two bending angles displayable with 3D graphs, which are clearer and easier to be understood and appreciated. All the graphs related to the operating areas were reported in a grid like shape, which has a constant angular step equal to $8 \cdot 10^{-2}$ rad (5 deg) for all the bending angles. Finally, it is important to underline that in all these simulations friction was neglected.

First simulation: T_{lim} constant

In this part the results related to four different simulations will be reported. For each of them the value of tension limit was kept constant and equal to 300 N, while the quality factor coefficients change among the four set as shown in

The Exoskeleton

Table 24. The four different set of coefficient \hat{K} change the ratio of importance between the dimension of the *operating area* and the maximum value of reactive torque applied on each joint. The more the coefficients of the three torques are high compared to the operating area one, the more it is important to keep lower values of torques. As it could be easily seen in Figure 127, passing from \hat{K}_{10} (top left) to \hat{K}_{200} (bottom right) the dimension of the operating area decreases, reducing the range of θ_i in which tendons tension smaller than 300N are guaranteed. This is due to the fact that, increasing the coefficient related to C , the dimension of the operating area assumes a secondary importance with respect the peak values of reactive torques. For each proposed solution the following informations were provided:

- Tendon configurations. The schematic representation of the passage of the tendons through the links of the structure.
- Behaviour of the reactive torque acting on the first joint represented both as a 3-D graph and with the *operating area* graph. Each cell of the operating area graph contain the value of the reacting torque in the specific configuration of θ_1 and θ_2 .
- Maximum value of the reactive torque inside the *operating area*.
- Behaviour of the three tendon tensions represented both as a 3-D graph and with the *operating area* graph.

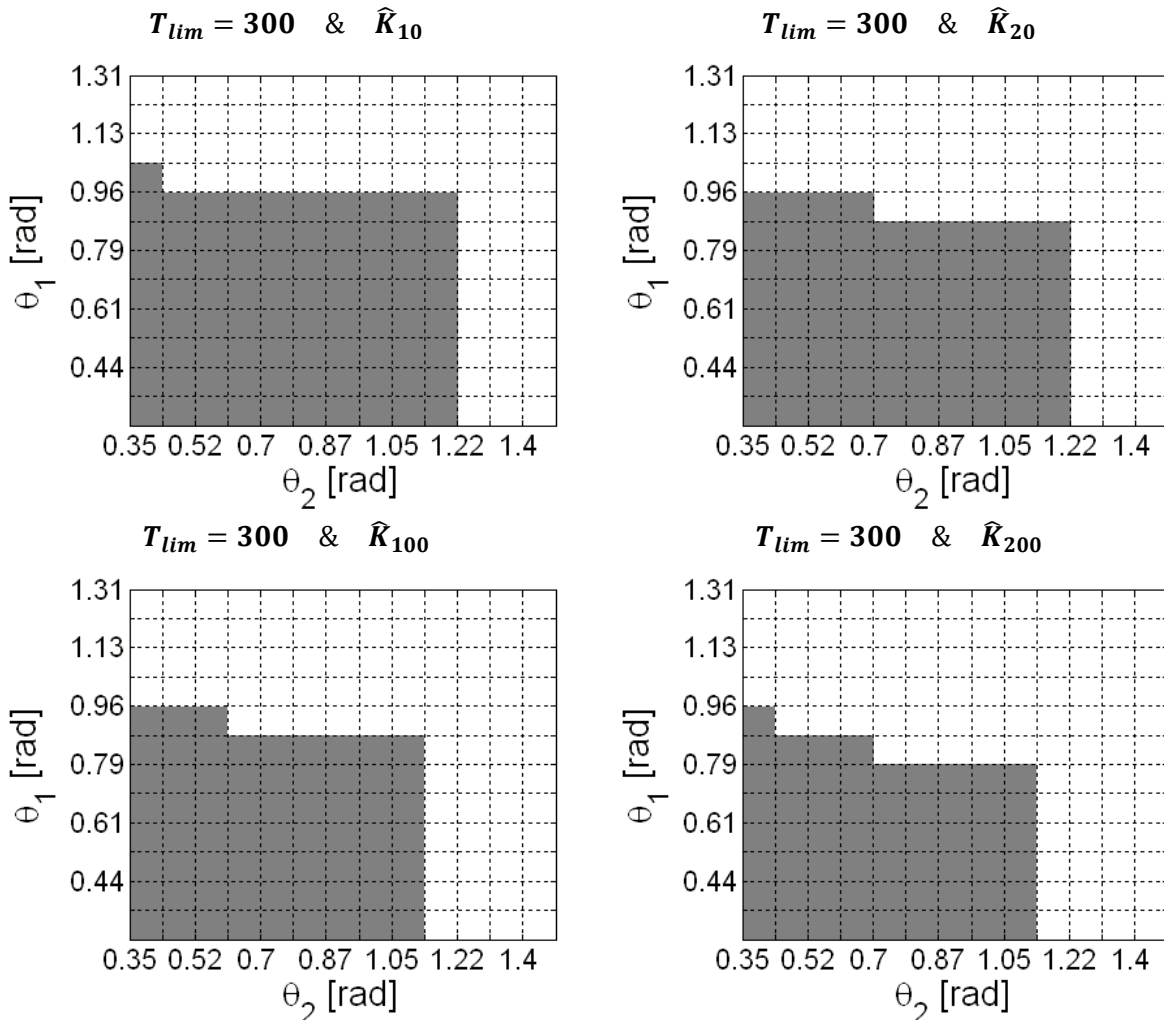
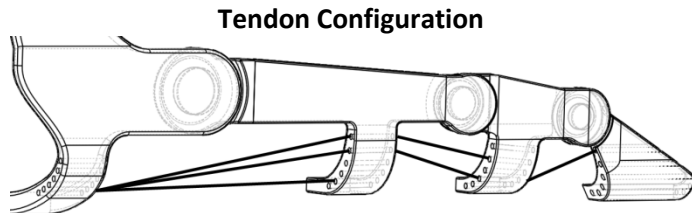


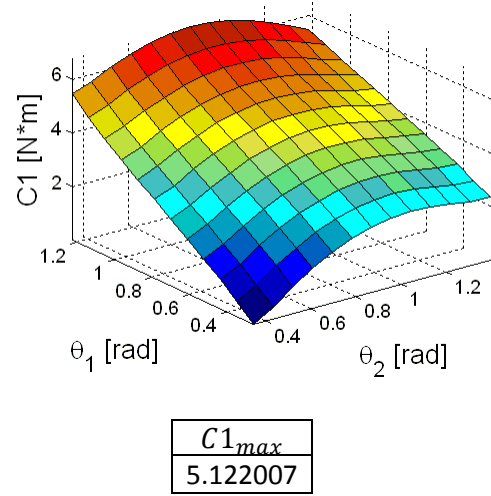
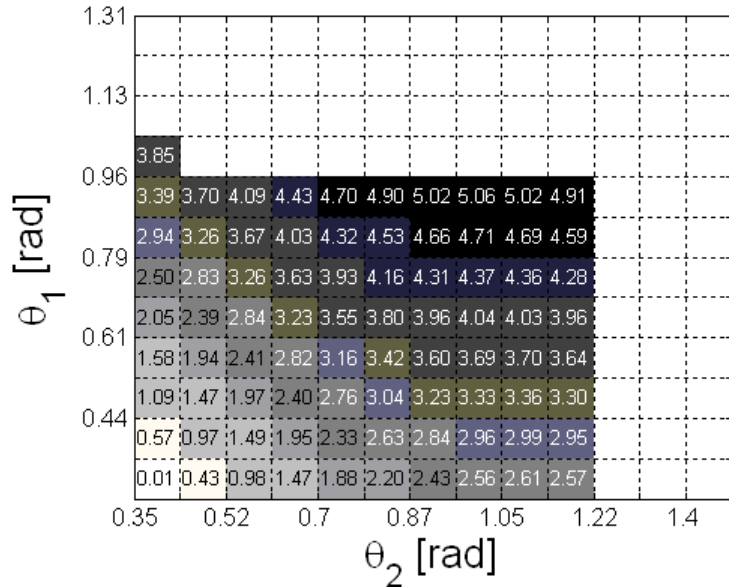
Figure 127: Comparison among the four *operating areas* of the simulation 1

The Exoskeleton

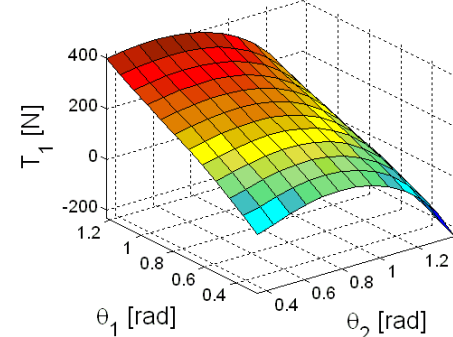
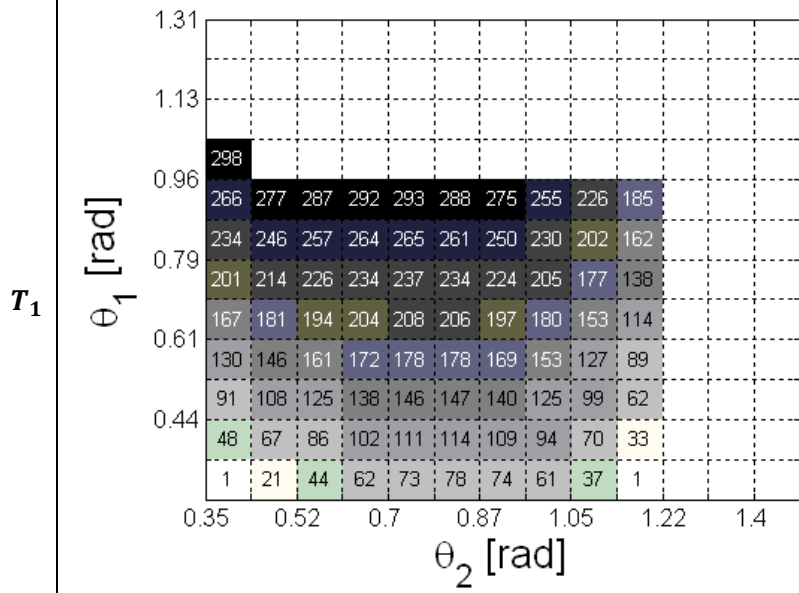
SIMULATION 1A: $T_{lim} = 300$ & \hat{K}_{10}



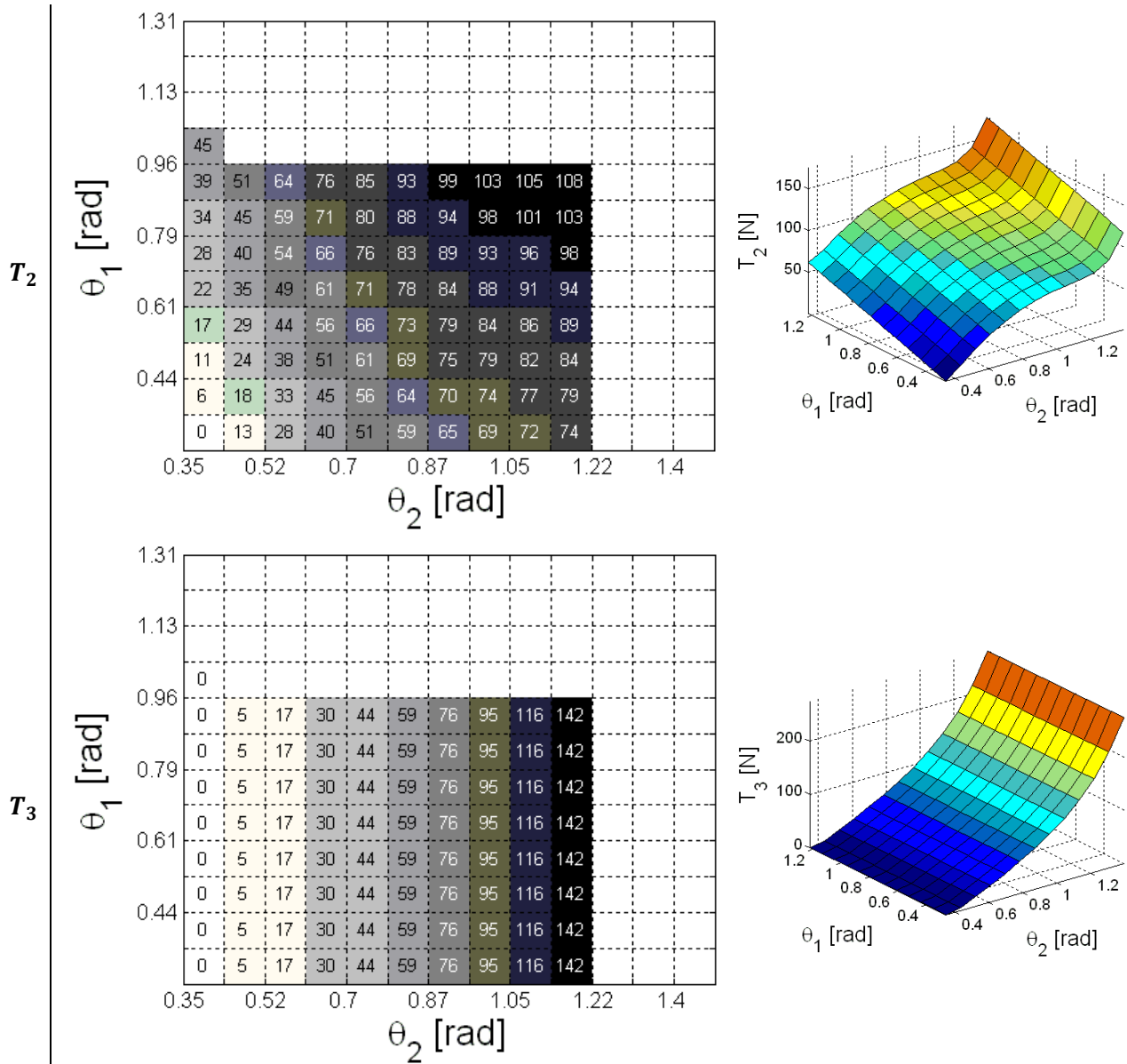
Reactive torque acting on the first joint: C_1



The Three Tendon Tensions

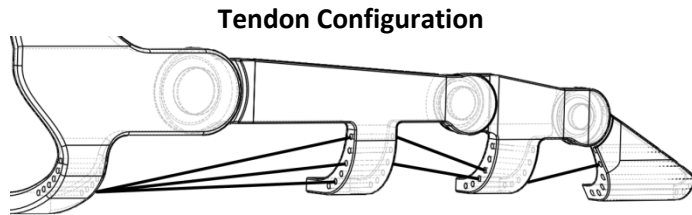


The Exoskeleton

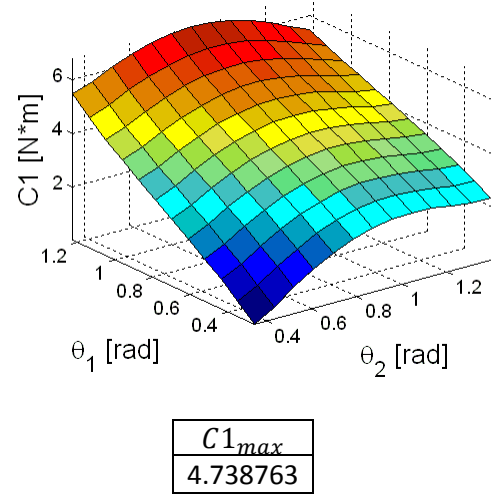
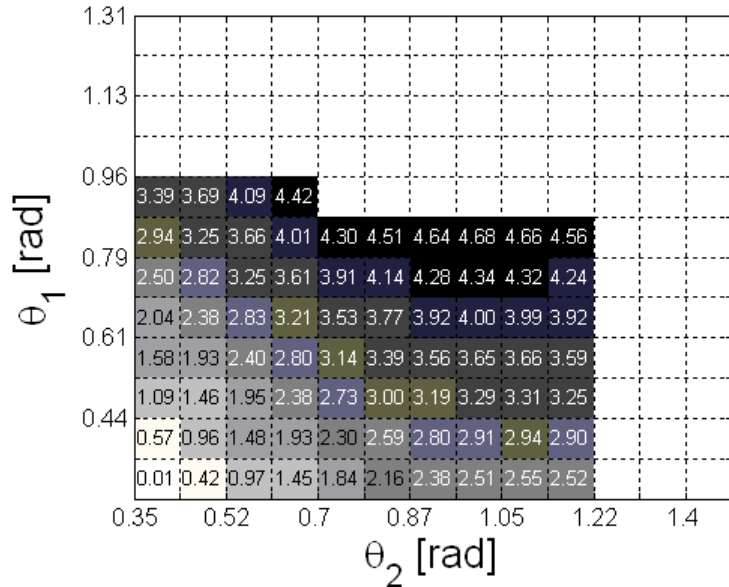


The Exoskeleton

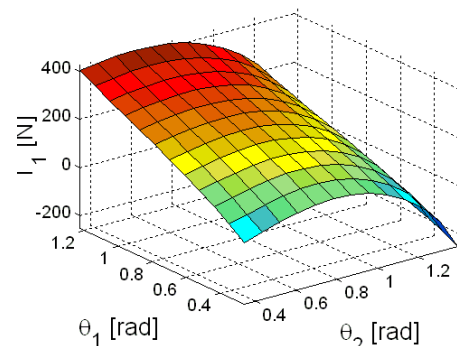
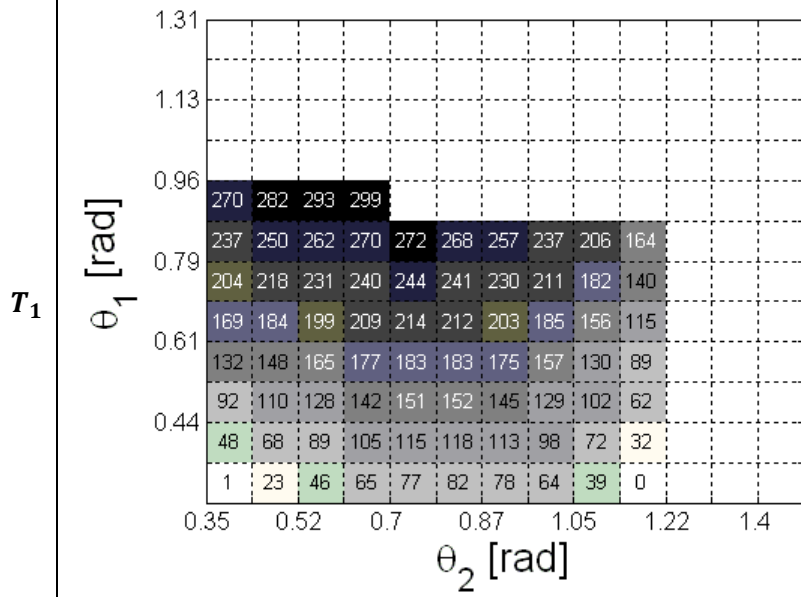
SIMULATION 1B: $T_{lim} = 300$ & \hat{K}_{20}



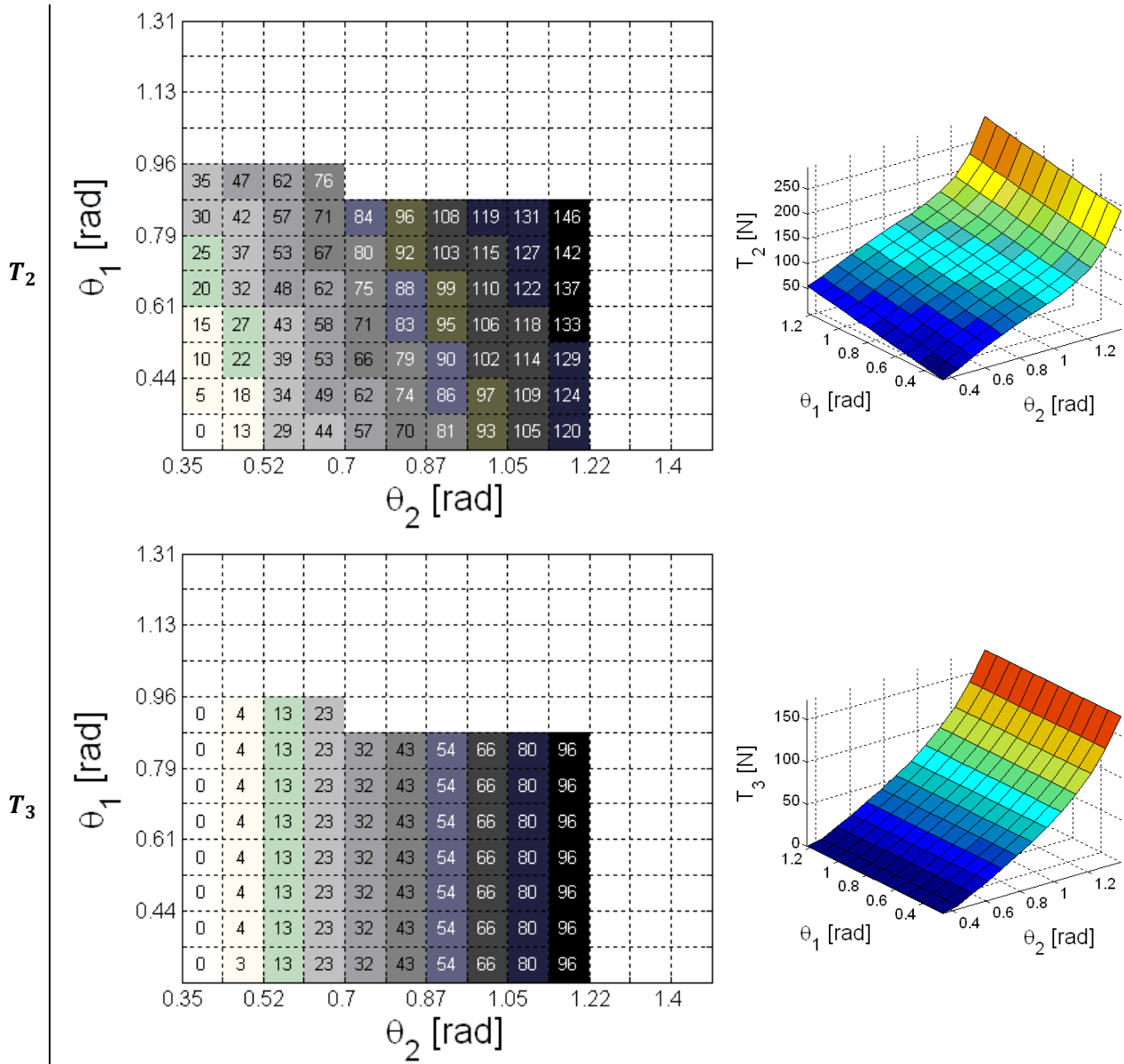
Reactive torque acting on the first joint: C_1



The Three Tendon Tensions

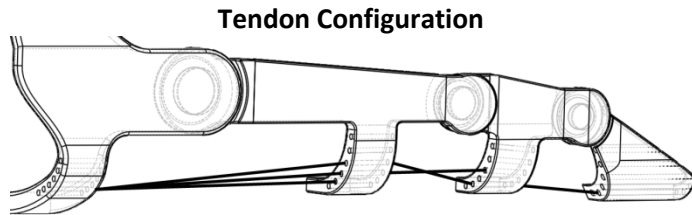


The Exoskeleton

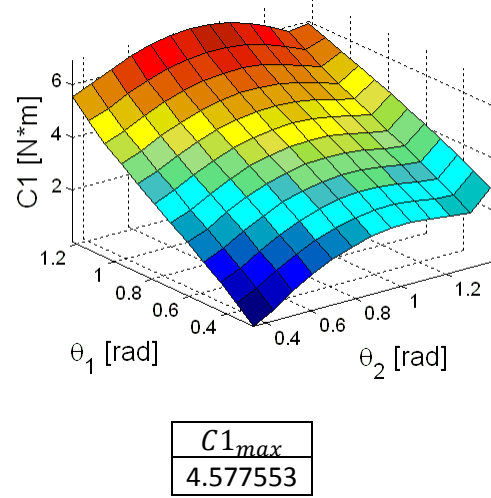
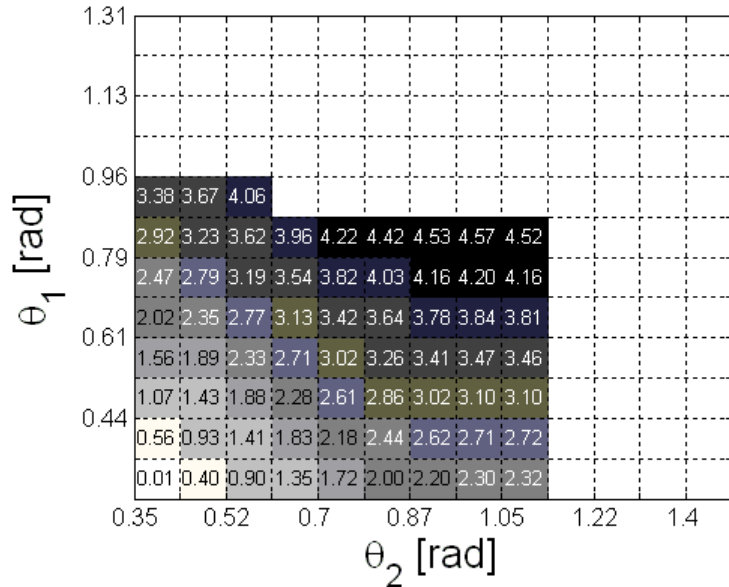


The Exoskeleton

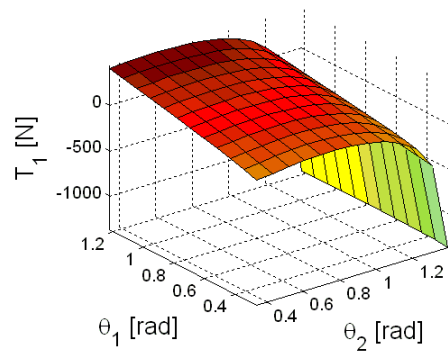
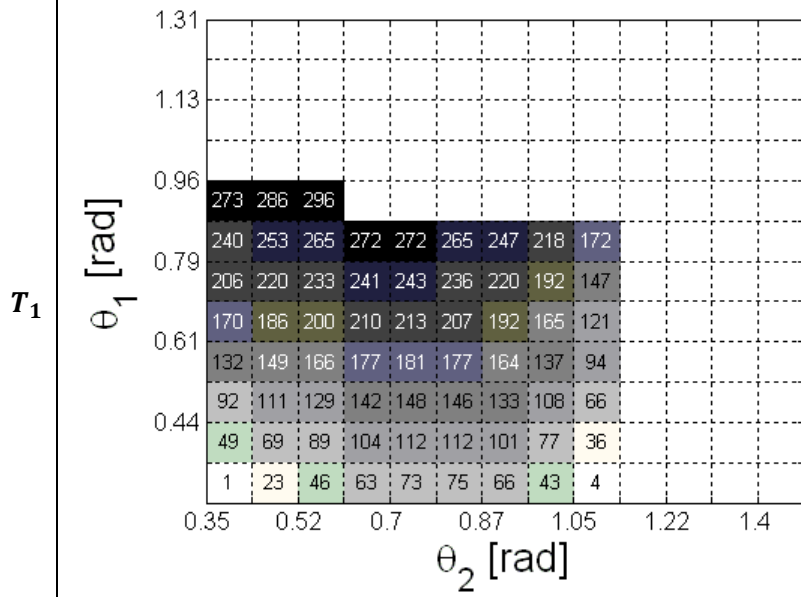
SIMULATION 1C: $T_{lim} = 300$ & \hat{K}_{100}

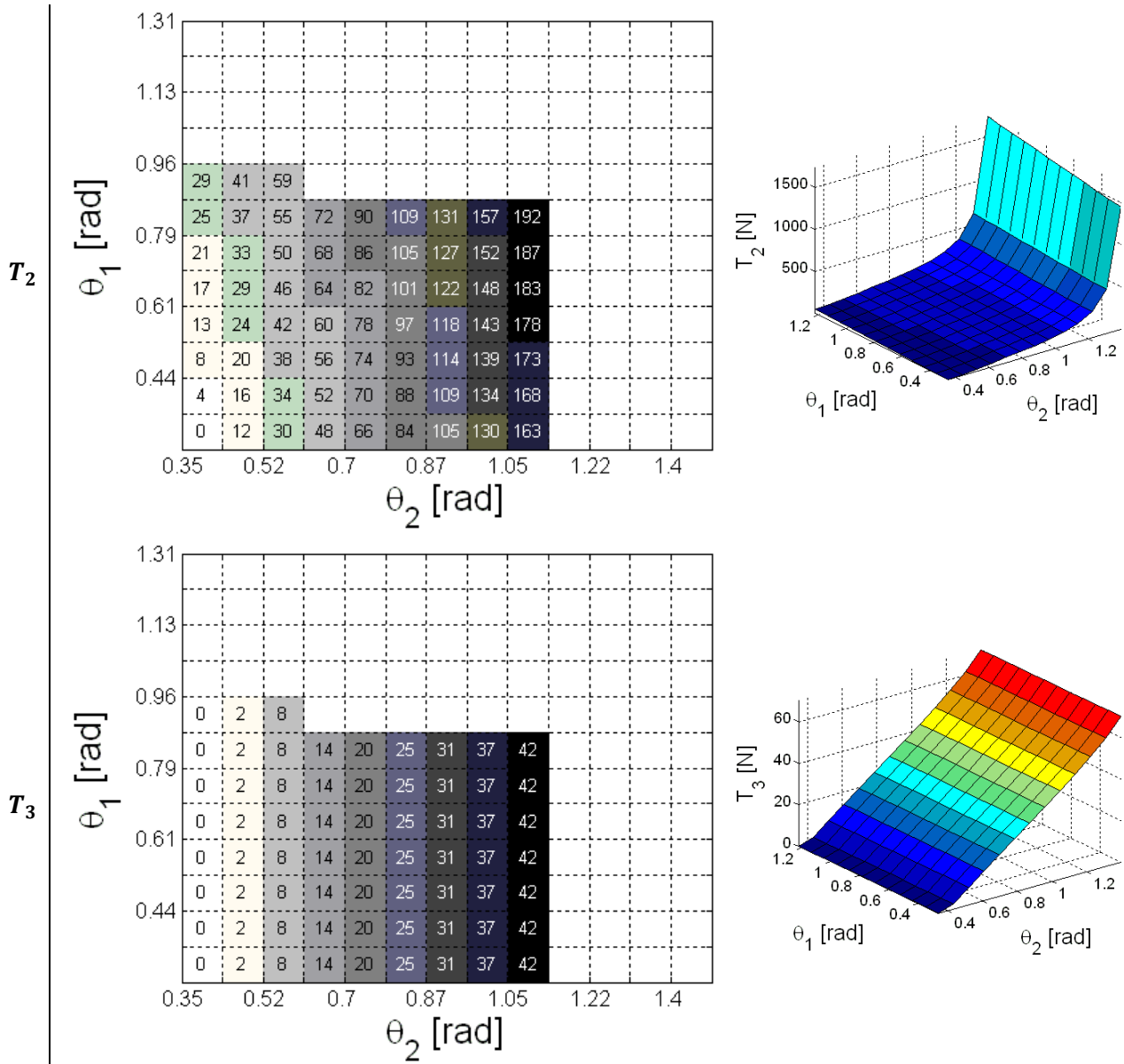


Reactive torque acting on the first joint: C_1



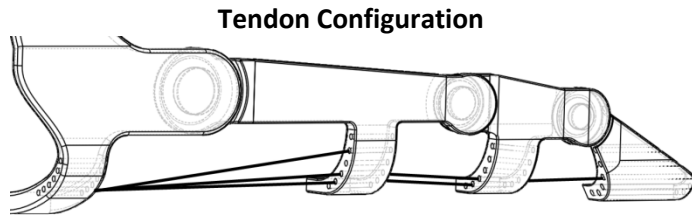
The Three Tendon Tensions



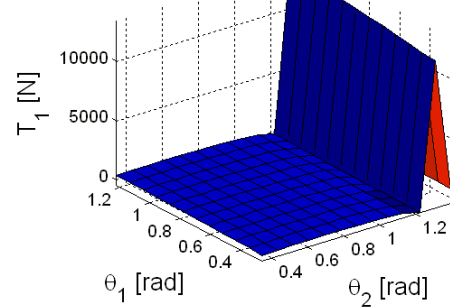
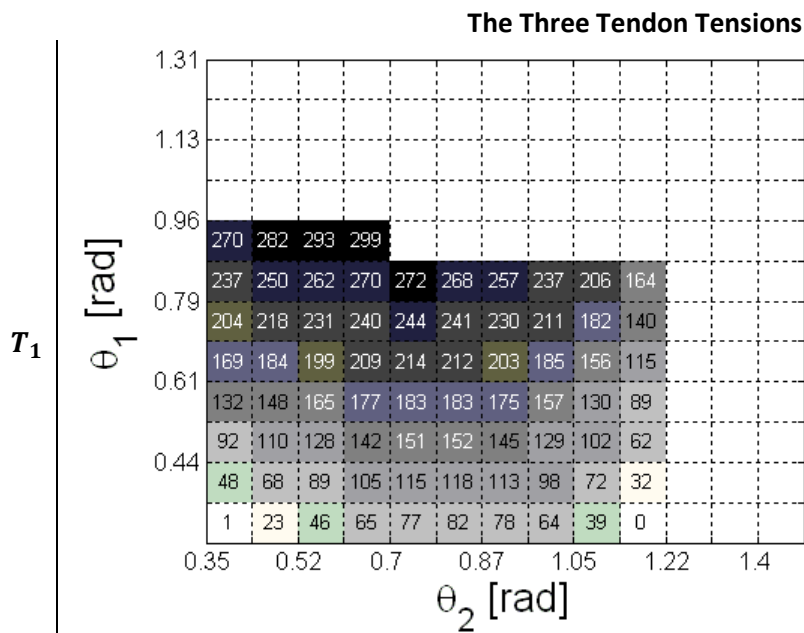
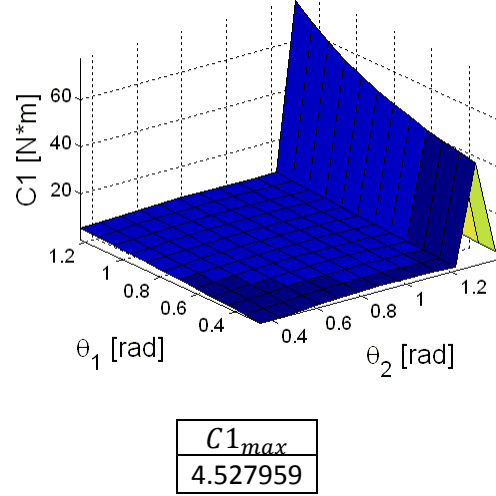
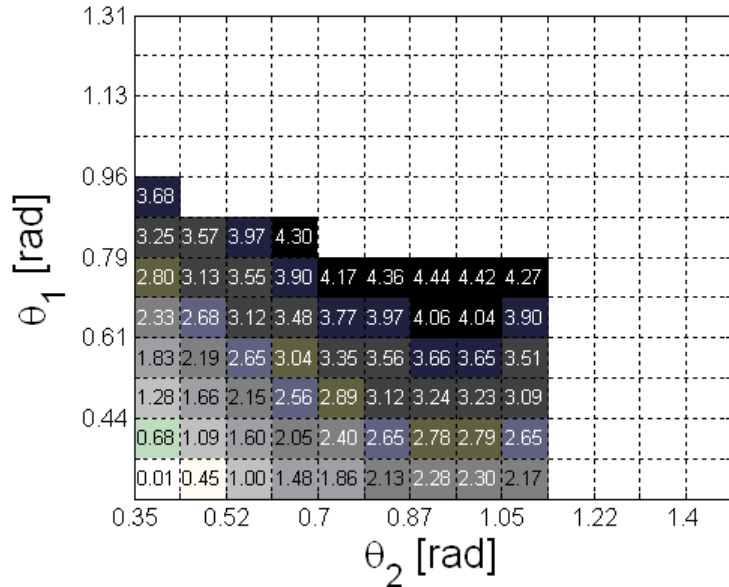


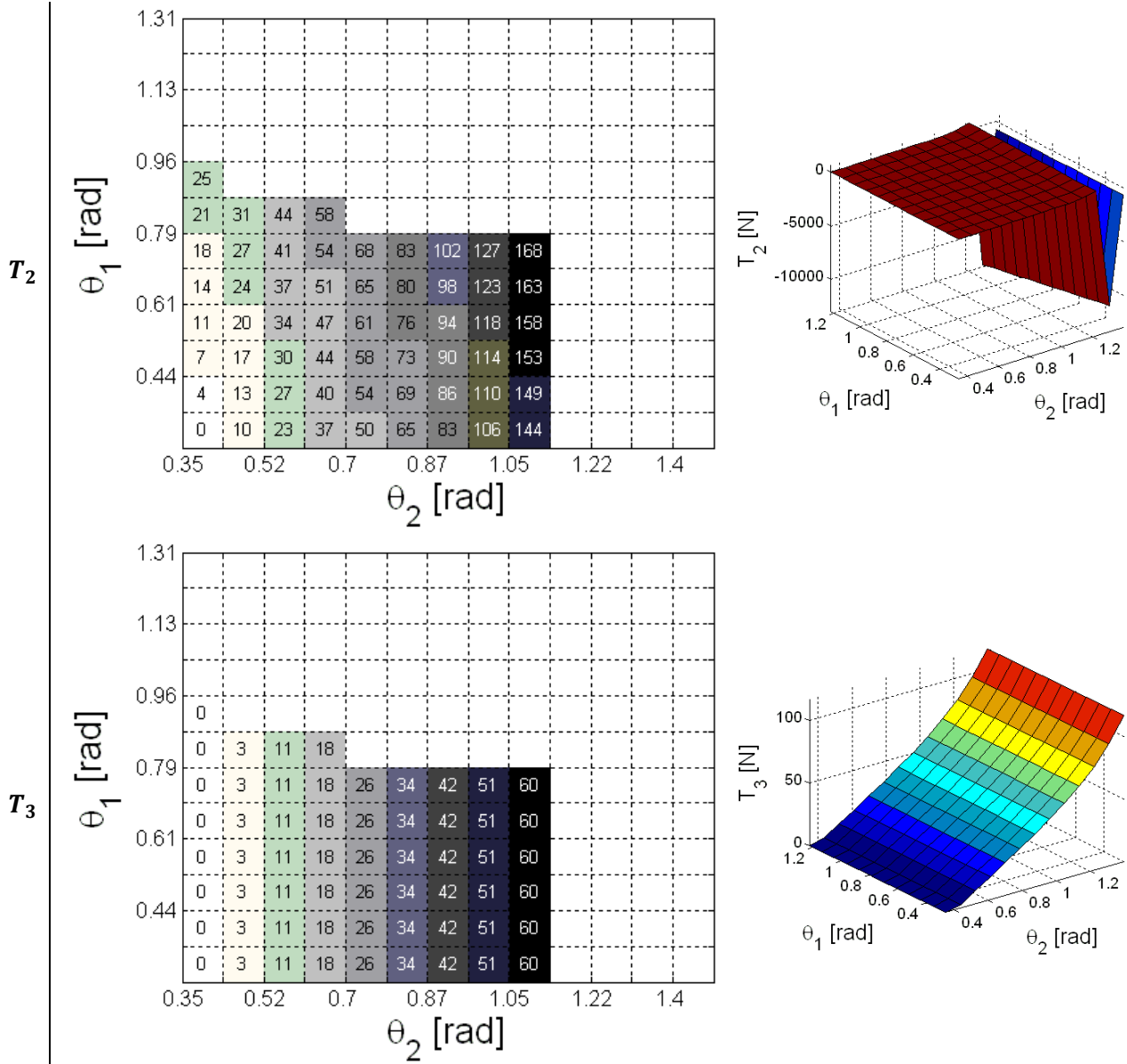
The Exoskeleton

SIMULATION 1D: $T_{lim} = 300$ & \hat{K}_{200}



Reactive torque acting on the first joint: C_1





From simulation 1a to simulation 1d all the information related to a single \hat{K} was provided. The trends of the reactive torque acting on the first joint and of the three tendon tensions were reported in each of the four figures. As it could be foreseen, passing from \hat{K}_{10} to \hat{K}_{200} the peak value of the reactive torque decreases due to the augmenting of the related importance value and at the same time the size of the operating area becomes smaller.

Second simulation: \hat{K} constant

In this second simulation the results related to others four simulations were reported. In this case, for each of them the quality factor coefficients were kept constant and equal to \hat{K}_{10} , while the value of tension limit changes among the four possibilities shown in

Table 24. The different values of T_{lim} directly influence the size of *operating area*; lower values of limit impose more stringent limitations, reducing the available size. It is important to underline that the variation of the limit tension provide an indirect effect also on maximum values of reactive torques and forces. Smaller tendon tensions generate smaller reactive torques inside the operating area; however this is caused mainly by the shrinking of the operating area itself. Figure 128 shows the four *operating areas* obtained; as it can be seen, the size of the operating area decreases sharply with the reduction of the tension value limit. Also in this second simulation the following informations were provided:

- The schematic representation of the passage of the tendons through the links of the structure.
- Behaviour of the reactive torque acting on the first joint.
- Maximum value of the reactive torque inside the *operating area*.
- Behaviour of the three tendon tensions.

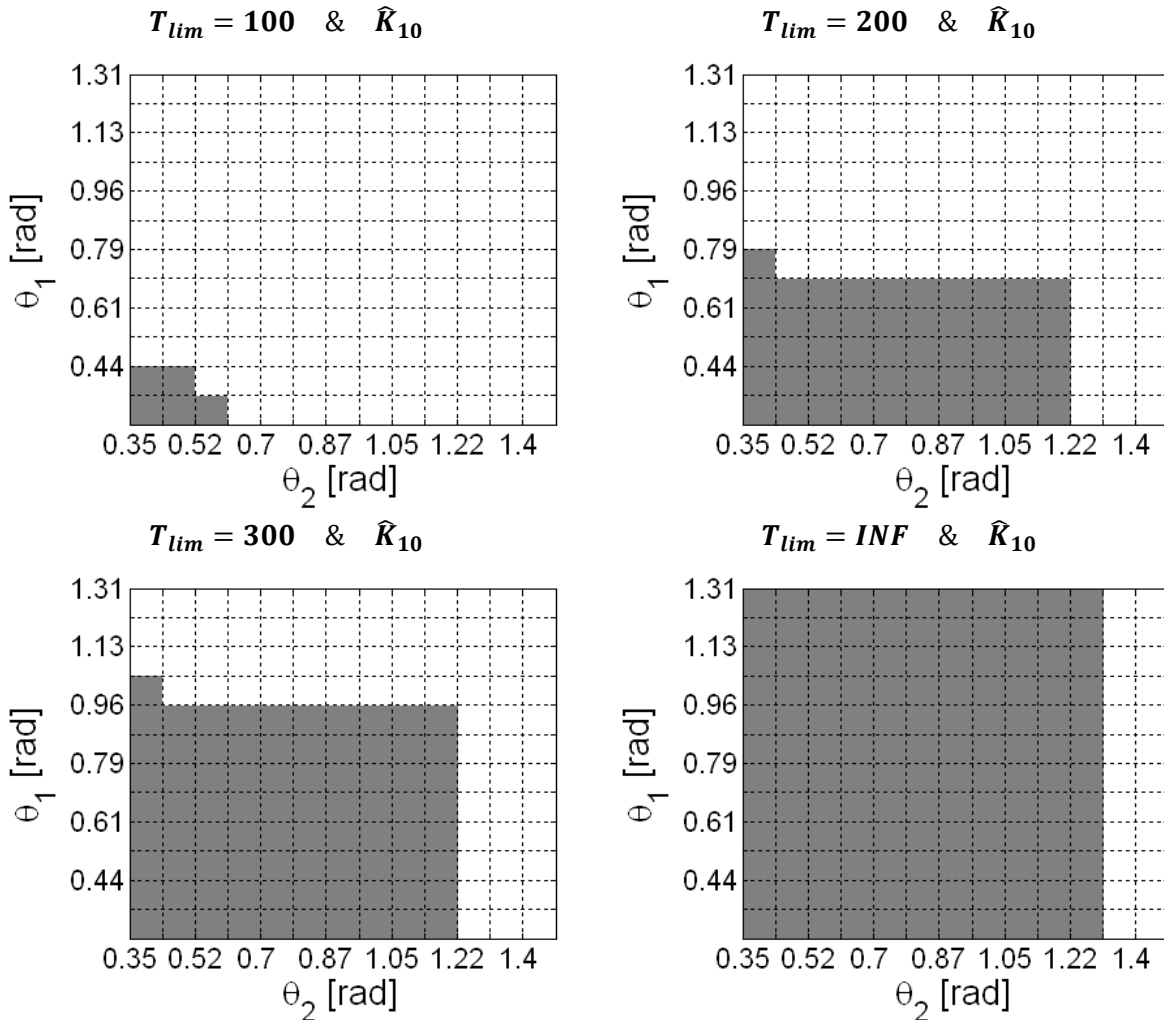
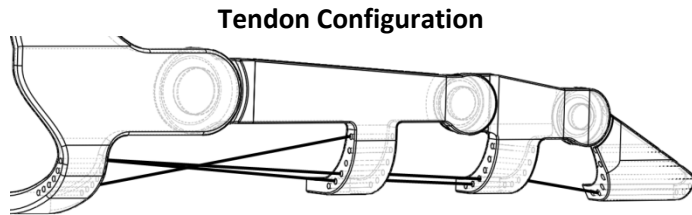


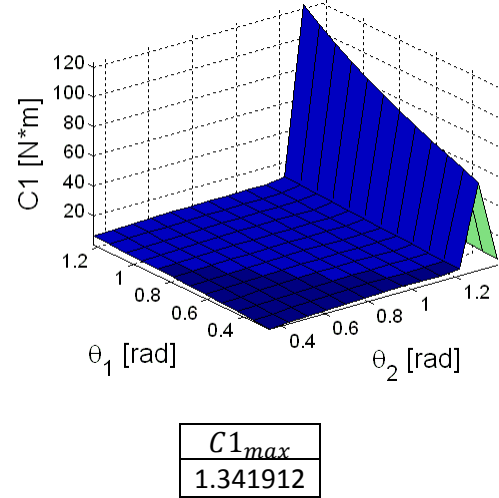
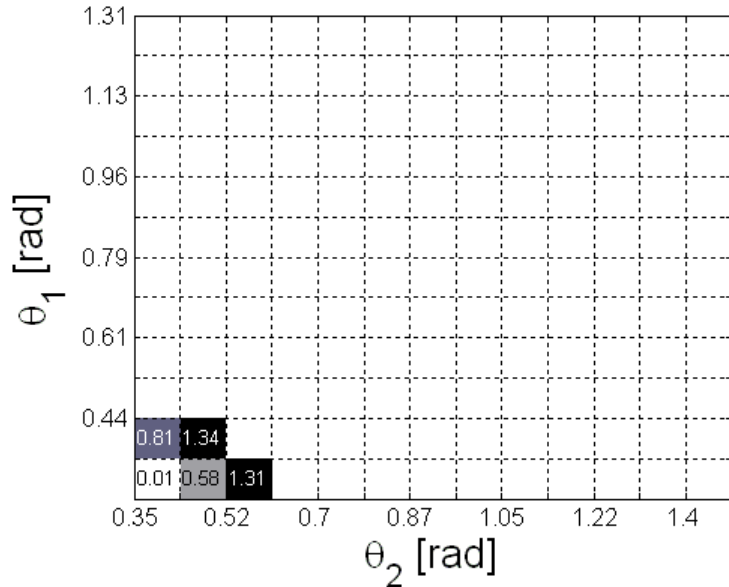
Figure 128: Comparison among the four *operating areas* of the simulation 2

The Exoskeleton

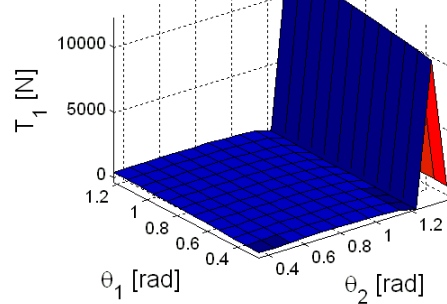
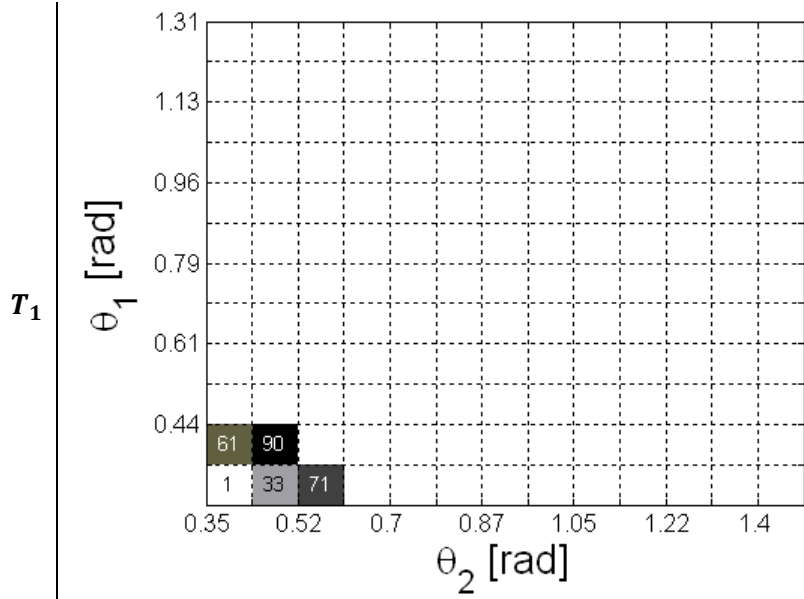
SIMULATION 2A: $T_{lim} = 100$ & \hat{K}_{10}

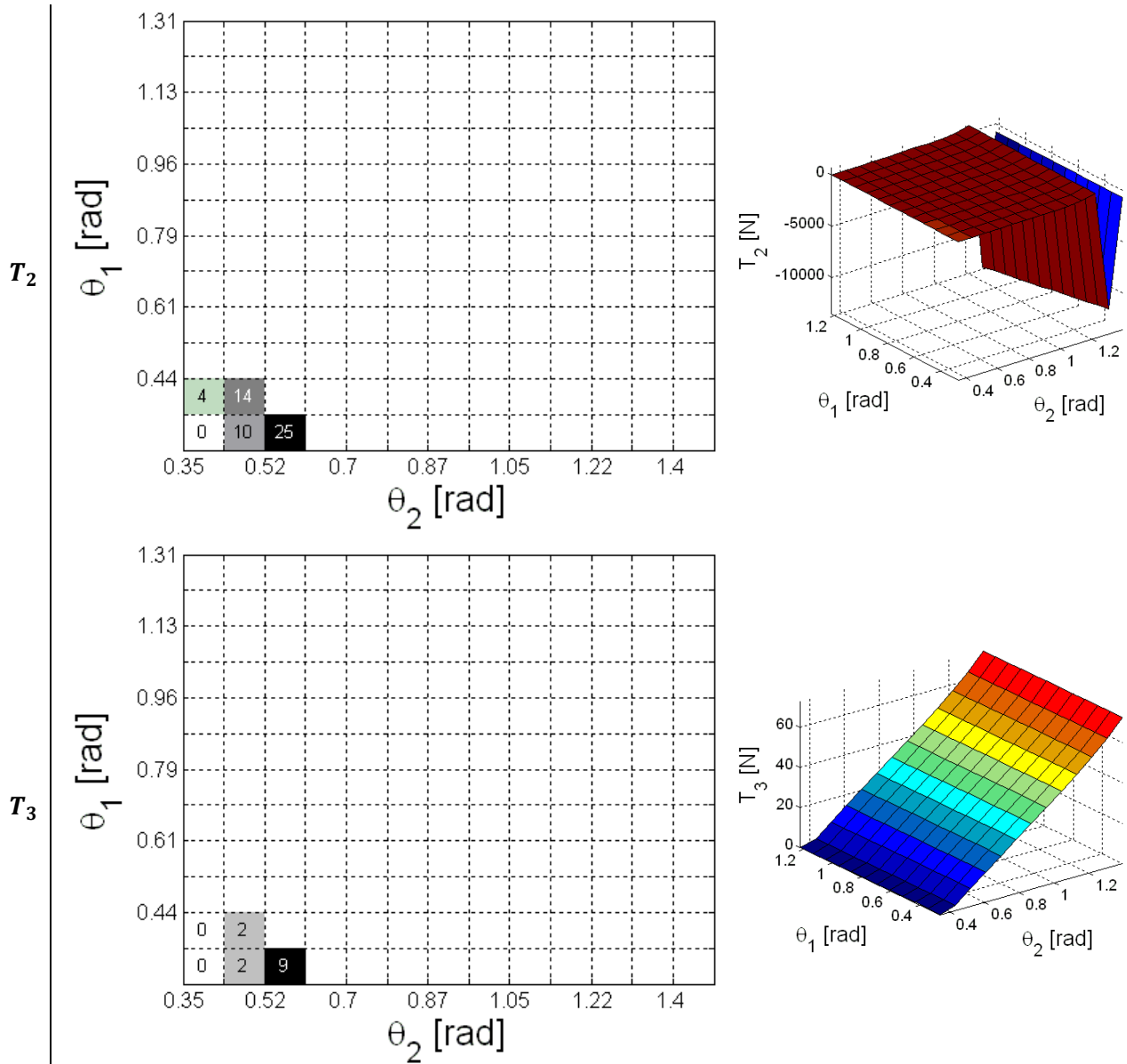


Reactive torque acting on the first joint: C_1



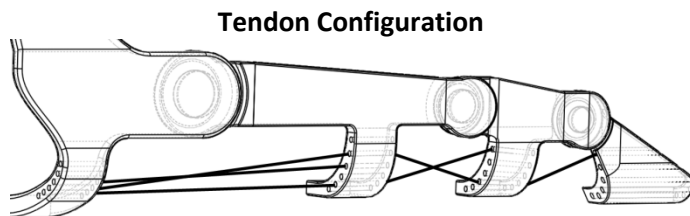
The Three Tendon Tensions



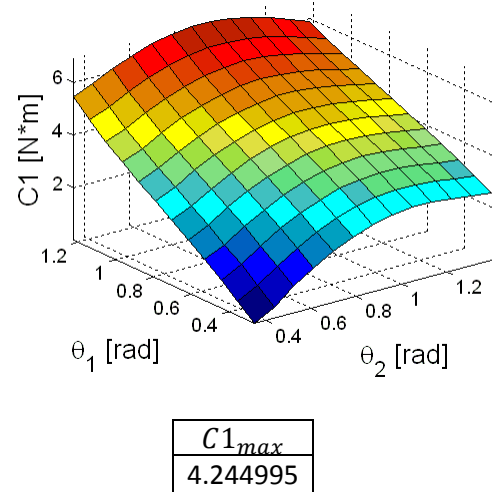
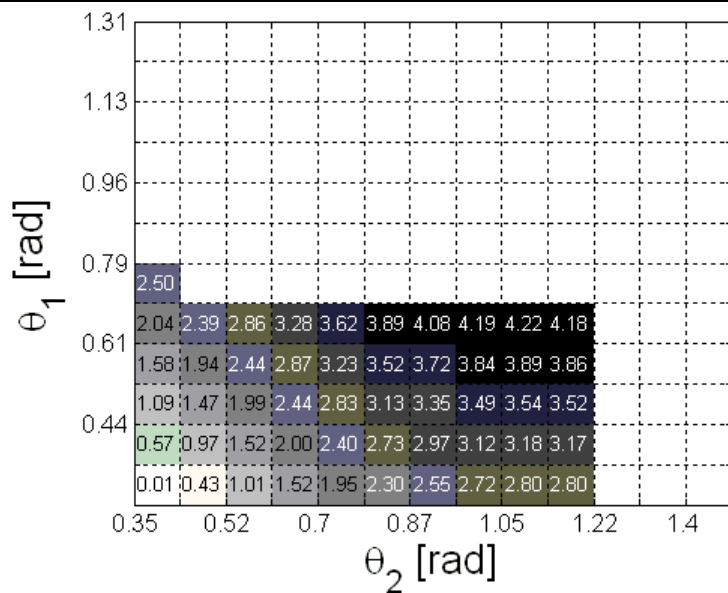


The Exoskeleton

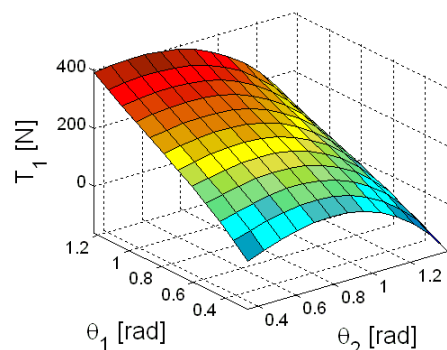
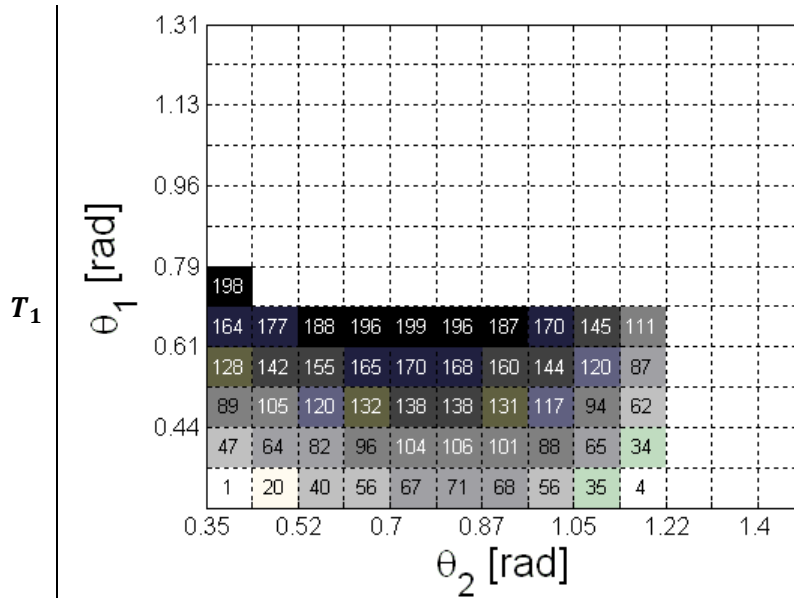
SIMULATION 2B: $T_{lim} = 200$ & \hat{K}_{10}

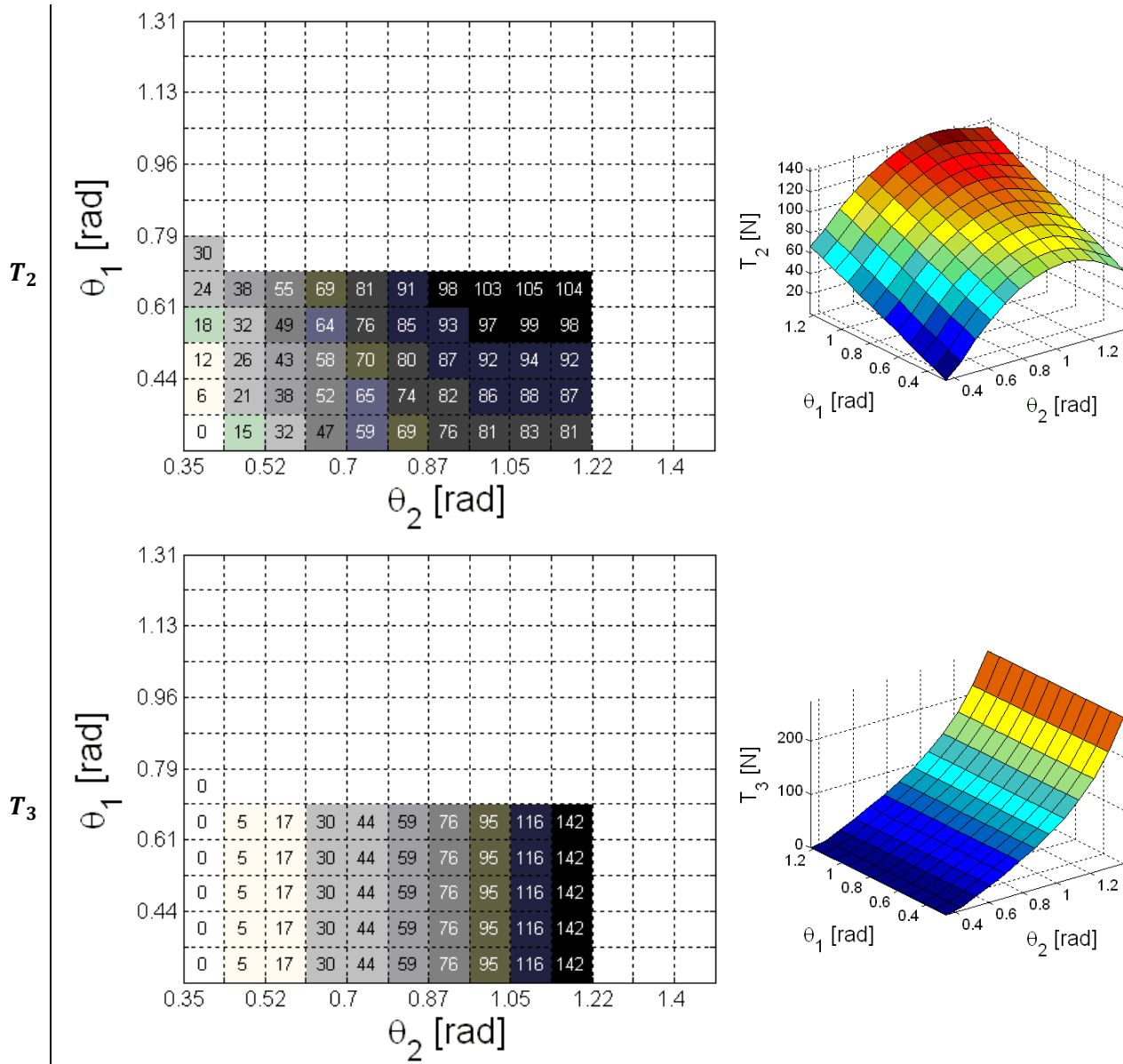


Reactive torque acting on the first joint: C_1



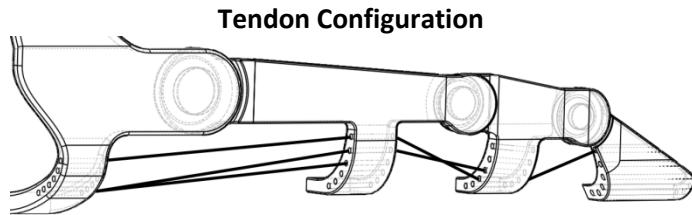
The Three Tendon Tensions



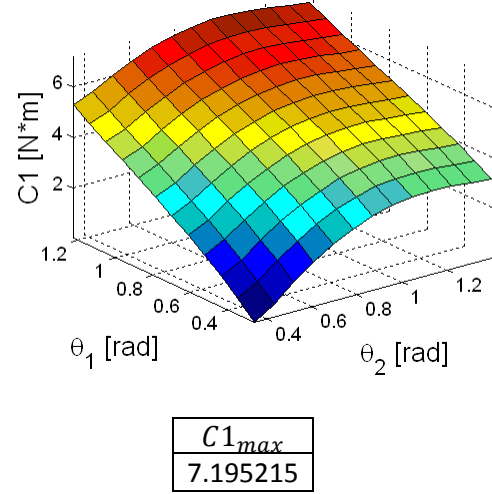
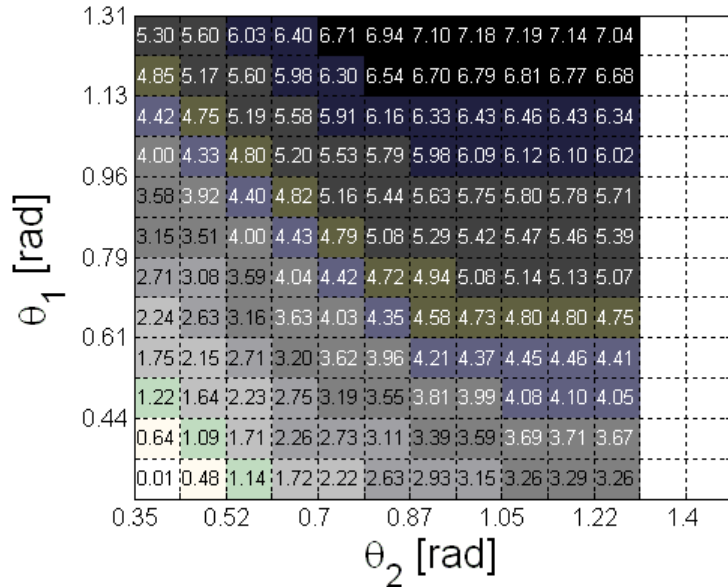


The Exoskeleton

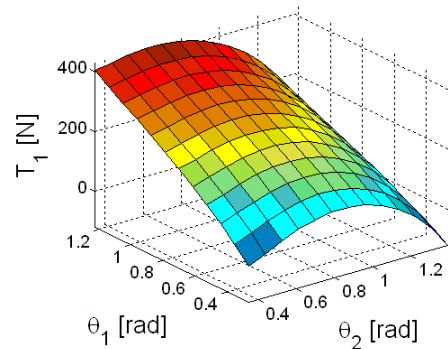
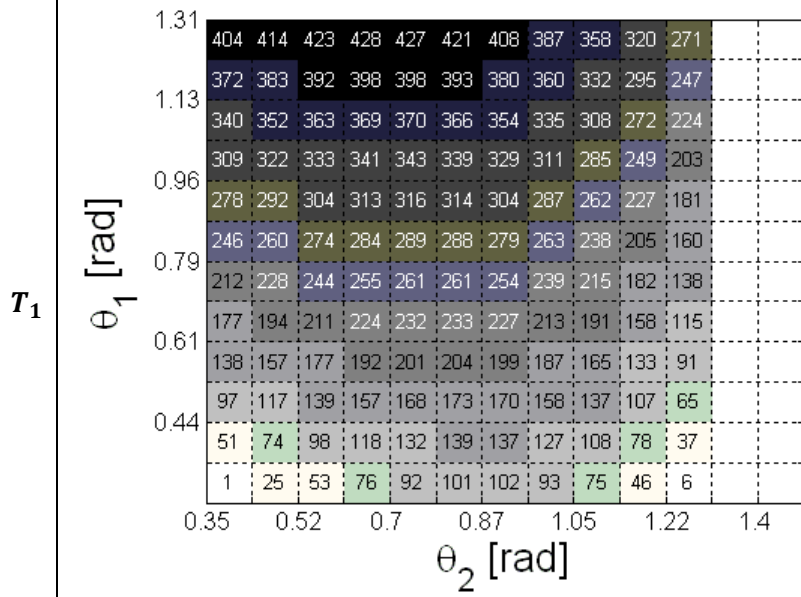
SIMULATION 2C: $T_{lim} = INF$ & \hat{K}_{10}

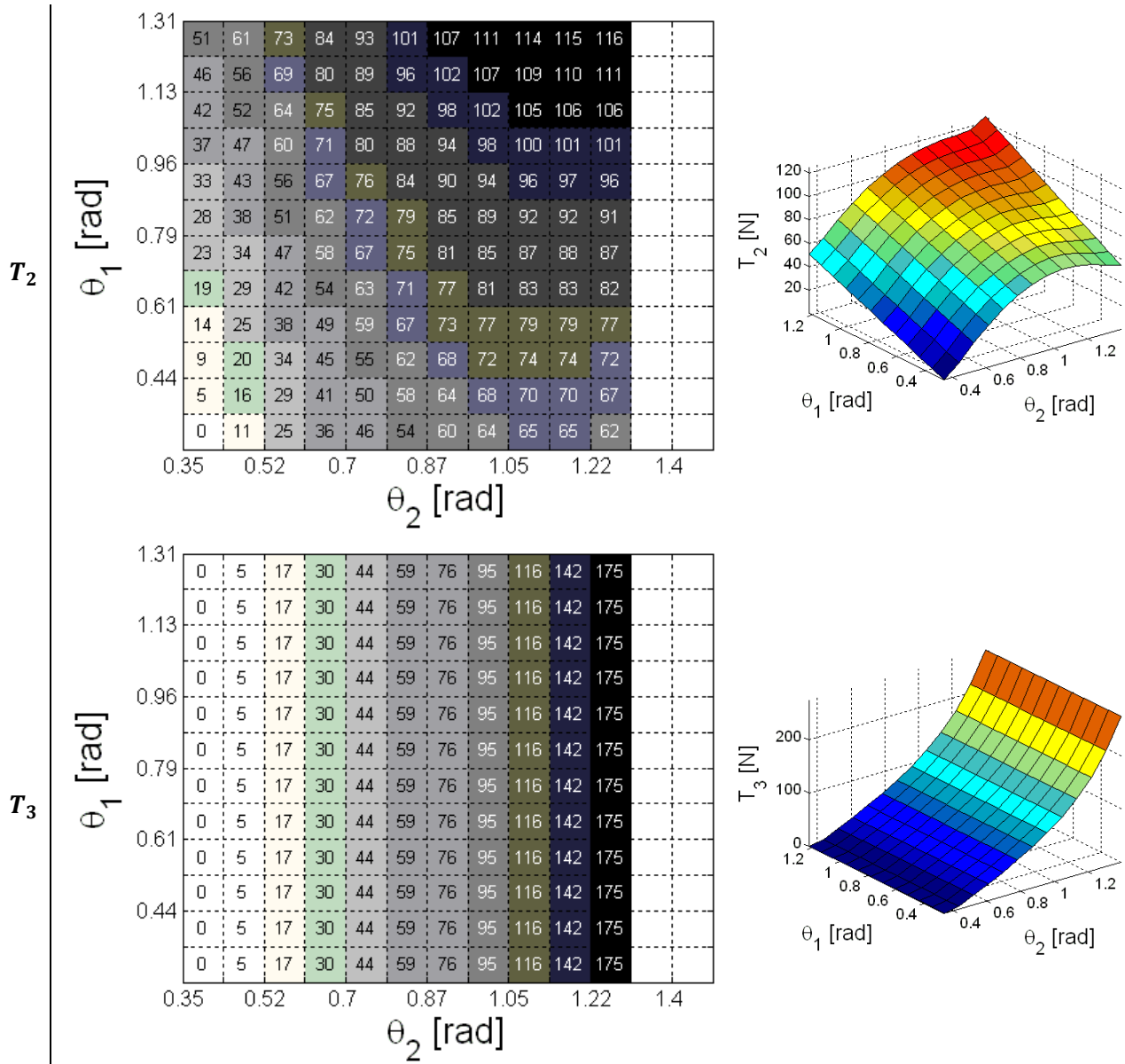


Reactive torque acting on the first joint: C_1



The Three Tendon Tensions





From simulation 2a to simulation 2c all the information related to the configurations were reported, similarly to the previous simulation. The results related to the simulations with $T_{lim} = 300$ were not reported here because already shown in the first four simulations and in particular in simulation 1a.

Third simulation: 2DoF vs. 3DoF

This last simulation shows the differences between two devices actuated respectively by three and two degrees of freedom. Due to the particular structure of the device, the value of the reactive torques and forces increases with the number of degrees of freedom. A link perceive a certain torque applied on by the following one; to compensate this effect an higher value of tendon tension is needed in order to actuate the joint and as a consequence bigger tendon tensions contribute to generate a bigger reactive force on the previous link. The reduction of the number of degrees of freedom could be an alternative solution to keep small values of torques and tensions. It is important to underline that not all the tasks can be accomplished with only two degrees of freedom, it is then mandatory to understand the feasibility of this strategy in the specific case. Figure 129 compares the two and three DoF *operating areas*, obtained with the same values of T_{lim} and \hat{K} .

Also in this third simulation the following informations were provided:

- Tendon configurations. The schematic representation of the passage of the tendons through the links of the structure.
- Behaviour of the reactive torque acting on the first joint represented both as a 3-D graph and with the *operating area* graph. Each cell of the operating area graph contain the value of the reacting torque in the specific configuration of θ_1 and θ_2 .
- Maximum value of the reactive torque inside the *operating area*.
- Behaviour of the three tendon tensions represented both as a 3-D graph and with the *operating area* graph.

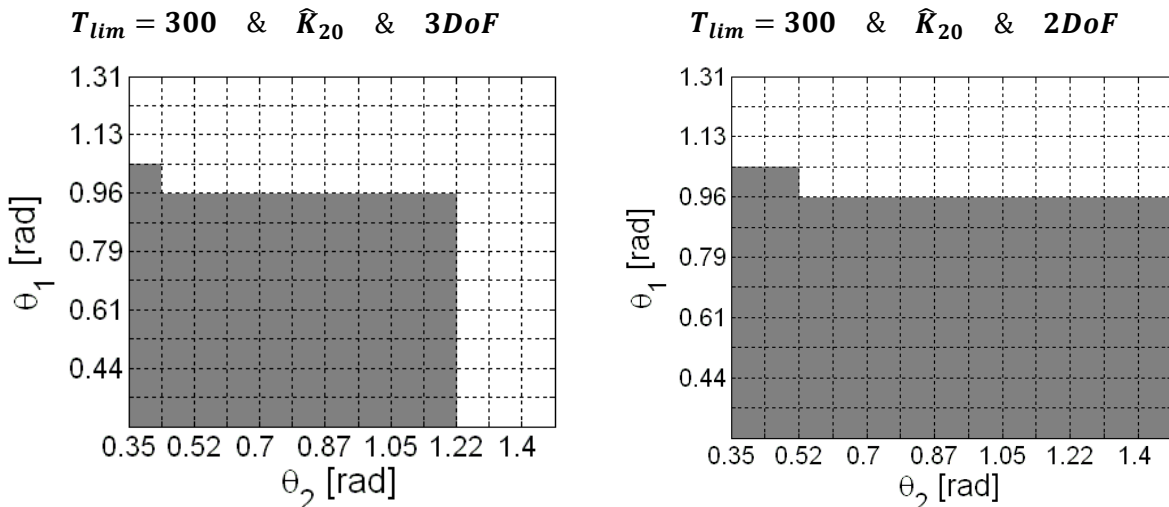
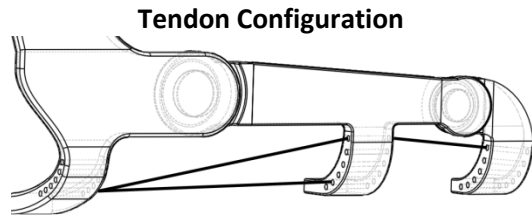


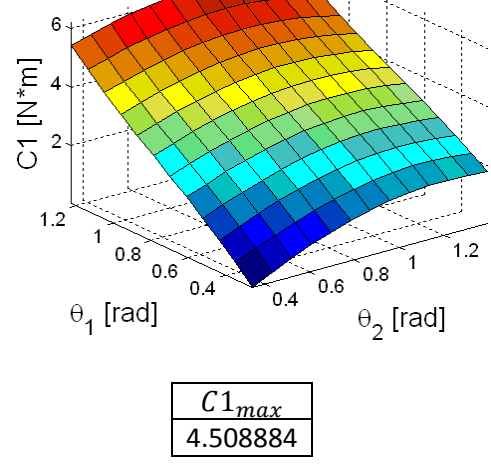
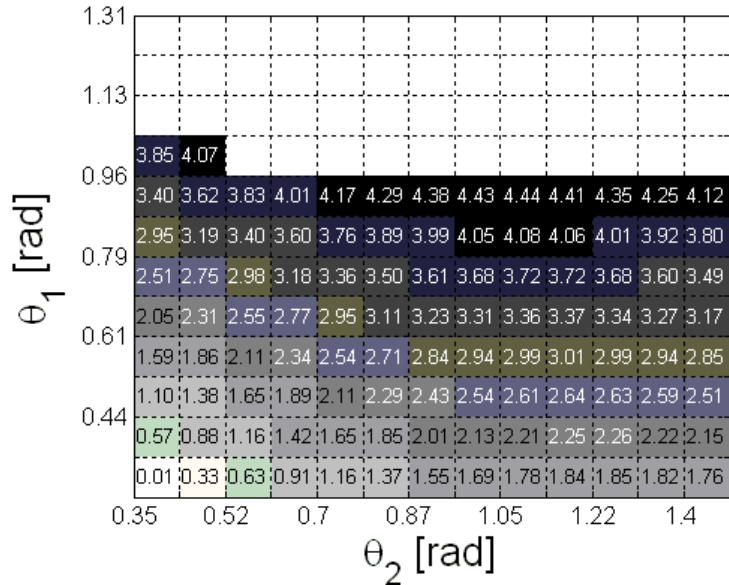
Figure 129: Comparison among the two *operating areas* of the simulation 3

The Exoskeleton

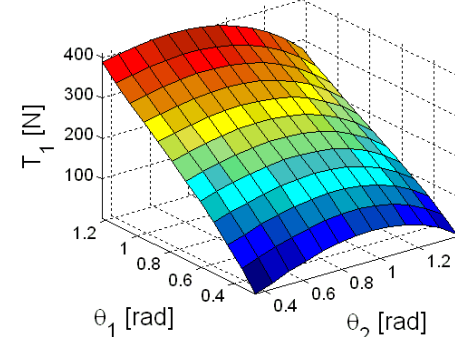
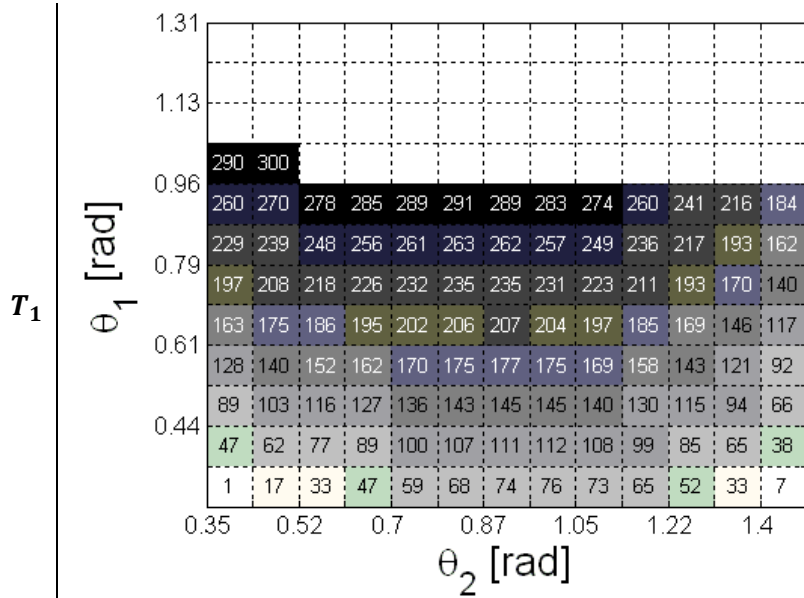
SIMULATION 3: $T_{lim} = 300$ & \hat{K}_{20} & 2Dof

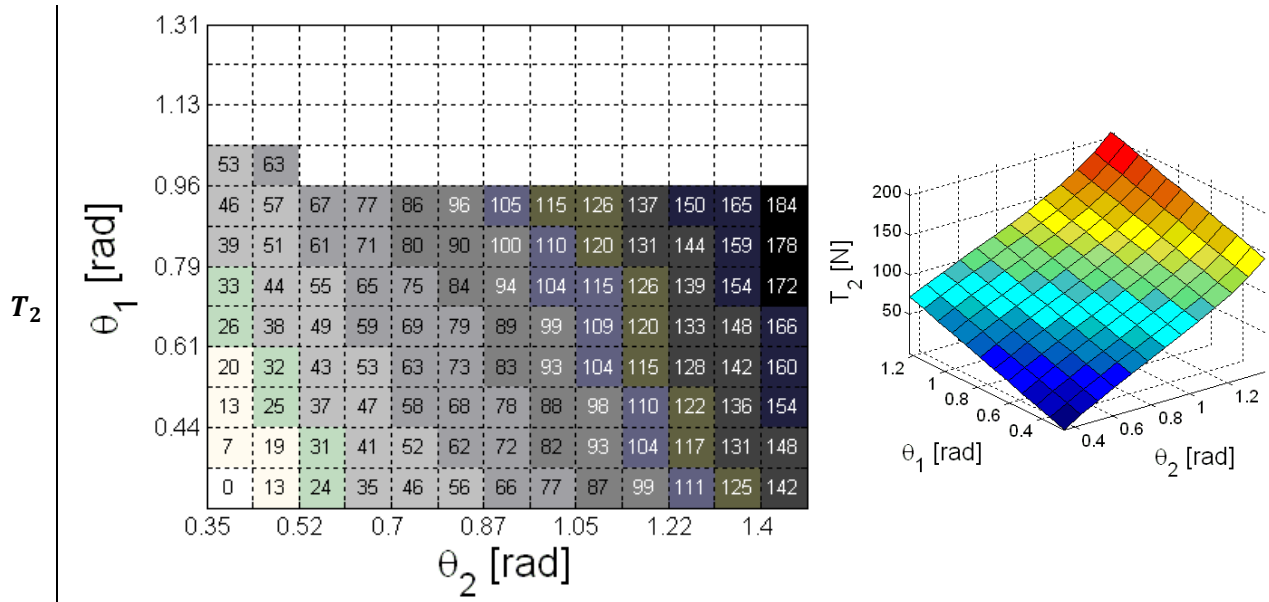


Reactive torque acting on the first joint: C_1



The Three Tendon Tensions





Simulation 3 shows the information related to the 2DoF solution, while that related to the 3DoF solution was already reported in simulation 1b. As it could be seen, both the 2DoF *operating area* and the peak value of reactive torque show better results with respect the 3DoF one. As already said, the reduction of number of DoF is not always applicable, but these results underline the importance of reducing the complexity of the device as much as possible, avoiding useless (or not so useful) DoFs.

Modified Optimization of the tendon configuration

The previously studied optimization method for the tendon configuration distinguished, for each point of the joint space, between only two different states of the device:

- The device can provide the tensions needed; $T < T_{\lim}$
- The device cannot provide the tensions needed; $T > T_{\lim}$

Due to the high values of tensions needed, as it could be seen in the previously reported results, this classification could be too stringent. It was therefore decided to introduce an additional intermediate condition that takes into account the possibility of partially actuate the device. For example, if a specific position requires $T_i = 2 \cdot T_{\lim}$, it can be decided to provide the maximum possible tension $T_i = T_{\lim}$ granting only the 50% of the actuation needed. In this way it is possible to augment the operative areas granting a portion of the power needed in the most critical zones. This strategy could be easily applied in the specific case of the hand exoskeleton, but it cannot be suitable for all the typologies of devices. In the specific case of exoskeleton, if the device grants a portion of the actuation needed, the remaining part has to be provided by the human being; however the remaining part always results smaller than the entire amount required without the exoskeleton. On the contrary it is mandatory to grant every time the whole actuation power for other typologies of devices; in these cases this solution cannot be applied. The three new states are the following:

- The device can provide the entire tensions needed; $T < T_{\lim}$
- The device can provide only one part of the tensions needed; $T_{\lim} < T < T_{\lim} \cdot (100/\text{Comp})$
- The device cannot provide the tensions needed; $T > T_{\lim} \cdot (100/\text{Comp})$

Where Comp is the minimum percentage of compensation required. In this strategy *operating area* is the convex surface, function of the bending angles, in which the tendon tension T_i results to be positive and the percentage of compensation is greater than the previously chosen minimum value Comp.

The Exoskeleton

Figure 130 shows an example of the modified area: in this example Comp is equal to 33. At this point it is necessary to introduce a new quality factor, able to take into account the modifications introduced. It was decided to calculate the integral of the tensions percentages inside the new operating area. The goal is to maximize this new quality factor. It is important to underline that the integral could grow up for two reasons: first the enlargement of the operation area and then the higher percentages of compensation inside the operating area. This new quality factor considers therefore both the size of the area and the actuation capabilities. In fact the optimal solution could be a configuration that grants a very wide operating area with low percentages of actuation capabilities or a set of parameters that provides a smaller operating area with higher compensation percentages.

Results

Also in this case a large number of simulations were performed changing the tunable parameters in a very similar way to the previously presented simulations. The same considerations and simplifications in terms of wire holes characteristics, friction and soft constraint remain valid and applied. It was decided to avoid the repetition of several examples because the main considerations were already provided. On the following part only a single simulation was reported in order to understand the main consequences of this optimization strategy. Also in this case the following information were provided:

- The behaviour of the reactive torque applied on the first joint in terms of trend and maximum value. This information was shown into two graphs. On the left the values of torque, obtained into a certain configuration, are inserted in each cell of the operating area graph; a gradient coloration allows to more easily understanding the trend. On the right a 3D graph shows the trend of the torque on the whole working space.
- The behaviour of the three tendon tensions. Unlike the previous graph, the percentages of the actuation that the device can provide are shown in each cell of the grid of the graph, instead of the relative value of tendon tension.
- Tendon configurations. It is the schematic graphical representation of the passage of the wires through the different links of the robotic structure.

In the following simulation were imposed a tension limit equal to 100N and a minimum percentage of compensation equal to 33%.

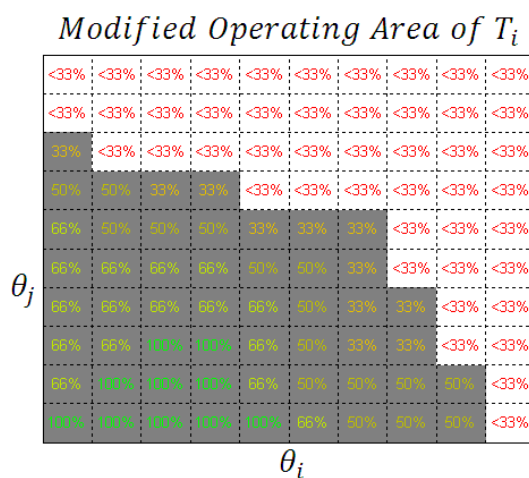
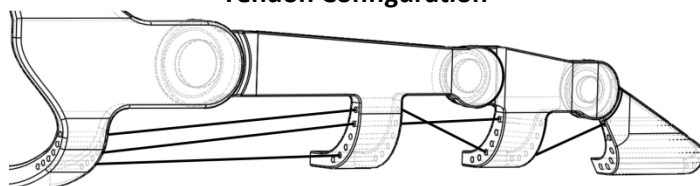


Figure 130: Modified operating area. In each cell the percentage of compensation guaranteed is reported.

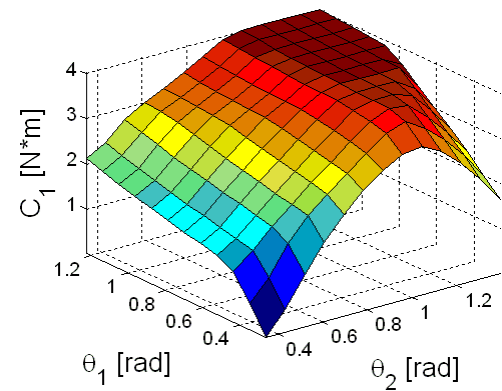
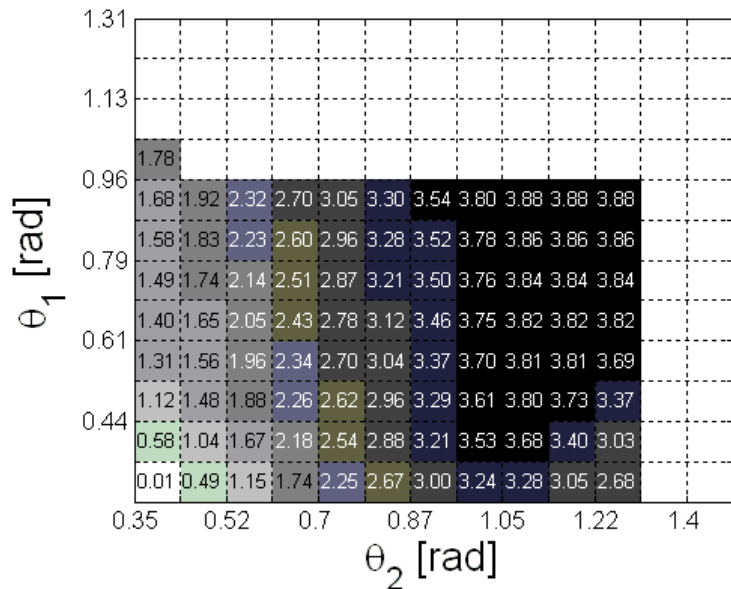
The Exoskeleton

SIMULATION 4: MODIFIED OPTIMIZATION

Tendon Configuration

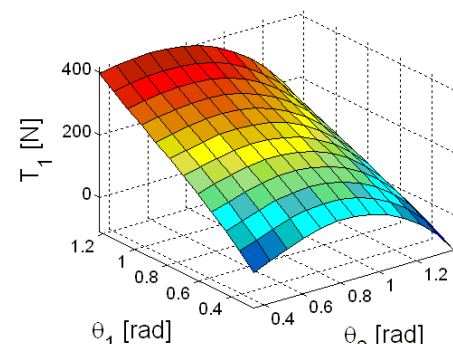
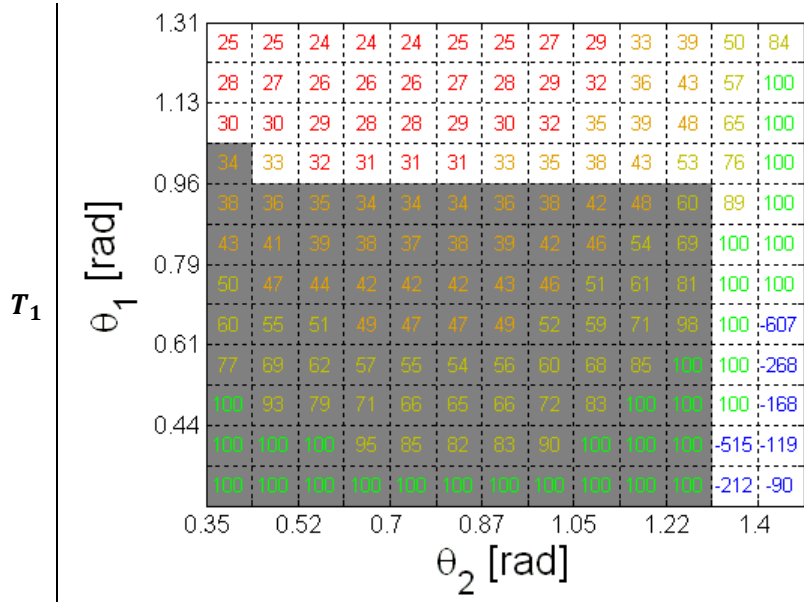


Reactive torque acting on the first joint: C_1

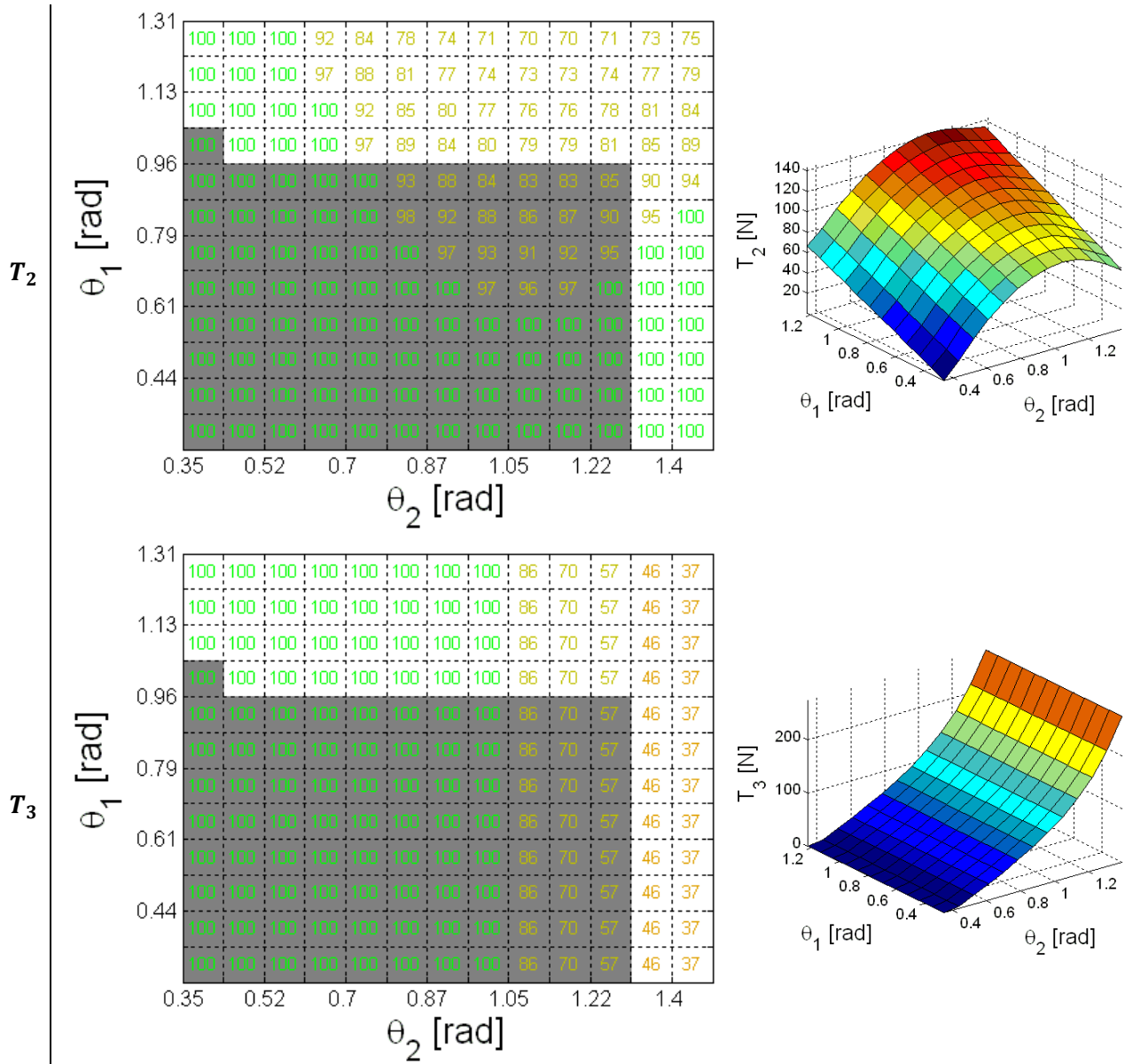


C_{1max}
3.8812

The Three Tendon Tensions



The Exoskeleton



Simulation 4 shows the information related to the modified optimization solution. As already said, a limit tension equal to 100N and a minimum compensation percentage equal to 33% were chosen. It means that the maximum acceptable tension to be partially compensated it is equal to 300N; therefore the more significant interpretation of the result of this last simulation has to be compared with the results obtained during simulation 1 (where $T_{\text{lim}} = 300$). The obtained *operating area* of this last simulation is bigger than all those relating to simulation 1 and at the same time the obtained reactive torque acting on the first joint is the smallest among all the obtained results (except from simulation 2a). The partial compensation of this strategy grants a large area and at the same time generates small internal forces, which cause lower reactive torques on the joints. The back of the medal of this strategy is that, granting only a percentage of the true actuation needed, it is very task dependant; in case of an hand exoskeleton device, the fatigue is not completely eliminated, but only partially reduced.

Observations

At this point, after all the results coming from the study and the optimization, it was possible to proceed to create a first prototype of this wire actuated solution. The mechanical structure of this second solution was created by means of DMLS (Direct Metal Laser Sintering) technology. As regards the tendons, it was chosen to utilize Dyneema wires already used for the previous proposed solution due to their high performances. Figure 131 shows the operator hand acting on the exoskeleton. All the obtained results from simulation do not guarantee an actuation on the whole working space. If all the *operating area* is smaller than the working space, it means that the solution does not grant an actuation on the entire range of movements of the human hand, helping only a portion of the motion. It has to be underlined that outside the operating area the device can still provide torques assisting the human hand, though in a percentage which could be very small, but still different from zero. Another big problem is related to the values of reactive torques acting on the joints: all the obtained values result very high and hardly sustainable by a structure which aims to be small enough to be embedded into a so tight space like the EVA glove.

In order to fully understand the feasibility of the proposed solution was mandatory to analyze the effects of forces and torques acting on the structure. A Finite Element Method (FEM) analysis was performed; this study allows to calculate the magnitude of the internal stresses generated by the internal and external forces. This tool allows to obtain the best value of the parameters related to the most critical geometrical dimensions and to understand the typology of structural material able to tolerate all the solicitations. The entire structure is subjected to various stress caused by the interaction with the external world. In particular those effects result to be greatly amplified in correspondence of the MCP joint, which is the most critical part of the whole device. The asymmetric design of this specific part of the exoskeleton means that, in addition to the compression stress, shear stresses were generated.

It was decided to investigate the effect acting on the “one-piece” joint solution (already shown in Figure 122). Two dimensions of the coupling are mainly involved in the stress calculation: the diameter of the internal pin and the thickness of the two surfaces of the joint. During the FEM analysis the values of those parameters were changed in order to appreciate the behavior of the stress and to be able to compare results related to different parameter configuration. Figure 132 show some examples of the results gathered from tests changing the two dimensions previously described. The obtained results confirmed some doubt related to the physical realization of this concept of device. Also considering the best wire configurations, the internal forces generated by the interaction with the actuators and the glove, result to be too high to be sustained by the structure and at the same time to grant high level of



Figure 131: Operator hand and exoskeleton; top view (left) and side view (right)

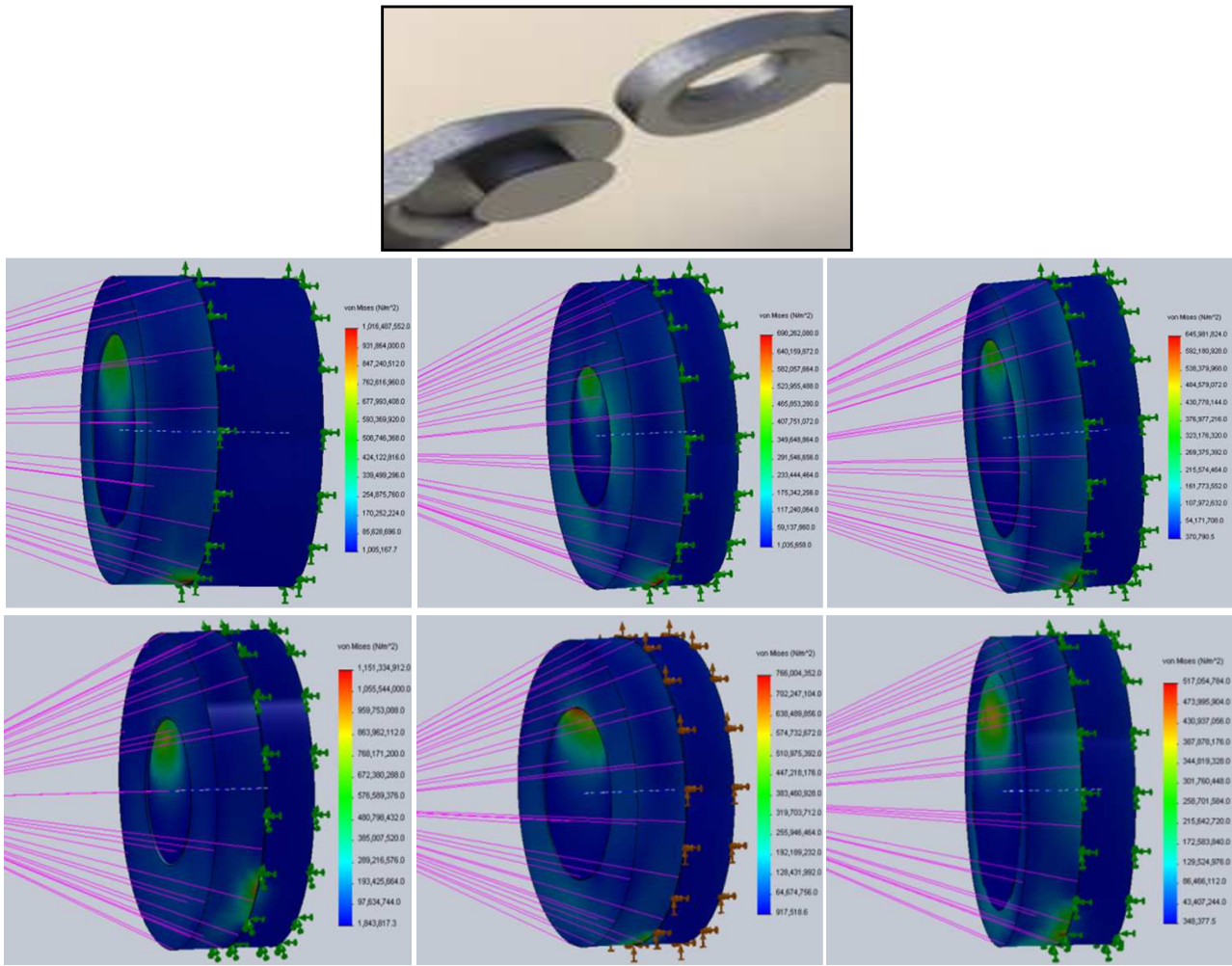


Figure 132: Some examples of the stress analysis of the joints in which the thickness and diameter of the pin and hole were changed to compare the stress results

safety for the operator. It is mandatory relax some constraints, for example those related to the dimensions and weight, in order to be able to design a truly feasible device.

The Double Parallelogram Solution

The results related to the wired actuated solution coming from the previous study and optimization show that this typology of actuation results hardly applicable. If on the one hand the wire solution is the best in terms of reduced dimension and weight (as already explained) on the other hand the reduced dimension of this device ensure that the tendon tensions have every time a very small arm. In order to be able to generate the magnitude of required torques, with so short arms, the tendon tensions have to be very high. High values of tendon tensions cause high requirements in terms of actuators and high stress on the structure (e.g. the reactive torques acting on the joints).

The second concept of proposed exoskeleton tries to solve this inconvenient partially neglecting the problems related to dimensions, against an increased importance of internal stress and a completely different transmission of movement: bidirectional actuation with double parallelogram mechanism.

The Exoskeleton

Bidirectional actuation is a symmetric transmission which generates movements both in flexion and extension; usually it results to be bigger than the single effect but it has the advantage of not relying on a passive element (e.g. elastic elements) to accomplish one of the two movements, overcoming problems related to non idealities and unpredicted behaviour.

The double parallelogram mechanism, shown in Figure 133 is a structure that generates a virtual joint, rotating around an instantaneous centre which has to coincide with that of the human hand. The correct dimensioning of the elements that compound the structure grants the correctness of the movements performed. This was the guiding factor in determining the length of each link and the initial angle between the links. This also means that the device has to be partially custom made due to the large amount of human variation in hand size. Some examples of exoskeleton made utilizing a four bar mechanism structure can be found in literature: Shield [147], Fang [148] and Choi [149] exoskeletons are probably the most important examples of this structural solution.

Using this structure both the good positioning of the center of rotation and the will to maintain the palm as free as possible are satisfied. Due to the compact structure of the human hand and the high number of DoF, a device that could be placed entirely on the back of the finger is the best solution to maintain the grasping capability. The downside of this solution is that dimensions are bigger than the previous one, in particular considering the back of the hand. There are no chances to embed this typology of device into an EVA glove without a complete redesign of the glove itself. For this reason this version of device is planned to be placed outside the EVA glove and, if possible, realized in order to be attached and detached quickly and easily. In this way the operator can perform tasks that require high force and produce high fatigue wearing the exoskeleton, removing it to accomplish tasks that need to insert the hand into tight spaces. It is important to underline that this solution allows to overcome completely problems related to the finger crotch due to the placement of all elements on the back side of the hand, and moreover it results to be finger independent. Unlike the previous solution, this strategy can be applied on each finger of the hand independently from the relative position inside the hand, without modifications. The above discussion provides a series of motivations for each choice and a functional idea of each element of the future physical device. This means that a family of devices could be unified under the same previously treated "*guidelines*", independently from the specific solutions. The number of DoF of the device, the kinematic constraints between joints (e.g. the soft constraint), the position of the actuation system, are some examples of possible variations that follow the main guidelines described, each of them with different advantages and disadvantages.

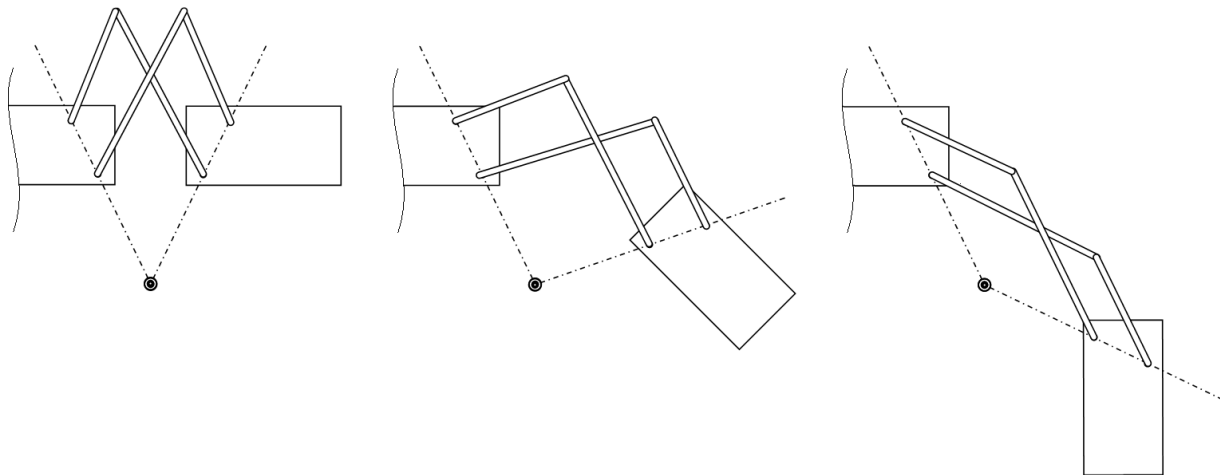


Figure 133: The double parallelogram mechanism

The Exoskeleton

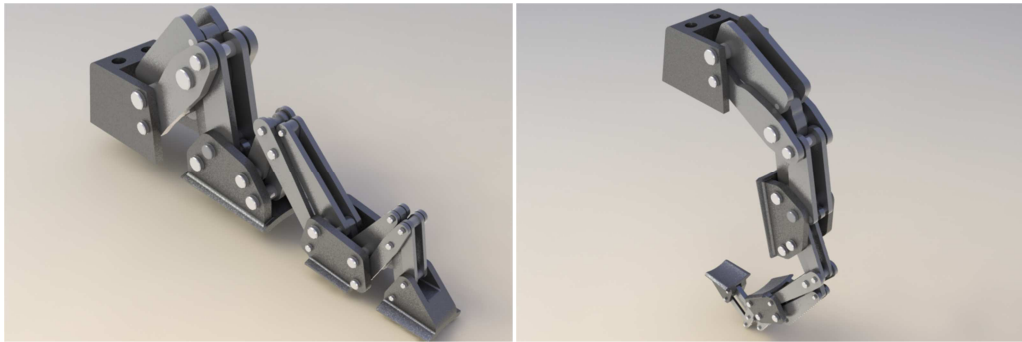


Figure 134: Second exoskeleton concept design.

The second concept of exoskeleton is shown in Figure 134; it is based on the main guidelines previously reported. It is composed by three joints, neglecting the abduction one kept it fixed into a position. In order to simplify the future actuation it was decided to simplify the concept introducing a kinematic ratio between the three joints, obtaining a finger exoskeleton with only one DoF. In order to reduce the number of degrees of freedom of the device, the three phalanges were coupled through additional four-bar transmissions dimensioned in order to guarantee the correct kinematic ratio. Figure 135 shows in detail the elements that couple the proximal and the middle phalanx. It is necessary to decide a specific kinematic ratio between the three phalanges in order to guarantee a natural movement during the operator's work. Once defined the behaviour the three joints have to perform, the dimensioning of the various length of each element has to be performed. It was decided to impose the kinematic constraints in order to guarantee an emulation of the sphere grip during the exoskeleton movements; on the basis of the study performed on the human hand and grasps the following two ratio were chosen:

$$\theta_{PIP} = \frac{3}{4}\theta_{MCP} \quad \theta_{DIP} = \frac{2}{3}\theta_{PIP} \quad 84$$

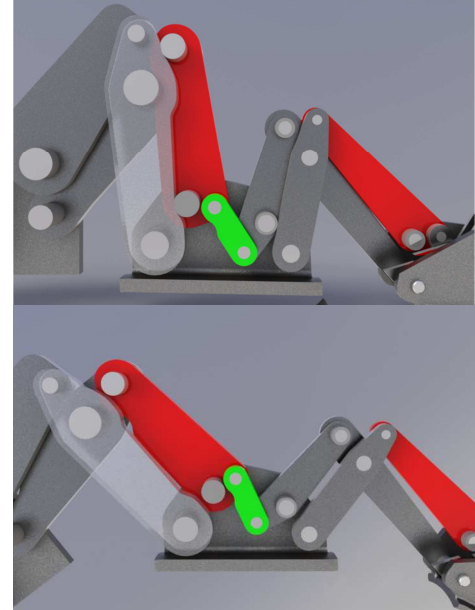
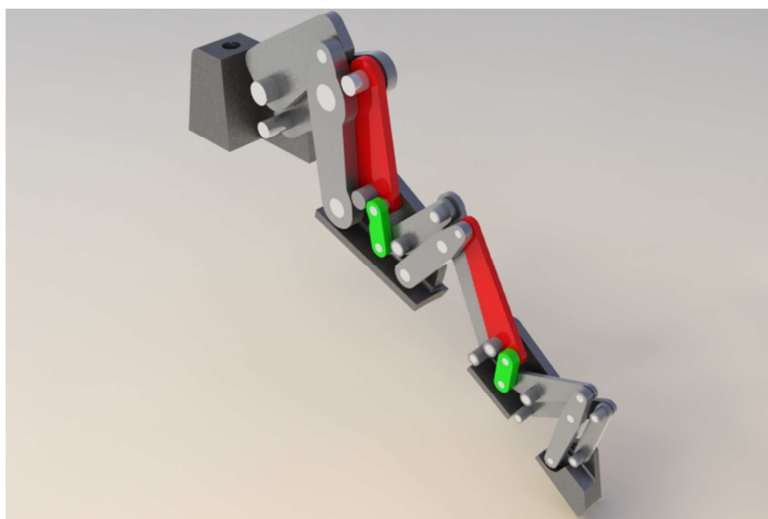


Figure 135: Detail of the kinematic constraints between two adjoining joints.

The Exoskeleton

Figure 136 shows six pictures of the first prototype of “double parallelogram exoskeleton” during the flexion movement. It could be appreciate that, acting the MCP joint of the exoskeleton, the movement is transmitted to the PIP and then to the DIP joint through the previously described kinematic ratios.

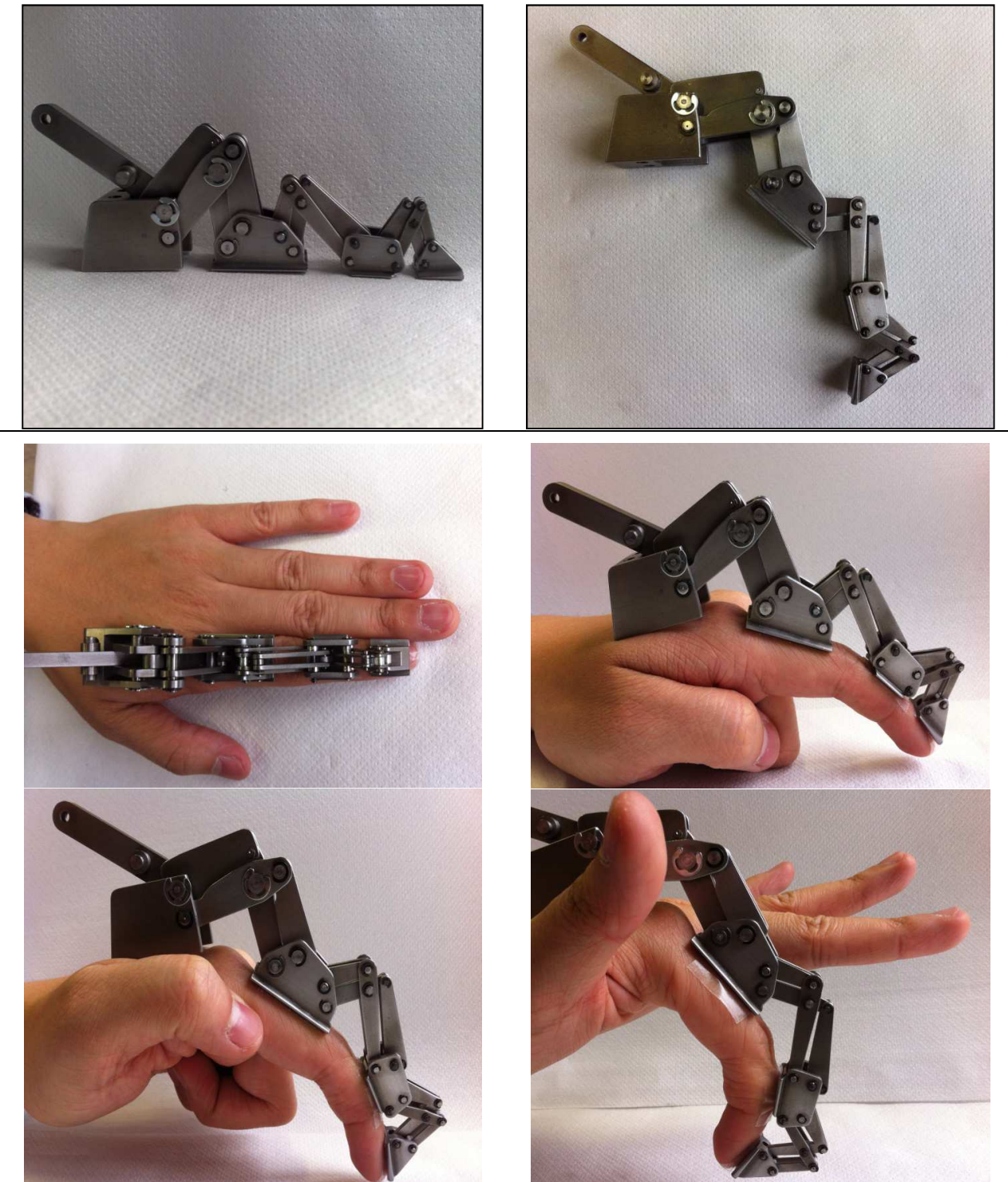


Figure 136: First prototipe of the double parallelogram exoskeleton during the flexion movement

The Exoskeleton



Figure 137: First prototype of the double parallelogram exoskeleton coupled with the EVA glove

Finally Figure 137 show the final prototype of the “double parallelogram exoskeleton” coupled with the EVA glove. With respect the first version already shown in Figure 136 the part placed on the back of the hand has been changed with a new one. This new element host a bevel gear that connect the exoskeleton with the rotary brushless motor placed on the back of the hand.

CHAPTER 6:

“Ends are not bad things, they just mean that something else is about to begin. And there are many things that don't really end, anyway, they just begin again in a new way. Ends are not bad and many ends aren't really an ending; some things are never-ending.”

C. JoyBell C.

CONCLUSIONS

The work presented in this thesis aims to describe the preliminary analysis and a possible solution to the stiffness problem of the EVA spacesuits and gloves in particular. In order to overcome the negative effects caused by the multilayer structure and the internal pressurization of the EVA glove, an exoskeleton prototype has been designed. A series of preliminary studies had to be done before designing the structure in order to deeply understand the requirements related to this kind of devices and this very particular environment.

During the past few years, the total time of Extravehicular Activities performed by astronauts increased significantly. Future mission will require a spacesuit which is capable of performing zero gravity operations composed by many different tasks. This multi-role mission will require garment qualities which are not available in any currently EVA spacesuit today. Future spacesuits will have to provide excellent full body mobility, be extremely lightweight, robust and comfortable. Several problems come from the current spacesuits during space missions. The bulk and the stiffness of the pressurized EVA spacesuit glove are the major causes of reduced dexterity, lack of adequate tactility and overall hand fatigue; all of these drawbacks reduce the duration of EVAs. This has led NASA to organize a specific plan to improve EVA suits, and gloves in particular.

The first chapter of the thesis provides a chronological overview of the American and Russian EVA spacesuits; a particular attention is paid to the EVA gloves in order to understand how they are composed and built and the main reasons that cause the previously mentioned issues. Moreover a brief discussion about the tomorrow's EVAs needs has been provided. To fulfill all the needs, a hand exoskeleton which can be embedded inside the space suit EVA glove has been proposed as a possible solution to overcome the stiffness of the garment and to support human finger during its movements.

First of all it is essential to know the state of art of the technologies used in similar projects for different type of applications, in particular robotic hands and exoskeletons hands. A comprehensive survey on

Conclusions

literature related of both these fields is presented in the second chapter; moreover particular attention to type of actuators, sensors and transmission strategy has been paid. The two major issues in the design of a hand exoskeleton are represented by sensors and actuators. In the second part of the chapter advantages and disadvantages of different kind of sensor and actuators have been briefly reported. The outcome of this investigation shows that nowadays is very difficult to design a hand exoskeleton that can be embedded completely inside the astronaut's glove due to strong technological limitations. The big size and the low power density of the existing actuators are obstacles in the design, since the requirement of dimensions and weight of the project are very important. Although different types of actuators are small enough to satisfy the requirements, they do not provide enough power to properly actuate the structure designed to overcome the stiffness generated by the EVA glove. Despite all the problems, classical electrical motors seem to be the most reliable option. Electrical motors do not have the power density required for direct placement on the back of the finger, or the dimension for directly driving those joints; these systems will continue to rely on performance-sapping transmissions and gear reduction, with actuators located on the back of the hand, forearm or elsewhere. An advance in actuation technology is a mandatory step to realize a device that today is beyond the edge of current technologies.

The exoskeleton hand will interact with two different objects: the human hand and the EVA glove. Both of them provide different constraints and so a deep knowledge of these two elements is mandatory.

The hand is the human best tool for handling, grasping, drawing, writing and many other tasks; in order to mimic it, the structure of the mechanism must have the same proportions, dimensions and capabilities. The third chapter provides a comprehensive study on the human hand as a preliminary step towards the development of any application or device to be interfaced with the human being, which needs to emulate and imitate the human hand shape and functionality, such as the exoskeleton. In the first part of the chapter an anatomical study of the human hand has been performed. The most important biometric parameters, such as anthropometric lengths, range of forces, torques and velocities, maximum displacement, intra and inter constraints have been gathered from several studies. Then, an overview on the various categories of grips and pinches has been reported. Moreover, a generalized model of the human hand is presented. The kinematic analysis of the human hand has been investigated in detail using the modified Denavit-Hartenberg convention to obtain the parameters, matrices and equations both for the direct and inverse kinematics. Finally the dynamics of a single finger has been obtained by means of the Euler Lagrange method.

The EVA glove is realized to protect from the harsh outer space conditions strongly reducing hand performances, in particular dexterity, tactile perception, mobility and strength. It is mandatory to understand the effects that this glove generates to the human hand as a consequence of its multilayer structure and internal pressurization. Chapter four provides results coming from experimental tests performed on a real Russian space glove, model Orlan-DM. First of all experimental data regarding the performances in terms of hand and finger strength reduction and hand fatigue augmentation have been obtained both in pressurized and unpressurized conditions. The main peculiarity of this study with respect to other similar works is the choice to investigate the left hand instead of the right one. The left hand results to be the "weaker hand" for a great percentage of the human beings, but covers a fundamental role in any kind of job and activity. Usually, in order to perform tasks that involve both hands, a human being uses its main hand to execute precision works (e.g. pull the trigger of a drill, turn a screwdriver), whereas utilizes his weak hand to perform power tasks (e.g. hold in position objects). The results show that the effects, especially in non-pressurized conditions, are strongly dependent on the specific executed task. Moreover the performances in pressurized conditions result to be dramatically reduced. Then it was important to quantify the stiffness of the EVA glove measuring the torque applied by the glove on each articulation of the human hand. The knowledge of the magnitudes of the torques is

Conclusions

fundamental in an exoskeleton design because it became an important constraint on the elements that compound the device. Two different series of tests, with two different measurements setups, have been performed. In the first one a thin distributed pressure sensor has been placed on the whole hand, while in the second one a robotic finger probe, equipped with accelerometers, has been utilized to achieve the goal. It can be noticed that the pressurization sharply increases the stiffness of the glove, moreover it increases further for big flexion angles, when the rigid or semi-rigid elements of the glove touch each other and the layers fold on each other.

In the fifth chapter three different possible options for an index exoskeleton have been proposed and all the steps toward their structure design were presented. The first two prototypes underlie the same actuation concept: the single effect wire actuation. This is an asymmetric transmission system made up by a series of wires that actuate the structure only in one direction, while the recall movement is effected through passive elements, e.g. elastic components. This kind of actuation system has been chosen in order to minimize the dimensions and weight of the final device. However, its compactness and small dimension causes very short arms of the forces transmitted by the tendons, and consequently low torques. In order to increase the values of the torques applied by the exoskeleton on the glove, the tendon tension, and then the power of the actuators, had to be increased. However stronger actuators mean higher stresses on the structure. Moreover this kind of actuation strategy generates a superposition effect between all the joints of the robotic structure: this makes the control of the system very difficult.

The third prototype relies on a completely different mechanical scheme based on the double parallelogram mechanism. The motion transmission in this case is performed by means of rigid linkages, instead of wires, and so a bidirectional actuation is now possible. Bidirectional actuation generates movements both in flexion and extension; usually it results to be bigger than the single effect. This actuation strategy tries to solve the inconvenient previously explained, partially neglecting the problems related to dimensions against an increased importance of internal stresses. Due to its dimension this solution cannot be embedded inside the EVA glove, while it has to be attached on the back of the hand. The peculiarity of the proposed architecture with respect to similar devices is that the dimensions of each single element have been optimized in order to reproduce a very specific movement: the cylindrical grasp.

Future Work

Since this thesis has dealt with a complex project, with a number of multidisciplinary open questions, then some aspects could be investigated more thoroughly, towards the development of a whole hand exoskeleton device.

For examples all the tests performed on the EVA glove were limited to one single EVA glove model. Moreover the physiological tests on the hand performances involved only four different tasks. Therefore it would be interesting to expand the experiments made on the Orlan-DM to other EVA gloves, increasing the number of tasks and with more subjects as well.

Moreover there is still a lot that remains to be done, especially in relation with actuators and structure. For what concern the actuators, new technologies need to be developed and implemented, in order to guarantee better performances with reduced dimensions. For example, a possible future actuating strategy could involve the usage of shape memory alloys and polymeric actuators, as their potentiality appear very promising.

Regarding the structure, first of all the single finger architecture has to be replicated to the other fingers in order to realize a complete hand exoskeleton. Particular attention has to be devoted to the thumb, whose complex kinematic scheme has to be properly analyzed.

Conclusions

Moreover, as the third prototype actuates a single degree of freedom with a very specific kinematic ratio between the phalanges, performing a single grip, a possible future development could be the realization of a device able to perform different grips and pinches. For example, under-actuations is a possible interesting solution, generating synergic movements that model the device as a function of the shape of the grasped object.

APPENDIX:

ELEMENTS OF ROTO-TRANSLATION MATRIX Q

$$Q_i = \begin{bmatrix} Q_{11} & Q_{12} & Q_{13} & Q_{14} \\ Q_{21} & Q_{22} & Q_{23} & Q_{24} \\ Q_{31} & Q_{32} & Q_{33} & Q_{34} \\ 0 & 0 & 0 & 1 \end{bmatrix}$$

Four Fingers Matrix Q_i

The subscript i related to the specific finger was omitted; $c\theta_j$ and $s\theta_j$ stand for cosine and sine of θ_j , respectively.

$$\begin{aligned} Q_{11} &= c(\theta_{PIP} + \theta_{DIP}) \left[c\theta_{MCP_{f/e}} (c\theta_{CMC} c\theta_{MCP_{a/a}}) - s\theta_{CMC} s\theta_{MCP_{f/e}} \right] + \\ &\quad - s(\theta_{PIP} + c\theta_{DIP}) \left[s\theta_{MCP_{f/e}} (c\theta_{CMC} c\theta_{MCP_{a/a}}) + s\theta_{CMC} c\theta_{MCP_{f/e}} \right]; \\ Q_{12} &= -s(\theta_{PIP} + \theta_{DIP}) \left[c\theta_{MCP_{f/e}} (c\theta_{CMC} c\theta_{MCP_{a/a}}) - s\theta_{CMC} s\theta_{MCP_{f/e}} \right] + \\ &\quad - c(\theta_{PIP} + \theta_{DIP}) \left[s\theta_{MCP_{f/e}} (c\theta_{CMC} c\theta_{MCP_{a/a}}) + s\theta_{CMC} c\theta_{MCP_{f/e}} \right]; \\ Q_{13} &= c\theta_{CMC} s\theta_{MCP_{a/a}}; \\ Q_{14} &= \left[c\theta_{MCP_{f/e}} (c\theta_{CMC} c\theta_{MCP_{a/a}}) - s\theta_{CMC} s\theta_{MCP_{f/e}} \right] \left[L_{3_x} c(\theta_{PIP} + \theta_{DIP}) - L_{3_y} s(\theta_{PIP} + \theta_{DIP}) + L_1 + L_2 c\theta_{PIP} \right] + \\ &\quad - \left[s\theta_{MCP_{f/e}} (c\theta_{CMC} c\theta_{MCP_{a/a}}) + s\theta_{CMC} c\theta_{MCP_{f/e}} \right] \left[L_{3_x} s(\theta_{PIP} + \theta_{DIP}) + L_{3_y} c(\theta_{PIP} + \theta_{DIP}) + L_2 s\theta_{PIP_{f/e}} \right] + \\ &\quad + L_{3_z} (c\theta_{CMC} s\theta_{MCP_{ab/ad}}) + L_0 c\theta_{CMC}; \end{aligned}$$

Elements of Roto-translation Matrix Q

$$\begin{aligned}
Q_{21} &= s\theta_{MCP_{a/a}}c\theta_{MCP_{f/e}}c(\theta_{PIP} + \theta_{DIP}) - s\theta_{MCP_{a/a}}s\theta_{MCP_{f/e}}s(\theta_{PIP} + \theta_{DIP}); \\
Q_{22} &= -s\theta_{MCP_{a/a}}c\theta_{MCP_{f/e}}s(\theta_{PIP} + \theta_{DIP}) - s\theta_{MCP_{a/a}}s\theta_{MCP_{f/e}}c(\theta_{PIP} + \theta_{DIP}); \\
Q_{23} &= -c\theta_{MCP_{a/a}}; \\
Q_{24} &= s\theta_{MCP_{a/a}}c\theta_{MCP_{f/e}} \left[L_{3_x}c(\theta_{PIP} + \theta_{DIP}) - L_{3_y}s(\theta_{PIP} + \theta_{DIP}) + L_1 + L_2c\theta_{PIP} \right] + \\
&\quad -s\theta_{MCP_{a/a}}s\theta_{MCP_{f/e}} \left[L_{3_x}s(\theta_{PIP} + \theta_{DIP}) + L_{3_y}c(\theta_{PIP} + \theta_{DIP}) + L_{2t}s\theta_{PIP_{f/e}} \right] - L_{3_z}c\theta_{MCP_{a/a}}; \\
Q_{31} &= c(\theta_{PIP} + \theta_{DIP}) \left[c\theta_{MCP_{f/e}}(s\theta_{CMC}c\theta_{MCP_{a/a}}) + c\theta_{CMC}s\theta_{MCP_{f/e}} \right] + \\
&\quad +s(\theta_{PIP} + \theta_{DIP}) \left[c\theta_{CMC}c\theta_{MCP_{f/e}} - s\theta_{MCP_{f/e}}(s\theta_{CMC}c\theta_{MCP_{a/a}}) \right]; \\
Q_{32} &= -s(\theta_{PIP} + \theta_{DIP}) \left[c\theta_{MCP_{f/e}}(s\theta_{CMC}c\theta_{MCP_{a/a}}) + c\theta_{CMC}s\theta_{MCP_{f/e}} \right] + \\
&\quad +c(\theta_{PIP} + \theta_{DIP}) \left[c\theta_{CMC}c\theta_{MCP_{f/e}} - s\theta_{MCP_{f/e}}(s\theta_{CMC}c\theta_{MCP_{a/a}}) \right]; \\
Q_{33} &= s\theta_{CMC}s\theta_{MCP_{a/a}}; \\
Q_{34} &= \left[c\theta_{MCP_{f/e}}(s\theta_{CMC}c\theta_{MCP_{a/a}}) + c\theta_{CMC}s\theta_{MCP_{f/e}} \right] \left[L_{3_x}c(\theta_{PIP} + \theta_{DIP}) - L_{3_y}s(\theta_{PIP} + \theta_{DIP}) + L_1 + L_2c\theta_{PIP} \right] + \\
&\quad + \left[c\theta_{CMC}c\theta_{MCP_{f/e}} - s\theta_{MCP_{f/e}}(s\theta_{CMC}c\theta_{MCP_{a/a}}) \right] \left[L_{3_x}s(\theta_{PIP} + \theta_{DIP}) + L_{3_y}c(\theta_{PIP} + \theta_{DIP}) + L_2s\theta_{PIP} \right] + \\
&\quad + L_{3_z}(s\theta_{CMC}s\theta_{MCP_{a/a}}) + L_0s\theta_{CMC};
\end{aligned}$$

Thumb Matrix Q_0

The subscript $i=0$ related to the thumb was omitted; $c\theta_j$ and $s\theta_j$ stand for cosine and sine of θ_j , respectively.

$$\begin{aligned}
Q_{11} &= c\theta_{TMC_{a/a}}c\theta_{TMC_{f/e}}c(\theta_{MCP} + \theta_{IP}) - c\theta_{TMC_{a/a}}s\theta_{TMC_{f/e}}s(\theta_{MCP} + \theta_{IP}); \\
Q_{12} &= -c\theta_{TMC_{a/a}}c\theta_{TMC_{f/e}}s(\theta_{MCP} + \theta_{IP}) - c\theta_{TMC_{a/a}}s\theta_{TMC_{f/e}}c(\theta_{MCP} + \theta_{IP}); \\
Q_{13} &= s\theta_{TMC_{a/a}}; \\
Q_{14} &= c\theta_{TMC_{a/a}}c\theta_{TMC_{f/e}} \left[L_{2_x}c(\theta_{MCP} + \theta_{IP}) - L_{2_y}s(\theta_{MCP} + \theta_{IP}) + L_1c\theta_{MCP_{f/e}} + L_0 \right] + \\
&\quad -c\theta_{TMC_{a/a}}s\theta_{TMC_{f/e}} \left[L_{2_x}s(\theta_{MCP} + \theta_{IP}) + L_{2_y}c(\theta_{MCP} + \theta_{IP}) + L_1s\theta_{MCP_{f/e}} \right] + L_{3_z}s\theta_{TMC_{a/a}}; \\
Q_{21} &= s\theta_{TMC_{a/a}}c\theta_{TMC_{f/e}}c(\theta_{MCP} + \theta_{IP}) - s\theta_{TMC_{a/a}}s\theta_{TMC_{f/e}}s(\theta_{MCP} + \theta_{IP}); \\
Q_{22} &= -s\theta_{TMC_{a/a}}c\theta_{TMC_{f/e}}s - s\theta_{TMC_{a/a}}s\theta_{TMC_{f/e}}c(\theta_{MCP} + \theta_{IP}); \\
Q_{23} &= -c\theta_{TMC_{a/a}}; \\
Q_{24} &= s\theta_{TMC_{a/a}}c\theta_{TMC_{f/e}} \left[L_{3_x}c(\theta_{MCP} + \theta_{IP}) - L_{3_y}s(\theta_{MCP} + \theta_{IP}) + L_1c\theta_{MCP_{f/e}} + L_0 \right] + \\
&\quad -s\theta_{TMC_{a/a}}s\theta_{TMC_{f/e}} \left[L_{3_x}s(\theta_{MCP} + \theta_{IP}) + L_{3_y}c(\theta_{MCP} + \theta_{IP}) + L_{10}s\theta_{MCP_{f/e}} \right] - c\theta_{TMC_{a/a}}L_{3_z}; \\
Q_{31} &= s\theta_{TMC_{f/e}}c(\theta_{MCP} + \theta_{IP}) + c\theta_{TMC_{f/e}}s(\theta_{MCP} + \theta_{IP}); \\
Q_{32} &= -s\theta_{TMC_{f/e}}s(\theta_{MCP} + \theta_{IP}) + c\theta_{TMC_{f/e}}c(\theta_{MCP} + \theta_{IP}); \\
Q_{33} &= 0; \\
Q_{34} &= s\theta_{TMC_{f/e}} \left[L_{3_x}c(\theta_{MCP} + \theta_{IP}) - L_{3_y}s(\theta_{MCP} + \theta_{IP}) + L_1c\theta_{MCP_{f/e}} + L_0 \right] + \\
&\quad +c\theta_{TMC_{f/e}} \left[L_{t0_x}s(\theta_{MCP} + \theta_{IP}) + L_{t0_y}c(\theta_{MCP} + \theta_{IP}) + L_1s\theta_{MCP_{f/e}} \right];
\end{aligned}$$

EULER-LAGRANGE EQUATION COEFFICIENTS

$$[A][\ddot{\psi}] = [\mathbf{b}]$$

$c\theta_j$ and $s\theta_j$ stand for cosine and sine of θ_j , respectively.

$$\begin{aligned}
 A_{11} &= m_3 \left[(b_{3x}s\psi_3 + b_{3y}c\psi_3)^2 + (b_{3x}c\psi_3 - b_{3y}s\psi_3)^2 \right] + (m_4 + m_5)L_1^2 + I_3 \\
 A_{12} &= m_4L_1 [s\psi_3(b_{4x}s\psi_4 + b_{4y}c\psi_4) + c\psi_3(b_{4x}c\psi_4 - b_{4y}s\psi_4)] + m_5L_1L_2c(\psi_3 - \psi_4) \\
 A_{13} &= m_5L_1 [s\psi_3(b_{5x}s\psi_5 + b_{5y}c\psi_5) + c\psi_3(b_{5x}c\psi_5 - b_{5y}s\psi_5)] \\
 A_{21} &= m_4L_1 [s\psi_3(b_{4x}s\psi_4 + b_{4y}c\psi_4) + c\psi_3(b_{4x}c\psi_4 - b_{4y}s\psi_4)] + m_5L_1L_2c(\psi_3 - \psi_4) \\
 A_{22} &= m_4 \left[(b_{4x}s\psi_4 + b_{4y}c\psi_4)^2 + (b_{4x}c\psi_4 - b_{4y}s\psi_4)^2 \right] + m_5L_2 + I_4 \\
 A_{23} &= m_5L_2 [s\psi_4(b_{5x}s\psi_5 + b_{5y}c\psi_5) + c\psi_4(b_{5x}c\psi_5 - b_{5y}s\psi_5)] \\
 A_{31} &= m_5L_1 [s\psi_3(b_{5x}s\psi_5 + b_{5y}c\psi_5) + c\psi_3(b_{5x}c\psi_5 - b_{5y}s\psi_5)] \\
 A_{32} &= m_5L_2 [s\psi_4(b_{5x}s\psi_5 + b_{5y}c\psi_5) + c\psi_4(b_{5x}c\psi_5 - b_{5y}s\psi_5)] \\
 A_{33} &= m_5 \left[(b_{5x}s\psi_5 + b_{5y}c\psi_5)^2 + (b_{5x}c\psi_5 - b_{5y}s\psi_5)^2 \right] + I_5 \\
 B_1 &= \tau_3 - k_3\psi_3 + k_4(\psi_4 - \psi_3) - \beta_3\dot{\psi}_3 + \beta_4(\dot{\psi}_4^2 - \dot{\psi}_3^2) + \\
 &\quad + m_3 \left(b_{3x}\dot{\psi}_3^2 s\psi_3 + b_{3y}\dot{\psi}_3^2 c\psi_3 - m_3g \right) (b_{3x}c\psi_3 - b_{3y}s\psi_3) + \\
 &\quad + m_4L_1s\psi_3 \left(b_{4y}\dot{\psi}_4^2 s\psi_4 - L_1\dot{\psi}_3^2 c\psi_3 - b_{4x}\dot{\psi}_4^2 c\psi_4 \right) + \\
 &\quad - m_4L_1c\psi_3 \left(g - L_1\dot{\psi}_3^2 s\psi_3 - b_{4x}\dot{\psi}_4^2 s\psi_4 - b_{4y}\dot{\psi}_4^2 c\psi_4 \right) + \\
 &\quad + m_5L_1s\psi_3 \left(\dot{\psi}_5^2 (b_{5y}s\psi_5 - b_{5x}c\psi_5) - L_1\dot{\psi}_3^2 c\psi_3 - L_2\dot{\psi}_4^2 c\psi_4 \right) + \\
 &\quad + m_5L_1c\psi_3 \left(\dot{\psi}_5^2 (b_{5x}s\psi_5 + b_{5y}c\psi_5) + L_1\dot{\psi}_3^2 s\psi_3 + L_2\dot{\psi}_4^2 s\psi_4 - g \right); \\
 B_2 &= \tau_4 - k_4(\psi_4 - \psi_3) + k_5(\psi_5 - \psi_4) - \beta_4(\dot{\psi}_4 - \dot{\psi}_3) + \beta_5(\dot{\psi}_5 - \dot{\psi}_4) \\
 &\quad + m_4 \left(-L_1\dot{\psi}_3^2 c\psi_3 - b_{4x}\dot{\psi}_4^2 c\psi_4 + b_{4y}\dot{\psi}_4^2 s\psi_4 \right) (b_{4x}s\psi_4 + b_{4y}c\psi_4) \\
 &\quad + m_4 \left(L_1\dot{\psi}_3^2 s\psi_3 + b_{4x}\dot{\psi}_4^2 s\psi_4 + b_{4y}\dot{\psi}_4^2 c\psi_4 - g \right) (b_{4x}c\psi_4 - b_{4y}s\psi_4) \\
 &\quad + m_5L_2s\psi_4 \left(-L_1\dot{\psi}_3^2 c\psi_3 - L_2\dot{\psi}_4^2 c\psi_4 - b_{5x}\dot{\psi}_5^2 c\psi_5 + b_{5y}\dot{\psi}_5^2 s\psi_5 \right) \\
 &\quad + m_5L_2c\psi_4 \left(L_1\dot{\psi}_3^2 s\psi_3 + L_2\dot{\psi}_4^2 s\psi_4 + b_{5x}\dot{\psi}_5^2 s\psi_5 + b_{5y}\dot{\psi}_5^2 c\psi_5 + g \right) \\
 B_3 &= \tau_5 - k_5(\psi_5 - \psi_4) - \beta_5(\dot{\psi}_5 - \dot{\psi}_4) + \\
 &\quad + m_5 \left(L_2\dot{\psi}_4^2 s\psi_4 + L_1\dot{\psi}_3^2 s\psi_3 + g \right) (b_{5x}c\psi_5 - b_{5y}s\psi_5) + \\
 &\quad - m_5 \left(L_1\dot{\psi}_3^2 c\psi_3 + L_2\dot{\psi}_4^2 c\psi_4 \right) (b_{5x}s\psi_5 + b_{5y}c\psi_5);
 \end{aligned}$$

LIST OF TABLES

Table 1: Historical Spacecraft Cabin and Spacesuit Atmospheres.....	11
Table 2: Summary of U.S. Extravehicular Activity Duration Program (1965 to 2009).	16
Table 3: Main dimension of the human hand measured on a sample of male and female U.S. Air Force members.	47
Table 4: Mean length of the human hand measured on a sample of male and female U.S. Air Force members.	48
Table 5: Main dimensions of each articulation on a sample of male and female U.S. Air Force members.	48
Table 6: Mean length of the human hand and phalanges of index, middle, ring and little.	48
Table 7: Main static constraints of the human hand.	50
Table 8: Dynamic constraints of the human hand during a circular grasp.	52
Table 9: Dynamic constraints of the human hand during a prismatic grasp.	52
Table 10: Exhaustive grasp taxonomy	54
Table 11: Maximum forces exerted by the human phalanges during cylindrical power grasp (An).....	56
Table 12: Assumed values of phalanges lengths and joints angles used to calculate the joint torque (An).	56
Table 13: Joint torques exerted by human fingers in cylindrical grasp (An).	57
Table 14: Average distribution of forces during a circular power grip (Lowe).	57
Table 15: Maximum forces measured at the fingertip (left) and the corresponding maximum torques (right) (Sutter).	58
Table 16: Maximum torque capabilities of human finger joints considering both An and Sutter works...58	58
Table 17: Measurement of the abduction adduction forces in different conditions (An).	59
Table 18: Comparison between results from Astin, Mathiowetz and Imrhan studies.....	59
Table 19: Results of the Bratz study.	59
Table 20: Modified Denavit Hartenberg parameters for the four fingers.....	64
Table 21: Modified Denavit Hartenberg parameters for the Thumb.	65
Table 22: Anthropometric data and numerical constants used in the simulation.	72
Table 23: Hand Capabilities and related Performances.....	77
Table 24: Values of quality factors coefficient used during the following simulations	148

LIST OF FIGURES

Figure 1: Three main milestones in the EVA history: Leonov during the first spacewalk March 18, 1965 (left), Ed White during the first U.S. spacewalk June 3, 1965 (center) and Buzz Aldrin during the first moon landing mission July 21, 1969 (right).	9
Figure 2: Annual cumulative hours of EVA, showing the "EVA Wall" achieved during ISS construction.	17
Figure 3: Annual cumulative hours of projected EVA, showing the "mountain of EVA" for Exploration Missions.	17
Figure 4: The transmission mechanism of Tokyo University Hand Exoskeleton	23
Figure 5: The University of Tokyo hand exoskeleton (left) and its Data Glove (right).....	23
Figure 6: The Berlin University Hand Exoskeleton.....	24
Figure 7: Mechanical structure of the AFX Hand.	24
Figure 8: Measurement system of the wire tension.....	25
Figure 9: The Pittsburg University Hand Exoskeleton.....	25
Figure 10: The mechanism for the first phalanx (left) and for the other two (right).	26
Figure 11: The HANDEXOS Exoskeleton in three different configurations.....	26
Figure 12: The actuation and transmission system.	27
Figure 13: The Sabanci University Hand Exoskeleton.....	28
Figure 14: The compliant mechanism.....	28
Figure 15: The SKK Hand Master.....	29
Figure 16: The PECRO Hand Exoskeleton.....	30
Figure 17: The double parallelogram mechanism (left) and the crossed parallelogram (right).....	30
Figure 18: Different wire driven solution with a single pulley (right) and multiple pulleys (middle and right).....	30
Figure 19: The DLR/HIT Hand Exoskeleton.	31
Figure 20: The Paris Hand Exoskeleton.....	32
Figure 21: The Nanjing University Hand Exoskeleton.	33
Figure 22: The Rutgers Master Hand Exoskeleton.....	34
Figure 23: The University of Tsukuba Hand Exoskeleton.....	34
Figure 24: The Okayama University Hand Exoskeleton (left) and the two different pneumatic artificial muscles (right).....	35
Figure 25: The Tokyo Institute of Technology Hand Exoskeleton.....	36
Figure 26: The Vanderbilt University Hand Exoskeleton.	37
Figure 27: The Shadow Hand.	38
Figure 28: The Yokoi Hand.	39
Figure 29: The RAPHaEL Hand.....	39
Figure 30: The EH1 Milano Hand.	40
Figure 31: Examples of sensors: 1) Electro-goniometer, 2) Flexible Stretch Sensor, 3) Bend or Flex Sensor, 4) Strain Gauge Sensors, 5) Surface EMG Sensor, 6) Finger Tactile Pressure Sensor, 7) Piezoelectric Sensors.....	41

List of Figures

Figure 32: Anatomical details of the human hand.....	46
Figure 33: Hand motion terminology.....	46
Figure 34: Six hand groups based on the grasped object shape.....	53
Figure 35: Two hand groups based on the purpose of the task: power grip (left) and precision grip (right)	53
Figure 36: Vector diagram for the torque computation.....	56
Figure 37: Kinematic chain of the human hand.....	61
Figure 38: Direct and Inverse Kinematics.	62
Figure 39: Visual representation of the modified Denavit Hartenberg parameters.	63
Figure 40: Inverse Kinematics of the four Fingers.	67
Figure 41: Inverse Kinematics of the Thumb.	68
Figure 42: Dynamic of the finger: reference frames and centre of masses.	69
Figure 43: Dynamic of the finger: external forces.	72
Figure 44: Behavior of the joint angles during the simulation.	73
Figure 45: Behaviour of the joint torques during the simulation.	74
Figure 46: Three elements of Orlan-DM EVA glove; from left to right: bladder, restraint, ITMG	78
Figure 47: The glove into the space (left) and the glove inside the glove box (right)	79
Figure 48: The custom-made glove box and all its elements	79
Figure 49: Detail of the airtight locking joint between the custom-made flange (blue) and the forearm Orlan-DM seal (green)	80
Figure 50: The Orlan-DM EVA glove inside the custom-made glove box with ITMG (left) and without ITMG (right).....	80
Figure 51: Pneumatic Dynamometer Circuit Scheme composed by Bulb Syringe (S), Constant Volume (V) and Manometer (M)	82
Figure 52: Home Made Measurement Setup outside (Left) and inside (Right) the Glove Box	82
Figure 53: The four typologies of Hand Tasks: Power Grip (Top Left), Two Finger Pinch (Top Right), Three Finger Pinch (Bottom Left) and Lateral Pinch (Bottom Right)	83
Figure 54: Difference between Man and Women barehanded Power Grip; results represented in absolute values (left) and represented as MVC percentage (right)	84
Figure 55: Effects of wearing the EVA glove in different conditions on power grip performances (top left)	85
Figure 56: Effects of wearing the EVA glove in different conditions on two-finger pinch performances (top right)	85
Figure 57: Effects of wearing the EVA glove in different conditions on three-finger pinch performances (bottom left).	85
Figure 58: Effects of wearing the EVA glove in different conditions on lateral pinch performances (bottom right)	85
Figure 59: Effects of wearing the EVA glove in different conditions on the total number of repetitions for different tasks	86
Figure 60: Effects of wearing the EVA glove in different conditions on the maximum force exerted for different tasks	87

List of Figures

Figure 61: Comparison between the performances obtained by executing the power grip and the three-finger pinch tasks in barehanded conditions (left) and wearing the unpressurized glove (right).....	88
Figure 62: Distributed pressure sensor Grip TM (left) and the suggested sensor placement on hand or glove (right).....	90
Figure 63: Distributed pressure sensor fixed on the latex glove	90
Figure 64: The Test Protocol composed by the sequence of Four Hand positions: finger straight (top left), only first phalanx bended (top right), first and second phalanges bended (bottom right) and second and third phalanx bended (bottom left).....	91
Figure 65: Two examples of the instantaneous pressure distribution plotted on the Hand-Like graph obtained from the acquisition system of the GripTM sensor.....	92
Figure 66: First 40 second of data acquired related to the force applied by the EVA glove on the Index Finger (top left)	93
Figure 67: First 40 second of data acquired related to the force applied by the EVA glove on the Middle Finger (top right)	93
Figure 68: First 40 second of data acquired related to the force applied by the EVA glove on the Ring Finger (bottom left).....	93
Figure 69: First 40 second of data acquired related to the force applied by the EVA glove on the Little Finger (bottom right)	93
Figure 70: The Four Hand Position with respect to the behavior of a general data collection.....	94
Figure 71: Behaviour of the position of instantaneous Centre of Force on each phalanx of the hand	94
Figure 72: Behaviour of the first 40 second of torques applied by the EVA glove on the Index Finger (top left)	95
Figure 73: Behaviour of the first 40 second of torques applied by the EVA glove on the Middle Finger (top right)	95
Figure 74: Behaviour of the first 40 second of torques applied by the EVA glove on the Ring Finger (bottom left).....	95
Figure 75: Behaviour of the first 40 second of torques applied by the EVA glove on the Little Finger (bottom right)	95
Figure 76: Torque selector and the behaviour of the torques related to the four different hand positions	96
Figure 77: Average values and associated standard deviation of the maximum torques applied on the Index finger phalanges during the four position of the hand protocol.....	97
Figure 78: Average values and associated standard deviation of the maximum torques applied on the Middle finger phalanges during the four position of the hand protocol.....	97
Figure 79: Average values and associated standard deviation of the maximum torques applied on the Ring finger phalanges during the four position of the hand protocol.....	97
Figure 80: Average values and associated standard deviation of the maximum torques applied on the Little finger phalanges during the four position of the hand protocol.....	97
Figure 81: The finger probe	98
Figure 82: Main dimensions of the finger probe	98
Figure 83: The pulley mechanism of the finger probe.....	99

List of Figures

Figure 84: Finger probe in front and inside the glove box.....	99
Figure 85: The mini-PCB installed on the distal phalange of the finger probe on a thin film of Kapton®	100
Figure 86: The sign convention of θ_P , θ_M and θ_D	100
Figure 87: Torque vs. angle of the proximal phalange θ_P in non-pressurized conditions.....	101
Figure 88: Torque vs. angle of the middle phalange θ_M for three values of θ_P in non-pressurized conditions.....	102
Figure 89: Interpolation surface describing the torque of the PIP joint in non-pressurized conditions ..	102
Figure 90: Torque vs. angle of the distal phalange θ_D non-pressurized conditions.....	103
Figure 91: Interpolation surface describing the torque of the DIP joint non-pressurized conditions.....	104
Figure 92: Torque vs. angle of the proximal phalange θ_P in pressurized conditions	104
Figure 93: Torque vs. angle of the middle phalange θ_M for three values of θ_P in pressurized conditions	105
Figure 94: Interpolation surface describing the torque of the PIP joint in pressurized conditions.....	105
Figure 95: Torque vs. angle of the distal phalange θ_D pressurized conditions	106
Figure 96: Interpolation surface describing the torque of the DIP joint pressurized conditions	106
Figure 97: Torque vs. angle of the proximal phalange θ_P in the two pressure conditions	107
Figure 98: Torque vs. angle of the middle phalange θ_M in the two pressure conditions	108
Figure 99: Torque vs. angle of the distal phalange θ_D in the two pressure conditions	108
Figure 100: Three possible solutions to overcome the problem of the finger crotch: sliding concentric surfaces (left), four bars mechanism (middle) and asymmetric design (right).....	112
Figure 101: Human knuckles Behaviour	113
Figure 102: Wire actuation with (left) and without (right) access to the joint.....	114
Figure 103: Concept structure with micro-machined holes (left) and with micro-pulleys (right).....	115
Figure 104: Main steps of the evolution of the wire actuated exoskeleton.....	116
Figure 105: First wire actuated design: detail of the phalanges (left), the whole test bench (middle) and the top view of the test bench (right).....	117
Figure 106: Three view of the exoskeleton phalanx.....	117
Figure 107: Generic i -th link of the exoskeleton.....	118
Figure 108: Third link of the exoskeleton	119
Figure 109: Third joint of the exoskeleton.....	120
Figure 110: Second link of the exoskeleton	121
Figure 111: Second and third joint of the exoskeleton.....	121
Figure 112: First link of the exoskeleton.....	122
Figure 113: Relationship between DIP and PIP joint	125
Figure 114: The free angle is the bending value obtained when no external torque is applied to the torsion spring.	126
Figure 115: Concept flow chart of the algorithm.....	127
Figure 116: Wire tension with different values of elastic parameters	129
Figure 117: Approaching towards a singularity configuration. From 1 to 3 the arm of the tension of wire decreases until it reaches the value zero in the fourth image.	130
Figure 118: Possible passing points of the wires through the phalanges.....	131

List of Figures

Figure 119: The first prototype of exoskeleton with its test bench	138
Figure 120: Operator hand and exoskeleton; top view (left) and side view (right)	139
Figure 121: Second wire actuated design: front view (left), the whole design (center) and the top view (right)	140
Figure 122: Two different joint solutions: two-piece joint (left) and one-piece joint (right)	140
Figure 123: Generic i-th link of the robotic structure.....	142
Figure 124: Friction effect due to the sliding of the wires inside the holes	143
Figure 125: Example of operating area. The green written cells respect the limit of tension.	146
Figure 126: Overall operating area (on the right), starting from a couple of operating areas (on the left).	147
Figure 127: Comparison among the four <i>operating areas</i> of the simulation 1	149
Figure 128: Comparison among the four <i>operating areas</i> of the simulation 2	158
Figure 129: Comparison among the two <i>operating areas</i> of the simulation 3.....	165
Figure 130: Modified operating area. In each cell the percentage of compensation guaranteed is reported.....	168
Figure 131: Operator hand and exoskeleton; top view (left) and side view (right)	171
Figure 132: Some examples of the stress analysis of the joints in which the thickness and diameter of the pin and hole were changed to compare the stress results.....	172
Figure 133: The double parallelogram mechanism	173
Figure 134: Second exoskeleton concept design.....	174
Figure 135: Detail of the kinematic constraints between two adjoining joints.....	174
Figure 136: First prototipe of the double parallelogram exoskeleton during the flexion movement	175
Figure 137: First prototipe of the double parallelogram exoskeleton coupled with the EVA glove	176

BIBLIOGRAPHY

- [1] T. Woods, "Advanced EVA System Design Requirements Study," MCDONNELL DOUGLAS: MDC-W0072, 1986.
- [2] D. S. F. Portree and T. R. C., Walking to Olympus: an EVA Chronology, University of Michigan Library, 1997.
- [3] P. E. Mack, From Engineering Science to Big Science: The NACA And NASA Collier Trophy Research Project Winners, NASA History Office, 1998.
- [4] T. W. Williams, "Techniques for Improving the Performance of Future EVA Maneuvering Systems," NTRS: NASA-CR-200882, 1995.
- [5] C. Murray and C. Bly Cox, Apollo: The Race to the Moon, Simon & Schuster, 1989.
- [6] A. A. Siddiqi, Sputnik and the Soviet Space Challenge, Univ Press of Florida, 2003.
- [7] M. A. Gast, "Commercial Spacewalking: Designing an EVA Qualification Program for Space Tourism," NTRS: JSC-CN-20156, 2010.
- [8] S. J. Cupples and S. A. Smith, "EVA - Don't Leave Earth Without It," NTRS: JSC-CN-24619, 2011.
- [9] N. R. Council, Recapturing a Future for Space Exploration: Life and Physical Sciences Research for a New Era, National Academies Press, 2011.
- [10] M. R. Powell, D. J. Horrigan, J. M. Waligora and N. W. T., Extravehicular Activities, Lea and Febiger, 1993.
- [11] J. T. Webb, M. D. Fischer, C. L. Heaps and A. A. Pilmanis, "Exercise with prebreathe appears to increase protection from decompression sickness: Preliminary findings," in *NASA. Johnson Space Center, Seventh Annual Workshop on Space Operations Applications and Research*, 1993.
- [12] J. Ross and M. Duncan, "Prebreathe Protocol for Extravehicular Activity Technical Consultation Report," NTRS: NASA/TM-2008-215124, 2008.
- [13] K. E. Lange, A. T. Perka, B. E. Duffield and J. F. F., "Bounding the Spacecraft Atmosphere Design Space for Future Exploration Missions," NTRS: NASA/CR—2005–213689, 2005.
- [14] C. W. Hixon, "Development and Fabrication of an Advanced Liquid Cooling Garment," NTRS: NASA-CR-125-101, 1978.
- [15] C. A. Watts and M. Vogel, "Spacesuit Portable Life Support System Breadboard (PLSS 1.0) Development and Test Results," in *42nd International Conference on Environmental Systems*, 2012.
- [16] S. J. Hoffman, "Advanced EVA Capabilities: A Study for NASA's Revolutionary Aerospace Systems Concept Programs," NTRS: NASA/TP—2004–212068, 2004.
- [17] ILCDover, "Space Suit Evolution From Custom Tailored To Off-The-Rack," ILC Dover Inc, 1994.
- [18] J. J. Kosmo, "Space suit extravehicular hazards protection development," NTRS: NASA-TM-100458, 1987.
- [19] J. F. Annis and P. Webb, "Development of a Space Activity Suit," NTRS: NASA-CR-1892, 1971.
- [20] S. T. Kenneth and J. M. Harold, US Spacesuits, Praxis Publishing Ltd., 2005.
- [21] R. Balinskas and R. Tepper, "Extravehicular Mobility Unit Requirements Evolution," NTRS: NAS 9-17873, 1994.

Bibliography

- [22] Hamilton, NASA Extravehicular Mobility Unit LSS/SSA Data Book, Hamilton Sundstrand, 2003.
- [23] N. C. Jordan, Multidisciplinary Spacesuit Modeling and Optimization: Requirement Changes and Recommendation for the Next-Generation Spacesuit Design, Master's Thesis, Dept of Aeronautics and Astronautics, Massachusetts Institute of Technology, 2006.
- [24] A. I. Skoog, I. P. Abramov, A. Y. Stoklitsky and M. N. Doodnik, "The Soviet-Russian spacesuits a historical overview of the 1960's," *Acta Astronautica*, vol. 51, no. 1-9, pp. 113-131, 2002.
- [25] A. Skoog and I. P. Abramov, Russian Spacesuits, Springer Verlag, 2003.
- [26] C. Gorguinpou, R. LeClair and D. Carval, "Advanced Two-System Space Suit," in *Fourth Annual HEDS-UP forum*, Berkley, California, USA, 2003.
- [27] D. Tourbier, J. Knudsen, A. Hargens, K. Tanaka, J. W. P. Waldie and C. Jarvis, "Physiological Effects of a Mechanical Counter Pressure Glove," in *31 st International Conference on Environmental Systems*, Orlando, Florida, USA, 2001.
- [28] K. Tanaka, J. Waldfie, G. Steinbach, P. Webb, D. Tourbier, J. Knudsen, C. Jarvis and A. Hargens, "Skin Microvascular flow during hypobaric exposure with and without a mechanical counter pressure space suit glove," *Journal of Aviation space and environmental Medicine*, vol. 73, no. 11, pp. 1074-1078, 2002.
- [29] D. Graziosi, J. Stein, A. Ross and J. Kosmo, "Phase VI Advanced EVA Glove Development and Certification for the International Space Station," in *31st International Conference on Environmental Systems*, 2001.
- [30] A. William, "ILC Space Suits & Related Products," *Apollo Lunar Surface Journal*, 2007.
- [31] L. A. Taylor, H. Scmitt, W. Carrier and N. M., "The lunar dust problem: From liability to asset," in *AIAA 1st Space Exploration Conference*, Orlando, Florida, 2005.
- [32] J. R. Gaier, "The Effects of Lunar Dust on EVA System during the Apollo Mission," NTRS: NASA/TM-2005-213610, Glenn Research Center, Cleveland, Ohio, 2005.
- [33] J. O'Hara, M. Briganti, J. Cleveland and D. Winfield, "Extravehicular Activities Limitation Study. Volume II: Establishment of Physiological and Performance Criteria for EVA Gloves," NTRS: AS-EVAL-FR-8701, New York, 1988.
- [34] L. Thompson, E. Kerstman and D. Butler, "Fingernail Injuries & NASA's Integrated Medical Model," NTRS: ID-20080043663, 2008.
- [35] S. England, E. Benson, M. Mesloh, S. Thompson and S. Rajulu, "Application of Spacesuit Glove Requirements Tools to Athletic and Personal Protective Equipment," JSC-CN-20022 , 2010.
- [36] S. Thompson, M. Mesloh, S. England, E. Benson and S. Rajulu, "The Effects of Extravehicular Activity (EVA) Glove Pressure on Tactility," JSC-CN-20034, 2010.
- [37] M. Mesloh, S. England, E. Benson, S. Thompson and S. Rajulu, "The Effects of Extravehicular Activity (EVA) Glove Pressure on Hand Strength," JSC-CN-19927, 2010.
- [38] S. Rajulu, M. Mesloh, S. Thompson, S. England and E. Benson, "The Effects of Extravehicular Activity (EVA) Glove Pressure on Hand Strength," 2010, Miami, Florida, U.S., 3rd International Conference on Applied Human.
- [39] R. Bishu and G. Klute, "Investigation of the effects of extravehicular activity (EVA) gloves on performance," NTRS: NASA-TP-3401, 1993.
- [40] R. Bishu and G. Klute, "The effects of extra vehicular activity (EVA) gloves on human performance," *International Journal of Industrial Ergonomics*, vol. 16, pp. 165-174, 1995.
- [41] W. Clapp, Design and Testing of an Advanced Spacesuit Glove, Space Systems Laboratory,

Bibliography

- Department of Aeronautics and Astronautics, Massachusetts Institute Technology, 1983.
- [42] F. Korona and D. Akin, "Evaluation of a hybrid elastic EVA glove," SAE: 2002-01-2311, 2002.
- [43] ILCDover, "Anti Microbial Material," ILCDover, [Online]. Available: <http://www.ilcdover.com/Anti-Microbial-Materials/>. [Accessed 06 June 2011].
- [44] J. Kosmo, J. Bassick and K. Porter, "Development of higher operating pressure extra vehicular space suit glove assemblies," in *18th Intersociety Conference on Environmental System*, San Francisco, California, 1988.
- [45] H. C. Wright, "Enhancement of Space suit Glove performance," in *AIAA 15th Intersociety Conference on Environmental System*, San Francisco, California, 1985.
- [46] K. Tanaka, P. Danaher and A. R. Hargens, "Mobility of the elastic counterpressure space suit glove," *Aviation, Space, and Environmental Medicine*, vol. 80, no. 10, pp. 890-893, 2009.
- [47] P. Danaher, K. Tanaka and A. R. Hargens, "Mechanical Counterpressure vs Gas-Pressurized spacesuit gloves: Grip and Sensitivity," *Aviation*, vol. 76, no. 4, pp. 381-384, 2005.
- [48] R. S. Heather, "Holding a Winning Hand," NASA Educational Technology Services, [Online]. Available: <http://www.nasa.gov/audience/foreducators/holding-a-winning-hand.html>. [Accessed 14 May 2011].
- [49] T. B. TV, "Astronaut Glove Challenge," Tech Brief TV, [Online]. Available: <http://video.techbriefs.com/video/Astronaut-Glove-Challenge>. [Accessed 27 June 2012].
- [50] "Cyber Glove Systems," Cyber Glove, [Online]. Available: <http://www.cyberglovesystems.com/>.
- [51] B. H. Choi and H. R. Choi, "A Semi-direct Drive Hand Exoskeleton Using Ultrasonic Motor," in *IEEE International Workshop on Robot and Human Interaction*, Pisa, Italy, 1999.
- [52] H. Fang, Z. Xie and L. H., "An Exoskeleton Master Hand for Controlling DLR/HIT Hand," in *IEEE/RSJ International Conference on Intelligent Robots and Systems*, St. Louis, USA, 2009.
- [53] S. Nakagawara, H. Kajimoto, N. Kawakami and S. Tachi, "An Encounter-Type Multi-Fingered Master Hand Using Circuitous Joints," in *IEEE International Conference on Robotics and Automation*, Barcelona, Spain, 2005.
- [54] L. Turki and P. Coiffet, "Dextrous Telemanipulation with Force Feedback in Virtual Reality," in *ACM-SIGCHI VRST*, Chiba, Japan, 1995.
- [55] H. Fang, Z. Xie, H. Liu, T. Lan and J. Xia, "An Exoskeleton Force Feedback Master Finger Distinguishing Contact and Non-contact mode," in *IEEE/ASME International Conference on Advanced Intelligent Mechatronics*, Singapore, 2009.
- [56] C. D. Takahashi, L. Der-Yeghaian, V. H. Le and S. C. Cramer, "A Robotic Device for Hand Motor Therapy After Stroke," in *IEEE 9th International Conference on Rehabilitation Robotics*, Chicago, IL (USA), 2005.
- [57] R. C. V. Loureiro and W. S. Harwin, "Reach & Grasp Therapy: Design and Control of a 9-DOF Robotic Neuro-rehabilitation System," in *IEEE 10th International Conference on Rehabilitation Robotics*, Noordwijk, The Netherlands, 2007.
- [58] Y. Hasegawa, Y. Mikami, K. Watanabe and Y. Sankai, "Five-Fingered Assistive Hand with Mechanical Compliance of Human Finger," in *IEEE International Conference on Robotics and Automation*, Pasadena, CA (USA), 2008.
- [59] A. Wege and G. Hommel, "Development and Control of a Hand Exoskeleton for Rehabilitation of Hand Injuries," in *IEEE International Conference on Robotics and Biomimetics*, Sanya, China, 2007.
- [60] L. Lucas, M. DiCicco and Y. Matsuoka, "An EMG-Controlled Hand Exoskeleton for Natural

Bibliography

- Pinching," *Journal of Robotics and Mechatronics*, vol. 16, no. 5, pp. 1-7, 2004.
- [61] M. Bouzit, G. Burdea, G. Popescu and R. Boian, "The Rutgers Master II—New Design Force-Feedback Glove," *IEEE/ASME Transactions On Mechatronics*, vol. 7, no. 2, pp. 256-263, 2002.
- [62] T. Noritsugu, H. Yamamoto, D. Sasaki and M. Takaiwa, "Wearable Power Assist Device for Hand Grasping Using Pneumatic Artificial Rubber Muscle," in *SICE Annual Conference*, Sapporo, Japan, 2004.
- [63] T. Kline, D. Kamper and B. Schmit, "Control System for Pneumatically Controlled Glove to Assist in Grasp Activities," in *IEEE, 9th International Conference on Rehabilitation Robotics*, Chicago, IL (USA), 2005.
- [64] H. Yamaura, K. Matsushita, R. Kato and H. Yokoi, "Development of Hand Rehabilitation System for Paralysis Patient – Universal Design Using Wire-Driven Mechanism," in *31st Annual International Conference of the IEEE EMBS*, Minneapolis, Minnesota (USA), 2009.
- [65] M. Fontana, A. Dettori, S. F. and B. M., "Mechanical design of a novel Hand Exoskeleton for accurate force displaying," in *IEEE International Conference on Robotics and Automation*, Kobe, Japan, 2009.
- [66] B. L. Shields, J. A. Main, S. W. Peterson and A. M. Strauss, "An Anthropomorphic Hand Exoskeleton to Prevent Astronaut Hand Fatigue During Extravehicular Activities," *IEEE Transactions on Systems, Man, and Cybernetics - Part A: Systems and Humans*, vol. 27, no. 5, pp. 668-673, 1997.
- [67] C. N. Schabowsky, S. B. Godfrey, R. J. Holley and P. S. Lum, "Development and pilot testing of HEXORR: Hand EXOskeleton Rehabilitation Robot," *Journal Of Neuroengineering And Rehabilitation*, vol. 7, no. 36, 2010.
- [68] "Robotic Technology Lends More Than Just a Helping Hand," NASA, [Online]. Available: http://www.nasa.gov/mission_pages/station/main/robo-glove.html.
- [69] T. T. Worsnopp, M. A. Peshkin, J. E. Colgate and D. G. Kamper, "An Actuated Finger Exoskeleton for Hand Rehabilitation Following Stroke," in *IEEE 10th International Conference on Rehabilitation Robotics*, Noordwijk, The Netherlands, 2007.
- [70] N. S. K. Ho, K. Y. Tong, X. L. Hu, K. L. Fung, X. J. Wei, W. Rong and E. A. Susanto, "An EMG-driven Exoskeleton Hand Robotic Training Device on Chronic Stroke Subjects," in *IEEE International Conference on Rehabilitation Robotics Rehabilitation*, Zurich, Switzerland, 2011.
- [71] H. Yamaura, K. Matsushita, R. Kato and H. Yokoi, "Development of Hand Rehabilitation System Using Wire-Driven Link Mechanism for Paralysis Patients," in *IEEE International Conference on Robotics and Biomimetics*, Guilin, China, 2009.
- [72] A. Wege and G. Hommel, "Development and Control of a Hand Exoskeleton for Rehabilitation of Hand Injuries," in *IEEE/RSJ International Conference on Intelligent Robots and Systems*, Berlin, Germany, 2005.
- [73] A. Wege, K. Kondak and H. G., "Force Control Strategy for a Hand Exoskeleton Based on Sliding Mode Position Control," in *IEEE/RSJ International Conference on Intelligent Robots and Systems*, Beijing, China, 2006.
- [74] M. DiCicco, L. Lucas and Y. Matsuoka, "Comparison of Control Strategies for an EMG Controlled Orthotic Exoskeleton for the Hand," in *IEEE International Conference on Robotics & Automation*, New Orleans, LA (USA), 2004.
- [75] A. Chiri, F. Giovacchini, N. Vitiello, E. Cattin, S. Roccella, F. Vecchi and M. C. Carrozza, "HANDEXOS: towards an exoskeleton device for the rehabilitation of the hand," in *IEEE/RSJ International Conference on Intelligent Robots and Systems*, St. Louis, USA, 2009.

Bibliography

- [76] I. H. Ertas, E. Hocaoglu, D. E. Barkana and V. Patoglu, "Finger Exoskeleton for Treatment of Tendon Injuries," in *IEEE 11th International Conference on Rehabilitation Robotics ICORR*, Kyoto, Japan, 2009.
- [77] B. H. Choi and H. R. Choi, "SKK Hand Master, -Hand Exoskeleton Driven by Ultrasonic Motors," in *IEEE/RSJ International Conference on Intelligent Robots and Systems*, Takamatsu, Japan, 2000.
- [78] M. Fontana, M. Bergamasco and F. Salsedo, ""Mechanical Design and Experimental Characterization of a Novel Hand Exoskeleton," in *AIMETA, Associazione Italiana di Meccanica Teorica e Applicata*, Ancona, Italy, 2009.
- [79] P. Stergiopoulos, P. Fuchs and C. Laugeau, "Design of a 2-Finger Hand Exoskeleton for VR Grasping Simulation," in *EuroHaptics 2003*, Dublin, Ireland, 2003.
- [80] S. L. Springer and N. J. Ferrier, "Design and Control of a Force-Reflecting Haptic Interface for Teleoperational Grasping," *Transaction of ASME - Journal of Mechanical Design*, vol. 124, no. 1, pp. 277-283, 2002.
- [81] Z. Sun, X. Miao and X. Li, "Design of a bidirectional force feedback dataglove based on pneumatic artificial muscles," in *IEEE International Conference on Mechatronics and Automation ICMA*, Changchun, China, 2009.
- [82] Y. Hasegawa, Y. Mikami, K. Watanabe, Z. Firouzimehr and Y. Sankai, "Wearable Handling Support System for Paralyzed Patient Yasuhisa," in *IEEE/RSJ International Conference on Intelligent Robots and Systems*, Nice, France, 2008.
- [83] D. Sasaki, T. Noritsugu and M. Takaiwa, "Development of Pneumatic soft Rubber Hand for Human Friendly Robot," *Journal of Robotic and Mechatronic*, vol. 15, no. 2, pp. 164-171, 2003.
- [84] T. Noritsugu, D. Sasaki and M. Takaiwa, "Application of Artificial Pneumatic Rubber Muscles to a Human Friendly Robot," in *IEEE International Conference on Robotics and Automation*, Taipei, Taiwan, 2003.
- [85] K. Tadano, M. Akai, K. Kadota and K. Kawashima, "Development of grip amplified glove using bi-articular mechanism with pneumatic artificial rubber muscle," in *IEEE International Conference on Robotics and Automation (ICRA)*, Anchorage, Alaska, USA, 2010.
- [86] "Shadow Dexterous Hand," Shadow Robot Company, [Online]. Available: <http://www.shadowrobot.com/products/dexterous-hand/>.
- [87] H. Yokoi, A. Hernandez-Arieta, R. Katoh and W. Yu, "Mutual adaptation in a prosthetics applications," *Embodied Artificial Intelligence*, pp. 146-159, 2004.
- [88] G. Gomez, A. H. Arieta, H. Yokoi and P. E. Hotz, "University Of Zurich - Robots," [Online]. Available: <http://www.ifi.uzh.ch/ailab/robots.html>.
- [89] "RAPHaEL: Robotic Air Powered Hand with Elastic Ligaments," Robotics and Mechanics Laboratory, [Online]. Available: http://www.romela.org/main/RAPHaEL:_Robotic_Air_Powered_Hand_with_Elastic_Ligaments.
- [90] "Robotic Forearms," Prensilia Grasping Innovation, [Online]. Available: <http://www.prensilia.com/index.php?q=en/node/41>.
- [91] "The best five anthropomorphic robotic hands/arms," [Online]. Available: <http://mindtrans.narod.ru/hands/hands.htm>.
- [92] M. M. Foumashi, M. Troncossi and V. P. Castelli, "State-of-the-Art of Hand Exoskeleton Systems," [Online]. Available: http://amsacta.unibo.it/3198/1/Mozaffari-et-al_2011.pdf.
- [93] "Survey of Haptic Interfaces: Force Feedback," [Online]. Available:

Bibliography

- [http://home.12move.nl/~sh290334/dbase_force/.](http://home.12move.nl/~sh290334/dbase_force/)
- [94] P. Creveri, P. Lopomo, A. Pedotti and G. Ferrigno, "Derivation of Centres and Axes of Rotation for Wrist and Fingers in a Hand Kinematic Model: Methods and Reliability Results," *Annals of Biomedical Engineering*, vol. 33, no. 3, pp. 402-412, 2005.
- [95] "Hand Anatomy," American Society for Surgery of the Hand, [Online]. Available: <http://www.assh.org/Public/HandAnatomy/Pages/default.aspx>.
- [96] J. D. Garrett, "Anthropometry of the hands of male air force flight personnel," Aerospace Medical Research Laboratory, Air Force system command, Wright-Patterson Air Force Base, Ohio, 1970.
- [97] J. W. Garrett, "Anthropometry of the hands of female air force flight personnel," Aerospace Medical Research Laboratory, Air Force system command, Wright-Patterson Air Force Base, Ohio, 1970.
- [98] S. R. Habib and N. N. Kamal, "Stature estimation from hand and phalanges lengths of Egyptians," *Journal of Forensic and Legal Medicine*, vol. 17, no. 3, pp. 156-160, 2010.
- [99] O. P. Jasuja and G. Singh, "Estimation of stature from hand phalange length," *Journal of Indian Academy of Forensic Medicine*, vol. 26, no. 3, 2004.
- [100] S. Cobos, M. Ferre, M. A. Sanchez-Uran and J. Ortego, "Constraints for Realistic Hand Manipulation," in *The 10th Annual International Workshop on Presence*, Barcelona, Spain, 2007.
- [101] H. Rijpkema and M. Girard, "Computer animation of Knowledge-based Human Grasping," in *Computer graphics and interactive techniques*, New York, U.S., 1991.
- [102] C. L. Taylor and R. J. Schwartz, "The Anatomy and Mechanics of the Human Hand," *Artificial Limbs*, vol. 2, pp. 22-35, 1955.
- [103] J. R. Napier, "The Prehensile Movements of The Human Hand," *Journal of bone and Joint Surgery*, vol. 38, no. 4, pp. 902-913, 1956.
- [104] T. Feix, R. Pawlik, S. H.B., J. Romero and D. Kragic, "A comprehensive grasp taxonomy," in *Robotics, Science and Systems: Workshop on Understanding the Human Hand for Advancing Robotic*, 2009.
- [105] O. Bock, T. Feix, J. Romero and D. Kragic, "Human Grasping Database," [Online]. Available: <http://grasp.xief.net/>. [Accessed 29 october 2012].
- [106] M. Mishkin and B. M. Jau, "Space-Based Multifunctional End Effector Systems: Functional Requirements and Proposed Design," NTRS: NASA-JPL-88-16, 1988.
- [107] J. K. Salisbury, Kinematic and Force Analysis of Articulated Hands, PhD thesis, Stanford University, Dept. of Mech. Eng, 1982.
- [108] S. C. Jacobsen, E. K. Iversen, C. C. Davis, M. D. Potter and T. W. McLain, "Design of a Multiple Degree of Freedom, Force Reflective Hand Master/Slave with a High Mobility Wrist," in *Third Topical Meeting on Robotics and Remote Systems*, Charleston, South Carolina, March 13-16, 1989.
- [109] G. Burdea, J. Zhuang, E. Roskos, D. Silver and N. Langrana, "A Portable Dextrous master With Force Feedback," *Presence*, vol. 1, no. 1, pp. 18-28, Januar January, 1992.
- [110] K. N. An, L. Askew and E. Y. Chao, "Biomechanics and Functional Assessment of Upper Extremities," *Trends in Ergonomics / Human Factors III*, pp. 573-580, 1986.
- [111] C. J. Hasser, "Force-Reflecting Anthropomorphic Hand Masters," Wright Patterson Air Force Base, Ohio, July, 1995.
- [112] B. D. Lowe, Y. Kong and J. Han, "Development and application of a hand force measurement system," in *XVIth Triennial Congress of the International Ergonomics Association*, Maastricht, The Netherlands, 2006.

Bibliography

- [113] P. H. Sutter, J. C. Iatridis and N. V. Thakor, "Response to Reflected-Force feedback to Fingers in Teleoperation," in *NASA Conference on Space Telerobotics*, NASA JPL, 1989.
- [114] K. H. Kroemer and E. M. Gienapp, "Hand Held Device to Measure Finger (Thumb) Strength," *Journal of Applied Physiology*, vol. 29, no. 4, pp. 526-527, October, 1970.
- [115] V. Mathiowetz, G. Kashman, G. Volland, K. Weber, M. Dowe and S. Rogers, "Grip and Pinch strength: normative data for adults," *Archives of Physical Medicine and Rehabilitation*, pp. 69-74, 1985.
- [116] S. N. Imrhan, "Trends in finger pinch strength in children, adults and the elderly," *Human Factors*, pp. 689-701, 1989.
- [117] K. J. Bretz, A. Jobbàgy and K. Bretz, "Force Measurement of Hand and Fingers," *Biomechanica Hungarica*, vol. 3, pp. 61-66, 2010.
- [118] W. G. Darling and K. J. Cole, "Muscle Activation Patterns and Kinetics of Human Index Finger Movements," *Journal of Neurophysiology*, vol. 63, no. 5, pp. 1098-1108, May, 1990.
- [119] W. G. Darling, "Personal Communication," 1995.
- [120] EXOS Inc, "Development of a Force Feedback Anthropomorphic Teleoperation Input Device for Control if Robot Hand," NTRS, NAS8-38910, Burlington, 1991.
- [121] J. M. Hollerbach, I. W. Hunter and J. Ballantyne, "A Comparative Analysis of Actuator Technologies for Robotics," *The Robotic Review* 2, 1991.
- [122] S. Cubero, Industrial Robotics: Theory, Modelling and Control, Germany: Pro Literatur Verlag, 2006.
- [123] J. J. Craig, Introduction to Robotics, Mechanics and Control, Upper Saddle River, New Jersey: Pearson Prentice Hall, 1986.
- [124] T. E. Milner and D. W. Franklin, "Characterization of Multijoint Finger Stiffness: Dependence on Finger Posture and Force Direction," *IEEE Transaction on Biomedical Engineering*, vol. 45, no. 11, pp. 1363-1375, 1998.
- [125] S. Rajulu, E. Benson, S. England, M. Mesloh and S. Thompson, "Use of a Tradition and Novel Methods to Evaluate the Influence of an EVA Glove on Hand Performance," in *40th International Conference on Environmental Systems*, Barcelona, Spain, 2010.
- [126] M. H. Welsh and D. L. Akin, "The Effects of Extravehicular Activity Gloves on Human Hand Performance," in *31st International Conference On Environmental Systems*, Orlando, Florida, U.S., 2001.
- [127] M. F. Ashby, Materials and the Environment, Butterworth-Heinemann, Elsevier, 2009.
- [128] G. S. Brady and H. R. Clouser, Materials Handbook, McGRAW-HILL, 1991.
- [129] G. G. Winspear, The Vanderbilt Rubber Handbook, Vanderbilt Company, 1968.
- [130] J. Brandup, E. H. Immergut and E. A. Grulke, Polymer handbook, Wiley, 1999.
- [131] T. Feix, R. Pawlik, H. Schmiedmayer, J. Romero and D. Kragic, "A comprehensive grasp taxonomy," in *Robotic Science and Systems: Workshop on Understanding the Human Hand for Advancing Robotic Manipulation*, 2009.
- [132] T. INC. [Online]. Available: www.tekscan.com.
- [133] A. Nicholas and S. Ariaifar, "Space environment threats and their impact on spacecrafts in near earth orbits," in *57th International Astronautical Congress*, 2006.
- [134] C. Dumont, G. Albus, D. Meesenburg, J. Fanghänel, K. Stürmer and H. Nägerl, "Morphology of the

Bibliography

- Interphalangeal Joint Surface and Its Functional Relevance," *Journal of Hand Surgery*, vol. 33, no. 1, pp. 9-18, 2008.
- [135] C. Ferraresi, M. Paoloni and F. Pescarmone, "A new 6-DOF parallel robotic structure actuated by wires: The Wiro-6.3," *Journal of Robotics Systems*, vol. 21, no. 11, pp. 581-595, 2004.
- [136] C. Ferraresi, C. Paoloni and F. Pescarmone, "A new methodology for the determination of the workspace of six-DOF redundant parallel structures actuated by nine wires," *Robotica*, vol. 25, no. 1, pp. 113-120, 2007.
- [137] K. Maeda, S. Tadokoro, T. Takamori, M. Hiller and R. Verhoeven, "On design of a redundant wire-driven parallel robot WARP manipulator," in *IEEE International Conference on Robotics and Automation*, Detroit, Michigan, 1999.
- [138] J. Albus, R. Bostelman and N. Dagalakis, "NIST Robocrane," *Journal of Robotic System*, vol. 10, no. 5, pp. 709-724, 1993.
- [139] S. Kawamura, W. Choe and S. Tanak, "Development of an ultralight speed robot falcon using wire driven systems," in *IEEE International Conference on Robotic and Automation*, Nagoya, Japan, 1995.
- [140] J. Merlet, *Parallel Robots*, Second Edition, Springer, Netherland, 2006.
- [141] J. Merlet, "Kinematics of a wire-driven parallel robot Marionet using linear actuators," in *International Conference on Robotics and Automation*, Pasadena, California, 2008.
- [142] M. Gouttefarde, J. P. Merlet and D. Daney, "Wrench, feasible workspace of parallel cable driven mechanism," in *International Conference on Robotics and Automation*, Rome, Italy, 2007.
- [143] S. R. Company, "The Shadow Dexterous Hand," [Online]. Available: <http://www.shadowrobot.com/hand/>.
- [144] R. a. M. C. DLR, "DLR Hand II," [Online]. Available: http://www.dlr.de/rm/en/desktopdefault.aspx/tabcid-3802/6102_read-8923/.
- [145] J. Leijnse, P. Quesada and C. Spoor, "Kinematic evaluation of the finger's interphalangeal joint coupling mechanism-variability, flexion-extension differences, triggers, locking swanneck deformities, anthropometric correlations," *Journal of Biomechanics*, vol. 43, no. 12, pp. 2381-2393, 2010.
- [146] H. In, D. Lee and K. J. Cho, "Investigation of friction characteristics of a tendon driven wearable robotic hand," in *International Conference on Control, Automation and Systems*, Gyeonggi-do, Korea, 2010.
- [147] L. B. Shields, J. A. Main, S. W. Peterson and A. M. Strauss, "An Anthropomorphic Hand Exoskeleton to Prevent Astronaut Hand Fatigue During Extravehicular Activities," *IEEE Transactions on systems, man, and cibernetics*, vol. 27, no. 5, pp. 668-673, 1997.
- [148] H.- Fang, Z. Xie and H. Liu, "An Exoskeleton Master Hand for Controlling DLR/HIT Hand," in *IEEE/RSJ International Conference on Intelligent Robots and Systems*, St. Luis, USA, 2009.
- [149] B. H. Choi and H. R. Choi, "SKK Hand Master, Hand Exoskeleton Driven by Ultrasonic Motors," in *IEEE/RSJ International Conference on Intelligent Robots and Systems*, 2000.
- [150] NASA, "Man-Systems Integration Standards, Volume I, Section 14," NASA-STD-3000, 1995.